

Table of Contents

Damage tolerant design: failure and crack propagation in composites., G. Pereira [et al.]	1
Convex Optimization of Space Frame Support Structures for Offshore Wind Turbines, K. Sandal [et al.]	6
Effect of laminate thickness on the static and fatigue properties of wind turbine composites, F. Lahuerta [et al.]	10
Development of a wind farm tool using advanced actuator disk models, M. Moens [et al.]	15
The right size matters: Investigating the offshore wind turbine market equilibrium, N. Ederer.....	19
DISTRIBUTED CONTROL OF WIND FARMS USING A FLOW INTERACTION MODEL AND A MULTI-AGENT APPROACH, M. Vali [et al.]	31
COMBINING MODEL-BASED AND DATA-DRIVEN OPTIMIZATION OF WIND FARM OPERATION IN A LEARNING DATABASE, A. Rott [et al.]	35
AGGREGATE WIND FARM POWER PERFORMANCE CURVES, A. Elmontaser.....	39
Towards Implementation of an Optimization Tool for Rotor Blades based on the Adjoint Method in OpenFOAM, L. Vorspel [et al.]	43
CFD analysis of a 2-bladed multi-megawatt turbine, L. Klein [et al.]	47
Numerical investigations of a passive load alleviation technique for wind turbines, A. Fischer [et al.] ...	51
LARGE-EDDY SIMULATIONS OF S826 AIRFOIL WITH DISCONTINUOUS GALERKIN METHODOLOGY, A. Frère [et al.]	55
Increased Order Modeling of the Aerodynamic Characteristics of Flexible Blades, Z. Wang.....	59
Hybrid aerodynamic analysis of wind turbines, M. Schwarz [et al.]	63
UNSTEADY AERODYNAMICS OF AIRFOILS FOR SMALL HAWT AT LOW REYNOLDS NUMBERS, D. Holst [et al.]	67
CFD coupled with WRF for Wind Power Prediction, E. Leblebici [et al.]	71
Aerodynamic Modeling for Equal Fidelity Aeroelastic Analysis, T. Hegberg.....	76
AERODYNAMIC DAMPING OF WIND TURBINES UNDER CONSTANT AND TURBULENT WIND, S. Schafhirt [et al.]	80
The Low Induction Rotor, P. Mills [et al.]	84
Aerodynamic Performance Losses due to Ice Buildup in Wind Turbines, O. Yirtici [et al.]	88
Implementation of Passive Control Strategies through Swept Blades, C. Pavese [et al.]	92
Integrated aero-structural optimization of wind turbine rotors, P. Bortolotti [et al.]	96
Design of a Floating Wind Turbine to Measure the Coupled Response to Wind and Wave Action, C. Gilmour.....	100
EXPERIMENTAL METHODS FOR THE OPTIMAL DESIGN OF SMALL WIND TURBINES, N. Bartolini [et al.]	105
FLAPS FOR WIND TURBINE APPLICATION: NOISE SOURCE LOCALIZATION ON A TEST AIRFOIL, C. Brand [et al.]	109
Numerical Investigation of an Airfoil with Morphing Trailing Edge for Load Reduction, T. Wolff [et al.]	

.....	114
CFD studies of a 10 MW wind turbine equipped with active trailing edge flaps, E. Jost [et al.]	119
Wake Flow Model for Wind Farm Control, T. Ahmad [et al.]	123
Effects of Tip-Injection on the Flow Downstream of a Model Wind Turbine Rotor Blade Tip, A. Abdulrahim [et al.]	127
Determining the Wind Speed Distribution within a Wind Farm considering Site Wind Characteristics and Wake Effects, T. Ahmad [et al.]	131
Feedback control of blades trailing edge flap for blade root load mitigation, R. Ungurán [et al.]	135
Investigate derivation of a wind turbine dynamics from measured data, L. Reguera [et al.]	139
Controlling Large Wind Turbines ? The effect of wind turbine size on controller design, C. Siddons [et al.]	143
CLARIFYING THE PERFORMANCE OF COORDINATED CONTROL FOR LARGE WIND TURBINE LOADS, D. Danzerl [et al.]	147
Simulation of wind turbines in complex terrain by means of direct CFD, C. Schulz [et al.]	151
3D stochastic gusts as an alternative to the Mexican hat wavelet, R. Bos [et al.]	155
Modelling and Evaluation of Wind Speed Time Series for Reliability Analysis of Offshore Wind Farms, C. Smith [et al.]	159
Investigating the interaction between wind turbines and atmospheric flow with a coupling of the aeroelastic code FAST and the LES code PALM, M. Bromm [et al.]	163
UNSTEADY AND TURBULENT ROTOR LOADS, S. Ehrich [et al.]	167
Influence of the atmospheric boundary layer on wind farm control, L. Vollmer [et al.]	171
Analysis of Inflow parameters using LiDARs, A. Giyanani [et al.]	175
Power System Dynamic Responses - Comparison between simple Simulink model and more complex time-step based dynamic response modelling, M. Argent.....	179
Investigating the Effects of Pitch Control Strategy on the Power Electronics Lifetime of a Vertical Axis Wind Turbine, R. Dawid.....	183
Vertical Axis Wind Turbine Hydraulic Drivetrain Options, E. Macmahon [et al.]	187
MARE-WINT Project: Improving the Reliability and Optimising O&M Strategies for Offshore Wind Turbines, R. Mehdi [et al.]	192
Wind Prediction Enhancement by Supplementing Measurements with Numerical Weather Prediction Now-Casts., A. Malvaldi [et al.]	196

“

Materials and structures

”

Damage tolerant design: failure and crack propagation in composites.

G. Pereira¹, L. Mikkelsen¹, M. McGugan¹

¹Technical University of Denmark, Wind Energy, Frederiksborgvej
399, 4000 Roskilde, gfpe@dtu.dk

1. Introduction

The most eye-catching trend for wind energy structural components is the up-scaling where new turbine designs have consistently provided larger towers, rotor diameters, and power ratings. The wind energy industry must compete with other energy sources by reducing the cost of energy, and the most cost effective way of increasing the power produced by a wind turbine is to increase the rotor diameter [1]. The industry relies on advances in materials technology and design philosophy to deliver the most cost-effective light-weight structures.

The historical design philosophy for reinforced polymer structures (main material of wind turbine blades) is based on conservative analysis methods, with large safety factors, underestimating the material properties, and considering only the linear behaviour of the material. As knowledge about the material and structure behaviour increased it became possible to safely adopt more advanced design philosophies, such damage tolerant design, where the material capability is fully exploited. This trend to more advanced structural design is described by *Braga*[2].

To achieve this, some research groups are working on a Multi-physics Global Model [3-7] as represented by the table 1. A Multi-physics Global Model is defined as a fluid-structural interaction model, which aims to integrate several phenomena models as aerodynamics, hydrodynamics, aero-elasticity, structural, vibration, energy output, control, etc. Moreover, damage tolerant design requires a good understanding of the material behaviour, and models capable to simulate the behaviour of the structure when damaged. However, this approach will not be achieved until all physical phenomena present on the wind energy field are fully understood. Wind turbines are a multi-physics problem, and the complexity of the structure, the unpredictability of the wind and the lack of understanding of specific phenomena create challenges for the application of damage tolerance design method.

Table 1: Multi-physics Global Model scale main research topics.

Scale 100-1000 Km	Weather Forecast; Environment Conditions; Transport and Assembly; Maritime risk assessment; Maritime route planning;
Scale 1-10 Km	Aerodynamic design- Large Eddy Simulation; Turbulence; Wake effect between towers; Maritime risk assessment: ship collision;
Scale 10-500 m	Aerodynamic design- Blade profile shape; Floating structuring; Hydrodynamics; Aero-Hydro-elastic coupling; Interaction between wind, waves and the structural; Maintenance planning; Electric components; Gearbox; etc.
Scale 1-80 m	Structural design; Vibrations; Fatigue; Aero-Hydro-elastic coupling; Multibody analysis;
Scale 1mm-2m	Detail sub-structure design; Vibrations; Fatigues; Non-Linear Materials; Delamination; Bonded/connection joints; Manufacturing Plan;
Scale 1µm-10mm	Micro-mechanics; Material resistance; Sensor integration; Fibre-Matrix interface;

“Problem!! We don’t fully understand the input, so how can we rely on the output?”

Is already accepted that a global model that compiles all the theory required and predicts when the damage will occur and how it will propagate is practically impossible to create. The solution starts by accepting the presence of damage and unpredictability, but still ensuring the structural health of each turbine.

“Solution?? If we can’t model the structure, we should monitor the material and understand damage propagation.”

Detectable changes in response must exist between damaged and undamaged states, thus implying damage tolerance. Damage tolerance is a property emerging from the particular combination of structure design, loading environment, and material characteristics. Accepting that a distribution of damage types and locations can exist across a group of operating wind turbine blades, it follows that

each structure must be characterized individually with a unique "damage map" for that structure. Evaluating the severity of the particular combination of damage types requires models that describe the progression parameters for each type under the full range of operating conditions. Only in this way can condition based maintenance be effectively implemented.

2. Damage tolerant materials and structures

A damage tolerant behaviour is obtained when the stress-strain relationship is initial linear-elastic, but possesses significant non-linearity before failure. The structure will be designed to be loaded below the stress-value corresponding to the onset of non-linearity, however if the structure at some point is loaded beyond the linear-elastic regime, the resulting changes in stiffness will result in a measurable change in the local compliance of the structure. With respect to the propagation of a crack, damage tolerance implies that the crack growth should be stable, requiring that the applied load level for unstable crack growth should be significantly higher than the load level that initiates crack growth. A way to create damage tolerance is thus to make the crack propagation stable. For instance in the composite material/adhesive the delamination is accompanied by the formation of a crack bridging zone, where intact fibres connect the crack faces behind the tip, thus increasing the energy required for crack propagation (Damage tolerance mechanism) [8].

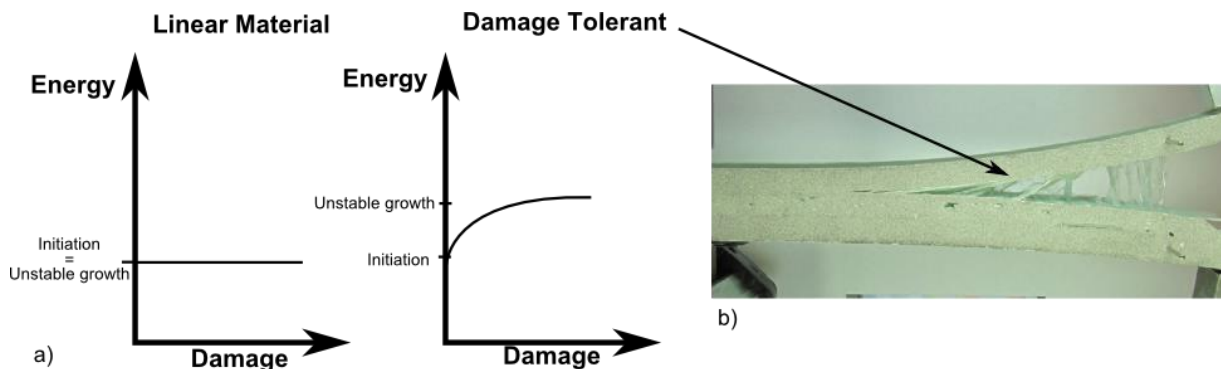


Figure 1: a) Conventional (Linear) material design philosophy vs Damage tolerant design; b) Damage tolerance mechanism- Fibre bridging.

With damage tolerant design philosophy the designers have the opportunity to create structures that can operate safely without propagating damage present in that structure, in this way they can fully exploit the material capability leading to structural optimisation.

3. Failure and crack propagation

In this study, the damage tolerance approach in wind turbine blade sub-structures was addressed, focusing on the crack growth mechanisms and detection methods. The trailing edge of the blade can develop damage in the composite material and adhesive interface. The delamination is accompanied by the formation of a crack bridging zone (Damage tolerance mechanism) [8]. A finite element model of the crack growth mechanisms in a double cantilever beam (DCB), representative of the trailing edge, was developed, where different fracture modes were addressed. Experimental tests were conducted in order to fully characterize this structure and support the model. Then a crack monitoring technique was implemented using Fibre Bragg Grating (FBG) sensors in order to track the crack and its propagation. This monitoring approach was incorporated into the finite element model (that was developed before) in order to predict the sensor output and extrapolate to a real trailing edge case. This sensor-structure makes possible to study the application of this monitoring technology in different components/ locations, with the objective of tracking different types of damage, as showed in figure 2.

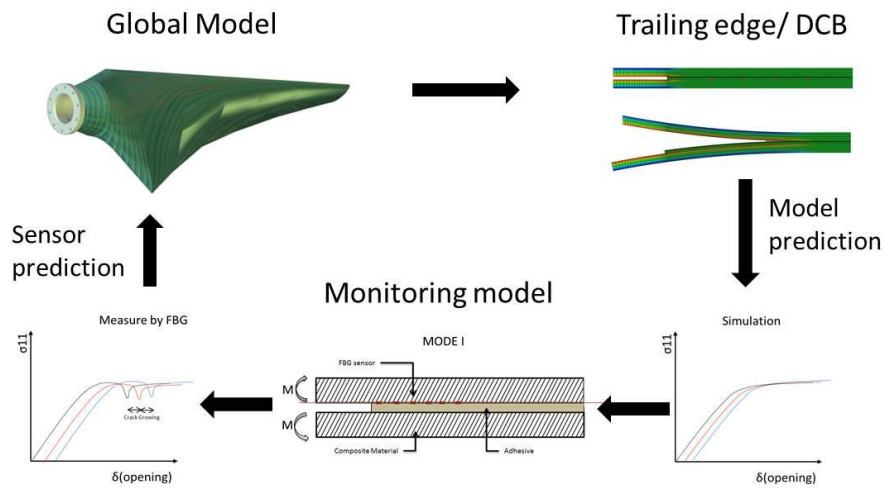
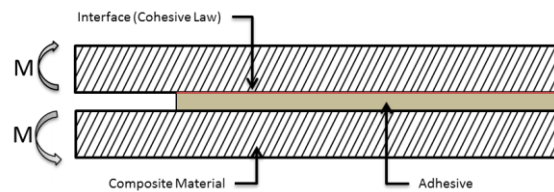


Figure 2: Modeling scheme of crack growing mechanisms and detection methods.

a. Finite element model and Sensor technology:

A 2D and 3D double cantilever beam (DCB) finite element model was developed in order to represent the crack growth phenomenon, based on a real trailing edge configuration used by the *DTU 10MW Reference Wind Turbine* [9]. It was used cohesive elements that describe the cohesive law that governs the crack growth mechanism. In table 2 the materials properties used in the DCB model is shown.

Table 2: Scheme and materials properties used in the DCB model.



Composite Material		Interface (Cohesive Law)		Adhesive	
Triaxial Fabric (Composite)	Uniaxial Fabric (Composite)	Elastic	Damage (Quadratic stress)	Damage Evolution	Elastic
$E_1=44.3$ GPa; $E_2=E_3=12.9$ GPa; $\nu_{12}=\nu_{13}=\nu_{23}=0.23$; $G_{12}=G_{13}=G_{23}=4393$	$E_1=23.8$ GPa; $E_2=E_3=15.05$ GPa; $\nu_{12}=\nu_{13}=\nu_{23}=0.513$; $G_{12}=G_{13}=G_{23}=4.393$ GPa	$K=4.2E12$ Pa;	$\sigma_n = 2.64$ MPa ; $\sigma_t = 22.15$ MPa	$\delta_1 = 1.4$; $\delta_2 = 0.37$;	$E=4.56$ GPa; $\nu=0.35$

Where E is the Young's modulus, ν is the Poisson's ration, G the shear modulus, K Penalty stiffness, δ displacement (opening) at failure, σ_n and σ_t the normal and shear traction.

b. Sensor technology:

Fibre optic sensors, such Fibre Bragg Gratings (FBG), can be embedded into the composite materials/adhesive, are virtually non-intrusive to the structure, and have the possibility to measure several points in a single fibre (multiplexing). This makes FBG's the perfect type of sensor to track the growing of certain damage types. A Fibre Bragg Grating (FBG) is formed when a permanent periodic modulation of the refractive index is induced along a section of an optical fibre, by exposing the optical fibre to an interference pattern of intense ultra-violet light[10]. The photosensitivity of the silica exposed to the ultra-violet light is increased, so when the optical fibre is illuminated by a broadband light source, the grating diffractive properties are such that only a very narrow wavelength band is reflected back.

When any external phenomenon creates a change on the grating, like temperature, strain, compression, non-uniform strain fields, etc. this will create a change in the reflected light. However, different phenomena acting on the grating will make different changes to the sensor response, like a fingerprint, so it will be possible to track specify phenomena, which are characteristic of damage.

c. Experimental validation:

After the FEM model been successful setup in order to represent the crack growth on the DCB specimen under the different loading conditions (Mode I/II). A dedicated algorithm predicted the sensor output, which allowed us to determine the presence of damage and it growth.

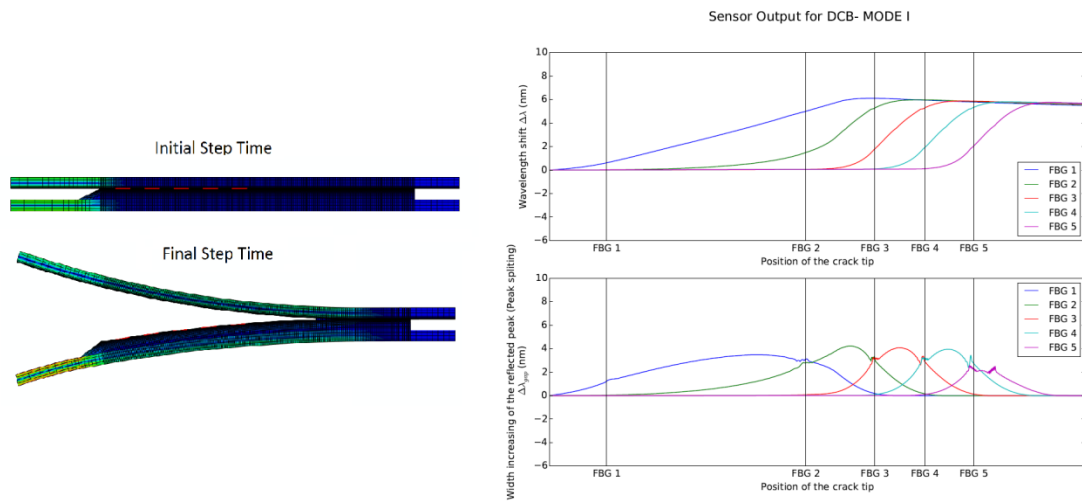


Figure 2: FEM model Sensor output for a Mode I loading case.

Then the same material/sensor configuration was tested in order to validate the pair structural-sensor model. The test was conducted using a double cantilever beam, as described by Sørensen [11] loaded in order to produce pure Mode I, Mode II and Mixed Mode fracture.

4. Results:

A good agreement between the FEM model and the experiments was found. The FEM model was able to represent the crack grow under the different loading cases. Also the sensor output model match the experiments, showing a specific sensor response (“fingerprint”) when under the effect of a crack.

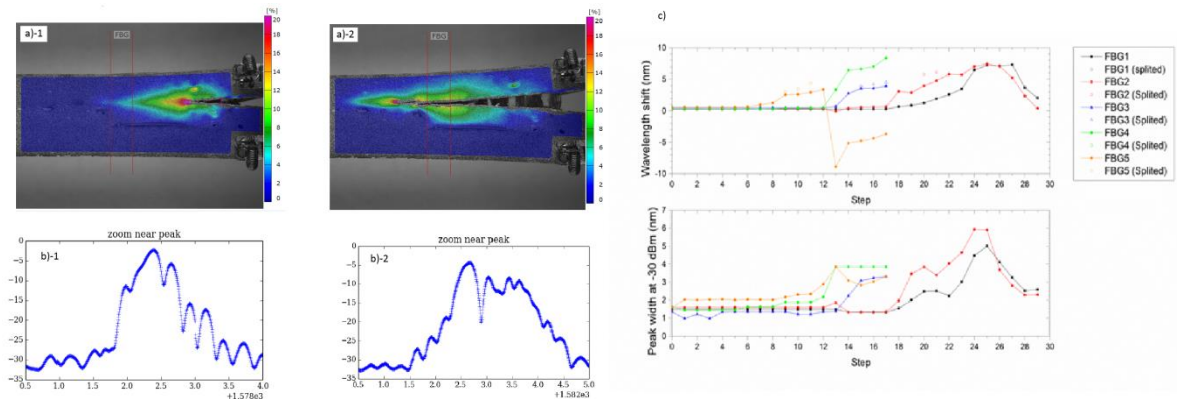


Figure 3: Experimental results for a Mode I loading case. a) Digital Image Correlation technic, b) FBG reflected peak, c) FBG sensor response.

5. Conclusion

In this article we present an approach where the use of damage tolerant structural design and damage tolerant materials combined with an embedded FBG can detect damage evolution. This concept eventually lead to a condition monitoring maintenance, which consists of the detection of damages by sensors, characterization of damage (type and size), model predictions of residual life, giving information that enables decision-making with respect to whether a damage blade should be repaired or replaced.

The crack growth phenomenon on the trailing edge of the blade was successfully modelled, representing with good accuracy the fracture mechanisms present. A good agreement between the sensor output prediction through the FEM model and experiments was found. This demonstrated the presence of specific fracture features near the crack, which the algorithm and model was cable to predict and translate into a sensor response change.

These experiments validate the coupled *structure/sensor* model, so it becomes possible to study the application of this monitoring technique in other locations, predict the sensor output and track different damage features. The application of damage tolerant materials and structural monitoring can lead to safe operation of loaded components even when in damage condition.

6. Acknowledgment

The author acknowledges the Seventh Framework Programme (FP7) for funding the project MareWint (Project reference: 309395) as Marie-Curie Initial Training Network, Fibersensing® for providing the FBG sensors and hardware, and SSP-Technology® for providing the material tested.

7. References

- [1] Jacobsen TK. 2011, *Materials technology for large wind turbine rotor blades - limits and challenges*, Risø Symposium-2011.
- [2] Braga D.F.O., Tavares S.M.O., Silva L.F.M., Moreira P.M.G.P., Castro P.M.S.T., *Advanced design for light weight structures: Review and prospects*. Progress in Aerospace Sciences (2014), <http://dx.doi.org/10.1016/j.paerosci.2014.03.003>
- [3] Qian C., *Multi-scale modelling of fatigue of wind turbine rotor blade composites*, PhD dissertation, Delft University of Technology, 2013.
- [4] Bauchau O.A., *Modeling rotorcraft dynamics with finite element multibody procedures*, *Mathematical and Computer Modelling*, Volume 33, Issues 10-11, May-June 2001, Pages 1113-1137.
- [5] Bottasso C.L., Campagnolo F., Petrovia G.V. , *Wind tunnel testing of scaled wind turbine models: Beyond aerodynamics*, *Journal of Wind Engineering and Industrial Aerodynamics*, Volume 127, April 2014, Pages 11-28
- [6] EERA-DTOC Seventh Framework Programme (FP7)- European Energy Research Alliance - Design Tool for Offshore Wind Farm Cluster, <http://www.eera-dtoc.eu/>
- [7] MAREWINT- Seventh Framework Programme (FP7)- new MAterials and REliability in offshore WIND Turbines technolog, <http://www.marewint.eu/>
- [8] Bent F. Sørensen, *Cohesive laws for assessment of materials failure: theory, experimental methods and application*. Doctor of technices thesis, Risø-R-1736(EN)
- [9] The DTU 10MW Reference Wind Turbine Project, <http://dtu-10mw-rwt.vindenergi.dtu.dk/>
- [10] Meltz G., Hill K.O., *Fiber Bragg grating technology fundamentals and overview*. *Journal of lightwave technology*, 15(8):1263-1276, 1997.
- [11] Sørensen B. F., Jørgensen K., Jacobsen T.K., Østergaard R.C., *DCB-specimen loaded with uneven bending moments*, *Int. J. Fract.*, vol. 141, no. 1–2, pp. 163–176, Sep. 2006.

CONVEX OPTIMIZATION OF SPACE FRAME SUPPORT STRUCTURES FOR OFFSHORE WIND TURBINES

K. Sandal, D. Zwick, M. Muskulus

Norwegian University of Science and Technology (NTNU),
Department of Civil and Transport Engineering, 7491 Trondheim,
kasper.sandal@outlook.com, daniel.zwick@ntnu.no, michael.muskulus@ntnu.no

ABSTRACT

The aim of the present project is to reduce the cost of support structures for offshore wind turbines by minimizing their total steel mass. Basic considerations for an iterative optimization approach were presented by Zwick, Muskulus and Moe (2012), and these have been improved with a convex problem formulation and faster convergence. Simplified fatigue load assessments have been studied, and computational expenses of site-specific optimization has been reduced with a factor of 66 compared to complete analysis. This has been accomplished by using load histories from the initial design to compute correction factors for each member, which enables a single load case of 10 minutes to represent 11 load cases of 60 minutes. A jacket has been optimized with this approach, and a benchmark with the full-height lattice tower concept is presented.

1. INTRODUCTION

Offshore wind turbines are mounted on costly bottom-fixed support structures such as monopiles and jackets. It is expected that significant cost reductions can be achieved by design optimization, particularly for space frame structures where members can be sized individually. Due to the large amount of vibrations that are being induced from both rotor and waves, it has been observed that fatigue is the dominant failure mode for such structures. Fatigue assessment requires comprehensive time-domain simulations, which makes optimization computationally expensive. In this paper, considerations for fast and accurate optimization of a full-height lattice tower (FLT) are presented.

2. METHODOLOGY

An iterative optimization approach was presented by Zwick et al [1], with the objective of reducing weight while maintaining a fatigue life of 20 years in all parts of the structure. Welded K-, X-, and Y-joints are connecting legs and braces as shown in fig.1, and though the method was developed for a FLT, it can be easily adapted to any space frame with similar structure. In this paper, a 10 MW turbine with a FLT support structure has been optimized for fatigue during power production load cases (3-25 m/s, DLC 1.2 in [6]). Fatigue damage is estimated by processing stress history from time-domain simulations with rainflow counting, SN-curve and Miners rule, which is the recommended practice [3]. An important assumption of this method is that the sections are uncoupled, meaning that the members in one section can be optimized without regard to changes in other sections. This is a bold claim, but numerical results have indicated that it works well enough to give convergence [1], [2] and [4]. Consequently, all sections can be optimized simultaneously, and the problem is split into N_{sec} (number of sections) problems, each with four variables (thickness and diameter of legs and braces).

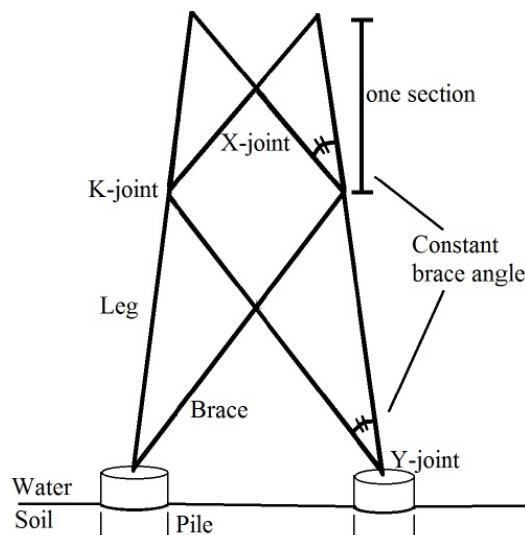


Figure 1: Illustration and terminology of space frame support structures

3. PROBLEM FORMULATION

Stress concentration factors (SCFs) are used to account for the extra loading experienced in the joints, and are computed from the DNV standard *Fatigue design of offshore steel structures* [3]. SCFs are evaluated at both sides of all welds, as it is normally not the weld that fails, but the nearby material in one of the connected members. With only thickness and diameter as variables, the formulas from the standard can be simplified. Note that D and T refer to legs, while d and t refer to braces.

$$SCF_{Leg} \propto \frac{t^{0.9} D^{0.5}}{T^{1.4}}$$

$$SCF_{Brace} \propto \frac{d}{t}$$

The scaling laws above are obtained from the dominating stress contribution in the critical hot spot. Since the dominating stress contribution will scale with its respective SCF ($\sigma_i = SCF_i \cdot \sigma_0$), it can also be argued that the total stress will scale with this SCF. Stress will of course also scale with the cross sectional area ($\sigma_0 = F/A$), which for thin walled pipes scales with thickness times diameter.

$$\sigma \propto \frac{SCF}{Area}$$

$$\sigma_{Leg} \propto \frac{SCF_{Leg}}{t^{0.9}}$$

$$\sigma_{Brace} \propto \frac{1}{t^2}$$

The SN-curve relation scales stress with maximum number of cycles, and Palmgren Miners rule scales maximum number of cycles (N) with fatigue damage (U).

$$\log N_i = \log a - m \log \Delta \sigma_i$$

$$U = \sum_i \frac{n_i}{N_i}$$

$$U \propto \sigma^m \quad (m = 5)$$

$\frac{D}{T}$ -ratio of both legs and braces should be kept fixed at a minimum value (proved in [4]), limited by the validity range of the SCF formulas ($16 < \frac{D}{T} < 64$). The objective function is then a function only of t and T , with a weighting constant $r = 2.3$ which must be included since there are more braces than legs. The problem (text box & fig.2) is convex, as the design space, the objective function and the two constraint functions are convex (their Hessians are all semi definite on the intervals described by the variable bounds). Given that fatigue damage U^j for both legs and braces have been calculated for design iteration j , analytical expressions for Δt and ΔT can be derived by setting $U^{j+1} = 1$.

$$\Delta t = t^j \left((U_{Brace}^j)^{\frac{1}{10}} - 1 \right)$$

$$\Delta T = T^j \left((U_{Leg}^j)^{\frac{1}{14.5}} \left(\frac{t^{j+\Delta t}}{t^j} \right)^{\frac{4.5}{14.5}} - 1 \right)$$

Optimization problem
 minimize: $f = T^2 + rt^2$
 T, t
 subject to $g_1 = U_{Leg} - 1 \leq 0 \quad \left(U_{Leg} \propto \frac{t^{4.5}}{T^{14.5}} \right)$
 $g_2 = U_{Brace} - 1 \leq 0 \quad \left(U_{Brace} \propto \frac{1}{t^{10}} \right)$
 when $t_{min} \leq t \leq T \leq T_{max}$

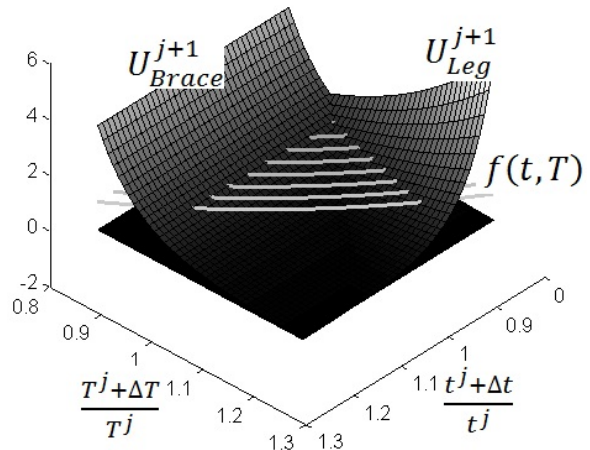


Figure 2: Convex optimization problem

4. SIMPLIFIED FATIGUE LOAD ASSESSMENT

For certification of support structures, the recommended practice is to assess the fatigue loads from simulations of a large number of load cases, each with a minimum length of one hour. For optimization purposes it is relevant to know how a fatigue load assessment can be simplified without sacrificing too much accuracy. Two assumptions were tested:

- A reduced number of load cases can represent all wind speeds.
- A reduced simulation length can represent 60 minutes.

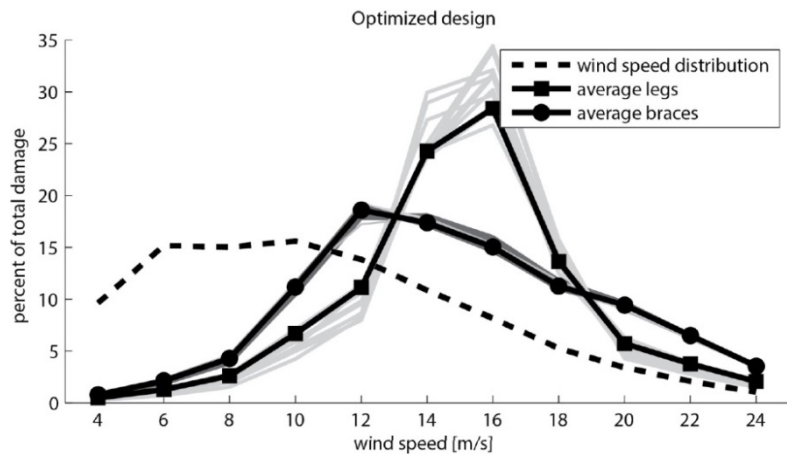


Figure 3: Distribution of normalized damage accumulation is plotted for all members (grey). Qualitatively different distributions are observed for legs and braces (black). This distribution remains relatively unchanged during large design modifications.

The problem formulation presented in section 3 was used, where fatigue damage U was evaluated with various simplified fatigue load assessments. An initial design with constant member dimensions was analyzed with a *complete* fatigue load assessment (11 load cases of 60 minutes), and the results of this was used to “adjust” the *simplified* assessments. During the optimization it was observed that the normalized damage accumulation from different wind speeds kept a more or less constant distribution (fig.3), even with large modifications to the design. The consequence is that one load case effectively can represent all wind speeds, and it was also demonstrated that simulation length down to about 10 minutes gives acceptable accuracy [4]. By reducing simulation length with a factor of 6, and the number of load cases with a factor of 11, it has been demonstrated that a conceptual design can be optimized ~66 times faster than the recommended practice. Optimization with simplified and complete fatigue load assessment achieved the same optimal design within a few percent, though statistical investigations should be performed to gain more knowledge about the accuracy.

5. JACKET VERSUS FULL-HEIGHT LATTICE TOWER

A jacket was designed with the topology from the bottom 4 sections of the FLT (fig.4), and connected to the turbine through a rigid transition piece and a scaled version of the tubular tower from the OC4 project [5]. The tubular tower was then further modified to obtain satisfying eigenmodes. When the models were optimized for the same conditions, both converged to about 700 tons (excluding transition pieces). While the FLT has the advantage of a significantly lighter transition piece than the jacket, it also has a more intricate structure (many welded joints). Thus, a fair comparison is difficult to do without a complete cost model.

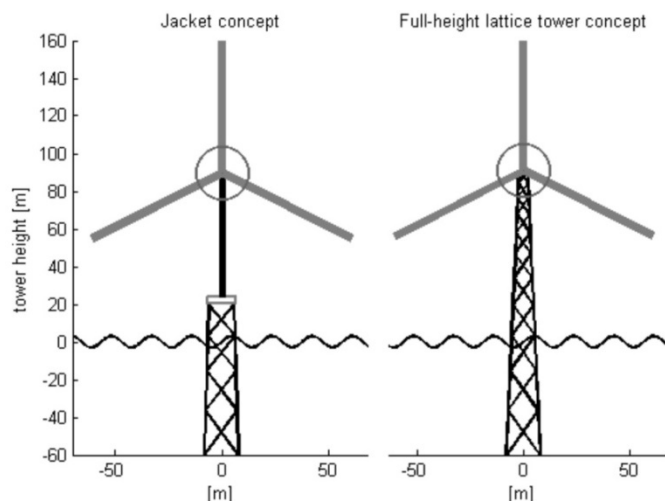


Figure 4: Two space frame support structure concepts that have been optimized with the presented method.

6. OPTIMIZATION RESULTS

The problem formulation presented in section 3, together with the simplified fatigue load assessment from section 4 was used to optimize both of the structures presented in section 5. Only the results of the FLT are presented here, as the jacket produced almost identical results. It can be observed in fig.4 (left) that the optimized design (black) is significantly modified compared to the initial design with constant dimensions (grey). In fig.5 (middle and right) the fatigue and ultimate limit state for the optimized design is presented, and it can be observed that fatigue is the design driver (for this DLC).

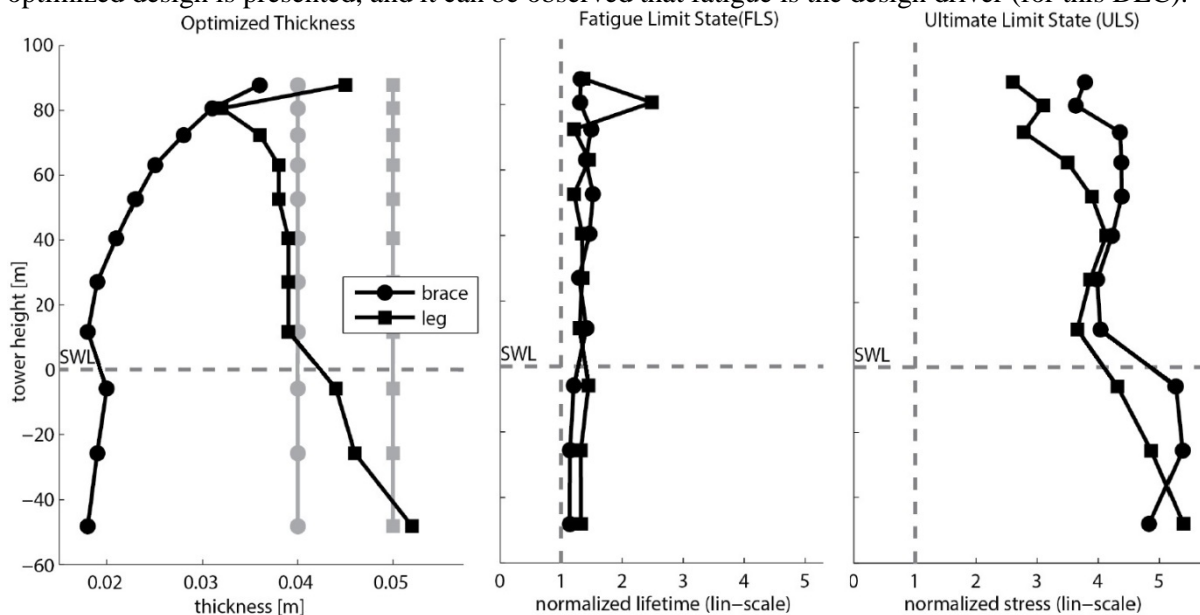


Figure 5: Results of the full-height lattice tower optimization. *Left*: Dimensions of the optimized design (diameter is 16 times thickness). *Middle*: Fatigue life normalized by 20 years. *Right*: Maximum stress normalized with yield stress (security factors shown). Below sea water level (SWL) the structure is also subjected to hydrodynamic loads.

7. DISCUSSION

Two different initial designs with masses of 450 and 1800 tons both converge to the same optimized design of about 700 tons. All sections have an acceptable fatigue lifetime close to the design limit (fig.5-middle), which means that the simplified fatigue load assessment has sufficient accuracy for optimization purposes. Legs are constrained to be thicker than braces, and this is the reason behind the high fatigue life for legs in the second uppermost section. Ultimate limit state (ULS) has not been included in this optimization, though the maximum stresses have been recorded, and it can be observed that all sections are far from yield. However, the simulations in this analysis only cover power production load cases, and extreme events should be studied to confirm the design.

REFERENCES

- [1] Zwick, D., Muskulus, M., Moe, G., *Iterative optimization approach for the design of full-height lattice towers for offshore wind turbines*, Energy Procedia 24, 297-304, 2012.
- [2] Muskulus, M., Christensen, E., Zwick, D., *Improved Tower Design of the NOWITECH 10 MW Reference Turbine*, Proceedings EWEA Offshore, 2013.
- [3] Det Norske Veritas, *DNV-RP-C203 Fatigue design of offshore steel structures*, 2008.
- [4] Sandal, K., *Improved design of the support structure for the Nowitech 10 MW Reference Turbine*, Master thesis, NTNU, 2014.
- [5] Vorpahl, F., Popko, W., Kaufer, D., *Description of a basic model of the 'UpWind reference jacket' for code comparison in the OC4 project under IEA Wind Annex 30*, Technical Report, Fraunhofer IWES, 2013.
- [6] IEC 61400-3, *Design requirements for offshore wind turbines*, 2009

Effect of laminate thickness on the static and fatigue properties of wind turbine composites

F. Lahuerta¹, R.P.L. Nijssen¹, F. P. van der Meer², L. J. Sluys²

¹Knowledge Centre WMC. Kluisgat 5, 1771 MV Wieringerwerf, The Netherlands

²Delft University of Technology. PO Box 5048, 2600 GA Delft, The Netherlands

E-mail¹: f.lahuerta@wmc.eu, t.westphal@wmc.eu, r.p.l.nijssen@wmc.eu

E-mail²: F.P.vanderMeer@tudelft.nl, L.J.Sluys@tudelft.nl

ABSTRACT

Thick laminates can be found in different wind turbine blade sections, such as the root or the spar caps. For 40 meter long blades, thicknesses between 30 to 50 mm are typical. Root and cap thicknesses between 100-150 mm can be considered as common for 60 to 70 meter long blades.

The aim of the project is to study the thickness effect in composite laminates with respect to the static and fatigue properties and to determine the main parameters which cause the differences between thin and thick laminates. A thick laminate is considered to have a thickness larger than 5mm. The approach followed in the present work is to identify the main factors involved in the thickness effect, and to evaluate each factor's contribution to the thickness effect separately. The factors considered in the present work are:

- **Self-heating during dynamic loading.** This is related to the material energy loss factor. During dynamic loading a certain percentage of mechanical energy is dissipated into heat, leading to a rise of the material temperature. When the temperature approaches the maximum service temperature of the material, a reduction in fatigue life can be observed [1].
- **The scaling effect and coupon geometry influence.** Scaled compression tests were performed on laminates up to 20 mm thick. The coupon design was based on finite element analysis and fracture mechanics [2] and the influence of the manufacturing process and self-heating was minimized [3]. Static tests on laminates with different thicknesses showed no significant change in the static ultimate stresses. Fatigue tests showed a decrease in the fatigue life for increasing thickness.
- **The manufacturing process influence.** Through-thickness lamina properties have been studied extracting sub-laminates from 60mm thick laminates.

MATERIALS AND METHODS

In order to evaluate the **self-heating** effect in thick laminates, two different fatigue tests setups were arranged. Transverse direction (90°) compression coupons, 30mm thick, were tested at different loading ratios for two different frequencies 0.25 and 0.5Hz in a 1000kN test frame. Furthermore, unidirectional (UD) 20mm thick coupons, end-loaded in compression, were tested at two different frequencies, 1.5 and 2.5 Hz and under semi-adiabatic condition in a 400kN test frame (see Figure 1).

Thickness scaled compression coupons of 4, 10, 20mm were tested in static and fatigue conditions in order to evaluate the **thickness effect** (see Figure 2). Compression tests were carried out in a

combined loading compression CLC setup according to ASTM D6641, in test frames of 100kN, 400kN and 1000kN, respectively for each thickness. Fatigue test frequencies were reduced from 2Hz to 0.5Hz as the thickness increased in order to minimize the influence of heating. Static tests were carried out at a test speed of 1mm/min in all cases. The coupon geometry with integrated tabs was designed and scaled with the help of a parametric FEM analysis aiming to minimize the geometry and test influence.

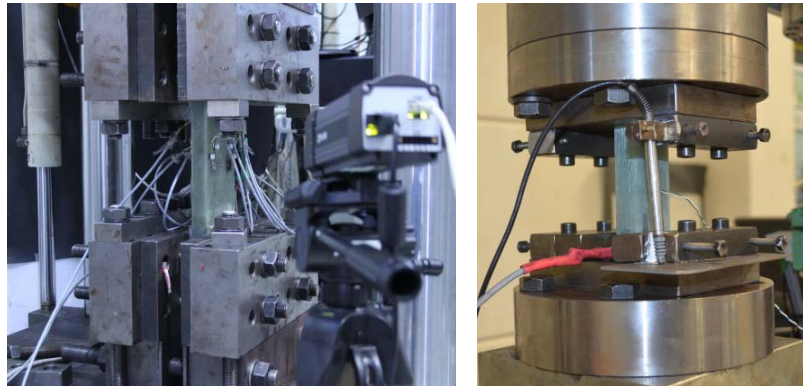


Figure 1: Heating effect specimens (90° laminate (left), 20mm end-loaded, compression)

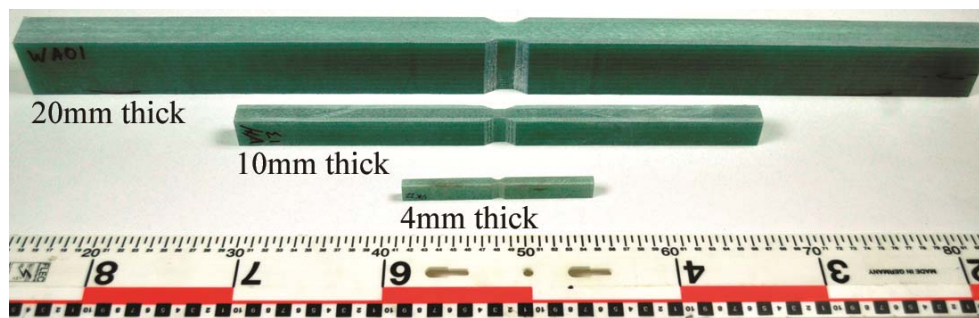


Figure 2: Thickness scaled compression coupons. 4, 10 and 20mm thick

With the help of peel-ply layers, sub-laminates at different thickness positions were extracted from 60mm infused thick plates (see Figure 3) in order to study the **manufacturing process influence** through the thickness. Compression coupons of 4mm thick with integrated tabs were manufactured from each sub-laminate and tested in static (1mm/min) and fatigue conditions, in order to compare the lamina properties at different thickness positions.

For all cases, coupons were obtained from plates infused with a common wind energy epoxy resin (Hexion RIM135) and glass fibre (GFRP) type E with 600 gr/m² non-crimp UD fabric. Averaged fibre weight ratios of 70%, void content around 0.1% and glass transition temperatures (T_g) between 80-85 °C were measured for each plate.

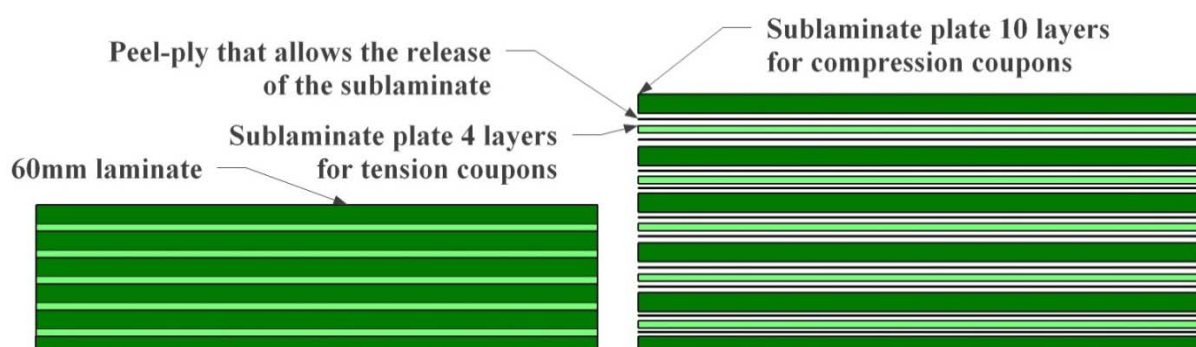


Figure 3: Sub-laminates plates extraction from a 60mm infused plate

RESULTS AND DISCUSSION

Due to the poor thermal conductivity properties of glass-fiber composites, **self-heating effects** might play a role in thick laminate fatigue tests. When a solid is dynamically loaded, a certain ratio of the total strain energy is transformed into heat. This volumetric heat raises the temperature of the solid up to an equilibrium defined by the boundary conditions. The temperature rise is mainly dominated by the loading ratio, the frequency, the thickness and the boundary conditions. Thus for thick laminates under certain loading conditions, laminate core temperatures might surpass the material service temperature, reducing the global rigidity and leading to premature failure.

In Figure 4 (left) a comparison is shown of 30mm thick coupons tested at different loading ratios and two different frequencies, 0.25 and 0.5Hz. While the mentioned testing frequencies did not influence the thinner coupons' fatigue life, 30mm thick coupons compression tests showed that fatigue life was reduced one order due to heating. During the test, differences in surface temperatures between both frequencies around 15 to 20°C were recorded, with maximum surface temperatures close to 40-50°C. Based on these surface temperatures, core temperatures up to 55-65°C were calculated. Such temperatures are out of the material maximum service temperature range and are likely to induce premature failure. Moreover, Figure 4 (right) shows S-N curves for 20mm thick coupons tested at two different frequencies (1.5 and 2.5Hz) and with the surface insulated (semi-adiabatic). The S-N curves show that the increase of the frequency and specially the reduction of the cooling surface reduced fatigue life and increased the scatter or confidence intervals.

In order to study the **thickness effect**, thickness scaled static and dynamic compression tests were performed for 4, 10 and 20mm thick coupons. Coupons with integrated tabs (not bonded) were designed with the help of the FEM for this purpose. Additionally, coupons with bonded tabs were tested. Both types of coupons, showed a similar performance in fatigue tests (see Figure 5, right), however the coupons with integrated tabs allowed to scale the thickness and could be used in static or fatigue tests independently.

Due to the strong role that the clamping pressure might play in the final compression results, static tests at different clamping pressures were carried out in order to find the optimal setup (see Figure 5, left). Once the clamping pressure was optimised, thickness scaled static compression tests showed no decrease of the ultimate stresses. However, fatigue tests for 4, 10 and 20mm thick coupons revealed a decrease of fatigue life and an increase of scatter as the thickness increased (see Figure 5, right). Further work is being carried out on this topic, in order to study the thickness effect in tension static and dynamic tests.

Thick laminates present certain variability of the lamina properties through the thickness. This might be related with the **manufacturing process**. As the thickness increases, the curing cycle temperature at each thickness position varies, promoting certain changes in the mechanical properties. Figure 6 (left) shows how the ultimate compression stresses change through the thickness showing smaller stresses in the outer layers than in the middle layers.

In addition, Figure 6 (right) shows S-N curves for 4mm thick coupons obtained from the middle of the thick laminate and coupons obtained from the outer parts. While the S-N curves' confidence intervals of both thickness positions are similar, the trend and slope of the outer layers shows a different behaviour than the middle layers. It appears that the fatigue life is dependent on the thickness position. Research is still in progress on this topic, aiming to determine the influence of different curing cycles on the through thickness lamina properties as well as to investigate the influence of different types of peel ply for the sub-laminates harvesting methodology.

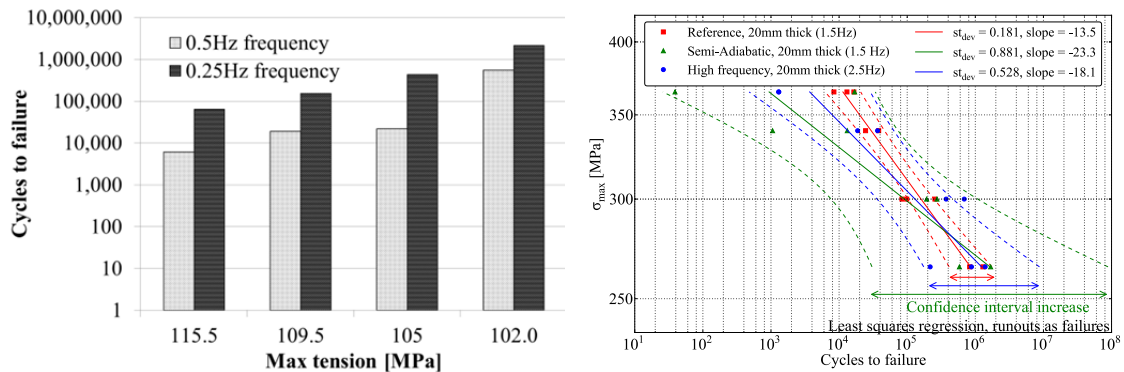


Figure 4: Self-heating fatigue tests. Left, fatigue life of transverse direction (90°) compression coupons 30mm thick tested at 0.5 and 0.25Hz. Right, S-N curves of 20mm thick compression end-loading coupons.

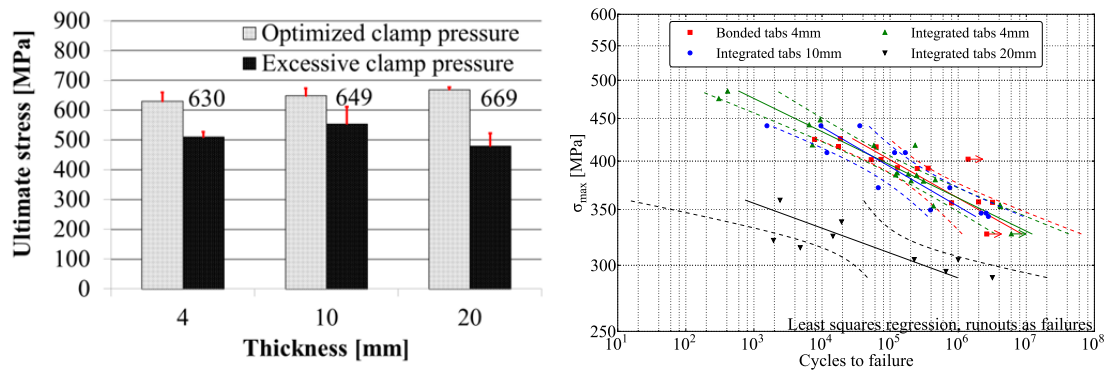


Figure 5: Left, static compression tests for 4, 10 and 20mm thick coupons, showing close compression ultimate stresses. Right, S-N curves for 4, 10 and 20mm coupons, showing a decrease in fatigue life.

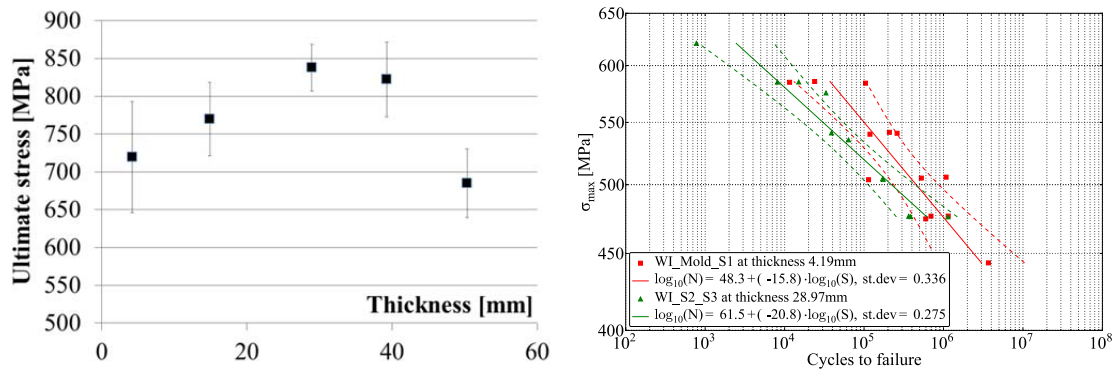


Figure 6: Manufacturing process. Left, static compression ultimate stresses through the thickness. Right, sub-laminate S-N curves at thickness position 4mm (mold-side) and 29mm (middle-plate).

CONCLUDING REMARKS

Static and dynamic properties of thick laminates can differ strongly from thin laminates. The present work shows that the thickness effect is influenced by different factors.

Under high loading frequencies or elevated temperatures, temperature increments in the core of thick laminates will occur, driving the material performance out of the operational ranges and occasionally leading to premature failure. Independent of the self-heating effect, tests show a decrease in fatigue

life as the thickness increases. In addition, the manufacturing process might play an important role, since the experimental data show that static and dynamic properties of the lamina through the thickness are varying, the full thickness properties scatter increase as the laminate thickness increase, promoting wider confidence intervals.

REFERENCES

- [1] F. Lahuerta, T. Westphal, and R. Nijssen, “Self-heating forecasting for thick laminates testing coupons in fatigue,” in *The Science of Making Torque from Wind, Torque, Oldenburg*, 2012.
- [2] F. Lahuerta, T. Westphal, R. P. L. Nijssen, F. P. van der Meer, and L. J. Sluys, “Measuring the delamination length in static and fatigue mode I tests using video image processing,” *Compos. Part B Eng.*, vol. 63, pp. 1–7, Jul. 2014.
- [3] F. Lahuerta, T. Westphal, R. P. L. Nijssen, F. P. van der Meer, and L. J. Sluys, “Static and fatigue performance of thick laminates test design and experimental compression results,” in *ECCM-16TH European conference on composite materials, Seville*, 2014, pp. 1–9.

“

Wind Parks

”

Development of a wind farm tool with advanced actuator disk models

M. Moens*, M. Duponcheel, G. Winckelmans, P. Chatelain

Institute of Mechanics, Materials and Civil Engineering, Université catholique de Louvain, B-1348 Louvain-la-Neuve, Belgium

1. Introduction

Over the last decades, more and more wind turbines have been installed in large wind farms. The grouping of wind turbines introduces two major issues : a reduction of power production and a diminution of lifetime of the rotor. These issues arise from the interaction between the wind turbines and the wakes of generators lying upstream, problems aggravated by the trend toward higher power densities and the limited space of concessions. The wake, which consists in the flow region downstream of the wind turbine rotor, is characterized by a high level of turbulence, a lower wind speed and unsteadiness. The wakes are very much inherent to the power extraction in a wind farm, and actually, responsible for several of the issues that affect the attractiveness of wind energy : difficulties in predicting production, its uncertainty, its intermittency. A better understanding of wakes in wind farm will be needed to reduce power losses and to increase the lifetime of the generators. It is however difficult to reproduce realistic wake behaviors experimentally ; numerical simulation offers a convenient framework for studying large wind farms.

Current commercial wind farm design tools involve simple wake models and are known to suffer from large uncertainties in the prediction of energy output. This uncertainty negatively impacts the market value of wind energy. Interestingly, these models have yet to capitalize on the advances of recent experimental [1], theoretical, and numerical [2] works. These research efforts have indeed led to a better understanding of the behavior of wind turbine wakes over large distances. They have also highlighted aspects of wakes which will remain challenging for operational/engineering models of wakes: the merging of wakes, their unsteady behavior, and their uncertainty in the shape of decay characteristics, or wake meandering [3].

Tools for accurate simulation of of wind farms have been developed for several years. The tool called Simulator for Wind Farm Applications (SOWFA), developed by the National Renewable Energy Laboratory, is one of them [4]. Based on the OpenFoam platform, it is however quite computationally expensive.

We propose to achieve high-fidelity levels through an alternative and less expensive approach based on classical structured mesh Computational Fluid Dynamic (CFD). It consists in the resort to Large Eddy Simulation (LES) and the use of an improved actuator disk model that remains simple and fast. We account for the variable wind conditions and the resulting varying operating conditions of the wind turbines are treated by including a realistic controller scheme.

In section 2 the flow solver and wind turbine model are described. Section 3 presents numerical results for the wind flow past a 'NREL offshore 5-MW baseline wind turbine' [5]. Two types of simulations are presented : an isolated wind turbine and a twenty-five machines wind farm. The power production is studied in each case, and the performances of the tool are highlighted.

2. Methodology

2.1. Flow solver

Large Eddy Simulations are performed by a solver developed at Université catholique de Louvain [6]. The incompressible Navier-Stokes equations are solved using fourth order finite differences on a staggered mesh. Its particularity lies in the conservation of the discrete kinetic energy in the absence of viscous dissipation and/or Subgrid Scale model, provided the time stepping is exact [7]. Wind turbines are accounted for by the introduction of a body force source term in the Navier-Stokes equations.

2.2. Turbulent wind

Turbulent fluctuations are added at the inlet boundary in order to produce a realistic wind. These fluctuations are generated by tool of DTU Wind Energy [8]. The approach is based on a model of

*Corresponding author: maud.moens@uclouvain.be

the spectral tensor for atmospheric boundary-layer turbulence. It can simulate Homogeneous Isotropic Turbulence (HIT) or fluctuations appearing above sea or land. The result is a three-dimensional box with the three components of the wind velocity turbulence. The streamwise axis of the turbulence box is inferred as a time axis in the simulation via Taylor’s frozen turbulence hypothesis and the pre-generated turbulence field is added to the mean flow at the inlet boundary.

2.3. Wind turbine model

This project aims at an efficient and faithful modelling of large wind farms including their unsteady effects. The wind turbine model must be then simple and fast. The most appropriate approach is the actuator disk coupled with the Blade Element Momentum (BEM) method [9]. Basically, the actuator disk method consists in representing the rotor by equivalent forces from the blades distributed on a permeable disk of zero thickness. It is divided into radially independent annular streamtubes, as in the classical BEM method. The effect of rotation are taken into account. By summing the contributions of all these elements, the performance of the turbine can be calculated. In order to improve the model a controller is implemented and allows realistic generator behavior.

The chosen wind turbine is the NREL-5MW model. It is a representative utility-scale multimegawatt turbine known as the ‘NREL offshore 5-MW baseline wind turbine’. It was created by using information of realistic offshore wind turbines. Data are available in an NREL report [5].

A mean velocity is computed one rotor diameter upstream of the wind turbine. It is the only input variable for the wind turbine model. The BEM model coupled with the controller then computes normal and tangential forces \mathbf{F} along the disk. To avoid singular behavior and numerical instabilities the induced forces are distributed smoothly on the mesh by using a three-dimensional Gaussian approach. A correction is added in the local forces in order to conserve global data (thrust and torque) between the BEM computation and the distribution of forces on the mesh.

3. Results

This section presents the results obtained with LES coupled to the wind turbine model. The first test case is an isolated wind turbine impacted by an offshore wind characterized by a turbulence intensity of about 4 %. We choose a mean hub-height wind speed of 9 m/s because it means that the turbines will operate in Region 2 [5], in which the maximum energy is extracted from the wind. This simulation is performed using a relatively fine mesh (64 points per rotor diameter). The mesh is coarsened for the next case, a twenty-five wind turbine array; this is motivated by our final objective of affordable wind farm scale simulations. The set-up of the two cases are available in Tab. 1.

Case	Number of rotor(s)	Lx	Ly	Lz	Nx	Ny	Nz	Location of the 1st rotor
1	1	12D	4D	4D	768	256	256	(3D,0.71D,2D)
2	25	42D	8D	36 D	672	128	576	(3D,0.71D,4D)

Table 1: Set-up ; the NREL diameter is equal to 126 m. The x direction is the streamwise direction and the y direction is the vertical direction. Case 2: rotors are located at 7D from each other in the streamwise direction and horizontal direction (z axis). There are five lines and five columns of wind turbines.

One can get an idea of the turbulence intensity with the hub-level instantaneous slice shown in Fig. 1(a). The simulation covers 1500 seconds of physical time; the associated electrical power is presented in Fig. 1(b) for 500 seconds of simulation. The flow periodicity and unsteadiness are such that the wind turbine controller has to react to long lulls and gusts in order to track the maximum power configuration. This simulation was performed in order to highlight the controller effect and its ability to account for wind variations.

For an isolated wind turbine, it is reasonable to choose a fine mesh and the resulting simulation time is not excessive. However we cannot afford such an accuracy when the number of wind turbines increases; the mesh is then twice coarser for case 2. We want to verify whether the tool remains efficient, still produces high-fidelity wake dynamics, and provides a good estimation of the produced power. Fig. 2 and 3 show the results; the simulation covers 3000 seconds of physical time.

When we look at Fig. 2(b), we can see that the wake recovers over a shorter distance for wind turbines located beyond the first row. It is due to the turbulence which raises mixing and exchanges between the low velocity fluid in the wake with the high velocity fluid outside it. The slice of the instantaneous resolved streamwise velocity can highlight the effect. We can still distinguish a structured wake for the first machine of each row but the wakes become more turbulent for the other machines. The turbulent

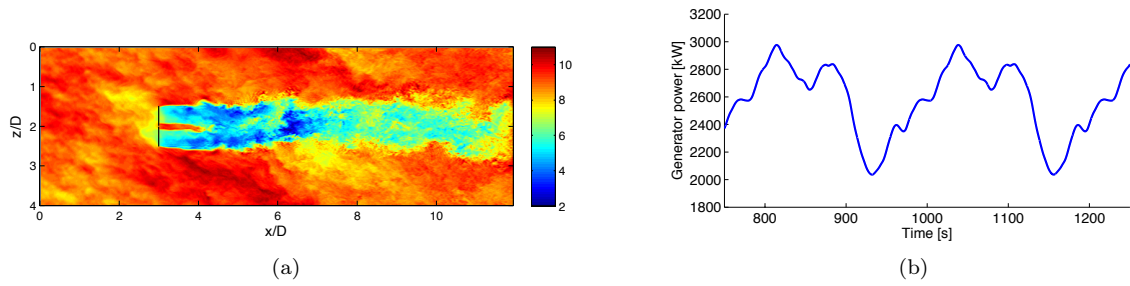


Figure 1: Contour taken in a horizontal plane through rotor center of instantaneous resolved streamwise velocity (a). The colorbar is in [m/s]. The black bar indicates the wind turbine. Associated generator power (b).

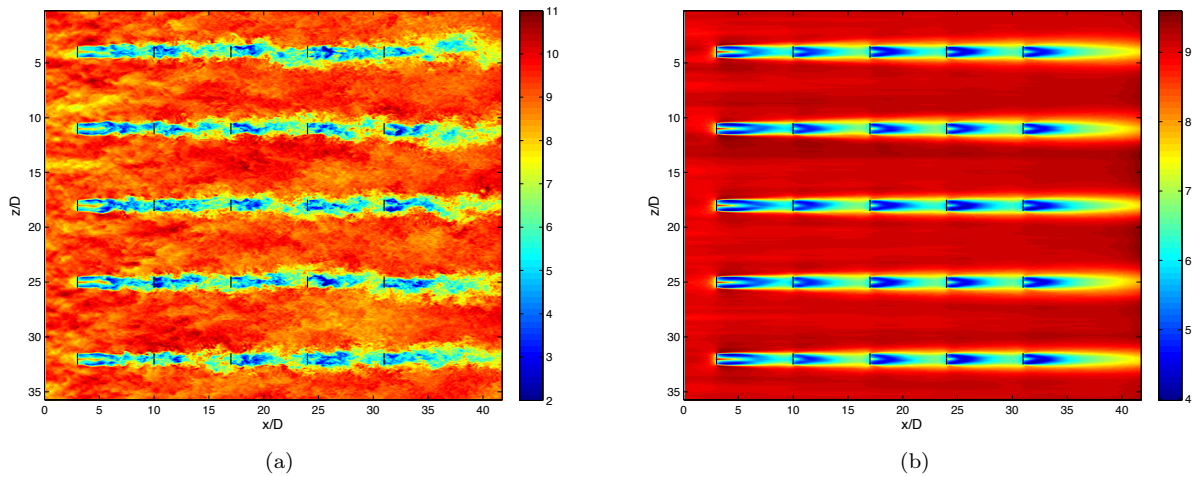


Figure 2: Contour taken in a horizontal plane through rotors center of (a) instantaneous and (b) time-averaged (right) resolved streamwise velocity. The colorbar is in [m/s]. Black bars indicate the wind turbines.

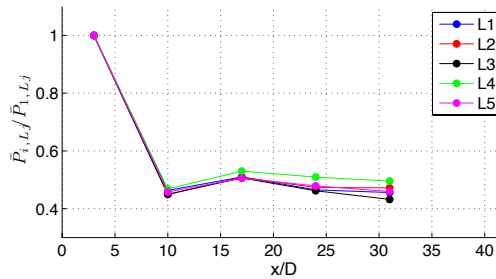


Figure 3: Simulated time-averaged power produced by each wind turbine $\bar{P}_{i,L,j}$, normalized by average power of the first rotor in the row $\bar{P}_{1,L,j}$.

effect allows a better mixing but it has a negative impact on the lifetime of the generator. It is one of the effects that this wind farm tool aims at reproducing, with a high fidelity reproduction of wake dynamics. An other main goal of this work consists in exploring the ability of the tool to predict power production at wind farm scales. Fig 3 shows the simulation time averaged power produced by each wind turbine, normalized by the averages of the corresponding first row rotors. The effects of the wake on power production are dramatic: the second through the fifth in the row produce only 40-50% of the power of the first rotor. It is an expected behavior, typical for wind turbine arrays.

Reproducing realistic characteristics of a wind farm is one of the objectives of the tool. The other main goal consists in having a fast code. By coarsening the mesh and using a simple wind turbine model the twenty-five wind turbines simulation required a reasonable computational time : a 1280 processor-hours time. The tool can then produce realistic results by using a efficient method. Of course, it needs further validation steps.

4. Conclusion and Future Work

The main features of wind farm tool have been presented and aerodynamics and power production can be found in the results from Large Eddy Simulations for offshore wind turbine and a twenty-five wind turbines array. These simulations are the first step towards validating the code. The results have shown that the tool is able to reproduce main typical characteristics of wind farm behavior and its performances have been highlighted; it accounts for unsteady effects and can give the power production for each generator.

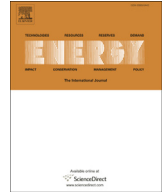
We can also remark that the simple actuator disk model is the best method to keep a fast code, able to simulate large array of wind turbines. It has been highlighted by the required processor-hour cost. However we aim at reproducing faithfully wake behaviors ; the actuator disk method is not the strategy which gives the most realistic behavior. The wake and its expansion and decay are governed by vortex instabilities which cannot be obtained by a basic approach. It is then necessary to find a good compromise between more complex wind turbine model and affordable wind farm simulations. More detailed modelling including moving blades would be more accurate and give more unsteadiness at the rotor level but it would make the tool more expensive. We will then implement an alternative approach: the generation of turbulence in the wake will be included by using statistics obtained with the Vortex Particle-Mesh and lifting line method developed at Université Catholique de Louvain [10]. A certain level of noise will be added at the disk in order to trigger instabilities in the wake and to match to a more realistic wake behavior. It is one of the main improvements which will be added in the rotor model. The second improvement consists in adding a *wall modeling* near the wall. Currently the solver uses the *wall-resolved* approach. In order to model the ground effect it is being extended to take into account a *law of wall*. In a final step, we will assess comparison of good accuracy/efficiency of the tool on actual measurements.

Acknowledgments

We gratefully acknowledge the support of GDF Suez for the fellowship of Mrs Maud Moens. We also thanks Mr Olivier Thiry for his improvements in the flow solver.

References

- [1] J. J. Trujillo, A. Rettenmeier, and D. Schlipf. Arrangements for enhanced measurements of a large turbine near-wake using lidar from the nacelle. IOP Conference Series: Earth and Environmental Science, 1(1), 2008.
- [2] J. N. Sorensen and W. Z. Shen. Numerical modeling of wind turbine wakes. Journal of Fluids Engineering - Transactions of the ASME, 124(2):393–399, Jun 2002.
- [3] Ferhat Bingöl, Jakob Mann, and Gunner C. Larsen. Light detection and ranging measurements of wake dynamics part i: one-dimensional scanning. Wind Energy, 13(1):51–61, 2010.
- [4] Sowfa. <http://wind.nrel.gov/designcodes/simulators/sowfa/>.
- [5] J. Jonkman, S. Butterfield, W. Musial, and G. Scott. Definition of a 5-mw reference wind turbine for offshore system development. Technical Report TP-500-38060, NREL, February 2009.
- [6] L. Bricteux, M. Duponcheel, G. Winckelmans, I. Tiselj, and Y. Bartosiewicz. Direct and large eddy simulation of turbulent heat transfer at very low prandtl number: application to lead-bismuth flows. Nucl. Eng. Des., (246):91–97, 2012.
- [7] O.V. Vasilyev. High order finite difference schemes on non-uniform meshes with good conservation properties. J. Comput. Phys., 2(157):746–761, 2000.
- [8] Jakob Mann. Wind field simulation. Probabilistic Engineering Mechanics, 13(4):269–282, 10 1998.
- [9] H.Glauert. Airplane Propellers, volume 4. Durand WF, Dover, New-York, 1963.
- [10] P. Chatelain, S. Backaert, G. Winckelmans, and S. Kern. Large eddy simulation of wind turbine wakes. In Wolfgang Rodi, editor, Proceedings of The 9th International Symposium on Engineering Turbulence Modelling and Measurements (ETMM-9), June 6–8, 2012, Thessaloniki, Greece, volume 91 of Flow, Turbulence and Combustion, pages 587–605. ERCOFTAC, Springer, Jun 2013.



The right size matters: Investigating the offshore wind turbine market equilibrium



Nikolaus Ederer*

Vienna University of Technology, Faculty of Electrical Engineering and Information Technology, Gußhausstr. 25–29, 1040 Vienna, Austria

ARTICLE INFO

Article history:

Received 27 November 2013

Received in revised form

2 February 2014

Accepted 16 February 2014

Available online 20 March 2014

Keywords:

Offshore wind energy

Offshore wind turbine

Upscaling

Market equilibrium

ABSTRACT

Although early experiences indicate that the maturity of deployed technology might not be sufficient for operating wind farms in large scale far away from shore, the rapid development of offshore wind energy is in full progress. Driven by the demand of customers and the pressure to keep pace with competitors, offshore wind turbine manufacturers continuously develop larger wind turbines instead of improving the present ones which would ensure reliability in harsh offshore environment. Pursuing the logic of larger turbines generating higher energy yield and therefore achieving higher efficiency, this trend is also supported by governmental subsidies under the expectation to bring down the cost of electricity from offshore wind. The aim of this article is to demonstrate that primarily due to the limited wind resource upscaling offshore wind turbines beyond the size of 10 MW (megawatt) is not reasonable. Applying the planning methodology of an offshore wind project developer to a case study wind farm in the German North Sea and assessing energy yield, lifetime project profitability and levelized cost of electricity substantiate this thesis. This is highly interesting for all stakeholders in the offshore wind industry and questions current subsidy policies supporting projects for developing turbines up to 20 MW.

© 2014 Elsevier Ltd. All rights reserved.

1. Introduction

The EWEA (European Wind Energy Association) reveals in their annual report about key trends and statistics in the European offshore wind industry 2012 [1], that the average size of wind turbines installed in European waters has continuously increased. During 2012, the average capacity of new wind turbines installed was 4 MW (megawatt) and it is very likely that this trend continues, since EWEA also reports that by the end of 2012 76% of the announced new OWTGs (offshore wind turbine generators) have a rated capacity of over 5 MW. Under the expectation of concomitant cost reductions [2,3], this trend is also fostered by governmental subsidy programs such as the European Wind Initiative [4], which is a ten years research and development programme of the European Union, that grants subsidies for developing and testing large-scale wind turbines (10–20 MW). For example the AZIMUT Offshore Wind Energy 2020 project [5], which has the objective to develop a 15 MW OWTG, and the already completed UpWind project [6] is supported by this European initiative. The latter investigated design limits and solutions for very large wind

turbines and showed that even 20 MW wind turbines are feasible from a technical point of view.

As a consequence, upscaling of wind turbines is a research topic with increasing popularity. For example Ref. [7], where this trend is investigated with the aim to provide recommendations for optimal design of large wind turbines [8], where a detailed analysis of costs in relation to upscaling is presented or [9] where an overview of upscaling trends for wind turbine gearboxes is given. This field of study is also related to the problem of finding optimal dimensions for wind turbines, e.g. in Ref. [10] it is argued why wind turbines with a low specific capacity are beneficial, in Ref. [11] an optimizer routine is presented which allows to determine the optimal rotor size for a given wind turbine rating, in Ref. [12] the optimal hub height for onshore wind turbines is investigated and in Ref. [13] the size of rotor/generator is site specific optimized. However, all these publications are written from the turbine designer point of view, whereas this article questions if larger OWTGs can ever be a competitive product assuming reasonable market conditions.

Therefore this article investigates the trend of growing OWTGs from the market point of view and answers the question if 20 MW OWTGs are ever reasonable or if there exists a market equilibrium that lies below this size. This market equilibrium would be of significant interest for stakeholders in the offshore wind industry. Early experiences revealed that the technology has not yet the

* Permanent address: Bandwirkerstraße 13, 22041 Hamburg, Germany. Tel.: +43 664 41 899 48.

E-mail address: nikolaus.ederer@gmail.com.

maturity to sustain the harsh offshore environment [14]. Due to the rapid development of this industry, wind turbine manufacturers are faced with tight market conditions and are forced to continuously bring larger turbines onto the market. Supported by the prevailing tendering system of their customers, i.e. offshore wind project developers, where OWTG purchase decisions are mainly based on purchase price rather than future operating costs, improving the technology regarding reliability is therefore often missed out. In addition to that, gaining efficiency and profitability through economies of scale is hard to realize when customers already purchase larger turbines while production of the current generation has started only recently. The intention of this article is to show that there is a market equilibrium that might be reached soon. Hence the focus should be on improving the technology at this level instead of investing in the development of larger turbines. This might also give advice to political decision makers, who intend to bring the cost of electricity from offshore wind to a competitive level, how to optimally design support schemes for offshore wind. A first indication for the actual presence of a market equilibrium is the fact that this seems to be already reached for onshore wind turbines. Since a few years manufacturers have focused on offering a size between 2 and 3 MW for the onshore market [15,16].

This investigation requires the consideration of both economic and technical aspects. Considering offshore wind industry solely from an economic point of view an increasing size of wind turbines seems reasonable. Although larger turbines cost more in terms of acquisition and operation, they generate more energy and consequently also gain more revenues. Hence the growth of turbines would only stop if costs increase disproportional with size or the additional gain in revenues is too little. But physics reveals some additional limitations apart from the engineering challenges that come along with the design of larger turbines. Firstly, a wind turbine transforms the kinetic energy content of the wind into electrical energy, which results in less kinetic energy and reduced wind speed downwind. Hence if a wake intersects with the rotor of a downwind turbine in the plant it is said to be shadowed by the turbine producing the wake and results in less energy output of the downwind turbine. [17] The larger the turbines the larger the wakes and this in turn means that the spacing between the turbines within the farm has to be increased in order to obtain the same energy yield. Based on a predefined planning area this would result in fewer turbines to be optimal within the farm. Secondly, the wind resource, which is the actual long-term kinetic energy content of the wind at a specific location and height, is limited [18]. Thus the size of wind turbines will only grow until the wind resource is not sufficient to efficiently operate the large turbines.

OWF (offshore wind farm) project developers, who determine the demand for OWTGs, are faced with exactly these contrary economic and technical relations when planning a plant. Hence the idea was to use the planning methodology of an OWF project developer and assuming that the only decision criteria for selecting a wind turbine is the profitability of the plant over its whole life cycle. Applying this methodology with different sizes of OWTGs reveals a market equilibrium for OWTGs in terms of size, where OWF developers do not have an incentive to purchase larger wind turbines as this would not increase profitability. In addition to this analysis investigating the demand side, also the optimal size of OWTGs from the view of energy policy planners was analysed assuming that their objective is to exploit sea areas as efficiently as possible. Thus also the LCOE (levelized cost of electricity) for different OWTG sizes was assessed.

In order to generate reasonable and significant results with the developed model the methodology had to be applied to real data. This is why it was assumed to plan an OWF in the EEZ (Exclusive Economic Zone) of the German North Sea. Since Germany has

envisaged installing 20–25 GW offshore wind capacity until 2030, the German offshore wind industry is one of the most promising markets for OWTGs in Europe [19]. There was taken particular care about the selection of data, the design of the methodology and assumptions in the sense being as close as possible to reality.

After a short clarification what is exactly understood by wind turbine size and the state of the art OWTG selection process, Section 2 describes the methodology used to identify the market equilibrium and the selected case study data. Section 3 provides the results of the analysis and in Section 4 a critical reflection based on a sensitivity analysis verifies the robustness of the results and individual conclusions for stakeholders in the offshore wind industry are discussed.

1.1. Clarification of wind turbine size and selection process

1.1.1. Wind turbine size

First of all it has to be defined how the size of a wind turbine is specified. As indicated earlier, the size of a wind turbine is usually determined by its rated power (also referred to as installed capacity) specified in kW (kilowatt) or MW. This defines the level of power the turbine and its components is designed for and thus is also the nameplate capacity of the generator. Therefore it is the maximum power a wind turbine is able to produce. The basic equation for power generation P from wind

$$P = \frac{1}{2} \cdot A \cdot \rho \cdot v^3 \cdot C_p \quad (1)$$

where A designates the swept area of the rotor, v the wind speed, ρ the air density and C_p the rotor power coefficient, reveals that the installed capacity also determines the geometric proportions. In order to ensure efficiency of the turbine the rotor area has to be increased with rated power. In addition to that, also the hub height, which is the distance between ground and rotor centre, has to be raised, because on the one hand a certain distance between rotor tip and ground has to be adhered and on the other hand increasing wind speed with height ensures sufficient power input [20].

1.1.2. OWTG selection process

Prior to developing a research methodology for the OWTG market equilibrium, it is important to understand how a purchase decision concerning the selection of an OWTG type is usually made. Fig. 1 provides a visualisation of the selection process using IDEFO modelling technique¹ [21] assuming that the main decision criterion is the overall project profitability. For this process basically two models are needed: a spatial planning model and an economic model. The spatial planning model calculates the optimal energy yield based on OWTG data, provided by turbine vendors, wind data of the site and an initial number of turbines. Hence this model uses an optimization algorithm in order to determine the ideal layout of the farm with regards to maximum energy output while observing the constraints of the project area. The optimal energy yield is used as an input for the economic model. This model calculates the profitability of the project using cost and remuneration data. In order to find the most profitable layout of the plant the economic model varies the number of turbines and feeds back the information to the spatial planning model. After some iterations the maximum profitability including

¹ This function modelling language is capable of graphically representing enterprise operations and has the main advantage that additional to input/output relations it is also possible to depict controls, which specify conditions required for the function to produce correct outputs, and mechanisms, which supports the execution of the function such as resources.

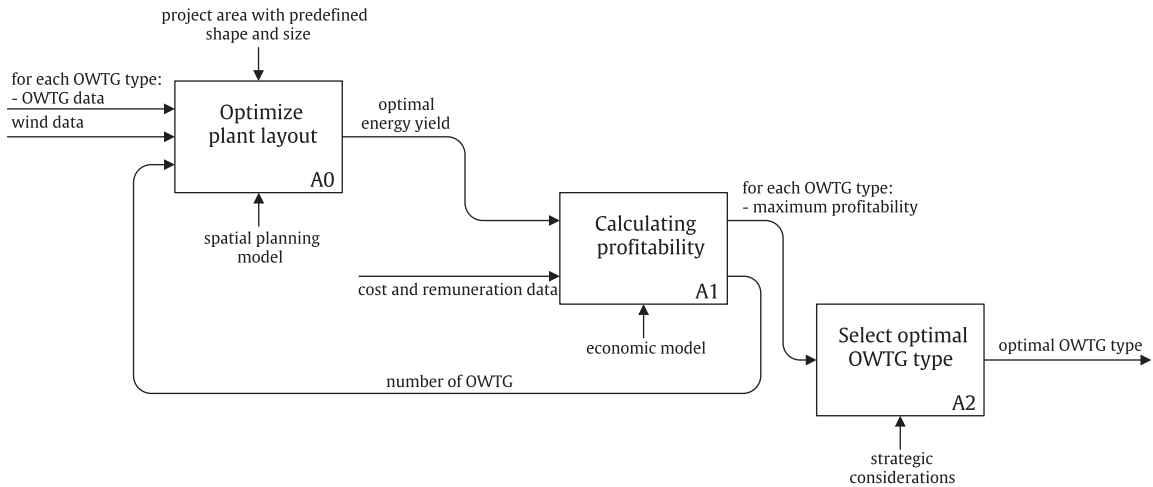


Fig. 1. OWTG selection process.

optimal number and positioning of turbines for each OWTG type is calculated. Usually also strategic considerations as for example financial standing and quality ratings of the potential suppliers are contributing to the decision, but this was not considered in the model developed in the following [22].

2. Methodology

The OWTG selection process served as a reference for developing the research methodology of this article, which is shown in Fig. 2. Instead of comparing different types of OWTGs from different vendors, the process was applied to OWTGs of different sizes. In order to obtain a clear picture and not being misled to jump to conclusions, the optimization loop was omitted. Instead of that the number of turbines was continuously increased within a range of installed capacity, which made it possible to trace the relations conditional on installed capacity. The methodology was also expanded by the LCOE model in order to evaluate the preferences of an energy policy planner. In the following sections spatial planning, profitability and LCOE model is described in detail.

2.1. Spatial planning model

An essential assumption for the spatial planning model was that the turbines are placed within an area of predefined shape and size. This is a reasonable approach, because the BSH (Federal Maritime and Hydrographic Agency) [23], which is the main authority for approving OWFs in the German seas, gives in the first instance (1st release) only a basic permission to build a wind farm within a specified project area and guarantees that no other project will be approved within this area for a given period of time. Type, number and arrangement of turbines are allowed to be modified later on (2nd release), but the boundaries of the planning area are fixed. Hence the approach, which is similar to other countries, is to first do a general planning in order to secure the site and afterwards determine details such as the selection of an OWTG type.

Due to the wake effects and their significant impact on energy yield an algorithm was needed in order to find the optimal layout. Considering the number of academic literature that addresses this particular issue, whereof Ref. [22] provides an excellent and comprehensive review, reveals that this is currently a popular research topic. But this is already not only an issue on academic

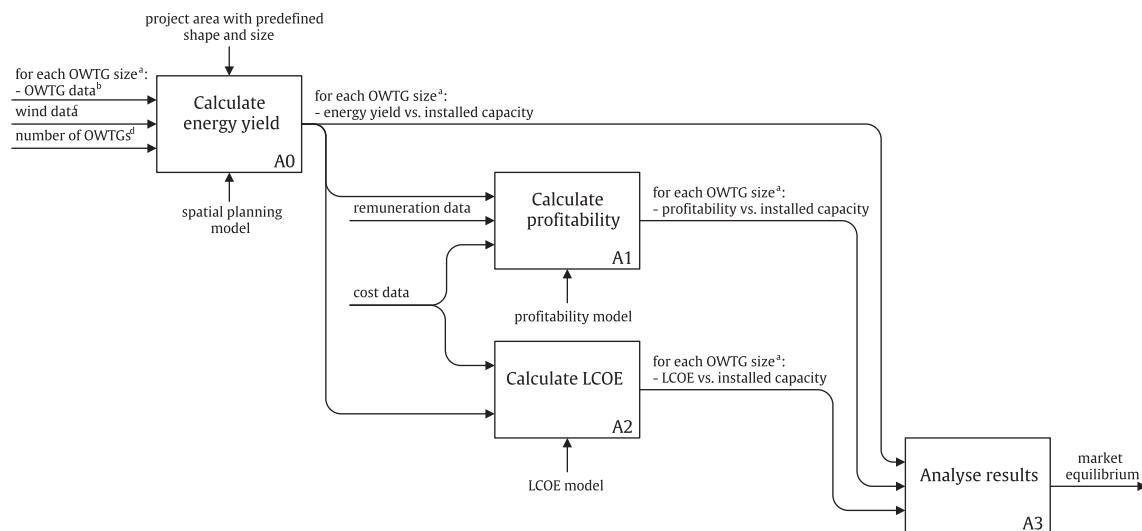


Fig. 2. Methodology. ^aOWTG sizes under investigation: 3 MW, 5 MW, 8 MW, 10 MW, 15 MW and 20 MW. ^bOWTG data: power curve, thrust curve, rated power, rotor diameter and hub height. ^cWind data: Weibull distribution and probability for each direction sector (30°). ^dNumber of turbines: varying between 300 and 600 MW installed capacity.

level. Wind farm planning software packages already contain optimization modules, which enable the users to optimize the plant layout using regular or random pattern regarding maximum energy capture [24,25] or even return on investment [26]. Considering this fact shows that the methodology presented in this article should be already state of the art for wind farm developers.

Although most papers propose algorithms using random patterns, the reality shows that symmetrical wind farm layouts are preferred especially in case of OWFs [22]. Since requirements concerning the safety and efficiency of vessel traffic in the German EEZ require that at least the outer line of turbines surrounding the OWF is placed in regular distance, it seemed to be obvious to place the turbines in a regular pattern for the whole OWF [27]. However, taking into account that this approach was applied to every OWTG size it seemed to be a minor issue.

The spatial planning model determined the layout using the number of horizontal and vertical turbines as an input. Fig. 3 shows as an example how 12 turbines were placed. P_{wr} designates the point that has been chosen for the case study within the German North Sea and where wind resource data was available. This is also the centre of the planning area with a horizontal length l_h and a vertical length l_v . Since the horizontal distance d_h respectively vertical distance d_v between turbines must always be equal they result from dividing the corresponding length by the number of turbines minus one. In case of different array combinations (4×3 , 3×4 , etc.) which result in the same number of overall turbines, the one that generated the highest energy yield was used for the result analysis. As mentioned before the overall number of turbines was varied in a predefined interval of installed capacity. Finally, turbines were placed with a minimum distance of four rotor diameters, which is the limit of the wake model applied and beyond that commonly recommended due to high mechanical loads caused by turbulence effects [28].

The output of the spatial planning model is the annual energy yield which can be obtained with the chosen wind farm pattern. The energy yield of one turbine Y_{WTG} within the farm per annum can be calculated using following equation:

$$Y_{WTG} = 8766 \cdot \sum_{\varphi} \rho(\varphi) \cdot \sum_{v_{hub} = v_{in} + 0.5}^{v_{out} - 0.5} f(v_{hwr}(v_{hub}), \varphi) \cdot P(v_{hub} - v_{def}(v_{hub}, \varphi)) \quad (2)$$

where 8766 is the number of hours per year, φ the wind direction, $\rho(\varphi)$ the probability of occurrence for a specific wind direction, v_{hub} the wind speed at hub height, v_{in} the cut-in and v_{out} the cut-out

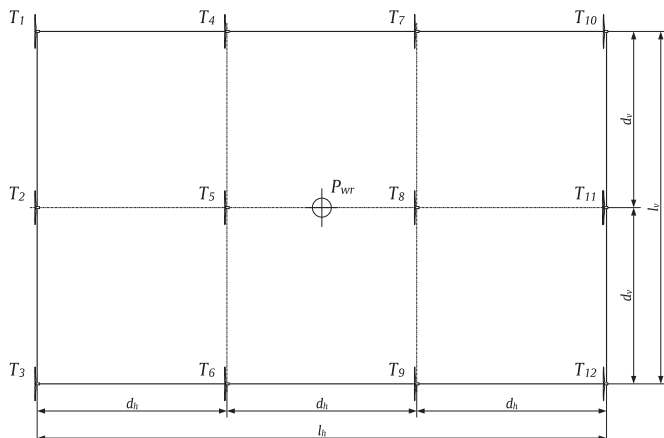


Fig. 3. Example for placement of 12 (4×3 array) turbines.

wind speed of the wind turbine, $f(v_{hwr}(v_{hub}), \varphi)$ the probability of occurrence for a specific wind speed at a specific height $v_{hwr}(v_{hub})$ in a specific direction, $P(v_{hub})$ the power output for different wind speeds of the turbine and $v_{def}(v_{hub}, \varphi)$ the wind speed deficit caused by wake effects for a specific wind speed and direction. The formula is based on a methodology using wind speed bins recommended in the international standard IEC (International Electrotechnical Commission) 61400-12-1 [29].

Due to the fact that the hub height of turbines increases with their size, the variability of the wind resource with height had to be included in this model. As stated in Ref. [30], using the power law instead of the stability dependent logarithmic law is suitable for a vertical extrapolation of the wind profiles for this application. The reason for that is that hub heights of OWTGs are in the Ekman sublayer of the marine atmospheric boundary layer, which begins about 100 m above sea level, and there only a slight wind speed increase occurs. According to the international standard IEC 61400-3 [31], the height adaption using the power law can be calculated using following formula:

$$v_{hwr}(v_{hub}) = v_{hub} \cdot \left(\frac{z_{hwr}}{z_{hub}} \right)^\alpha \quad (3)$$

where v_{hwr} designates the wind speed at the height where the wind resource is given, v_{hub} the wind speed at hub height of the turbine, z_{hwr} the height where the wind resource is given, z_{hub} the hub height of the turbine and α the power law exponent. This standard also recommends to use 0.14 for latter which should be suitable for offshore conditions. Considering the fact of only a slight wind speed increase in this heights and the results of measurement campaigns in this area (e.g. Ref. [32] claims an α of 0.10) this value seemed to be a quite conservative assumption.

For determining the wind speed deficit the wake model proposed by Ref. [33] and further developed by Ref. [34] was used, which is according to Ref. [22] the most widely accepted model by the wind industry and with regard to the objective of this article it seemed to be the right balance between computational effort and accuracy. For a single wake the wind speed deficit caused by a turbine in a distance x , can be calculate using the following equation:

$$v_{def_single}(v_{hub}, \varphi) = v_{hub} \cdot \left(1 - \sqrt{1 - C_T(v_{hub})} \right) \cdot \left(\frac{d_R}{d_R + 2 \cdot k \cdot x} \right)^2 \cdot \frac{A_{shadow}}{A_R} \quad (4)$$

where $C_T(v_{hub})$ is the thrust coefficient, d_R the rotor diameter, k the wake decay constant, x the distance between the turbines, A_{shadow} the shadowed area by the wake and A_R the rotor swept area. The wake decay constant k was assumed to be 0.04 which is a reasonable assumption for offshore wind farms [35]. In case of multiple interacting wakes Ref. [34] proposes to use following equation in order to calculate the resulting velocity deficit:

$$v_{def}(v_{hub}, \varphi) = \sqrt{\sum_{i=1}^n (v_{def_single}(v_{hub}, \varphi)_i)^2} \quad (5)$$

Hence for every wind turbine the energy yield was calculated including the wake effects of all other turbines. This required the consideration of geometric relations between the turbines subject to the wind direction. Refs. [17,36,37] provide good guidance how to calculate them.

Finally, the annual energy yield of the whole wind power plant can be calculated using

$$Y_{\text{farm}} = \eta \cdot \sum_{j=1}^{\text{TN}} Y_{\text{WTG},j} \quad (6)$$

where η is the efficiency of the plant and TN the number of turbines within the farm. A plant efficiency of 95% was assumed, which includes losses due to unavailability, electrical transmission, power curve degradation, wind hysteresis, etc.

2.2. Economic models

2.2.1. Profitability model

As described before, it was assumed that OWF project developers try to maximize their profit and thus their only decision criteria for selecting an OWTG of a specific size is the resulting profitability of the project. As an indicator for profitability of the OWF the IRR (internal rate of return) was used, as it does not require assumptions on discount rates and it incorporates both costs and revenues [38]. This profitability parameter is calculated with a standard discounted cash flow model, which means that all cash flows – costs and revenues – are discounted over the lifetime of the plant to a base year. Using similar cash flow models of wind power plants (e.g. Refs. [37,39,40]) as basis the IRR can be derived by solving following equation:

$$0 = -C_{\text{Dev}} - P_{\text{R}} \cdot \text{TN} \cdot (c_{\text{Inv}} + c_{\text{Dis}}) + \sum_{t=1}^T \frac{Y_{\text{farm}} \cdot (r_t - c_{\text{Op}} \cdot (1 + i_{\text{Op}})^{t-1})}{(1 + \text{IRR})^t} \quad (8)$$

where C_{Dev} designates the onetime development costs, c_{Inv} the specific investment costs, c_{Dis} the specific dismantling costs, T the lifetime of the wind farm, r_t the remuneration per unit of energy for the respective year, c_{Op} the specific operation costs and i_{Op} the annual increase of the operation costs. Considering the facts that current offshore turbines are designed for a lifetime of 20–25 years, wind farm approvals in Germany expire after 25 years [41] and a construction and dismantling period of a few years, the assumption of 20 years for the lifetime T of the plant seemed reasonable and is also conform with literature [38]. For the sake of simplicity, it was assumed that all turbines are fully commissioned respectively dismantled at the same point in time.

The development costs comprise all expenditures for developing an OWF from scratch such as soil examination, environmental assessments and appraisals that have to be provided to the authorities during the approval process. All expenditures incurred during the construction and commissioning of the power plant are the investment costs, which are typically standardized to the base of kW or MW. Thus included are all costs for plant components (OWTG, foundation, offshore substation, inner-array cabling), project management, logistics and others until the OWF is commissioned. Costs arising during operation such as maintenance, insurance and administrative costs are operation costs and are usually standardized to the unit of produced energy. Due to decreasing reliability of technical machines, it is reasonable to include an annual increase of operational expenditures. After the lifetime the plant has to be dismantled. All costs that arise in this phase are dismantling costs and are reduced by the residual value of the components [42].

For the economic model it was assumed that the investment costs increase linearly with the installed capacity respectively operation costs with the energy produced, which influences the numerical results significantly. Therefore Section 4.1 provides a critical reflection based on a comprehensive sensitivity analysis where the impacts of total cost variations and effects on costs such

as economies of scale, cost development subject to upscaling, etc. are discussed in detail.

2.2.2. LCOE model

In order to be able to analyse the market equilibrium also from the perspective of an energy policy planner, the average lifetime LCOE was calculated. Adapting the formula defined by Ref. [43] to wind energy, LCOE can be calculated using following equation:

$$\text{LCOE} = \frac{C_{\text{Dev}} + P_{\text{R}} \cdot \text{TN} \cdot (c_{\text{Inv}} + c_{\text{Dis}}) + \sum_{t=1}^N \frac{Y_{\text{farm}} \cdot (c_{\text{Op}} \cdot (1 + i_{\text{Op}})^{t-1})}{(1+r)^t}}{\sum_{t=1}^N \frac{Y_{\text{farm}}}{(1+r)^t}} \quad (9)$$

where r is the discount rate, which was assumed to be 10% [44].

2.3. Case study

2.3.1. Position and area

The position P_{WR} within the German EEZ for implementing the case study was chosen taking into account the areas that are approved for OWF projects by BSH and the availability of wind resource data. Fig. 4 shows the chosen $P_{\text{WR}} = 54^\circ 28' 42.44'' \text{ N}/6^\circ 19' 56.30'' \text{ E}$, which lies in an area with a water depth of 30–40 m and is about 100 km away from shore. Considering the 25 wind farm projects in the North Sea that have been approved so far (status April 2013) by the BSH [41], an ordinary project area has a size of about 40 km², a shape with straight borders and comprises 80 wind turbines.² Hence a planning area with rectangular shape, vertical length of 5 km and horizontal width of 8 km was used for the case study.

2.3.2. Wind resource data

In order to obtain reasonable results, it is important to use wind data of high quality and not limiting their significance by simplification in the model such as using an average wind speed or only one wind direction. Basically, for calculating the energy yield of the wind farm including the wake effects a probability of occurrence for different wind speeds in the different directions is needed. It is common to provide the wind data as Weibull distribution which is defined as follows:

$$f(v, \varphi) = \frac{k(\varphi)}{c(\varphi)} \cdot \left(\frac{v}{c(\varphi)} \right)^{k(\varphi)-1} \cdot e^{-\left(\frac{v}{c(\varphi)}\right)^{k(\varphi)}} \quad (10)$$

where $k(\varphi)$ and $c(\varphi)$ represent the shape and scale parameter. For this analysis one point of the North Sea wind atlas developed by NORSEWInD research consortium [46] was used. They acquired, collated, quality controlled and analysed wind data from different measurement stations around the North Sea using different kinds of technologies with the aim to provide a reliable data basis for the wind industry. The wind resource data for the chosen point comprise $k(\varphi)$ and $c(\varphi)$ for 12 sectors of 30° width and the probability of occurrence for each wind direction $\rho(\varphi)$. As stated in Ref. [36], this is a good data basis for energy yield estimations. In order to generate results that make it possible to draw representative conclusions, a position with a quite good wind resource for the German EEZ was chosen. Fig. 5 shows the wind rose at P_{WR} , where

² The reason for these characteristics of an ordinary project area might be that the BSH states that they have so far only projects approved that comprise maximally 80 wind turbines, because the impact of offshore wind farms on navigational safety and the marine environment has not yet been finally assessed.

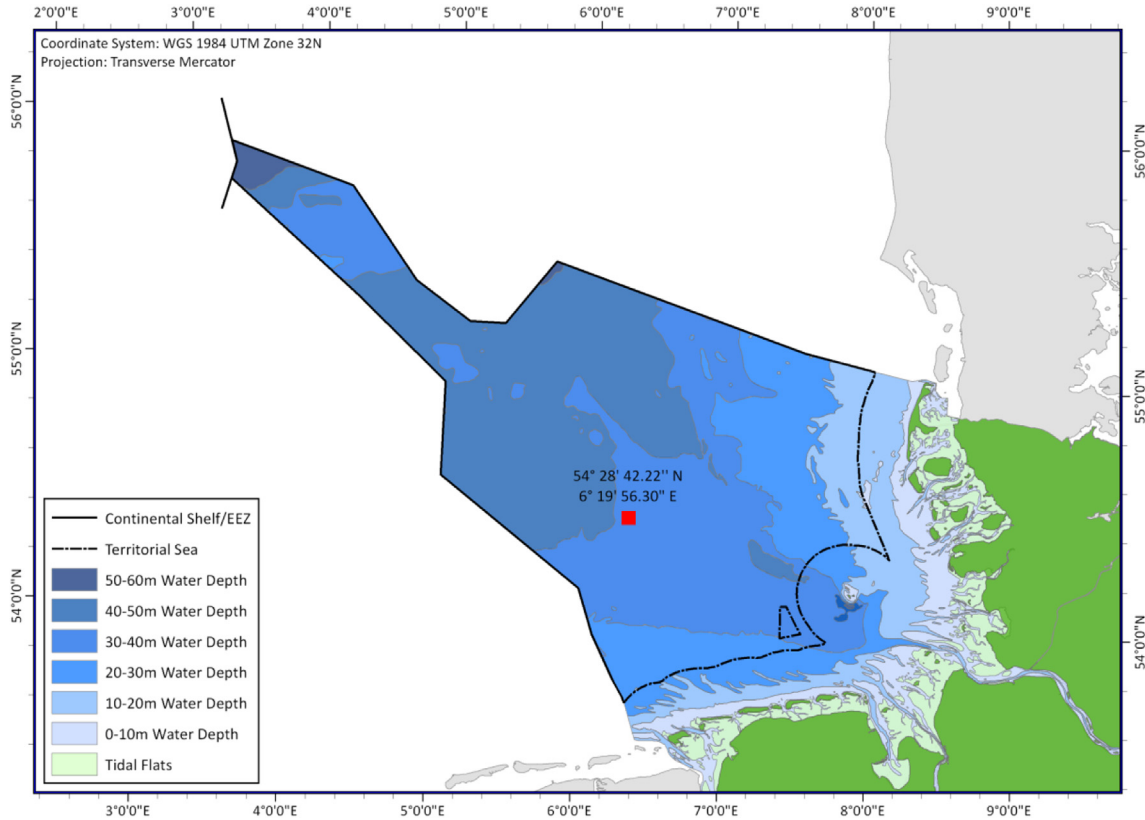


Fig. 4. Position for case study (based on data provided by Ref. [45]).

the total distribution parameters equal $c_{total} = 11.7$ m/s and $k_{total} = 2.12$.

2.3.3. Wind turbine data

The methodology described above reveals that following data of every OWTG is needed: rated power, hub height, rotor diameter, power curve (power output vs. wind speed) and thrust curve (thrust coefficient vs. wind speed). This input data was defined based on specifications of current commercially available OWTGs ([47] provides a good overview), projections of the upscaling trend [48] and scientific concepts (e.g. Refs. [5–7]). Furthermore wind turbine data was determined very carefully in order to be as close as possible to reality, but also to have a clear difference between the different sizes. Table 1 provides the chosen dimensions of the different OWTG sizes.³

The smallest size that was included in the analysis is 3 MW. As a reference for the data the Vestas V90-3.0 MW [49] was used. This OWTG belongs to the last generation and has been deployed for example for the UK round 1 OWF projects at Kentish Flats and Barrow [14]. The data of the largest wind turbine were used from the UpWind project [6]. As a reference for OWTGs of the near future, data of the Vestas V164-8.0 MW [50] and SeaTitan 10 MW [51] wind turbines were used. The dimensions of the 5 MW size, which is the current generation, and the 15 MW size were calculated using the others as basis and trendlines provided by Ref. [48]. The power curves were defined using the data of the turbines mentioned above and harmonizing them with each other to ensure

that manufacturer specific deviations do not falsify the analysis. Ref. [52] presents a fast and efficient method of how rescaling of power curves can be done based on equation (1). Fig. 6 shows the applied power curves. The same thrust curve, cut-in wind speed (4 m/s) and cut-out wind speed (25 m/s) were used for all turbines.

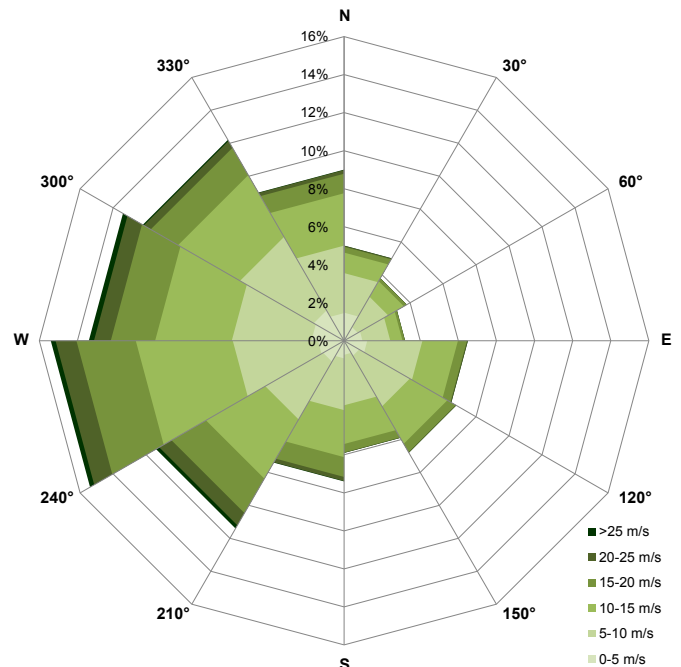


Fig. 5. Wind rose at position 54° 28' 42.44" N/6° 19' 56.30" E.

³ It has to be commented that the results of this analysis do not reflect the relative performance of the turbines used as a reference, because the power curves and thrust curve were significantly modified.

Table 1
OWTG dimensions.

Rated power	3 MW	5 MW	8 MW	10 MW	15 MW	20 MW
Hub height	80 m	90 m	105 m	125 m	140 m	153 m
Rotor diameter	90 m	130 m	164 m	190 m	222 m	252 m

2.3.4. Cost assumptions

There are several sources available where the cost components of OWFs are assessed and analysed (e.g. Refs. [39,53]). For the model developed in this paper it was more important that the relation of the cost components relative to each other is reasonable than their individual level. This is why all values were used from one source, because cost data vary significantly between different projects and in that way the same data basis is ensured. Hence cost data of the German offshore market provided by Ref. [42] were used for the analysis (see Table 2).

2.3.5. Remuneration assumptions

According to the renewable energy law (EEG (Erneuerbare-Energien-Gesetz)) in Germany [54], an operator of an OWF can choose between three remuneration options (see Table 3). For this model it was assumed that 16 years after commissioning the energy is remunerated with a tariff of 150 EUR/MWh, which corresponds to the standard option plus an extension period of four years (36 m water depth and 100 km distance to shore). Subsequently it was assumed that the energy is traded for the remaining four years. The average market price in this period was calculated using 50 EUR/MWh as basis for the year of commissioning and adding an escalation of 2% every year.

3. Results

The model was evaluated for an OWF with an installed capacity between 300 and 600 MW, which seemed to be reasonable for the selected case study parameters. In addition to the economic parameters IRR and LCOE the energy yield was calculated in order to determine also the behaviour of the physical basis. Placing turbines with a reasonable proportion between horizontal and vertical quantity and within the installed capacity limits revealed an almost linear relationship between installed capacity and energy yield (see Fig. 7).

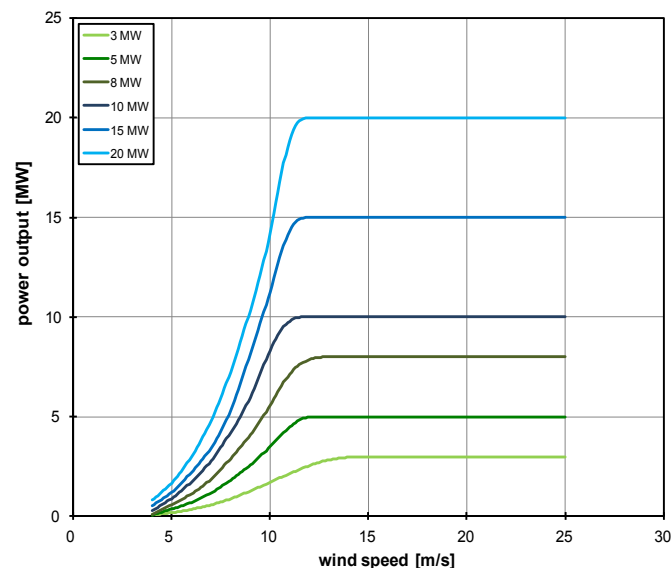


Fig. 6. Power curves.

Table 2
Overview of cost assumptions.

C_{Dev}	35 EUR million
c_{Inv}	3.6 EUR million per MW
c_{Op}	25.5 EUR/MWh
i_{Op}	2.0% per year
c_{Dis}	0.2 EUR million per MW

Table 3
Remuneration scheme (commissioning before 1.1.2018 assumed).

	Initial period	Extension period	Remaining period
Trading Standard	150 EUR/MWh 12 years	Market price 150 EUR/MWh +0.5 months for every nautical mile beyond 12 nautical miles to shore	35 EUR/MWh
Compression	190 EUR/MWh 8 years	+1.7 months for every meter beyond 20 m water depth	

Since the economic parameters highly depend on the energy yield they also follow an almost linear trend conditional on the installed capacity. Therefore Table 4 provides the results in the form of linear regression factors including the coefficient of determination.

In order to be able to derive conclusions Fig. 8 shows the mean relative deviations subject to the OWTG size using the 10 MW turbine as a benchmark.

4. Discussion and analysis of results

The results apparently indicate a market equilibrium for OWTGs with a size of 10 MW. The fact that doubling the size from 10 MW to 20 MW, which entails substantial technical challenges, gains only a minor increase in energy yield and thus also in IRR, which is the customers' key figure for a purchase decision, suggests that the incentive for wind turbine manufacturers to invest in the development of 20 MW turbines at least for the German offshore wind

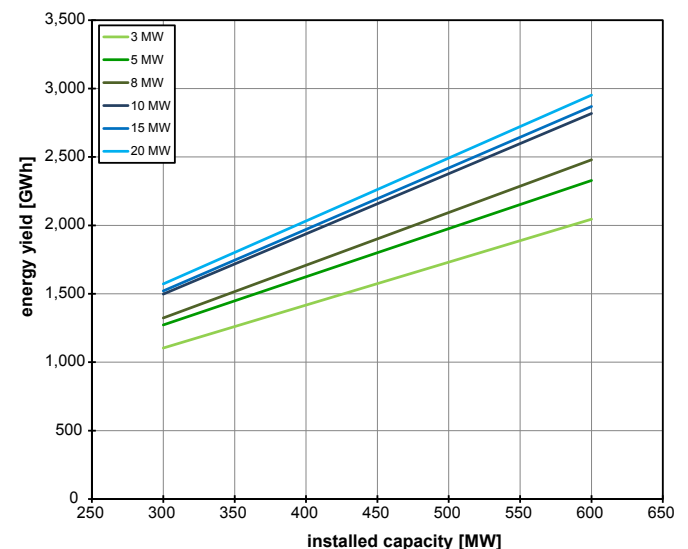


Fig. 7. Energy yield vs. installed capacity.

Table 4
Relationship between energy yield/IRR/LCOE and OWTG size specified in form of linear regression factors.

OWTG size, MW	Energy yield			IRR			LCOE		
	MWh		R^2	%		R^2	EUR/MWh		R^2
	m	b		m	b		m	b	
3	3139.50	161,281	0.9967	-2.73E-05	9.28%	0.8219	2.37E-02	148.23	0.7722
5	3523.19	214,794	0.9987	-3.77E-05	11.87%	0.9343	2.61E-02	130.80	0.9344
8	3854.41	166,978	0.9978	-2.67E-05	12.27%	0.7890	1.70E-02	128.92	0.7887
10	4403.55	176,287	0.9990	-2.75E-05	14.53%	0.7997	1.40E-02	117.54	0.7809
15	4489.80	174,544	0.9996	-2.72E-05	14.84%	0.8422	1.35E-02	116.17	0.8354
20	4536.84	217,894	0.9995	-2.48E-05	15.32%	0.9080	1.19E-02	114.01	0.9051

- Valid within range between 300 and 600 MW installed capacity.
 - $y = m \cdot P_R \cdot TN + b$ where y is the energy yield/IRR/LCOE.
 - Linear least squares regression applied.

market is insufficient. The results indicate that the potential increase of the energy yield and the significantly decreasing potential sales volume may not compensate the effort for developing larger OWTGs, setting up new manufacturing facilities and elaborating new installation and service concepts. Cost reductions that can be obtained due to increasing reliability and standardization may have a similar or even higher cost-benefit effect [44,55]. Apart from that the trend of the LCOE subject to OWTG size questions governmental subsidies, which support the development of OWTGs beyond the size of 10 MW, since this does not lead to the intended significant cost degression. The reason for a flattening of the energy yield and as a consequence also of the IRR and LCOE with increasing OWTG size is simply the limited available wind resource. Something similar was already reported in Ref. [56], where the results reveal that higher yield from larger OWTGs far away from shore do not compensate for the increased costs compared to smaller OWTGs near the coast.

4.1. Critical reflection and sensitivity analysis

Admittedly, the analysis is based on several assumptions that were needed to anticipate the future development of OWTGs. Therefore this section provides a critical reflection of the input parameters in order to prove if the methodology presented generated representative results. It has to be pointed out that the aim of this article was to show that there is an indication for a market equilibrium. Especially the analysis of the economic

parameters IRR and LCOE was not aiming at providing an exact numerical projection of these parameters. The intention was to show that these key figures, which are the basis for a purchase decision of the wind turbine manufacturers' customers respectively the basis for decision-making for energy policy planners, are also flattening with increasing OWTG size similar to the energy yield. Thus the economic analysis presented before should only give evidence with regard to future market behaviour. The critical discussion in the following is based on a comprehensive sensitivity analysis (see Supplementary Notes for detailed results).

For the sake of simplicity and considering the fact that all result parameter functions are almost linear and parallel subject to the installed capacity it is useful to discuss only the relative and absolute effect of each sensitivity case. Relative effect means that the average relative distance between the result function for a specific wind turbine size and the 10 MW benchmark either increases or decreases. Or in other words the graphs shown in Fig. 7 are either expanded or contracted. In contrast to that, absolute effect means that all result functions are shifted either to lower or higher values without changing their relative distance to the 10 MW benchmark. Fig. 9 provides a visualisation of these effects. With regard to the aim of this article only the relative effect of an increased distance (expansion) to the 10 MW benchmark would oppose the conclusion of a 10 MW market equilibrium.

The main input parameter with regard to the impact on energy yield is clearly the wind resource. Table 5 provides an overview of the effects caused by the associated sensitivity cases. For the case study only one position of the NORSEWinD atlas [46] was used, which questions how representative the selected wind resource for the German EEZ is. Analysing the NORSEWinD atlas within the German EEZ and considering only areas which are allocated for offshore wind reveals that the minimum ($c_{total} = 11.5 \text{ m/s}/k_{total} = 2.12$) and maximum ($c_{total} = 11.8 \text{ m/s}/k_{total} = 2.12$) wind resource do not significantly deviate from the one used for the analysis. Thus basing the analysis on these two wind resources leads subsequently only to minor deviations and mainly to a shift to lower respectively higher values.

Another critical aspect of the analysis is the height adaption using the power law with an exponent of 0.14, which is, as discussed before, a quite conservative assumption. The result using a lower power law exponent ($\alpha = 0.00$) is obvious: lowering the power law exponent leads to the relative effect of contraction, because the assumption causes that the wind resource is the same for every turbine size and thus larger turbines with higher hub height do not have a higher wind resource available. Moreover, this admittedly extreme sensitivity case exhibits that the losses due to wake effects would be also higher for larger OWTGs resulting in less energy yield for the same installed capacity compared to the 10 MW benchmark.

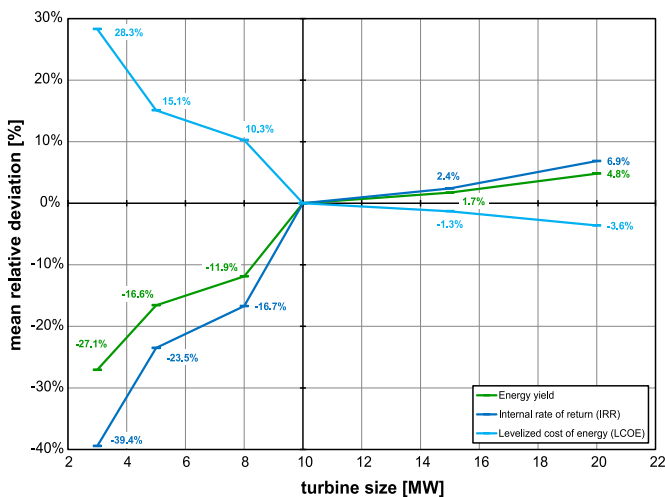


Fig. 8. Mean relative deviations of energy yield/IRR/LCOE subject to OWTG size using 10 MW as a benchmark.

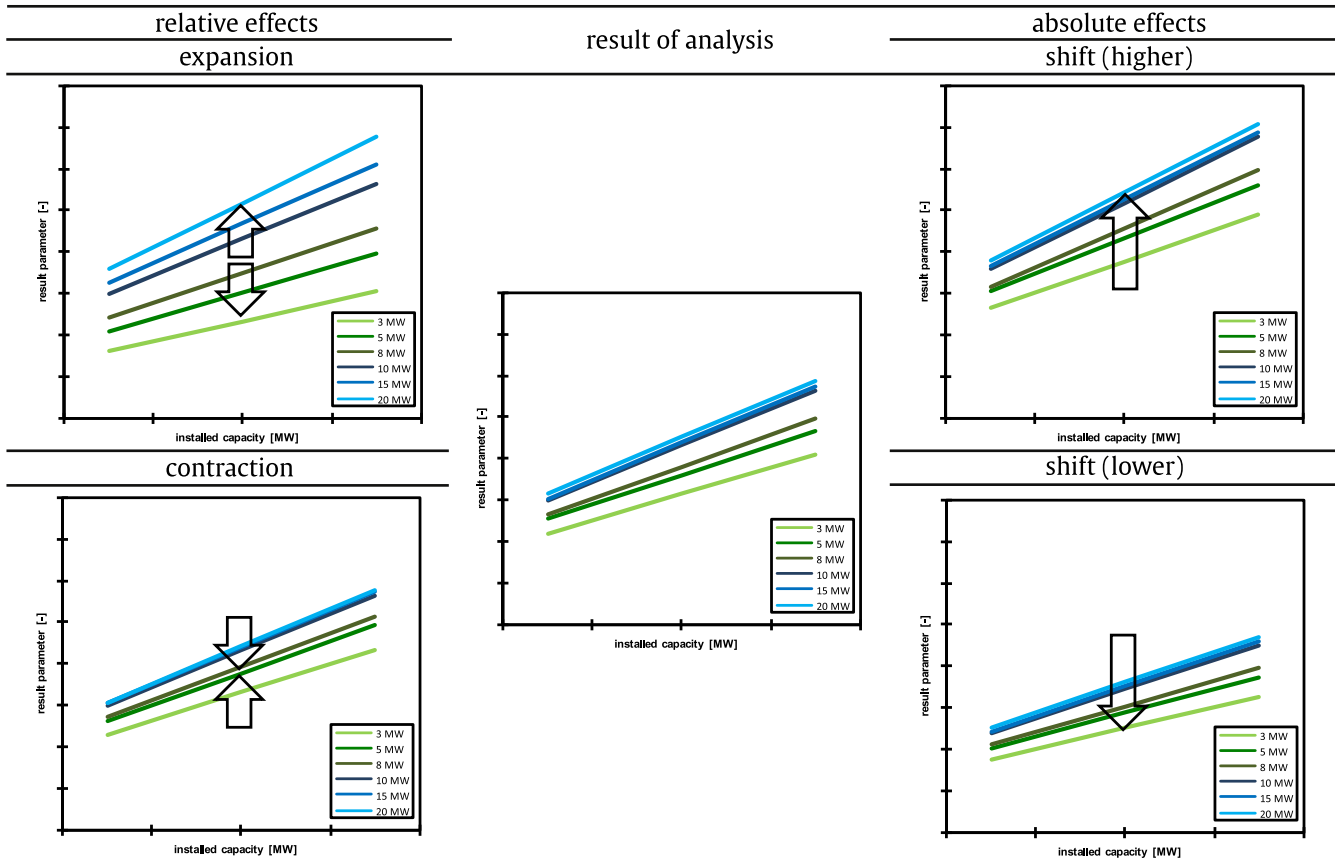


Fig. 9. Visualisation of possible relative and absolute effects caused by sensitivity investigations.

Considering these sensitivity cases investigating the effects caused by changes of the input wind resource shows that although they have an impact on the numerical result, they prove that the article's statement regarding the presence of a market equilibrium is robust. Apart from that, also wind turbine data and the wake model could have influenced the energy yield. Possible deviations caused by those inputs can be ruled out since the data for the 3 MW, 8 MW, 10 MW and 20 MW size stem from reliable sources and the wake model was verified using professional wind energy assessment software.

But apart from the assumptions used for calculating the energy yield, also the effects of varying cost inputs should be discussed in more detail (see Table 6). First of all the level of costs are worthy of discussion, because for example the specific investment costs depend significantly on distance to shore and water depth [57]. Apart from that substantial cost reductions are intended in the near future in order to make electricity from offshore wind more competitive [2,3]. However cost may develop in future, when assuming that all sizes experience the same negative or positive cost trend, the effect on IRR and LCOE is only absolute. This effect is

the same for any change in feed-in remuneration scheme as long as electricity from larger OWTGs is not remunerated differently than that from smaller OWTGs. Since costs and remuneration determine profitability and therefore investment decisions any absolute change would only influence the sales volume for OWTGs, but not affect the purchase decision regarding OWTG size. Thus the conclusion of the presence of a market equilibrium is independent of the level of cost or feed-in remuneration.

Another point of criticism might be the assumption that no economies of scale occur, which seems to be unrealistic and the resulting linear functions for IRR and LCOE implausible. First of all, it has to be commented that the survey done by Ref. [58] clearly shows that economies of scale for OWFs do not occur so far. However, the presence of economies of scale may again have an impact on the numerical results of this analysis, but it is not reasonable that this would change the conclusion. The reason for that is the simple fact that economies of scale for smaller OWTGs will always occur before they do for larger ones, because for an OWF with the same installed capacity always less larger than smaller turbines are needed. Hence considering this effect in a chronological view, it rather promotes the theory of a market equilibrium, because wind turbine manufacturers, who are facing the decision of either developing a larger OWTG or continuing to exploit economies of scale with the current generation, are aware that economies of scale for the larger OWTGs take only effect again after selling large quantities, which is more difficult since they can only sell less OWTGs for the same OWF size [59]. Even it is assumed that economies of scale become effective in the same quantity range this would only change the shape of the graph, but not have a relative effect on IRR or LCOE.

Table 5
Sensitivity effects due to changes in wind resource assumptions.

Sensitivity case	Energy yield	
	Relative effect	Absolute effect
Higher wind resource	Slight contraction	Shift (higher)
Lower wind resource	Slight expansion	Shift (lower)
Lower power law exponent	Contraction	–

Table 6
Sensitivity effects due to changes in cost assumptions.

Sensitivity case	Internal rate of return		Levelized cost of energy	
	Relative effect	Absolute effect	Relative effect	Absolute effect
Cost reduction	Slight concentration	Shift (higher)	–	Shift (lower)
Cost increase	Slight expansion	Shift (lower)	–	Shift (higher)
Larger comparatively less expensive than smaller	Expansion	–	Expansion	–
Smaller comparatively less expensive than larger	Concentration	–	Concentration	–

More interesting is the question how cost will develop with increasing size. Would larger wind turbines be comparatively less (more) expensive than smaller, an expansion (contraction) of the graphs would be the consequence, which would disprove the statement of this article. But investigations about costs in relation to upscaling clearly reveal a disproportional increase of costs with size due to the impact on weight and loads [7]. A good example is Ref. [8], where after a comprehensive analysis is concluded that turbine sizes lower than 10 MW will be optimal due to the exponential increase of cost subject to size. In conclusion, although the analysis presented in this article is based on several assumptions, the sensitivity analysis showed that the theory of a market equilibrium for 10 MW OWTGs is robust.

4.2. Managerial implications

In case of the presence of a market equilibrium for OWTGs the conclusion for stakeholders in the offshore wind industry is obvious. Focussing instantaneously on developing 10 MW OWTGs and placing them onto the German offshore wind market, would promise wind turbine manufacturers a sustainable competitiveness. This would be also applicable for the supplying industry as for example foundation and ship vendors that are forced to adapt their products to the size of OWTGs. Interestingly, the analysis also revealed a significant increase in efficiency for installing 5 MW turbines instead of 3 MW respectively 10 MW instead of 8 MW and only a minor increase between 5 MW and 8 MW OWTGs. This would be an indication for the 8 MW size being only an intermediate technology level.

For energy policy planners and governmental decision makers the market equilibrium would suggest that it should be preferred to grant subsidies to research projects that investigate how it is possible to improve the maturity of the technology instead of investing in projects that investigate OWTGs of a size that might be never reasonable. For example fostering technology transfer from other successful industries such as oil & gas, which have considerable experience in offshore operations, might gain more efficiency in order to significantly reduce the cost of electricity generation from offshore wind [60]. It has to be mentioned that the cumulative discounted operating costs over the whole life cycle account for 35–45% of the overall project costs. Considering also the cost reduction potentials for operation & maintenance costs of

about 12% [61] resp. 14% [62], which could decrease the overall OWF costs of up to 7.8% [2], suggests that supporting a reduction of operating costs is as important as research projects that aim for lowering the initial investment costs.

Moreover, the results presented in this article also enable to estimate average installed capacity respectively annual energy yield per unit area and their relation to OWTG size (see Table 7). Applying the common recommendation for wind farm layout design presented in Ref. [28] to all OWTG sizes reveals that the average installed capacity per unit area remains nearly constant, which does not surprise considering the geometric relations. Although an average value of 12.5 MW/km² seems to be quite high (Ref. [63] reports 9 MW/km² respectively 7 MW/km² for UK round 1 resp. 2 OWFs), the fact that it is independent of the OWTG size contradicts investigations about the future trend (e.g. Ref. [64]) that claim an increase of this value with technological development. Apart from that, this information is of particular interest for transmission system operators and offshore substation suppliers since it enables to estimate the maximum capacities expected from sea areas. It also allows the conclusion that the development of standard sizes is reasonable, which would help to reduce costs. Finally the annual energy yield per unit area gives advice to energy policy planners since it answers the question what maximum energy extraction can be expected from sea areas in the German EEZ.

5. Conclusion

This article refers to the current issues of the offshore wind industry with the tight market conditions due to the pressure to continuously place larger OWTGs onto the market. A model was developed with the objective to identify a market equilibrium for OWTGs. This was identified investigating the trend of growing OWTGs from an OWF project developer's point of view, which reflects the demand side of the market, and from the point of view of an energy policy planner. In order to be able to generate reasonable conclusions, the model was applied to a case study wind farm in the German EEZ. Finally, a sensitivity analysis verified the robustness of the article's statement.

The results indicate a market equilibrium for 10 MW OWTGs due to the limited available wind resource. This is highly interesting for stakeholders in the offshore wind industry and allows individual conclusions. The strategic focus on this size might promise

Table 7
Average installed capacity and energy yield per unit area.

OWTG size, MW	Maximum number of turbines ^a , –	Maximum installed capacity ^a , MW	Average installed capacity per unit area, MW/km ²	Average annual energy yield per unit area, MWh/km ²
3	182	546	13.7	46.9
5	90	450	11.3	45.0
8	64	512	12.8	53.5
10	49	490	12.3	58.4
15	36	540	13.5	65.0
20	25	500	12.5	62.3

^aWithin 40 km² assuming minimum horizontal distance of seven and vertical four rotor diameters.

OWTG manufacturers and the supplying industry a sustainable competitiveness. A governmental planner might be better advised to support research projects with funding that aim for improving the 10 MW range instead of the development of OWTGs that do not gain a significant yield and efficiency increase. Finally, the analysis gives information about how much energy yield and installed capacity can be expected from German North Sea areas.

Although the German EEZ is one of the most promising markets for offshore wind in Europe, it would be interesting to investigate the OWTG market equilibrium also for other regions in the world. This could be done using the methodology presented in this article, if necessary adapting it to the legal framework for OWFs in the respective country and applying the respective local wind resource. However, the wind resource used is quite good and experiences reveal that already these conditions are challenging the reliability of currently used technology far away from shore.

Acknowledgements

I would like to thank Strabag OWEVS GmbH for their permission to use data and software tools, Prof. Andreas J. Novak and Prof. Franz Wirl for their advice and several colleagues within the offshore wind industry as well as three independent reviewers for their constructive comments.

Abbreviations

BSH	Federal Maritime and Hydrographic Agency
EEZ	Exclusive Economic Zone
EWEA	European Wind Energy Association
IRR	internal rate of return
kW	kilowatt
LCOE	levelized cost of electricity
MW	megawatt
OWF	offshore wind farm
OWTG	offshore wind turbine generator

Appendix A. Supplementary data

Supplementary data related to this article can be found at <http://dx.doi.org/10.1016/j.energy.2014.02.060>.

References

- [1] European Wind Energy Association (EWEA). The European offshore wind industry – key trends and statistics 2012; 2013.
- [2] Prognos AG, Fichtner GmbH & Co. KG. Cost reduction potentials of offshore wind power in Germany – short version; 2013.
- [3] The Crown Estate. Offshore wind cost reduction – pathways study; 2012.
- [4] European Wind Energy Association (EWEA). The European wind initiative – wind power research and development for the next ten years; 2010.
- [5] European Commission. SET-plan implementation – Azimut offshore wind energy 2020. URL: <http://setis.ec.europa.eu/implementation/project-mapping/wind/AZIMUT.pdf/view> [accessed 18.11.13].
- [6] UpWind Consortium. UpWind – design limits and solutions for very large wind turbines; 2011.
- [7] Sieros G, Chaviaropoulos P, Sørensen JD, Bulder BH, Jamieson P. Upscaling wind turbines: theoretical and practical aspects and their impact on the cost of energy. *Wind Energy* 2012;15:3–17.
- [8] Kjeldsen KS. Cost reduction and stochastic modelling of uncertainties for wind turbine design. Master thesis. Aalborg University; 2009.
- [9] Helsen J, Vanhollenbeke F, Vandepitte D, Desmet W. Some trends and challenges in wind turbine upscaling. In: Proc. ISMA2012; 2012. pp. 4335–50.
- [10] Molly JP. Rated power of wind turbines: what is best? *DEWI Mag* 2011;38:49–57.
- [11] Lee KT, Raina A, Wetzel KK. Optimal rotor size for cost reduction and wind farm profitability. In: Proc. China Wind Power Conf. 2012; 2012.
- [12] Alam MM, Rehman S, Meyer JP, Al-Hadhrami LM. Review of 600–2500 kW sized wind turbines and optimization of hub height for maximum wind energy yield realization. *Renew Sustain Energy Rev* 2011;15:3839–49.
- [13] Kirk M. Site specific optimization of rotor/generator sizing of wind turbines. Master thesis. Georgia Institute of Technology; 2006.
- [14] Feng Y, Tavner PJ, Long H. Early experiences with UK round 1 offshore wind farms. *Proc Inst Civ Eng Energy* 2010;163:167–81.
- [15] European Commission. Technology information sheet – wind energy generation. URL: [http://setis.ec.europa.eu/system/files/Technology Information Sheet - Wind Energy Generation.pdf](http://setis.ec.europa.eu/system/files/Technology%20Information%20Sheet%20-%20Wind%20Energy%20Generation.pdf); 2012 [accessed 23.11.13].
- [16] Kaldellis JK, Zafirakis D. The wind energy (r)evolution: a short review of a long history. *Renew Energy* 2011;36:1887–901.
- [17] González-Longatt F, Wall P, Terzija V. Wake effect in wind farm performance: steady-state and dynamic behavior. *Renew Energy* 2012;39:329–38.
- [18] Landberg L, Myllerup L, Rathmann O, Petersen EL, Jørgensen BH, Badger J, et al. Wind resource estimation – an overview. *Wind Energy* 2003;6:261–71.
- [19] Bundesregierung der Bundesrepublik Deutschland. Strategie der Bundesregierung zur Windenergienutzung auf See; 2002.
- [20] Hau E. Wind turbines – fundamentals, technologies, application, economics. 2nd ed. Berlin, Heidelberg; Springer-Verlag; 2006.
- [21] National Institute of Standards and Technology (NIST). Integration definition for function modeling (IDEFO); 1993.
- [22] Serrano González J, Burgos Payán M, Santos JMR, González-Longatt F. A review and recent developments in the optimal wind-turbine micro-siting problem. *Renew Sustain Energy Rev* 2014;30:133–44.
- [23] Federal Maritime and Hydrographic Agency (BSH). Standard – design of offshore wind turbines (BSH no. 7005); 2007. Hamburg and Rostock.
- [24] EMD International A/S. WindPRO software – module description. URL: [http://www.emd.dk/files/windpro/WindPRO Modules ENGLISH.pdf](http://www.emd.dk/files/windpro/WindPRO%20Modules%20ENGLISH.pdf); 2013 [accessed 25.11.13].
- [25] AWS Truepower. OpenWind user manual – version 1.4. Albany, NY; 2012.
- [26] GL Garrad Hassan. WindFarmer V5 – wind farm design software (product data sheet); 2012.
- [27] Federal Waterways and Shipping Administration. Guidelines for the design, marking and operation of wind generators in the area of responsibility of the federal waterways and shipping directorates north-west and north to guarantee the safety and efficiency of vessel traffic; 2009.
- [28] Wagner H-J, Mathur J. Introduction to wind energy systems – basics, technology and operation. Berlin, Heidelberg; Springer-Verlag; 2009.
- [29] International Electrotechnical Commission (IEC). Wind turbines – part 12-1: power performance measurements of electricity producing wind turbines (IEC 61400-12-1). Geneva; 2005.
- [30] Emeis S. Wind energy meteorology – atmospheric physics for wind power generation. Berlin, Heidelberg; Springer-Verlag; 2013.
- [31] International Electrotechnical Commission (IEC). Wind turbines – part 3: design requirements for offshore wind turbines (IEC 61400-3). Geneva; 2009.
- [32] Türk M, Grigutsch K, Emeis S. The wind profile above the sea – investigations basing on four years of FINO 1 data. *DEWI Mag* 2008;33:12–5.
- [33] Jensen NO. A note on wind generator interaction (RISØ-M-2411). Roskilde; 1983.
- [34] Katić I, Højstrup J, Jensen NO. A simple model for cluster efficiency. In: EWEC'86. Proceedings, vol. 1; 1986. pp. 407–10. Rome.
- [35] Phillips JL, Cox SD, Henderson AR, Gill JP. Wake effects within and between large wind projects: the challenge of scale, density and neighbours – onshore and offshore. GL Garrad Hassan; 2010.
- [36] Pérez B, Mínguez R, Guanache R. Offshore wind farm layout optimization using mathematical programming techniques. *Renew Energy* 2013;53:389–99.
- [37] González JS, Rodríguez ÁGG, Mora JC, Burgos Payán M, Santos JR. Overall design optimization of wind farms. *Renew Energy* 2011;36:1973–82.
- [38] Prässler T, Schaechtele J. Comparison of the financial attractiveness among prospective offshore wind parks in selected European countries. *Energy Policy* 2012;45:86–101.
- [39] Weaver T. Financial appraisal of operational offshore wind energy projects. *Renew Sustain Energy Rev* 2012;16:5110–20.
- [40] González JS, González Rodríguez AG, Mora JC, Santos JR, Payan MB. Optimization of wind farm turbines layout using an evolutive algorithm. *Renew Energy* 2010;35:1671–81.
- [41] Federal Maritime and Hydrographic Agency (BSH). Approval of offshore wind farms. URL: <http://www.bsh.de/de/Meeresnutzung/Wirtschaft/Windparks/index.jsp>; 2013 [accessed 20.04.13].
- [42] KPMG AG Wirtschaftsprüfungsgesellschaft. Offshore wind in Europe – 2010 market report; 2010.
- [43] Nuclear Energy Agency (NEA)/International Energy Agency (IEA)/Organisation for Economic Co-operation and Development (OECD). Projected costs of generating electricity – 2005 update; 2005. Paris.
- [44] Heptonstall P, Gross R, Greenacre P, Cockerill T. The cost of offshore wind: understanding the past and projecting the future. *Energy Policy* 2012;41:815–21.
- [45] Federal Maritime and Hydrographic Agency (BSH). Continental shelf research information system (CONTIS). URL: http://www.bsh.de/en/Marine_uses/Industry/CONTIS_maps/; 2013 [accessed 23.05.13].
- [46] NORSEWInD consortium. NORSEWInD – northern seas wind index database. URL: <http://www.norsewind.eu/norse/index.php>; 2013 [accessed 14.02.13].
- [47] Madariaga A, Martín JL, Zamora I, Martínez de Alegría I, Ceballos S. Technological trends in electric topologies for offshore wind power plants. *Renew Sustain Energy Rev* 2013;24:32–44.
- [48] Sánchez de Lara García JP. Wind turbine database: modelling and analysis with focus on upscaling. Chalmers University of Technology; 2013.

- [49] Vestas Wind Systems A/S. Vestas V90-3.0MW (product data sheet). Randers; 2011.
- [50] Vestas Wind Systems A/S. Vestas V164-8.0MW (product data sheet). Aarhus; 2011.
- [51] AMSC. SeaTitan 10 MW wind turbine (product data sheet); 2012.
- [52] Engel P, Hartkopf T. Introduction of a method to scale and compare wind turbine characteristic curves. In: EWEA 2012 Conf. Proc.; 2012.
- [53] Dicorato M, Forte G, Pisani M, Trovato M. Guidelines for assessment of investment cost for offshore wind generation. *Renew Energy* 2011;36:2043–51.
- [54] Bundesministerium der Justiz. Gesetz für den Vorrang Erneuerbarer Energien (Erneuerbare-Energien-Gesetz – EEG); 2008.
- [55] Kaldellis JK, Kapsali M. Shifting towards offshore wind energy—recent activity and future development. *Energy Policy* 2013;53:136–48.
- [56] Möller B, Hong L, Lonsing R, Hvelplund F. Evaluation of offshore wind resources by scale of development. *Energy* 2012;48:314–22.
- [57] Eerens H, de Visser E. Wind-energy potential in Europe 2020-2030. Biltoven; 2008.
- [58] Kaiser MJ, Snyder BF. Offshore wind energy cost modeling – installation and decommissioning. London: Springer-Verlag London; 2012.
- [59] Wind Power Monthly. Article – REpower holds fire on offshore turbines beyond 6 MW. URL: <http://www.windpowermonthly.com/article/1186757/repower-holds-fire-offshore-turbines-beyond-6mw>; 2013 [accessed 13.11.13].
- [60] Marsh G. Renewable energy focus – oil, gas and wind: offshore harmony?. URL: <http://www.renewableenergyfocus.com/view/31166/oil-gas-and-wind-offshore-harmony/>; 2013 [accessed 31.01.14].
- [61] Maples B, Saur G, Hand M, van de Pietermen R, Obdam T. Installation, operation, and maintenance strategies to reduce the cost of offshore wind energy [Technical Report NREL/TP-5000-57403]; 2013.
- [62] Roland Berger Consultants GmbH. Offshore wind toward 2020 – on the pathway to cost competitiveness. URL: http://www.rolandberger.com/media/pdf/Roland_Berger_Offshore_Wind_Study_20130506.pdf; 2013 [accessed 28.01.14].
- [63] Carbon Trust. Offshore wind power: big challenge, big opportunity – maximising the environmental, economic and security benefits. London; 2008.
- [64] European Environment Agency (EEA). Europe’s onshore and offshore wind energy potential – an assessment of environmental and economic constraints. Copenhagen; 2009.

DISTRIBUTED CONTROL OF WIND FARMS USING A FLOW INTERACTION MODEL AND A MULT-AGENT APPROACH

M. Vali*, M. Kühn

*ForWind - University of Oldenburg, Research Group Wind Energy Systems, Oldenburg, Germany+49 (441) 798 5063, mehdi.vali@uni-oldenburg.de.

Introduction

Large-scale wind farms (WFs) are rapidly growing worldwide due to more deployment of wind energy. EWEA has reported wind energy targets to produce almost half of EU electricity demand by 2050. One pathway to materialize this ambitious goal is the further improvement of the cost-effectiveness of wind energy e.g. with the exploitation of WFs with new advanced control algorithms. The wind farm control (WFC) sub-objectives can be categorized as: 1) maximizing the total power production; 2) power reference tracking; and 3) alleviation of loads on wind turbines in the farm [1].

WFC is much more challenging than control of a single wind turbine due to aerodynamic interactions among turbines. These interactions come from the fact that downwind turbines are in the wake of upwind turbines extracting energy from the flow. The amount of turbine interactions in a wind farm via wake on one hand depends on time-varying atmospheric conditions e.g. inflow direction, speed and turbulence, and atmospheric stability. On the other hand, individual turbine control settings can influence the wake-induced velocity deficit and flow direction in the wake. In today commercial WFs, individual turbines are regulated independently disregarding their interactions (greedy control). Thus, new advanced control algorithms for both individual wind turbines and WFs are needed to minimize wake-induced loads and energy losses.

The main focus of this PhD project is to elaborate the exploration in WFC. The next two steps aim firstly to develop a simple control-oriented model of wake-induced interactions of wind turbines. Thus, it is possible to analyze WF behaviour as a unique multi-agent system. Secondly, a distributed control system is developed for a WF. In comparison with model-free optimization approaches verifying the effectiveness of distributed control despite their inevitable drawbacks such as slow convergence and inaccuracy, this PhD project intends to explore the importance of aerodynamic models for WFC. This paper presents an initial WFC idea developed for a simple WF model containing three machines in a row. Finally, the effectiveness of the two newly developed approaches for the present case study is evaluated through some simulations made by open source *SimWindFarm (SWF)*[4] simulation model.

Flow interaction model

For initially developing the control approaches based on flow interaction models, we assume uniform wind of constant speed U_∞ and constant direction. We use the wake interaction model proposed by Jensen et.al. [5] based on axial induction factor (AIF) a_i as individual turbine control settings. The AIF is the fractional decrease in wind velocity between the free-stream and the turbine rotor. As illustrated in Figure 1, the Jensen model approximates the downstream velocity profile statically as

$$V_i(x, r, a_i) = U_\infty(1 - \delta V_i(x, r, a_i)) \quad (1)$$

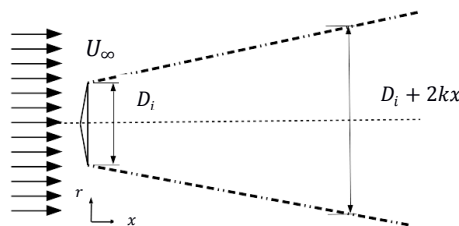


Figure 1: The wake expansion parameters of Jensen wake model.

where $\delta V_i(x, r, a_i)$ represents the fractional deficit of the velocity at the point (x, r) inside the wake of upstream turbine i can be formulated as

$$\delta V_i(x, r, a_i) = \begin{cases} 2a_i \left(\frac{D_i}{D_i + 2kx} \right)^2 & \text{for } r \leq \frac{D_i}{D_i + 2kx} \\ 0 & \text{for } r > \frac{D_i}{D_i + 2kx} \end{cases} \quad (2)$$

where D_i is the rotor diameter and k represents a tunable wake expansion coefficient [3].

Jensen's model is extended to include multiple turbines with interacting wakes [2]. Thus, the effective wind speed for downstream turbines can be approximated by accumulating wind velocity deficits of each upstream turbine individually. When the effective wind speed at each turbine is approximated, the steady-state power of each turbine can be calculated as

$$P_i = \frac{1}{2} \rho A_i C_p(a_i) V_i^3 \quad (3)$$

where ρ is the air density, A_i is the swept area of the rotor, C_p is the power efficiency coefficient and V_i is the effective wind speed at turbine i approximated by the wake model. According to actuator disk theory, the power extraction from flow has a relation with AIF as

$$C_p(a_i) = \eta 4a_i(1 - a_i)^2 \quad (4)$$

where η is a factor applied in the Jensen model to account for losses based on power curve of the NREL 5MW turbines. It is clear from Equation 4, the maximum value of C_p occurs when $a = \frac{1}{3}$.

Distributed control of wind farms

In this section, an initial multi-agent control architecture based on AIF is proposed. As illustrated in Figure 2, it contains a high-level WFC which utilizes information from a flow interaction model, ambient wind speed, power demand and power production history to calculate AIF based power references ($P_{i,ref}(a_{i,nom})$). This control setting is called here as nominal AIF $a_{i,nom}$.

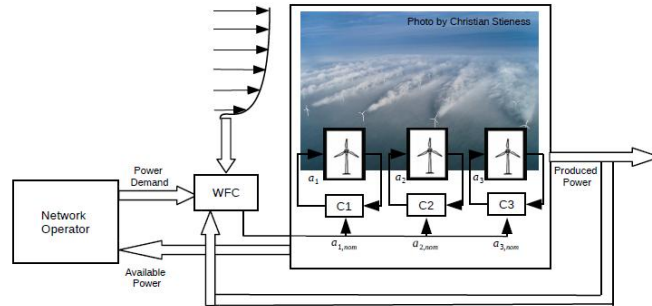


Figure 2: Schematic demonstration of distributed architecture of wind farm control.

The low-level individual WTCs (agents) with faster sample time using generator torque and blade pitch as realistic control variables affecting AIF of each turbine. The baseline PI-based torque and pitch controllers are modified simply in such a way they can degrade power production of each turbine in both partial and full load regions. Due to inherent robustness of PI controllers, it is expected each low-level WTC updates its own AIF against inevitable uncertainties via feed-back as

$$a_i = a_{i,nom} + \Delta a_i \quad (5)$$

Since the focus of this paper is the total power maximization, a well-known game theoretic (GT) WFC approach [2] is applied to distribute power references based on $a_{i,nom}$. In this algorithm, the decision of turbine i , at any iteration $t > 0$, depends on $a_{i,nom}$ and the total power production $\sum_{i=1}^N P_i$ from the previous iteration. The pair $[\bar{a}_{i,nom}, \bar{P}]$ is defined to keep the proper action and WF response (power increment). As a result, each turbine either selects the previous proper action with high probability or experiments a new random action with low probability. If this random action leads to power increase, the non-decreasing pair $[\bar{a}_{i,nom}, \bar{P}]$ is updated. This procedure is repeated until a desirable objective would be achieved. More details about GT algorithm can be found in [2].

After decision making by the high-level WFC, each turbine tries to track distributed $P_{i,ref}(a_{i,nom})$ by influencing its own AIF using torque and pitch controllers. Finally, the total produced power as a result of this decision and agent modifications will be analyzed by WFC via feedback for next decision making.

Simulation studies

In this section, the performance of the presented distributed WFC based on multi-agent approach is illustrated through some simulations. Our case study WF contains three turbines in a row with NREL 5MW reference turbine specifications. Each turbine has a diameter of $D_i = 126 \text{ m}$ and the turbines are spaced $5D$ apart from one another. The ambient wind is parallel to the turbine axes with a constant speed 8 m.s^{-1} . Moreover, a constant air density $\rho = 1.225 \text{ kg.m}^{-3}$ is assumed. A factor $\eta = 0.821$ is used to attribute $a = 0.33$ to the maximum power coefficient of the individual NREL 5MW turbine ($C_p = 0.4865$). Finally, the wake expansion coefficient is tuned as $k = 0.0871$ to meet *SimWindFarm (SWF)* simulation model which is developed for exploration in WFC. It utilizes also Jensen model calculating the wake velocity deficit using a thrust coefficient table of the NREL 5MW reference offshore wind turbine [4].

1-GT-based WFC:

In the first step, the performance of the high-level GT-based WFC is analyzed individually. To evaluate the GT-based WFC performance for power maximization, the analytical solution is found numerically for our WF case study using the tuned Jensen model (1). The total produced power by the WF can be formulated as

$$P = \frac{1}{2} \rho \sum_{i=1}^3 A_i C_p(a_i) V_i^3 \quad (6)$$

Constrained optimization over the set of admissible control variable $0 \leq a_i \leq 0.33$ leads to a global optimal solution as

$$\{a_1^{opt}, a_2^{opt}, a_3^{opt}\} = \{0.24 \quad 0.22 \quad 0.33\} \quad (7)$$

Figure 3 depicts the performance of GT-based WFC versus the greedy control structure ($a_i^{greedy} = 0.33$). Note that here the produced power is approximated using the tuned wake model (1). It explicitly demonstrates that the total power production converges to the global optimal solution (7) after finite number of iterations. The power production increases 3.31% with respect to the greedy control settings just by taking into account the flow interaction model.

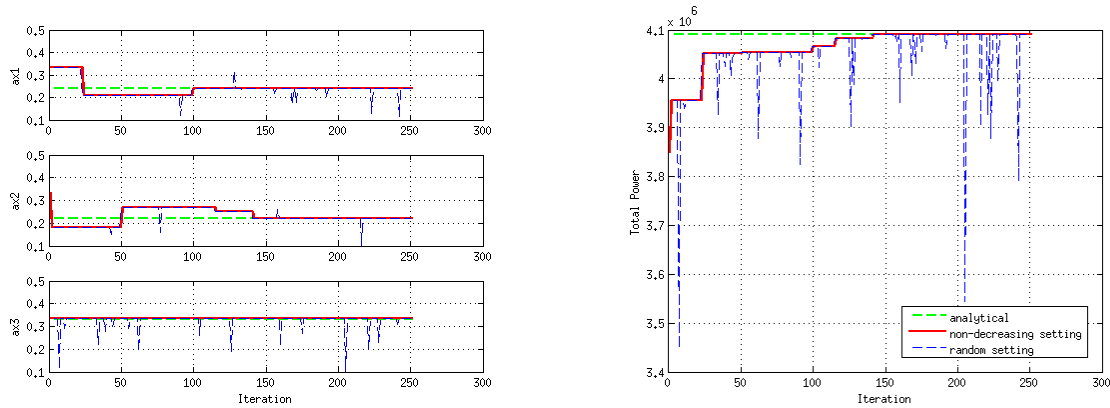


Figure 3: GT-based WFC: a) the nominal AIF adjustments, b) total power production.

2- Multi-agent WFC:

Now the performance of WFC based on the multi-agent approach is simulated with the open source *SWF* simulation model. Here the effective wind speed at each turbine is derived from the turbine thrust table. In this approach, the individual WTCs are adjusted to influence their own AIF using torque and pitch controllers. In other words, the calculated set of AIF ($a_{i,nom}$) illustrated in Figure 3a will be updated according to (5) against model uncertainties by considering *SWF* simulated produced power via feedback.

In Figure 4a it is tried first to examine the multi-agent WFC performance in the WF total power maximization. Thus, the control setting of each turbine is initialized as $a_i^{initial} = 0.1$. Over a 50000 sec simulation run it is explicitly shown that the individual WTC systems are successfully able to maximize the total power production using the torque and pitch controllers. It seems that the total produced power approaches its maximum value in a finite time. This value is close to the global maximum power obtained in Figure 3b.

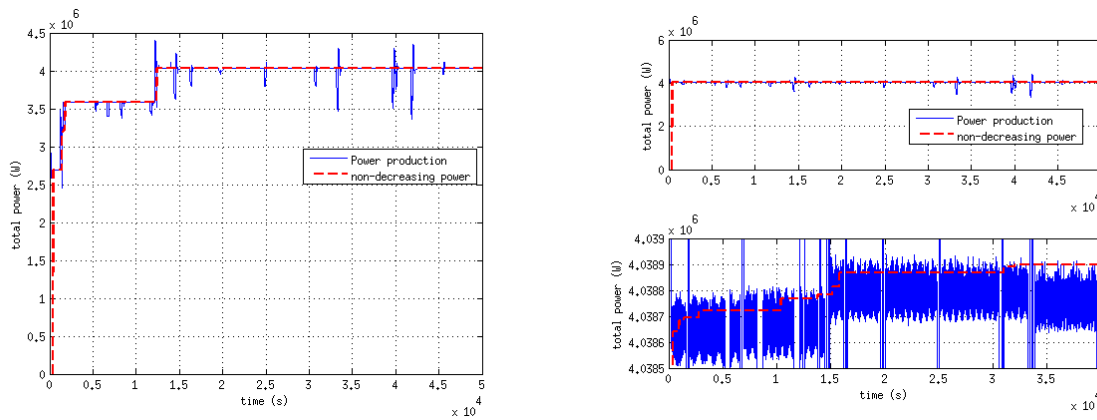


Figure 4: WF power production with distributed WFC: a) $a_i^{initial} = 0.1$, b) $a_i^{initial} = a_i^{greedy} = 0.33$.

Figure 4b aims to illustrate behaviour of the multi-agent WFC in power maximization with respect to greedy control structure similar to the first simulation study (Figure 3). It can be seen from the enlarged plot that WFC based on the multi-agent approach tries to maximize the total power but improvement is so limited (0.0074%). Actually, looking at the pitch controller action of the individual turbines reveals that WFC examines several different control settings. However, every degrading power production of the upstream wind turbine cannot be compensated by the new settings of the downstream turbines.

It is important to note that comparing the produced power level for the greedy control settings in figure 3b and 4b ($a_i^{initial} = a_i^{greedy} = 0.33$) shows a significant difference in the magnitude which is believed to result from different implementation of the Jensen wake model and/or different parameter setting for the wake expansion. A comparison of the steady state effective wind speed of each turbine under greedy control architecture yields significant higher values for the SWF simulation model. This explains the higher power level at initial time of Figure 4b. Consequently, in the sense of AIF-based WFC control, the greedy control setting is almost the same as a global optimal solution of our case study WF simulated in SWF. This conclusion can be also verified by looking at the simulation case study shown in Figure 4a. The AIF of the individual turbines converges iteratively to its optimal solution which in this case study is the same as the greedy AIF value 0.33.

Conclusions

The engineering Jensen model is utilized to estimate the wake induced velocity deficit at each downstream turbine in two WFC approaches. Firstly, a high-level AIF-based WFC is developed using the GT-based approach to distribute power references leading to total power maximization. Secondly, using a multi-agent approach the individual WTCs are adjusted to influence their AIF using torque and pitch controllers. The effectiveness of the developed control architecture in power maximization is evaluated via some simulation studies. The proposed AIF-based WFC is capable to increase the WF power production against the model inaccuracies. Although model-based control theoretically shows promising improvement with respect to the greedy control setting in power maximization, preliminary simulation results with the Aeolus *SimWindFarm* simulation model does not confirm this improvement. This discrepancy is likely caused by different implementations or parameterization of the used wake models. In other words, the evaluation of the potential in decentralized power maximization with respect to greedy architecture of WTC requires more concentration on the flow interaction model modification.

References

- [1] T. Knudsen, T. Bak and M. Srenstrup: "Survey of wind farm control – power and fatigue optimization", Wind Energy, Published online 9 May 2014 in Wiley Library.
- [2] J.R. Marden, S.D. Ruben and L.Y. Pao: "A Model-free approach to wind farm control using game theoretic methods, IEEE Transactions on Control and Systems Technology", 21(4), 2013.
- [3] P.M.O. Gebrard and J. W. van Wingerden: "Maximum power-point tracking control for wind farms" Wind Energy, Published online 2014 in Wiley Library.
- [4] J.D. Grunnet, M. Soltani, T. Kundsens, M. Kragelund and T. Bak: "Aeolus toolbox for dynamics wind farm model, simulation and control", In: European Wind Energy Conference and Exhibition (EWEC) 2010, European Wind Energy Association (EWEA), Poland, 2010.
- [5] I. Katic and N.O. Jensen: "A simple model for cluster efficiency", in Proceeding of European Wind Energy Conference, pp. 407-410, 1986.

COMBINING MODEL-BASED AND DATA-DRIVEN OPTIMIZATION OF WIND FARM OPERATION IN A LEARNING DATABASE

A. Rott*, M. Kühn

ForWind – University of Oldenburg, Research Group Wind Energy Systems, Oldenburg,
Germany

+49 (441) 798 5066, andreas.rott@forwind.de

Extended Abstract

Introduction

The typical control strategy of a wind turbine is designed to maximize the energy yield of the individual turbine subject to load and electrical requirements. Previous studies [1] could demonstrate that this strategy does not necessarily maximize the energy capture of a wind farm, because of substantial losses in the energy production due to the aerodynamic interaction of the wind turbines. Mitigation of these wake effects in order to enhance the energy conversion process of the wind farm as a whole therefore requires to leave the ideal point of operation of the individual turbines with respect of power and loads.

The present investigation in the scope of a PhD project is implementing a combination of model-based and data-driven optimization techniques into a learning database in order to manage the challenges of the continuously changing wind farm flow conditions.

This paper surveys a brief overview of model-based and data-driven optimization algorithms to improve the operation of an arbitrary wind farm with respect of maximizing the power conversion. Furthermore the concept of a learning database that makes use of both approaches in order to combine the advantages of the two techniques is described.

Approach

Different control strategies to increase the energy yield of a wind farm by considering the wake effects were presented in recent studies [2], [3]. In the following two different approaches of active wake control (AWC) that are being used in the presented optimization method, are described.

Axial induction

The *axial induction factor* a is defined as the proportion of the wind speed deficit at the rotor to the free stream velocity ($a = \frac{U_\infty - U_{rotor}}{U_\infty}$).

The generator torque and the blade pitch angle of a turbine can be controlled to manipulate the *axial induction factor*. In [2] it was shown that reducing the *axial induction factor* of an upstream turbine can increase the overall energy output of a two turbine array in steady, uniform inflow.

Wake deflection

Several studies [1], [3] investigated the possibility of deflecting the wake behind a wind turbine by yawing the nacelle slightly out of the wind direction. While the power production of a yawed turbine reduces and the loads increase to some degree, a controlled use of this technique is supposed to enhance the energy yield of a wind farm by steering wakes away from downstream turbines.

Model

For the optimization of the axial induction factor and yaw angle set-points models can be used to calculate the tradeoffs in the power production of the mentioned AWC methods. In order to keep the calculation time for the optimization within limits, engineering models with a low computational expense were employed in the present analysis.

The wake model used for the optimization consists of three major components to describe the effects of the AWC methods.

The wind speed deficit in one wake is determined using a modified Jensen model [4], where a Gaussian distribution is fitted on top, to obtain more realistic results and avoid discontinuity. Where a superposition of multiple wakes occurs the wind speed deficit is calculated so that the kinetic energy deficit of a mixed wake is the same as the sum of the energy deficits for each wake according to I. Katic et. al. [5]. To represent the deflection of a wake due to a yaw angle offset of a turbine three different methods ([3], [6], [7]) were implemented in the model between it can be chosen. Further studies shall evaluate the accuracies of these models. A visualization of the combination of the three model components can be seen in Fig. 1.

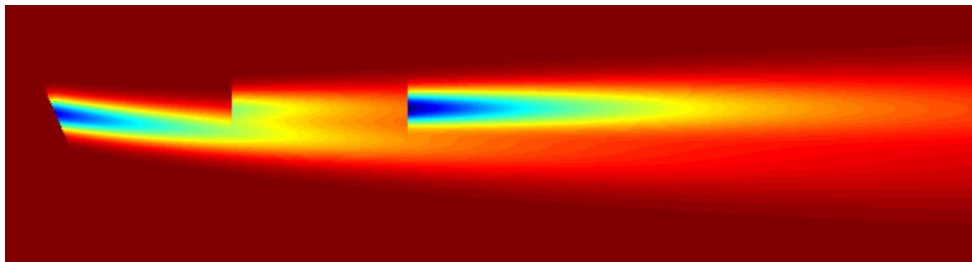


Fig. 1: Visualization of the model components in an example. (First turbine: yaw angle = 23.5° , second turbine: $a = 0.16$)

Model-based optimization (MBO) algorithm

After parameterizing the model and choosing a wind farm layout an optimization can find set-points for the axial induction factor and the yaw angle of each turbine that result in a very close to optimal power production for the wind farm regarding the model. For the optimization several different algorithms (e.g. particle swarm optimization (PSO), game-theoretic approach (GT) [8], local increment-based optimization (IBO), simulated annealing (SA), sequential quadratic programming (SQP)) have been implemented. Additionally some of the algorithms were prepared for a distributed optimization approach, where the optimization problem is separated into smaller sub problems, which can be solved individually. This offers new possibilities (e.g. parallelization of the algorithm) that will be analyzed in a further investigation. So far it can be concluded that after calibrating the algorithms all methods find satisfying solutions for the optimization. The model-based optimization was tested with parameters and a layout based on the EnBW Baltic I offshore wind farm with 21 wind turbines (Baltic I) with a rotor diameter of 93 m. For a wind direction of 245° , losses of 24.28 % in the energy yield due to wake situations were estimated by the model for a standard control approach. In an optimized operation these losses are reduced to 14.12 %. Fig. 2 shows the wind farm layout and wake flow in the optimized situation.

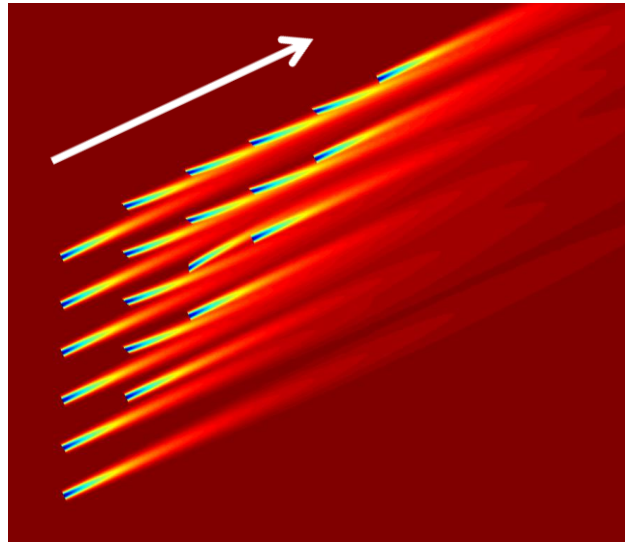


Fig. 2: Optimized wake situation for Baltic I (Wind direction 245°)

Data-driven optimization (DDO)

A data-driven optimization (also called model-free optimization) is based on measurements and it calculates the set-point changes for each iteration of the algorithm without the help of a model. The computation time depends on the response time of the system, which is the time it takes for the measurements to adjust according to the changes of the set-points. In a wind farm this time is in the range of minutes due to the travelling time of a wake even with the simplifying assumption that only neighboring turbines have a significant aerodynamic interaction. Therefore the convergence of such an algorithm can take hours of time, in which the wind conditions have to be stable. To improve the convergence time a local optimization that is called increment-based optimization (IBO) and works similar to the GA-approach in [9], has been chosen. A detailed analysis of the algorithm will be executed in a coupling of an aeroelastic and a large eddy simulation (LES) code, which is currently under development at ForWind-Oldenburg. So far this optimization could only be tested in the introduced static model environment. In Fig. 3 the evolutions of the set-points (“axial induction factor” and “yaw angle”) for 21 turbines in a wind farm based on Baltic I as well as the resulting power output, that were calculated with the IBO over 30 iterations, are shown.

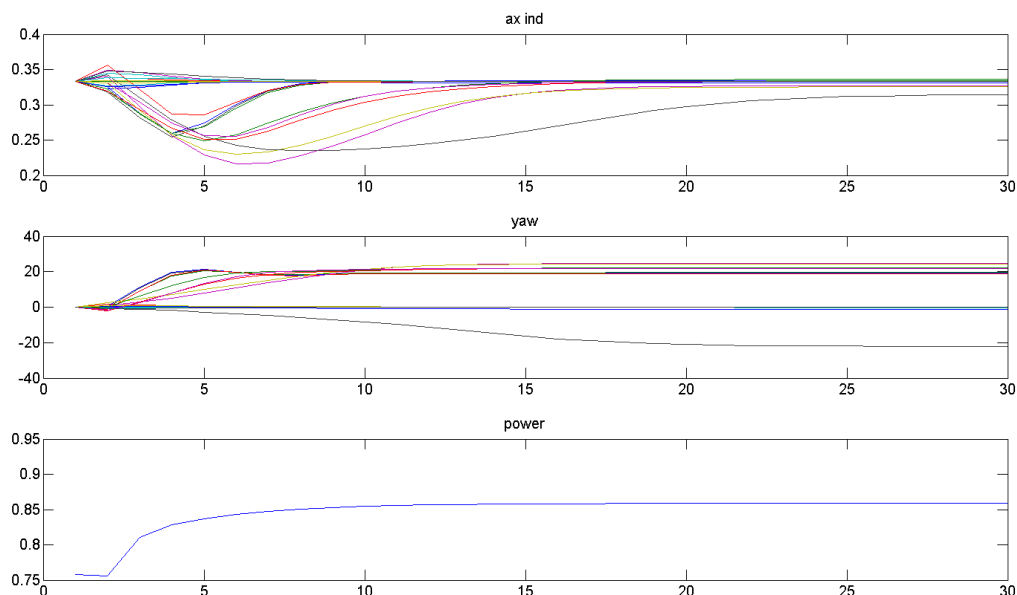


Fig. 3: Evolution of axial induction factor and yaw angle in the IBO (x-axis = Number of iterations)

Operation of a wind farm with a combination of MBO and DDO in a learning database

The first step is the development of a real time application that analyses the variation of the wind speed and direction by measurement e.g. by wind turbine nacelle anemometry. The wind conditions, the farm layout and a dynamic wake model are used to estimate the current wind farm flow and to store the result in a database. Simultaneously a graph of the turbine interactions is generated. For every wind flow situation in the database the model-based optimization is calculating the best initial operating set-points for the turbines. During the operation of the wind farm these initial set-points are used as starting points of the data-driven optimization to improve the database values for the specific wind flow situation. The purpose of this twofold approach is to combine the advantages of the two techniques. The feedback of the data-driven algorithm will partly compensate the inherent inaccuracies of a wake model, while the model-based method is expected to improve the rate of convergence of the data-driven method.

Conclusions

The optimizations that were executed using the described model with a number of different wind farm layouts and parameters could show a promising improvement in the control strategy regarding the power production. To improve the stability of the method it is planned to develop some additional features that will be implemented in the procedure, like a post processing algorithm for the measurements of the DDO (e.g. validation and averaging). To ensure that the presented optimization concept is operating correctly it will be tested and validated in more realistic environments (e.g. LES and wind tunnel tests) as well as further developed in the future.

Acknowledgment

The work was funded by the German Federal Ministry for Economic Affairs and Energy (BMWi) in the scope of the CompactWind project (FKZ 0325492B).

References

- [1] D. Medici, "Wind turbine wakes-control and vortex shedding," *KTM Mech. R. Inst. Technol. Stock.*, p. 103, 2004.
- [2] K. E. Johnson and N. Thomas, "Wind farm control: Addressing the aerodynamic interaction among wind turbines," *2009 Am. Control Conf.*, pp. 2104–2109, 2009.
- [3] Á. Jiménez, A. Crespo, and E. Migoya, "Application of a LES technique to characterize the wake deflection of a wind turbine in yaw," *Wind Energy*, vol. 13, no. 6, pp. 559–572, 2010.
- [4] N. Jensen, "A note on wind generator interaction," *Tech. report, Risø*, 1983.
- [5] I. Katic, J. Højstrup, and N. Jensen, "A simple model for cluster efficiency," *Eur. Wind energy Assoc. Conf. Exhib.*, no. October, pp. 407–410, 1986.
- [6] T. Burton, N. Jenkins, D. Sharpe, and E. Bossanyi, *Wind energy handbook*. Chichester, 2011.
- [7] D. Miccallef, "MEXICO Data Analysis, Stage V—Investigation of the Limitations of Inverse Free Wake Vortex Codes on the Basis of the MEXICO Experiment," *TU Delft/University of Malta*.
- [8] J. R. Marden, S. D. Ruben, and L. Y. Pao, "A Model-Free Approach to Wind Farm Control Using Game Theoretic Methods," *IEEE Trans. Control Syst. Technol.*, vol. 21, no. 4, pp. 1207–1214, Jul. 2013.
- [9] P. Gebraad and J. Wingerden, "Maximum power point tracking control for wind farms," *Wind Energy*, 2014.

Aggregate Wind Farm Power Performance Curves

A. Elmontaser, PhD Student, Department of Electrical and Electronic Engineering, Doctorial Training Center, University of Strathclyde, Glasgow, Scotland , UK , email : ashraf.elmontaser@strath.ac.uk

Abstract— The aim of this paper is to obtain the aggregate wind farm power curves for Whitelee wind farm based on real data collected using SCADA system. The power curve is plotted for a group of turbines and the wind farm. The aggregate wind farm power performance was examined as a single power curve that describes the power characteristics of this wind farm. The impact of size of the wind farm, density of the wind turbines, spacing distance between them and wake effect were examined by making careful sub-selections of wind turbines in a given area by using the method of bins. Also a statistical model was developed to model the aggregate wind farm power curve based on manufacturer wind turbine power curve and actual wind speed probability distribution function in the area.

Keywords— Aggregate power curve, density of turbines, multi-turbine power curve, wake effect.

I. INTRODUCTION

Wind turbines power curves are important to determine the overall performance of a wind farm. These curves are used for planning purposes and estimating total wind power production of wind farms. The entire wind farm will be treated as single generator so that an equivalent wind farm power curve becomes highly desirable and useful in predicting wind farm output for a given wind forecast. The power curve for each wind turbine varies depends on the location of each wind turbine in the wind farm. The location is affected by the terrain effect and spatial distance between wind turbines in the wind farm. The wind speeds are subject to turbulence resulted from wake effect that cause wind speed reduction at wind turbines located at wake of upstream wind turbines.

A measured power curve of a wind turbine consists of the 10 minutes mean electrical active power plotted against the 10 minute mean wind speed at hub height. Such a plot shows scattered measured values of active power corresponding to measured wind speeds at the site. Met towers are used to measure the mean wind speed and air density at hub height at a distance of 2 to 4 rotor diameters upstream [1]. Data was measured based on industry standard IEC 61400-12 [2]. The aggregated wind farm power curve was obtained using method of bins .This curve is dependent on the impacts of local terrain, wind direction, turbine wakes, which are investigated in this paper. Such a curve, can help system operators to predict the power generated from the wind farm for a given wind speed; so that it is important to construct an equivalent wind power curve for the entire wind farm.

There are some research papers that handle this topic. In [3] a statistical approach was introduced to model the aggregate wind farm power curve based on the spatial distance between

the wind turbines and level of turbulence intensity. In [4], an equivalent power curve model of a wind farm was demonstrated based on field measurement data. The model was used to construct the total wind farm power curve by using two methods the aggregate measured power curve and cluster-measured power curves. The first method was used to compute the total power performance of the wind farm as a single wind turbine and the second method was used to divide the wind farm into small groups and each group a single power cure was plotted so each cluster of wind turbines was represented by a single power curve. This method is useful for large wind farms that extend over a large area.

The goal of this paper is to plot the aggregate power curve from raw data from SCADA system in Whitelee wind farm, the method of bins [5] was used to build the power curve by averaging the raw data at each bin, 0.5 m/s as specified by industry standard IEC 61400-12 [2], and the averaged active power versus averaged 10 minute mean wind speed curve was plotted. This procedure was done to different wind turbine groups to examine the effect of density of wind turbines by making careful sub-selections of turbines in a given area.

II. POWER CURVE CALCULATIONS

To construct the power curve from the raw data of the wind farm, the method of bins [3] was used to calculate the averaged active power versus averaged 10 minute mean wind speed in bins throughout the range of wind speeds. This range is divided into a series of 0.5m/s bins as specified by industry standard IEC 61400-12 [2]. The averaged power and averaged 10 minute mean wind speed at each bin was calculated using the following formula:

$$V_i = \frac{1}{N_i} \sum_{j=1}^{N_i} V_{ij} \quad (1)$$

$$P_i = \frac{1}{N_i} \sum_{j=1}^{N_i} P_{ij} \quad (2)$$

Where V_i is the averaged 10 minute mean wind speed in bin i , V_{ij} is the 10 minute mean wind speed of data set j in bin i , P_i is the averaged active power output in bin i , P_{ij} is the 10 minute average active power output of data set j in bin i and N_i is the numbers of data sets in bin i .

The total generated power from the wind farm composed of N_{wt} wind turbines is the sum of active power output from all individual wind turbines as mentioned below [3]:

$$P_{wf} = \sum_{i=1}^{N_{wt}} P_{wti} \quad (3)$$

Where P_{wf} is the total power of the wind farm and P_{wti} is the active power output of the individual wind turbine. The output power of each wind turbine is not the same at each time because of the stochastic nature of the wind and the spatial distribution of the individual wind turbines. The total power depends on the extent of the wind farm and the turbulence intensity in the wind [3].

The method of bins was used to calculate the averaged active power for each individual wind turbine and then these averaged active power values were plotted versus averaged 10 minute mean wind speeds resulted from method of bins as shown in Figure 1. The aggregate power curve of Whitelee wind farm was obtained using 140 wind turbines to produce rated power at 322 MW. By dividing by 140 the average aggregate wind farm power curve is obtained as shown in Figure 2. The average power was calculated by adding the output power of all wind turbines divided by number of wind turbines, i.e. 140 wind turbines to produce rated average power at 2300 KW. The measured data was taken from met mast 81, which is located at the front end of the wind farm, was used to produce the aggregate wind farm power curve.

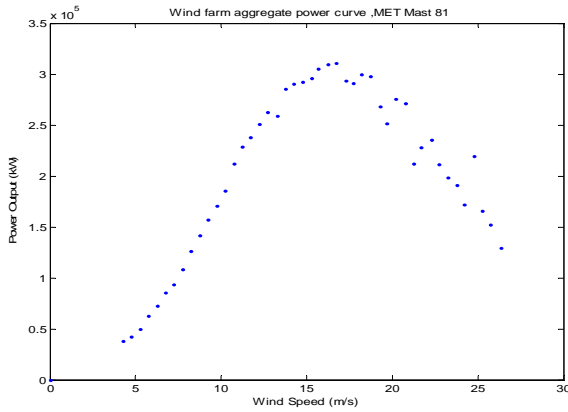


Figure 1: The aggregate power curve of Whitelee wind farm.

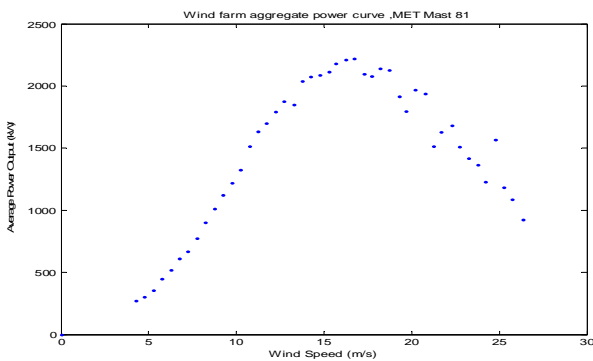


Figure 2: The average power curve of Whitelee wind farm.

III. STATISTICAL POWER CURVE MODELLING

A statistical wind farm model was developed to estimate the power performance of the wind farm as mentioned in [4]. Because of the stochastic nature of wind speed, this model was introduced using the steps provided in this paper that depends on the spatial distribution of individual wind turbines in the wind farm and the turbulence of the wind. This model was adjusted to be similar to the actual aggregate wind farm power curve. A Gaussian distribution was used to represent the probability distribution function for the wind speeds for individual wind turbines. The Gaussian distribution has a standard deviation of the wind speeds at the wind farm and zero mean. It was calculated based of the area dimension, mean wind speed at the wind farm and turbulence level. Then it was used to calculate the aggregate wind farm power curve using the following equation:

$$Pm_j = \sum_i P_{s_{j+i}} P_{s_i} \quad (5)$$

Where Pm_j is the modelled wind farm power, P_{s_j} is the j^{th} element of individual wind turbine power curve and ps_i is the probability distribution function of the spatial distribution of the wind turbines. Each value of power on modelled wind farm power curve was calculated by summing the product of both the power values of individual power curve, using manufacturer data, and the probability distribution function at many points as shown in Figure 3. This procedure was done at all wind speed range until the modelled wind farm power curve was plotted. The mean value of the Gaussian distribution is zero to be used at all wind speeds and had a standard deviation σ_w .

To calculate the value of σ_w , the actual standard deviation of wind speed, it is equal to the product of normalized standard deviation, σ_n , and mean wind speed of the wind farm, w_m , as mentioned below:

$$\sigma_w = w_m \sigma_n \quad (6)$$

The mean wind speed of the wind farm was calculated from the measure wind speed data from met mast 81 as follows [8]:

$$w_m = \frac{1}{n} \sum_{i=1}^n w_i \quad (7)$$

Where w_i is 10 minute mean wind speed from the wind farm data and n is the number of observations. Therefore the value of w_m was calculated to be 7.9 m/s for Whitelee wind farm. The value of the normalized standard deviation, σ_n , was calculated from Figure 4. It depends on the dimension of the wind farm D and turbulence intensity I . The area of Whitelee wind farm is 55 square kilometers, therefore $D = \sqrt{55} = 7.42$ kilometers. The turbulence intensity was calculated from the data which is equal to 0.15. From Figure 4, the value of the normalized standard deviation is 0.04. The actual standard deviation of the wind speed range was calculated using (6) to be 0.316 m/s. The normal distribution

which is corresponding to zero mean and standard deviation 0.316 m/s is shown in Figure 5.

The modelled wind farm power curve as shown in Figure 6 was calculated by using (5), using the manufacturer power curve of an individual wind turbine and probability distribution of Figure 5.

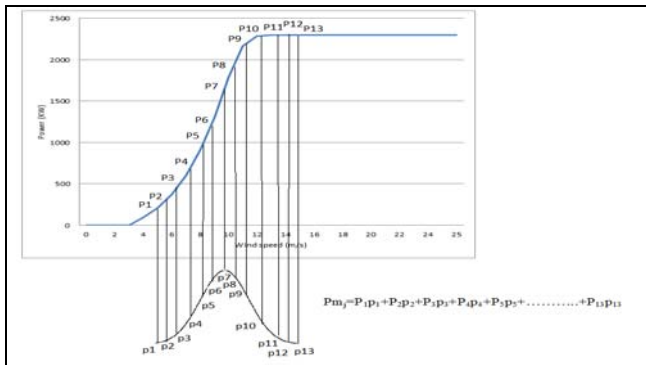


Figure 3: Modelled wind farm power calculations.

The modelled wind farm shown in Figure 6 is not similar to the actual aggregate wind farm power curve, so that an adjustment to the statistical model was made by changing the value of the standard deviation and adding offset until a similar modelled wind farm power curve to the actual one was obtained at standard deviation value 10 m/s as shown in Figure 7. The manufacturer individual wind turbine, modelled wind farm and actual aggregate wind farm power curves were plotted together to examine the symmetry between them. It can be seen that there is slight difference between them because of an offset was added below wind speed 10 m/s.

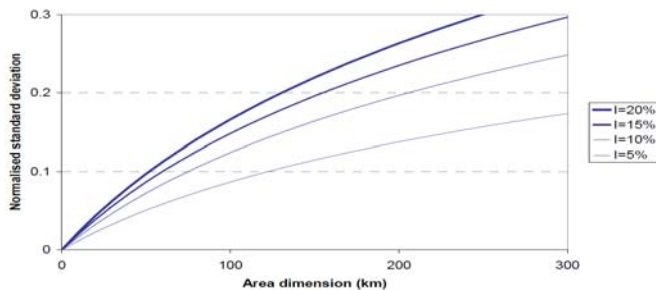


Figure 4: Normalized standard deviation as a function of dimension of the wind farm D and turbulence intensity I [4].

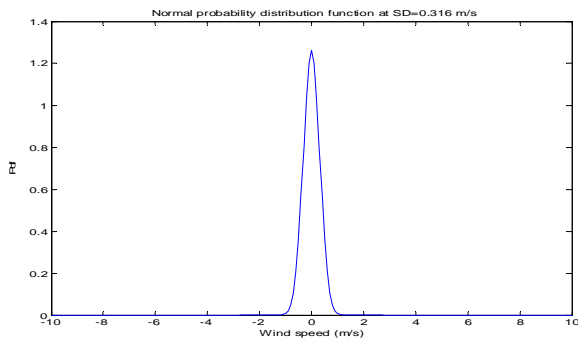


Figure 5: Normal Distribution of the statistical model at zero mean and standard deviation 0.316 m/s.

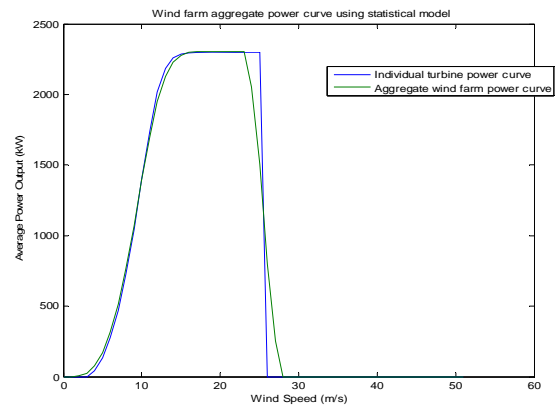


Figure 6: Modelled wind farm power curve at SD = 0.316 m/s.

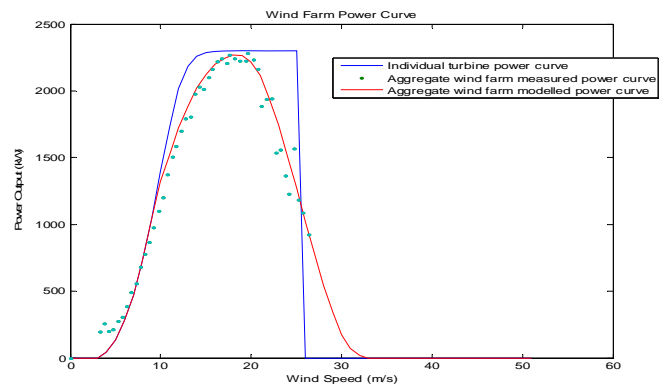


Figure 7: Modelled and actual wind farm power curve with an offset at wind speed range below 10 m/s.

IV. RESULTS AND DISCUSSION

The power curve calculations were performed for the whole wind farm and groups of wind turbines. This was achieved by investigating the effect of wind directions, wake effect and density of wind turbines on the power performance. The real data obtained from met mast 81 which is located at the front end of the wind farm. There are two met masts in the wind farm, met 81 and met mast 82 which is placed at the back end of the wind farm. From the analysis of the power curve calculations, it was found that met mast 81 is used to measure the wind speeds, wind directions, temperature pressure and humidity at front end of the wind farm, while met mast 82 is used to measure the wake effect that causes reduction in the measured wind speeds at back end of the wind farm.

The wake effect was examined by choosing an array of wind turbines TB01, TB04, TB07, TB10 and TB40. The wind directions were filtered between 145 and 260 degrees to observe their effect on the power performance as is shown in Figure 8. These power curves were plotted together to see the effect of wake losses on the power output for wind turbines TB04, TB07, TB10 & TB40. The power performance of these

wind turbines decreases as the wind turbine is placed away from met mast 81. This is because of the wake effect that causes decrease in the power performance as distance increases from met mast 81. It is obvious that wind turbine TB40 has the lowest power performance among the group because it is placed at the end of this array.

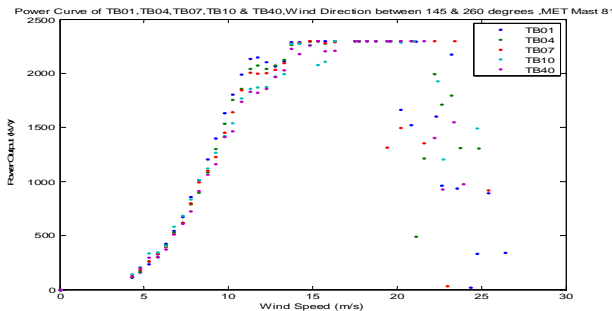
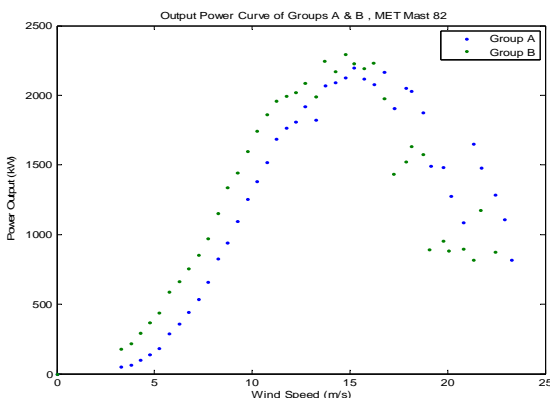
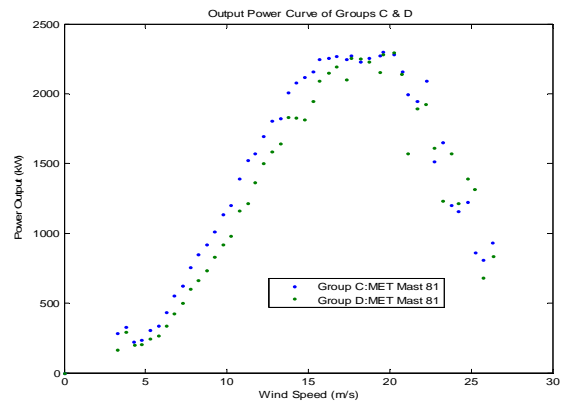


Figure 8: Power curve of an array of wind turbines TB01, TB04, TB07, TB10 and TB40.

Several groups of wind turbines were examined to observe their effect on the power performance. These groups have different density of wind turbines with different spacing distance between them. Groups A & B each has six wind turbines; the spacing distance is different to examine the spacing effect on their output power performance. As can be seen in Figure 9a, group B has better power performance than group A ; this due to the spacing effect between the wind turbines in the two groups .Group A has less spacing distance between the turbines than group B that leads to group A to produce less power than group B . This is due to wake losses that are more effective at smaller spacing between the wind turbines like in the case of group A that is affected by these losses. The power performance of other two groups C and D is shown in Figure 9b. Each group C and D has 13 wind turbines and group D has smaller spacing distance between the wind turbines than group C. The power curve of group C has better performance than group D. It occurred because of wake losses that reduce the wind speed in the wake and less power was produced from group D. The wake effect has more impact on power performance at lower spacing distance between wind turbines.



(a)



(b)

Figure 9: Power curves of groups A, D, C and D

V. CONCLUSION

The power performance of Whitelee wind farm was illustrated by using real data obtained from SCADA system. The impact of density of the wind turbines and wake losses on the power performance of the wind farm were also investigated. Also a statistical model was developed to represent the aggregate wind farm power curve and it was used to calculate the annual energy yield which gave nearly similar result to actual annual energy yield produced from the wind farm.

ACKNOWLEDGMENT

I take this opportunity to express my greatest gratitude to my supervisor Professor David Infield, at Strathclyde University in Glasgow, for his support throughout the project. I also thank my family for their constant encouragement without which this assignment would not be possible.

REFERENCES

- [1] IEC 61400-12-1. Wind Turbines – Part 12-1: Power performance measurements of electricity producing wind turbines; 2005.
- [2] IEC 61400-12-1 Wind Turbines – Part 12-1: Power Performance Measurements of Electricity Producing wind Turbines; first edition 2005-12.
- [3] H. Holttinen , “A Multi-turbine Power Curve Approach” , RISO national laboratory , Wind Energy 2005.
- [4] B. P. Hayes, I.S. Ilie, A. Porpodas, S. Z. Djokic, and G. Chicco, “Equivalent Power Curve Model of a Wind Farm Based on Field Measurement Data”, *IEEE Trondheim PowerTech*. pp1-6, 2011.
- [5] Akins RE. “Performance evaluation of wind energy conversion systems using the method of bins” - current status. Sandia Laboratory, Albuquerque, USA, internal report SAND-77-1375, 1978.
- [6] “Wind Structure and Statistics”, by U. Hassan and D. M. Sykes, Chapter 2 in *Wind Energy Conversion Systems*, L. L. Freris, Prentice Hall, 1990.
- [7] Christensen CJ and Dragt JB, etal, “Accuracy of power curve measurements”, *Riso-M-2632*, 1986.
- [8] E. C. Morgan , M. Lackner, R. M. Vogel, L. G. Baise , “Probability distributions for offshore wind speeds”, *Energy Conversion and Management* 52 (2011) 15–26 , pp 15-26, 2011.

“

Aerodynamics

”

TOWARDS IMPLEMENTATION OF AN OPTIMIZATION TOOL FOR ROTOR BLADES BASED ON THE ADJOINT METHOD IN OpenFOAM

L. Vorspel^{1*}, M. Schramm²⁺, B. Stoevesandt², J. Peinke¹

¹University of Oldenburg, ForWind, Institut of Physics, *Email: Lena.Vorspel@Forwind.de

²Fraunhofer IWES, Oldenburg, +Email: Matthias.Schramm@iwes.fraunhofer.de

ABSTRACT

Wind turbine blades are constant object of optimization, e.g. in order to reduce the cost of production, increase life time, adapt for different wind fields and many more. As blades are rather complex geometries, possibly with twisted and pre-bended parts, optimization becomes complex as solutions are not intuitive. We want to focus on the optimal aerodynamic shapes and behavior of blades in the turbulent wind field. Stationary computational fluid dynamics (CFD) are used as a source of information about the flow around such blades and the forces acting on them. As the computational time needed for CFD is already high, the optimization process has to be computational cheap. Based on the work for ducted flow optimization by Othmer [1] the adjoint method for computing the gradient, which is used in the optimization algorithm, is proposed. In the past we implemented the adjoint method based on the work of [1] for external flows in OpenFOAM. The first conducted test case is a drag minimization of a NACA profile, as validation of the optimization is needed. Besides the method of finite differences (FD) is used for a case with a low Reynolds number (Re) to verify the gradients.

INTRODUCTION

The rotor blades of wind turbines are constantly growing bigger [2]. Thus the swept rotor area and the capacity of wind turbines increase. However larger blades also have a higher contact surface and a higher weight, so the resulting forces increase as well, i.e. gravitational and rotational forces. In order to guarantee safe operation behavior, the blades have to overcome these forces, become lighter and keep a minimum stability. Modern blades are build using fiber composite materials, mostly based on carbon or glass fiber [3]. As wind turbines have a life time cycle up to 20 years, the estimated total amount of rotations is about $100 \cdot 10^8$, which means $5 \cdot 10^8 - 10 \cdot 10^8$ load changes. There are for example periodic loads due to the wind velocity gradient and tower shadow, each one of them proportional to the blade rotation frequency [4]. Besides, the blades are exposed to alternating wind loads, gusts and turbulences.

Reducing loads but keeping the blade geometry constant can be considered as an optimization problem. To solve this in combination with CFD we propose adjoint methods. It is a gradient based algorithm (GBA), and therefore the search direction in order to reach a minimum (or maximum) of the cost function can be determined numerically. Another advantage is that the adjoint method is independent of the number of design parameters. So it is highly suitable for the combination with CFD, as the fine discretized blade geometries from CFD can be directly used as design parameters for the optimization. The CFD simulations and the implementation of the optimization algorithm for this task are conducted in OpenFOAM, which is an open-source simulation tool suitable for wind turbine simulation among many other possible applications [5].

Before extending the tool that combines CFD with optimization towards the usage for rotor blades, test cases with 2D airfoils are carried out. These offer the advantages of a faster flow development and convergence, as well as less demanding case set-ups and grid generations.

ADJOINT METHOD IN CFD

As the adjoint method is a GBA, the gradient of a predefined cost (or objective) function I_c , e.g. minimization of drag or maximization of lift, is calculated depending on the the desired design parameters. As the aerodynamics depend on the flow around the blade, the optimization is constrained by the Navier Stokes Equations (NSE). Additional constraints, like a constant shape, surface area or minimal thickness can be added as well. Various authors used the adjoint method for these types of optimization problems [1, 6]. We propose to use the continuous adjoint method, in which the adjoint equations are derived from the NSE and afterwards discretized. The main idea of the continuous adjoint method is to build a Lagrange function with the adjoint variables as Lagrange multiplier to couple the cost function with the NSE:

$$\text{Optimize } I_c(\mathbf{U}, \boldsymbol{\beta}) \text{ subject to } G(\mathbf{U}, \boldsymbol{\beta}) \text{ and } \mathbf{R}(\mathbf{U}, \boldsymbol{\beta}) \in \Omega$$

Here, the NSE are denoted as \mathbf{R} and \mathbf{G} are any geometric constraints, that are added. All functions depend on the flow variables \mathbf{U} and the design parameters $\boldsymbol{\beta}$. For this general, constrained optimization problem, the Lagrange function L can be build as follows. For simplicity, the geometric constraints are not considered here, but the syntax is the same for all constraining functions.

$$L(\mathbf{U}, \boldsymbol{\beta}) = I_c(\mathbf{U}, \boldsymbol{\beta}) + \int_{\Omega} \boldsymbol{\Psi} \cdot \mathbf{R}$$

Now the total variation of the Lagrange function, which is the variation regarding the flow variables and the variation regarding the design parameters is build:

$$\delta L = \left(\frac{\partial I_c}{\partial \boldsymbol{\beta}} + \int_{\Omega} \boldsymbol{\Psi} \cdot \frac{\partial \mathbf{R}}{\partial \boldsymbol{\beta}} \right) \delta \boldsymbol{\beta} + \left(\frac{\partial I_c}{\partial \mathbf{U}} + \int_{\Omega} \boldsymbol{\Psi} \cdot \frac{\partial \mathbf{R}}{\partial \mathbf{U}} \right) \delta \mathbf{U}$$

The second summand of the r.h.s. is put to Zero now:

$$\left(\frac{\partial I_c}{\partial \mathbf{U}} + \int_{\Omega} \boldsymbol{\Psi} \cdot \frac{\partial \mathbf{R}}{\partial \mathbf{U}} \right) \delta \mathbf{U} = 0$$

Integrating this equation by parts leads to a linearized function for the adjoint variables, that is similar to the NSE, so that similar solver strategies can be used. For using the continuous adjoint approach, that is presented here, the following steps have to be done: First, compute the field variables \mathbf{U} , then use these variables as an input for the adjoint equation. Finally use the adjoint variables and field variables to calculate the gradient. According the direction and size of the gradient, which is the search direction, changes are performed for all concerning design points.

Regarding step size and the evaluation of the gradients, there exist many different numerical methods, varying in speed, stability and convergence. For first tests the steepest descent method is used, which is easy to implement but is known to tend to zigzagging close to the optimum. For further cases, other methods like line search will be tested as well. There will be the gradient information for as many design points as there are points used to discretize the surface of the blade or airfoil, respectively. Subsequently, methods estimating the Hessian can be difficult to use, as it will be computational expensive. By this, the advantage of the adjoint method would get lost.

As the convergence of the flow field is important, because the adjoint field depends on the flow variables, the optimization cannot be conducted every iteration step of the simulation. Instead we wait

until a certain residual of the flow variables is met, before the adjoint field for the computation of the gradients is evaluated.

EVALUATING THE GRADIENTS

In order to validate the gradients computed with the adjoint method, a test case was created. A quasi-2D airfoil is parametrized with 20-40 design parameters defining splines. This airfoil is within a low-Re-flow. The low Re number in combination with high requirements regarding the accuracy of the simulation results, e.g. the residuals, guarantees a highly converged solution for the flow field. Thus the input variables for the calculation of the adjoint variables are highly converged and thus the quality of the computed gradients is high. Besides, as the gradients shall be compared with those obtained by using FD, which need high convergence as well. For the FD an optimal step size of 10^{-6} up to 10^{-5} was found. These values show the needed accuracy, as changes in the fifth or sixth decimal place become relevant.

For this case and the optimal step sizes, the gradients calculated by FD and by the adjoint method, normalized by their maximal value, followed exactly the same path. Thus, the implementation of the adjoint method and the used solver can be considered correct.

As a further investigation of the adjoint method, a test case is set up. A drag minimization of a quasi-2D airfoil in combination with CFD shall be conducted with our tool in OpenFOAM. The results and optimization process shall be compared with other widely used algorithms, like the Nelder-Mead method. Therefore the usage of the equation of 4-digit NACA profiles is convenient, as this allows to describe an airfoil shape basing on the variables chord, thickness, camber and point of maximal camber. This shape description is suitable for optimization algorithms that depend strongly on the amount design parameters. Different ways to describe the shape of an airfoil are used in our OpenFOAM tool as well. The equation for 4-digit NACA profiles was implemented as well and the mesh movement in this case calculates directly the new position of the points by using this equation. As a closed trailing edge is needed for CFD, the last coefficient of the equation is put to -0.1036 instead of -0.1015. The primal shape of a first test run with a NACA 4415 airfoil and the according simulation grid can be seen in fig. 1.

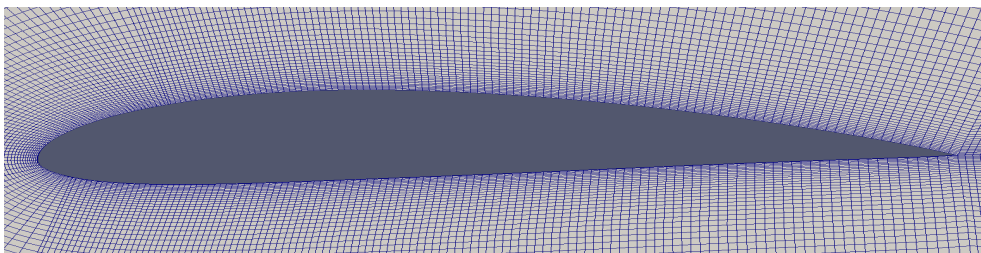


Figure 1: Primal shape of the airfoil NACA 4415 and simulation grid

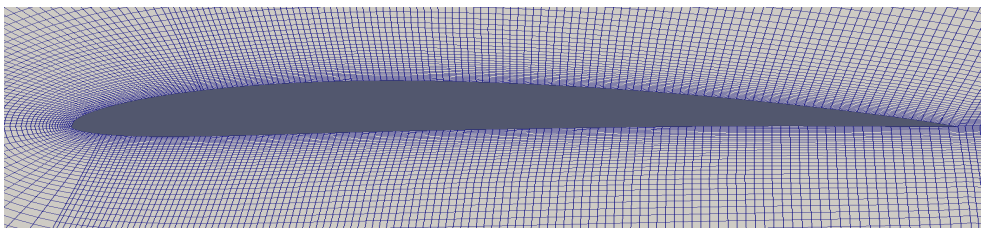


Figure 2: Shape of the optimized airfoil after 8 optimization steps and the moved grid

In fig. 2 one can see the resulting shape for a drag minimization after 5000 CFD iterations and eight optimization steps. The improved shape is thinner (now the thickness is 0.11 compared to 0.15 in the beginning), which one would expect for a drag minimization as well. The chord and position of maximal camber are constant in this approach. Furthermore the gradients are evaluated, comparing the

calculated search direction for the suction and pressure side. So in one optimization step either the camber or the thickness is changed. For this case, the camber did not change at all, as the reduction of thickness dominates the change of the camber. Up to now, problems with the moving mesh occur, as the leading edge is very fine discretized and if the points move according to the NACA equation, the cells can overlap which leads to an abort of the simulation. This can be seen in fig. 3.

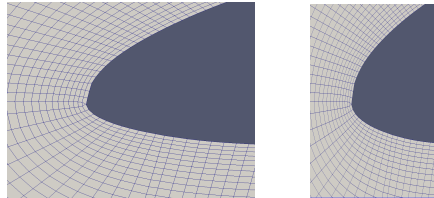


Figure 3: a) Grid around the leading edge b) Closeup of the collapsed cell

OUTLOOK

Next steps will be the improvement of the mesh movement method for the usage of the NACA equation. Furthermore optimizations will be run for a drag minimization with an constant aim drag coefficient. Different ways to discretize the shape will be used. First the NACA equation method, described above will be used. Then a usage of splines, that are based on some dozen design parameters will be used and finally all grid points will be design points as well. Former tests have shown, that smoothing of the gradients may be necessary for the last approach, as kinks and sharp edges have to be avoided on the surface of the airfoils. These results will then be compared with those from other optimization techniques.

After this comparison, the tool will be extended for 3D simulations, so whole rotor blades shall be optimized. As an optimal bend twist coupling shall be investigated, the 3D tool will be used for different load cases.

ACKNOWLEDGEMENT

For the simulations of this project we use the FLOW Cluster of the University of Oldenburg [7]. We highly acknowledge the work of Dr. Stefan Albensoeder, who keeps the Cluster running.

This work is part of the Smart Blades project supported by the Federal Ministry of Economics and Technology (BMU) under the support code 0325601 A/B/C/D on the basis of a decision by the German Bundestag.

REFERENCES

- [1] C. Othmer, E. de Villiers, H.G. Weller “Implementation of a continuous adjoint for topology optimization of ducted flows”, 18 th AIAA Computational Fluid Dynamics Conference, USA
- [2] European Wind Energy Association (EWEA), 2013. Factsheet 2013, Aug.
- [3] Brønsted, P., Loholt, H., and Lystrup, A. “Composite materials for wind power turbine blades”. Annual Review of Materials Research, Vol. 35.
- [4] Gasch, R., and Twele, J., 2007. Windkraftanlagen, 5 ed. Gasch, R., and Twele, J., 2007. Windkraftanlagen, 5 ed.
- [5] OpenFOAM, open source CFD toolbox, <http://www.openfoam.com/>
- [6] Soto, O., and Löhner, R. “On the computation of flow sensitivities from boundary integrals”. In 42nd AIAA Aerospace Sciences Meeting and Exhibit.
- [7] FLOW (Facility for Large-scale Computations in Wind Energy Research), <http://www.uni-oldenburg.de/fk5/wissenschaftliches-rechnen/hpc-facilities/flow/>

CFD ANALYSIS OF A 2-BLADED MULTI-MEGAWATT TURBINE

L. Klein¹, Th. Lutz¹, E. Krämer¹

¹University of Stuttgart, Institute of Aerodynamics and Gas Dynamics (IAG), Germany,
levin.klein@iag.uni-stuttgart.de

ABSTRACT

To deal with transient aerodynamic and structural loads the prototype of the 3.4MW Skywind horizontal axis wind turbine is equipped with an innovative load reduction system. In the present study the aerodynamic behavior will be investigated using full CFD simulations. A grid convergence study for the half model of the turbine is performed according to the highly accepted grid convergence index method which is used to quantify the uncertainty of the numerical results.

1 Introduction

There are several reasons why most of nowadays horizontal axis wind turbines have three blades, reaching from visual appearance to noise emission. Probably the main reason for tree bladed wind turbines is that the loads are more constant. On a two bladed wind turbine loads like the yawing moment on the turbine are oscillating much heavier under asymmetric inflow which leads to higher fatigue loads [1]. Nevertheless two bladed wind turbines have a high potential to improve the cost-efficiency especially in complex terrain or in offshore sites. The prototype of the two bladed Skywind 3.4MW turbine includes new concepts to achieve these goals, e.g. a lift device which makes an external crane for the installation of the assembled rotor and drive train unnecessary. To reduce the transient loads on the turbine elastic elements are added at the connection between the rotor head and the nacelle to enable a tumbling motion of the rotor.

In this project the aerodynamic behavior of the turbine is investigated by means of high fidelity CFD simulations with the German Aerospace Center (DLR) developed code FLOWer [2], already employed in various other wind energy projects, e.g. [3] and [4]. Various operating conditions will be considered to get a detailed insight into the transient aerodynamic loads on the rotor blades and to evaluate the accuracy of the aerodynamic load prediction of simpler models like BEM or free vortex wake [5]. Before simulating the whole turbine studies on a half model without tumbling motion of the rotor are carried out to evaluate the uncertainty of the numerical setup.

2 Numerical setup and meshing

The general setup for the half model studies consists of three independent block structured grids for background, blade and hub. The background grid has the shape of a half cylinder with a length of 2700 m (~25 rotor diameters) and a diameter of 1440 m (~13 rotor diameters) using a pole connector in the cylinder axis. It is refined in axial and radial direction. In circumferential direction the spacing is equidistant. The refinement region with uniform spacing reaches from approximately 0.5 rotor diameters upstream the rotor to 2.5 diameters downstream and radial to approximately 1.5 rotor radii. The refinement region downstream the turbine was chosen to better resolve the wake and especially the tip vortices. The hub and blade grid are located in the middle of the background grid. The different grids are connected using the Chimera technique which works with overlapping grids [6]. To ensure an appropriate transfer of the solution between the grids, the overlapping area is either located in regions with small gradients of the field variables or the cells are made small enough to capture high gradients. The size of the overlapping Chimera boundary cells should be of the same size. The blade is meshed in a C-grid topology using a rotor blade meshing script developed at the IAG for the commercial mesh generation software gridgen by Pointwise, Inc. The hub was meshed by hand having only a small overlapping area to the blade grid. All grids fulfill the requirement of a y^+ lower or equal 1 in wall nearest cell.

To verify the results on the half model a grid convergence study has been carried out according to [7] using 3 grids of different resolution. As recommended the grid refinement factor has been chosen to be greater than 1.3. The number of cells in each direction has been varied based on this factor and under consideration of multigrid capability, see Table 1. In the background grid the cell size located at the blade tip region was chosen to be of 0.75 m edge length in the fine, 1 m in the medium and 1.32 m in the coarse grid. As mentioned above the Chimera boundary cells in the blade and hub grid have been adapted to this size to guarantee a good interpolation. The total dimensions of the grids have not been changed between the grids of different resolution.

Table 1: Number of cells for the grid convergence study

	Coarse	Medium	Fine
total	6,852,864	15,720,576	35,713,664
refinement factor	-	1.319	1.315

FLOWer is a compressible finite volume URANS solver. The used numerical scheme is 2nd order accurate in time and in space, the time integration is done using dual-time stepping and the applied turbulence model is the Menter SST. The half model simulations have been performed at uniform inflow conditions using farfield and rotational periodic boundary conditions.

3 Results

For each of the three setups 30 revolutions using a time step corresponding to 3° azimuth have been performed reaching convergence of the average values of the integral loads after approximately 20 revolutions. Figure 1 shows the thrust and power over the last 10 revolutions. For the analysis of the grid convergence the loads have been time averaged over these 10 revolutions. The fluctuations in the loads are caused by the flow separation in the inner region of the rotor blade, especially in the root section where the profile of the blade is cylindrical.

Table 2 shows the results of the grid convergence study on the half model of the turbine. According to [7] several values are reported. Looking at the integral values of thrust and power the convergence of the fine grid indicated by the grid convergence index (GCI_{fine}^{21}) is good, as the approximate error e_a^{21} is very small.

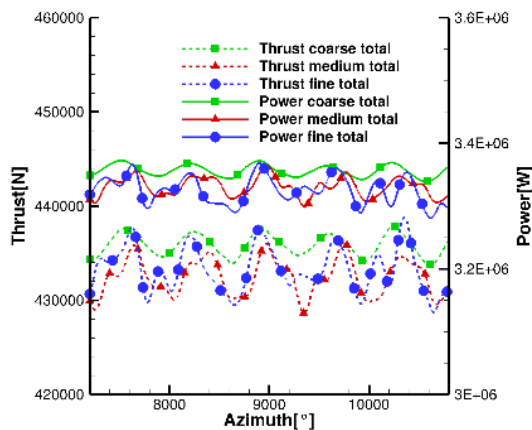


Figure 1: Thrust and power over the last 10 revolutions

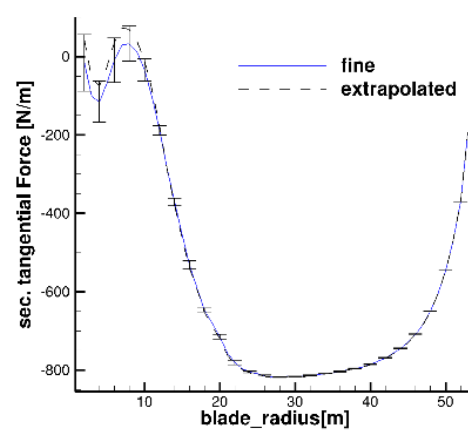


Figure 2: Averaged sectional tangential force for the fine grid

The factor s for the thrust is negative, because the value of the fine grid solution lays in between the coarse and the medium grid. According to [7] this is an indication for oscillatory convergence or more unlikely for the exact solution. It has to be mentioned too that there is an error caused by the time

averaging as the curves don't oscillate clearly periodical and the averaging is just done over the last 10 revolutions, see Figure 1. This error is estimated to have only a small influence on the results.

Table 2: Calculation of GCI discretization error according to [7]

Cell count	N_1, N_2, N_3	Power [MW]		Thrust [kN]		Tangential Force [kN]	
		35,713,664	15,720,576	6,852,864			
Value Fine	ϕ_1	3.3255		433.31		-28.933	
Value Medium	ϕ_2	3.3306		432.42		-29.517	
Value Coarse	ϕ_3	3.3563		435.87		-30.527	
Apparent order	p	5.84		4.90		1.94	
Extrapolated value	ϕ_{ext}^{21}	3.3242		433.63		-28.099	
Approx. rel. error	e_a^{21}	0.15%		0.21%		2.02%	
Extrapolated rel. error	e_{ext}^1	0.04%		0.07%		2.97%	
	e_{ext}^2	0,19%		0,28%		5,05%	
	e_{ext}^3	0,96%		0,52%		8,64%	
Fine grid convergence index	GCI_{fine}^{21}	0.05%		0.09%		3.60%	
	s	1		-1		1	

The tangential force on the blade shows a much higher uncertainty, as the GCI indicates an error of 3.6%. Since the power is mainly generated by tangential force this makes doubt about the very low GCI value calculated for the power. To better understand this, the GCI of the sectional loads, averaged over 10 revolutions, have been evaluated using the mean apparent order of p as suggested in [7]. Analyzing the sectional tangential force shows that the highest uncertainty, indicated by error bars using the GCI value, is located very close to the blade root, see Figure 2. Due to the small lever arm the sectional tangential force in the blade root region has only little influence on the total torque and therefore on the generated power. The comparison between the sectional tangential force resulting for the fine grid and the extrapolated values indicates that the positive effect on the power generation in the root section is still overestimated by the simulation.

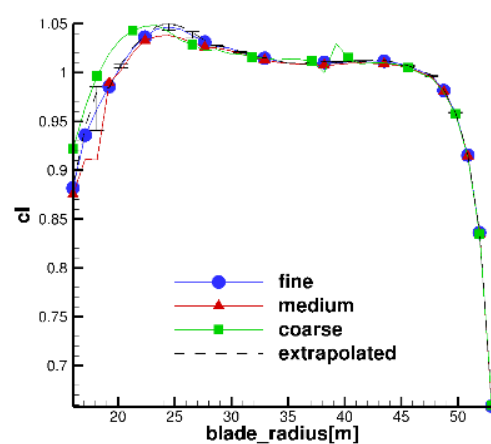
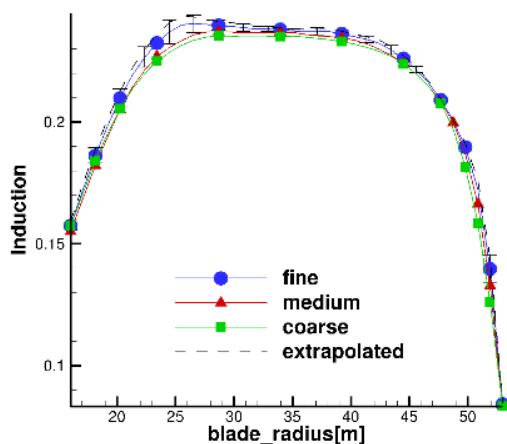


Figure 3: Axial induction with fine grid error bars **Figure 4:** Lift coefficient with fine grid error bars

To compare not only the forces on the rotor blade, but also the force coefficients and the induction of the turbine the results have been evaluated according to the induced velocity method [8]. As the method only works for steady calculations the unsteady effects in the blade root section cannot be captured correctly. Using a Tecplot macro the annular averaged velocity is calculated one mean chord length upstream and downstream the rotor for several radial positions. In contrast to [8] the tangential induction

has not been neglected in the present work. The comparison for the fine grid at 50% radial position showed that the consideration of the tangential induction leads to a reduction of the angle of attack (AoA) of only 0.09° . But the lift coefficient is reduced by 1.71% and the drag coefficient by 12.7% which cannot be neglected. Figure 3 shows the axial induction factor for the 3 grids as well as the extrapolated value for the axial induction and the GCI error bars for the fine grid. Over most of the radius the error is around 0.5% with the highest values at a radial position of approximately 25 m and a peak close to the tip. Looking at the extrapolated value the GCI method predicts a higher induction over the whole length of the blade. In contrast to the induction the GCI errors bars of the lift coefficient are very small, reaching only 0.05% to 0.1% in the outer region of the blade (Figure 4). This also explains the small GCI for the integral value of power and thrust. The axial induction in the blade tip region is lower for the coarser grids which leads to a higher angle of attack. However there is almost no difference in the lift coefficient in the tip region.

4 Conclusion

The grid convergence study carried out on 3 different grids according to [7] for a half model of the Skywind 3.4 MW turbine shows very good results. The uncertainty for power and thrust prediction is already on the coarsest grid quite good as the extrapolated relative error is approximately 1% for power and 0.5% for thrust. Since the extrapolated relative error of the medium grid for power is less than 0.2% and for thrust less than 0.3% the medium grid can be used for further investigations. The comparison of the sectional loads shows the biggest uncertainty in the blade root region. The GCI method indicates an overestimation of the tangential force and thereby the power production in this region.

As next step full model simulations for various inflow conditions will be performed and the setup will be adapted to allow a prescribed tumbling motion of the rotor.

5 Acknowledgements

This project is funded by the German Federal Ministry for the Environment, Nature Conservation, Building and Nuclear Safety (BMUB). The simulations have been carried out at High Performance Computing Center Stuttgart (HLRS) and bwUniCluster funded by the Ministry of Science, Research and Arts and the Universities of the State of Baden-Württemberg, Germany, within the framework program bwHPC.

REFERENCES

- [1] Hau, Erich, and Horst Von Renouard. Wind turbines: fundamentals, technologies, application, economics. Springer, 2013.
- [2] Kroll, N., and Fassbender, J. „MEGAFLOW-Numerical flow simulation for aircraft design.“ Springer, 2002.
- [3] Schulz, Christoph, et al. "CFD Studies on Wind Turbines in Complex Terrain under Atmospheric Inflow Conditions." Journal of Physics: Conference Series. Vol. 524. No. 1. IOP Publishing, 2014.
- [4] Weihing, Pascal, et al. "CFD Simulations on Interference Effects between Offshore Wind Turbines." Journal of Physics: Conference Series. Vol. 524. No. 1. IOP Publishing, 2014.
- [5] Luhmann, B. & Cheng, P. W.. Advanced Aero-Elastic Modeling of 2-bladed Wind Turbines using Multibody Simulation. In Proceedings of the 9th PhD Seminar on Wind Energy in Europe. Visby, Gotland/Sweden, 2013.
- [6] Benek, J.; Steger, J. L.; Dougherty, F. C.: "A Flexible Grid Embedding Technique with Application to the Euler Equations." AIAA Paper 83-1944, 1983.
- [7] Celik, Ishmail B., Urmila Ghia, and Patrick J. Roache. "Procedure for estimation and reporting of uncertainty due to discretization in CFD applications." Journal of fluids Engineering-Transactions of the ASME 130.7, 2008.
- [8] Johansen, Jeppe, and Niels N. Sørensen. "Aerofoil characteristics from 3D CFD rotor computations." Wind Energy 7.4 (2004): 283-294.

Numerical investigations of a passive load alleviation technique for wind turbines

A. Fischer¹, E. Jost¹, T. Lutz¹, E. Krämer¹

¹University of Stuttgart, Institute of Aerodynamics and Gas Dynamics (IAG),
fischer@iag.uni-stuttgart.de

ABSTRACT

In order to increase the wind energy yield, the diameter of wind turbine rotors grew significantly larger over the past few years, which results in higher loads on the whole turbine. To reduce these peak and fatigue loads, the development of new load control concepts and the improvement of calculation methods for wind turbines are necessary. This article deals with 2D investigations of a passive load alleviation concept under steady inflow conditions and compares the results of different numerical setups with wind tunnel data.

1. Introduction

The extending of the competitiveness of the wind power industry towards conventional forms of power generation will become increasingly important. Therefore the reduction of the cost of energy of onshore and offshore wind turbines is essential. This can be achieved through two major aspects: the increase of the efficiency and reliability of wind energy and the enlargement of the energy yield. On the one hand, this can be done by an improvement of the aeroelastic calculation methods to receive a more accurate (fatigue) load prediction. This is important as inaccuracies in the load prediction resulting from simplifications e.g. when using blade element momentum (BEM) theory models, can negatively affect the blade design yielding to either too heavy blades or to structural problems during (long term) operation. Up to now only simplified BEM aerodynamic models in combination with generic wind field models are used for the load prediction in the design and verification process of wind turbines. These models however do not consider important three-dimensional, unsteady and viscous effects with sufficient accuracy and the imposed time-variant inflow fields are generated from empirical turbulence spectra. On the other hand, the power production of the wind turbine can be increased by an enlargement of the rotor diameter. This results in higher manufacturing costs and moreover almost all characteristic parameters, like blade mass or thrust, grow relatively stronger than the rotor diameter. For future rotors with further increased diameter load alleviation techniques are desired to limit for example the weight of the blades.

The DFG PAK 780 is a collaborative research project of five German universities, which is funded by the German Research Foundation (DFG). The task of the University of Stuttgart is the numerical verification of passive and active load alleviation techniques for wind turbines in atmospheric turbulence. Therefore, an existing CFD-based numerical process chain, [1], has been extended to enable the calculation of unsteady load fluctuations of a wind turbine with and without load reduction concepts under realistic inflow conditions considering three-dimensional, unsteady and viscous effects with sufficient accuracy. The complexity of the process chain shall be increased step by step, starting from a 2D airfoil at uniform inflow with load alleviation concept up to a generic 5MW wind turbine with a load control concept at atmospheric boundary conditions. So far, such a high-fidelity approach has not been applied to study load control concepts but is deemed necessary to enable a numerical assessment of innovative load control concepts for realistic operation conditions.

2. Experimental and numerical setup

The load alleviation concept which is investigated within the project was developed at TU Darmstadt, [2]. The novel concept uses the pressure changes caused by angle of attack (AoA) variations to adapt

the airfoil camber through kinematically coupled leading (LE) and trailing edge (TE) flaps (Figure 1). It is a passive load control concept and the flap motions are therefore caused only by the aerodynamics. The response behavior of the system can be influenced by variation of the spring stiffness, the preload moment and the coupling ratio, leading, for an appropriate choice, to a reduction of the lift curve slope.

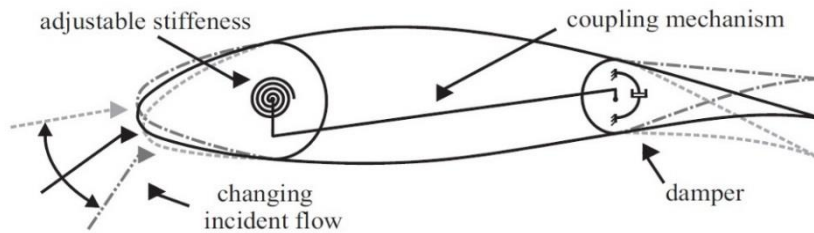
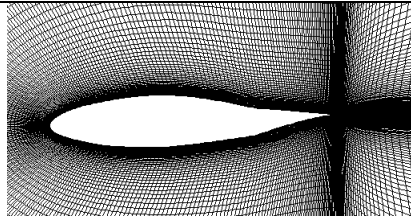
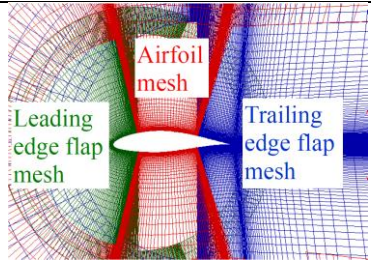


Figure 1: structure of an airfoil with coupled leading and trailing edge flap, [2].

The wind tunnel tests on a NACA 64₃618 airfoil with this novel load alleviation concept, which were performed by Lambie, [2], were reproduced by URANS simulations, taking into account the relevant viscous and unsteady aerodynamic effects that may be caused by flow separation.

The simulations were carried out with FLOWer, a block structured code developed by the German Aerospace Center (DLR), which solves the compressible Navier-Stokes-Equations, [3]. The deflections of leading and trailing edge flaps were chosen consistently to the experiments for each angle of attack. The characteristic parameters of the two different setups under investigation can be found in Table 1.

Table 1: General mesh properties

Parameter	FLOWer-XFOIL	FLOWer-Chimera
Number of Meshes	1	3
Mesh Topology	 Block structured	 Block structured [4]
Dimension	2D	
Cell number	≈60000	≈192400
Boundary Conditions	No slip wall, Farfield	No slip wall, Farfield, Chimera
y+	≈1	
Turbulence Model	Menter SST	
Time Discretization	Dual time stepping method (100 time steps per convective time unit) with 30 inner iterations	

In the first setup, called FLOWer-XFOIL, the corresponding airfoil shape was generated using XFOIL, an airfoil design and analysis code developed by M. Drela, [5]. As the gaps in chordwise direction between the middle part of the airfoil and the flaps were sealed in the experiment, one mesh, which was created in IGGTM, a multi-block structured grid generator of NUMECA, was sufficient to reproduce the experimental setup. For more information about this setup, see Hummel [6]. Another setup, denoted as FLOWer-Chimera, uses the Chimera technique, [7], and consists of three independent components (leading edge flap, middle section and trailing edge flap) and therefore features three independent overlapping meshes. The meshes were generated in Pointwise @ Pointwise, Inc.. The advantage of this

setup is the simplicity of the definition of the flap motion and the possibility to realize a gap in chordwise direction and additionally in spanwise direction for a 3D configuration and so to get a spanwise defined flap with sharp edges. The gaps between the three components of the FLOWer-Chimera setup were sealed for these studies to be in line with the experiment. More information can be found in Busse, [4]. The experiments were performed for a wind tunnel model with endplates (Figure 2). Therefore an effective 2D AoA α_{eff} was prescribed for the simulations that accounts for the impact of the endplates. The formula used for the calculation was proposed by Schlichting and Truckenbrodt, [8]. To determine α_{eff} the induced angle of attack α_{ind} and the effective wing aspect ratio Λ_{eff} has to be calculated with the following formulae

$$\alpha_{ind} = \frac{F_N \cdot \cos(\alpha(t)) - F_T \cdot \sin(\alpha(t))}{b \cdot t \cdot q \cdot \pi \cdot \Lambda_{eff}} \quad \text{and} \quad \Lambda_{eff} = \frac{b}{t} \cdot \left[1 + 0.5 \cdot \frac{b_S}{l_S} \cdot \left(\frac{l_S}{t} \right)^2 \right]$$

The effective angle of attack can finally be determined as:

$$\alpha_{eff} = \alpha - \alpha_{ind}$$

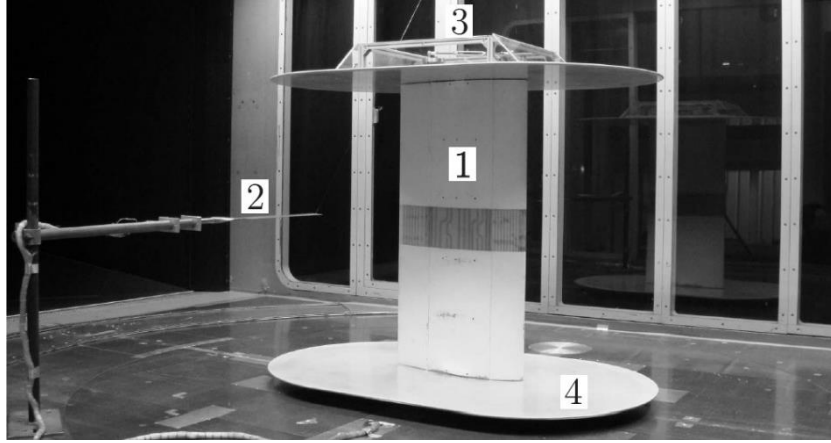


Figure 2: Experimental setup: 1. suction side; 2. wake rake; 3. coupling Mechanism; 4. end plates, [2].

3. Results

The predicted polars and pressure distributions were compared to the available experimental results documented in Reference [2]. Figure 3 shows the polar for a test case with a spring stiffness of $k_\gamma = 30 \frac{Nm}{rad}$, a preload moment of $M_0 = 2 Nm$, a steady inflow of $v = 40 \frac{m}{s}$ and a coupling ratio of $n = 3$, which means, that the deflection angle of the TE flap is three times the size of the LE deflection angle.

The purple line shows the polar for the airfoil without load alleviation concept calculated by FLOWer. Compared to the other curves, which represent results for the airfoil with activated load alleviation, it becomes obvious that the variable camber concept significantly reduces the lift curve slope and thus effectively reduces the load variations caused by AoA fluctuations.

The FLOWer-XFOIL and the XFOIL results show a fair agreement to the experimental results, while the FLOWer-Chimera calculations show stronger differences. The deviations between predictions and measurements are mainly attributed to three-dimensional effects of the configuration with end plates (Figure 2) that are not captured by the above mentioned AoA correction. No further wind tunnel corrections were applied to the experiments.

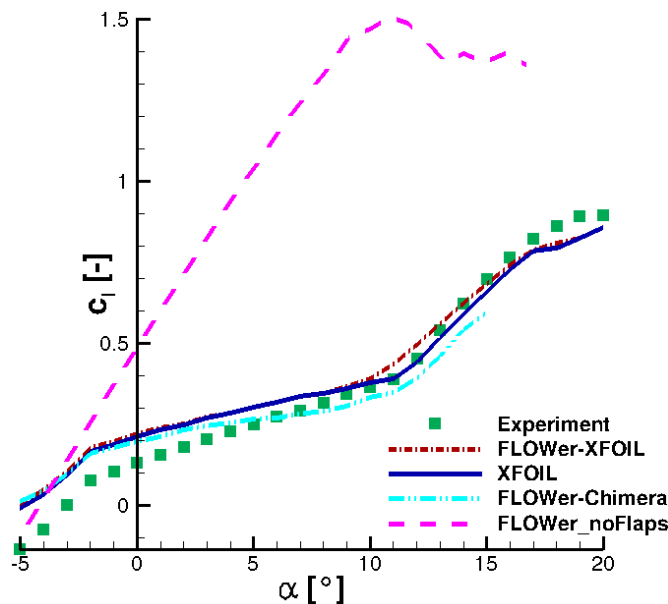


Figure 3: Comparison of different simulation methods.

measurements. The differences might be a result of 3D effects in the wind tunnel caused by the endplates. Now, the FLOWer code is going to be extended to directly realize arbitrary deflected leading and trailing edge flaps for 2D as well as for 3D setups

5. Acknowledgements

The present investigations were performed in the DFG PAK 780 project. The authors gratefully acknowledge the *German Research Foundation (DFG)* for funding the studies, as well as *Benjamin Lambie, Ulrike Cordes* and *TU Darmstadt* for supplying us with the experimental results.

REFERENCES

- [1] K. Meister, T. Lutz und E. Krämer, "Considerations of unsteady inflow conditions in wind turbine CFD simulations", Proc. DEWEK, 2010.
- [2] B. Lambie, "Aeroelastic Investigation of a Wind Turbine Airfoil with Self-Adaptive Camber", Doctoral thesis, TU Darmstadt, 2011.
- [3] N. Kroll und J. Fassbender, "MEGAFLOW - Numerical Flow Simulation for Aircraft Design", Springer Verlag Berlin/Heidelberg/NewYork, ISBN 3-540-24383-6, 2002.
- [4] K. Busse, "Numerical studies of an airfoil with coupled leading and trailing edge flap using chimera technology", Bachelor thesis, Institute of Aerodynamics and Gas Dynamics, University of Stuttgart, 2014.
- [5] M. Drela, "XFOIL: An Analysis and Design System for Low Reynolds Number Airfoils", Low Reynolds Number Aerodynamics (Conference Proc.), University of Notre Dame, USA, June 1989.
- [6] H. Hummel, "Numerical investigations of an airfoil with coupled leading- and trailingedge flaps for the load reduction at wind turbines", Study thesis, Institute of Aerodynamics and Gas Dynamics, University of Stuttgart, 2013.
- [7] J. Benek, J. Steger, F. Dougherty und P. Buning, "Chimera: A Grid-Embedding Technique", NASA Ames Research Center, 1986.
- [8] H. Schlichting und E. Truckenbrodt, "Aerodynamik des Flugzeugs", Band 1, Berlin / Heidelberg / New York: Springer-Verlag, 1967.

4. Conclusion

2D URANS simulations of a NACA 64₃618 airfoil equipped with coupled leading and trailing edge flaps were performed for different setups and were compared to results of wind tunnel test. The flap deflections were chosen consistently to the experiments for each AoA leading to an increase respectively decrease of the airfoil camber. This modified camber line reduces the lift curve slope and consequently reduces load fluctuations caused by variations of the angle of attack. The comparison of the lift polar of the different setups shows a fairly good accordance between the simulations and the

LARGE-EDDY SIMULATIONS OF A S826 AIRFOIL WITH THE DISCONTINUOUS GALERKIN METHOD

A. Frère^{1,2}, H. S. Chivae³, R. F. Mikkelsen³, P. Chatelain², K. Hillewaert¹

¹Cenaero, 29 rue des Frères Wright, 6042 Gosselies Belgium, ariane.frere@cenaero.be

²Université Catholique de Louvain, 1 Place de l'Université, 1348 Louvain-la-Neuve Belgium

³Technical University of Denmark, 403 Nils Koppels Alle, 2800 Lyngby Denmark, hsar@dtu.dk

ABSTRACT

The aim of the present work is to improve the understanding of low Reynolds flow physics by performing Large-Eddy Simulations (LES) of the NREL S826 airfoil. The paper compares the results obtained with a novel high order code based on the Discontinuous Galerkin Method (ArgoDG) and a recent experiment performed at the Technical University of Denmark. Chordwise pressure evolutions, integrated lift and drag forces are compared at Reynolds number $4 \cdot 10^4$ and angles of attack (AoA) 10 and 12 degrees. Important differences are observed between the simulations and the experiment. These differences are, however, partially explained by the strong sensitivity to the tunnel environment. To overcome this source of error, the ArgoDG LES results are also compared to LES performed with the Finite Volume Method (FVM) code EllipSys3D, a well established wind turbine Computational Fluid Dynamics (CFD) code. The similarity of the results obtained by these two inherently different methodologies provide strong confidence in the validity of the computations.

INTRODUCTION

Accurate prediction of low Reynolds number ($Re < 10^5$) airfoil characteristics is difficult since the transitional flows often feature laminar separation bubbles (LSB), highly three-dimensional stall cells, performance hysteresis as well as a high sensitivity to inlet turbulence. As a result, high uncertainties on the wind tunnel measurements are observed. Therefore, the use of CFD is a very attractive perspective.

The main difficulty of the CFD simulations is the modeling of flow turbulence. Due to the presence of laminar to turbulent transition and the 3D boundary layer development at higher AoA, Reynolds Averaged Navier-Stokes (RANS) is not suited for the prediction of low Reynolds number flows. Instead, scale-resolving approaches such as LES, which compute part of the turbulent structures directly, should be used. The challenge of LES remains its large computational cost for high Reynolds number, although with the present computing capacity, $Re=10^5$ can be modeled fully. For LES computations, high-order discretizations are considered to be more adapted than those typically used in state of the art solvers, as illustrated by the use of high-order finite difference or spectral codes in academia. Due to the lack of geometric flexibility of these methods, novel unstructured high-order discretization techniques as the Discontinuous Galerkin Method (DGM) are currently being developed for industrial applications. The ArgoDG code, based on DGM, has been successfully validated on DNS and Implicit LES (ILES) benchmarks [1][3]. In particular, the validity of the ILES approach, where the subgrid scale stresses are provided by the numerical scheme, has been demonstrated. Argo DGM starts to be used on industrial benchmarks featuring transitional flow and the wind turbine airfoil simulation of this paper is a step forward in the validation of the DG methodology for industrial applications.

In this paper, the ArgoDG code is used for LES of the S826 airfoil at Reynolds number $4 \cdot 10^4$. The S826 airfoil is a 14% thick NREL airfoil which has been used recently in a blind test comparing different wind turbine wake modeling codes. This test demonstrated the importance of capturing correctly the low Reynolds flow physics [4]. This airfoil is hence well representative of the current wind energy challenges.

NUMERICAL SETUP

The discontinuous Galerkin method can be seen as a collection of elementwise defined small finite element problems coupled by “boundary conditions” on the common faces between elements. The high order of convergence is ensured by the polynomial interpolation. In the present study cubic polynomials have been used throughout the domain, formally leading to fourth order grid convergence.

The 3D mesh used for ArgoDG computations is obtained by the extrusion in the spanwise direction of an unstructured O-type mesh composed mainly of triangles in the far-field combined to quadrangles in the boundary layer region, see Figure 1. The span length is equivalent to 20% of the chord and to simulate an infinite span, periodic boundaries are imposed.

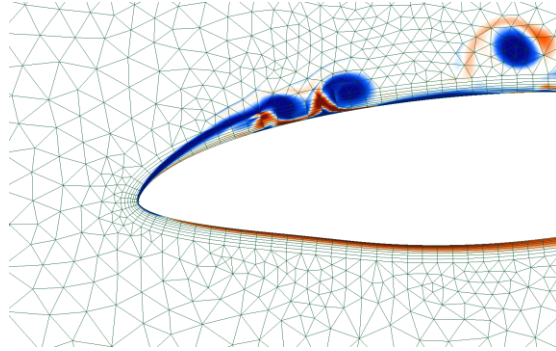


Figure 1: Vorticity and mesh of the Argo run at AoA=12° and Re=4.10⁴.

Rigorous mesh criteria for LES computations are unfortunately not available. For the classical periodic channel flow, Piomelli and Balaras [5] advise streamwise and spanwise resolution as $\Delta x^+ \leq 100$ and $\Delta z^+ \leq 20$ respectively, while the wall normal direction should satisfy $\Delta y^+ \leq 1$. This rule of thumb is however probably too restrictive for high-order methods, and not appropriate for reattachment zones where one would expect to need a more isotropic mesh parallel to the wall to reflect a highly chaotic flow. The runs were hence made on a slightly coarser mesh providing $\Delta y^+ \leq 1.5$, Δx^+ and $\Delta z^+ \leq 20$ in the turbulent region. The 3D mesh lead to computations of 5.0M degrees of freedom.

LES OF THE S826 AIRFOIL AT REYNOLDS NUMBER 4.10⁴

Sarlak [6] demonstrates the presence of hysteresis for $Re \leq 8.10^4$ and for angles just above 10°. Re of 4.10⁴ and AoA of 10 and 12° were hence considered for ArgoDG simulations with flow conditions such that the freestream Mach number is $M = 0.15$. Figure 2 presents a global view of the flow at AoA=10° with the instantaneous z-wise vorticity, showing a laminar separation close to the leading-edge followed by a transition close to 40% of the chord.

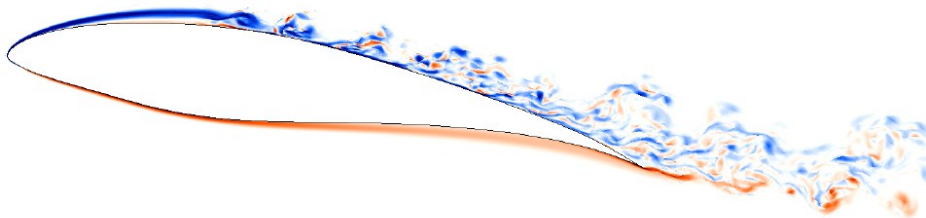


Figure 2: Separation region visualized by z-wise vorticity in the periodic plane for S826 airfoil at $Re = 4.10^4$ and $AoA = 10^\circ$ with ArgoDG.

Figure 3 provides the experimental lift and drag curves for two different inflow turbulence intensities (TI), respectively 0.1% and 0.8%. A slight increase of the inlet turbulence is hence enough to drastically change the airfoil performance. This figure presents as well computational results obtained with ArgoDG. It is surprising to notice that the CFD results, obtained without imposed inflow turbulence, are much closer to the experimental values obtained at the higher turbulence levels.

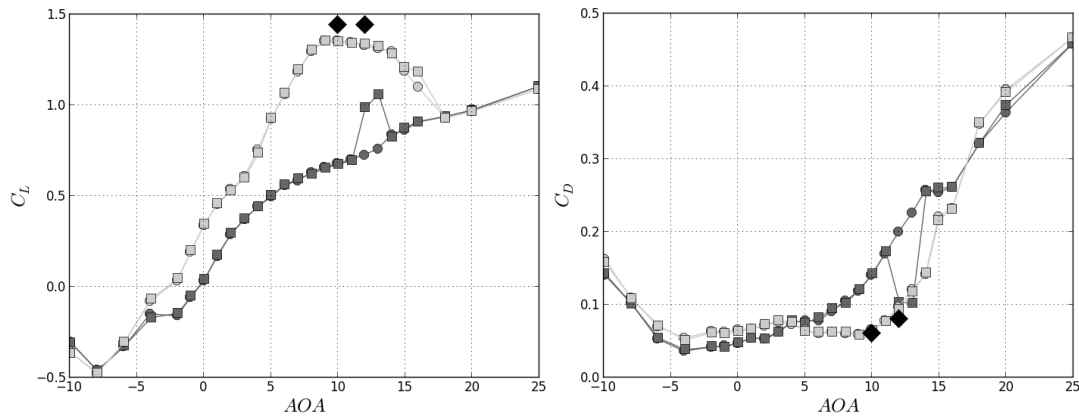


Figure 3: Experimental lift and drag coefficients for increasing (circles) and decreasing (squares) AoA[6]. Dark and light gray markers represent TI= 0.1% and 0.8%. Black diamonds are ArgoDG.

Figure 4 further compares ArgoDG results to the experimental results at different TI by presenting the pressure coefficient evolution along the airfoil chord. This figure shows clearly that the computed flow is very close to the experiment with the highest inflow turbulence. The computational curve and the experimental curve with TI=0.8% are both presenting a pressure plateau, revealing the presence of a LSB. The pressure level and the length of the plateau are not coinciding between the computation and the experiment. Their evolutions between 10 and 12° are however similar: the pressure level increases and the length reduces. The LSB moves hence to the leading-edge and reduces in size when the AoA increases.

The experimental curve at lower TI does not present a pressure plateau. The flow seems to separate close to the leading-edge, without reattachment. The inflow turbulence has hence a very strong impact on the flow characteristics. As mentioned by Genç [2], Schubauer and Skramstad [7] demonstrated that the transition over a flat plate is already affected by a turbulence level of 0.1%. The step from TI = 0.1 to 0.8% realized in the experiment has hence a strong impact on the LSB stability. This , however, does not explain why the computation is closer to the case with inflow turbulence.

A potential explanation lies in the numerical dissipation of the code. In order to verify this effect, the results obtained with ArgoDG for an AoA of 12° are compared to those obtained with EllipSys3D, code based on a very different discretization scheme and therefore featuring a distinct dissipation behavior. Figure 4 shows that the two computations provide very similar results, increasing the confidence in their validity. Both computations, performed without inflow turbulence, are very close to the experiment performed with TI=0.8% and they both present a lower and longer pressure plateau.

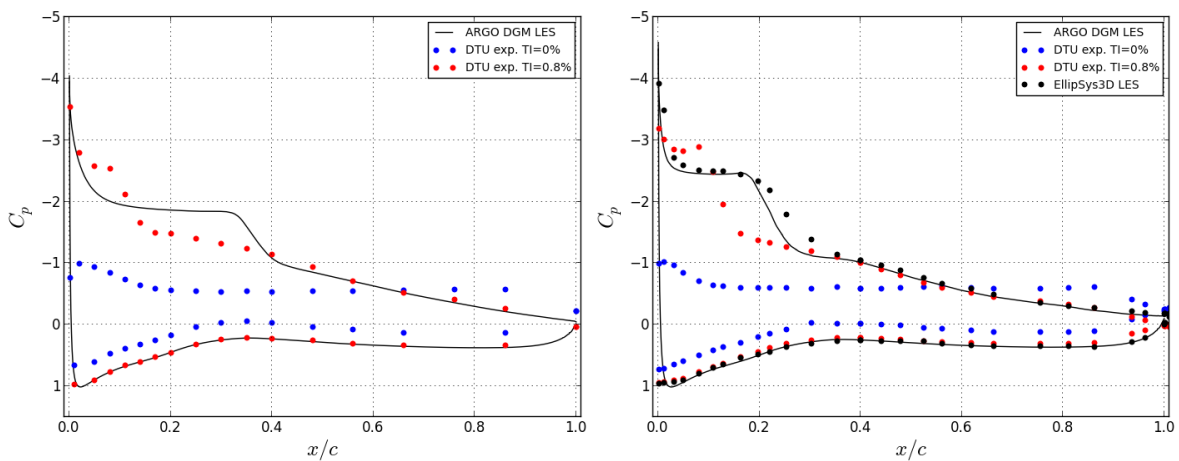


Figure 4: Pressure coefficient at $Re=4.10^4$, for AoA=10°(left) and AoA=12° (right)

Other reasons for the discrepancy between the LES and the experiments are, on the computation side, unadapted grid refinement or insufficient span width to allow the development of long wavelength structures and stall cells. On the experimental side, one can mention the impact of pressure taps on the transition and separation of the boundary layer as well as the interaction of the flow with the wind tunnel leading to secondary flow near the walls, or interaction with large stall cells. To verify and understand these discrepancies, further mesh and span analyses will be performed on the computational side, and more detailed experiments will be undertaken, including oil visualization.

CONCLUSION

ILES of the S826 airfoil were performed at a Reynolds number of $4 \cdot 10^4$ and at angles of attacks of 10 and 12 degrees with a novel high order code based on the Discontinuous Galerkin Method, ArgoDG. The pressure distribution over the airfoil as well as the lift and drag coefficients obtained with ArgoDG were compared with experiments and LES performed at DTU Wind Energy. The results obtained by ArgoDG are very similar to those predicted by EllypSys3D, providing a good confidence in ArgoDG ILES accuracy.

Some differences are however observed with the experimentation. Although the computations are both realized without inflow turbulence, the results match better the experimentation performed with the highest inflow turbulence. Multiple authors showed however that at low Reynolds, the inflow turbulence plays a crucial role in the establishment of the flow, leading to cases with or without turbulent reattachment. In view of the extreme sensitivity to the tunnel environment and considering the similarity with Ellipsys3D simulations, the ArgoDG results obtained in this paper are considered as a good step forward in the use of DG Method for solving low Reynolds number flows around airfoils.

Further studies, based on oil flow visualization, Reynolds number and inflow turbulence sensitivity analyses are expected to shed some light on the details of separation behavior and contribute to reconcile the simulations and observations at various TI and Re.

ACKNOWLEDGMENT

A. Frère gratefully acknowledges her funding by the Walloon Region in the frame of the FirstDocA framework and thanks Torben J. Larsen and Jens N. Sørensen for the fruitful discussions and precious inputs.

REFERENCES

- [1] Carton de Wiart, C. (2014). “Towards a discontinuous Galerkin solver for scale-resolving simulations of moderate Reynolds number flows, and application to industrial cases”. Ph.D. thesis, Ecole polytechnique de Louvain/iMMC.
- [2] Genç, M. S., Karasu, I., Açikel, H. H., and Akpolat, M. T. (2012). “Low Reynolds Number Aerodynamics and Transition”. InTech. ISBN:978-953-51-0492-6.
- [3] Hillewaert, K. (2013). “Development of the Discontinuous Galerkin Method for high-resolution, large scale CFD and acoustics in industrial geometries”. Ph.D. thesis, Ecole polytechnique de Louvain/iMMC.
- [4] Pierella, F., Krogstad, P., and Sætran, L. (2014). “Blind test 2 calculations for two in-line model wind turbines where the downstream turbine operates at various rotational speeds”. *Renewable Energy*, 70, 62–77.
- [5] Piomelli, U. and Balaras, E. (2002). “Wall-Layer Models for Large-Eddy Simulations. Annual review of fluid mechanics”, 34(1), 349–374.
- [6] Sarlak, H. (2014). “Large Eddy Simulation of turbulent flows in wind energy”. Ph.D. thesis, DTU.
- [7] Schubauer, G. B. and Skramstad, H. K. (1947). “Laminar boundary layer oscillations and stability of laminar flow”. *Journal of Aeronautical Sciences*, 14(2), 69–78.

Increased Order Modeling of the Aerodynamic Characteristics of Flexible Blades

Z. Wang¹, E. A. Ferede¹, G. J.W. van Bussel¹

¹Delft University of Technology, Faculty of Aerospace Engineering , Kluyverweg 1, 2629HS Delft, The Netherlands, z.wang-3@tudelft.nl

ABSTRACT

Aerodynamic performance has become an important issue with the increasing size of wind turbine. Blades are not only becoming longer but also more flexible. So far Blade Element Momentum theory (BEM) is extensively used in the design of rotor blade, but its validity starts to decrease for large flexible rotor blades.

This paper aims to investigate that how far can BEM be used accurately for the aerodynamic performance of large flexible blades and if vortex panel codes are a better alternative. So a comparative study is performed between three aerodynamic models: BEM, BEM with first order correction and a panel code implementation. Starting from a straight blade and then for increased curvature, the angle of attack is calculated and compared between these three aerodynamic models.

In the future, several methods are investigated to calculate the aerodynamic characteristics of flexible blades or blades with generic initial shape, with the accuracy close to panel method and computational time in the same order of magnitude as BEM theory, making it suitable for optimization purposes. An extended lifting line method seems to be a good choice and will be studied in the future work.

1. Introduction

How to improve the output efficiency is always the primary target of the wind turbine technology. Li [1] has studied the relationship between the size and the output power of wind turbines, and the paper shows that when the size increases by 50%, the power will be up to 165% accordingly. So it is expected that in the following years, the size of wind turbine will go larger.

But technical problems occur with the increases in size of wind turbines, among which there is no doubt that the aerodynamics has been recognized as the primary issue. The accurate prediction of aerodynamic loads becomes very necessary to improve the efficiency of energy extraction and the performance of the wind turbines, as well as to reduce the power generation cost and make the wind turbines operated in safe.

Sheng et al [2] assessed two methods to study the aerodynamic performance of the large wind turbine blades: wind tunnel test and numerical simulation. In general they show that results of wind tunnel test are of high reliability but also with greatly high cost and with a long experimental process time. In comparison, the numerical simulation method is more economical for both cost and time. According to the increasing levels of fidelity, the numerical simulations comprise Blade Element Momentum (BEM) methods, vortex methods and Computational Fluid Dynamics (CFD) methods.

2. Methodology

In order to investigate how far can BEM be used accurately for the aerodynamic performance of flexible blades, a comparative study is performed among three aerodynamic codes: BEM, BEM with first order correction and a panel code implementation to calculate and compare the aerodynamic characteristics of various blade shapes.

In this paper three blades with different curvatures are considered. All blades share the same mid chord length of 42 meters and use the same NACA0015 airfoil. Blade 1 is a straight blade. Blade 2 and 3 start to curve at the blade length of 21 meters. The curved part is presented by the part of a circle that is tangent to the straight part. The shorter the radius, the larger the curvature. A radius of 42 meters is used in Blade 2 and a radius of 13.4 meters is used in Blade 3, as shown in figure 1.

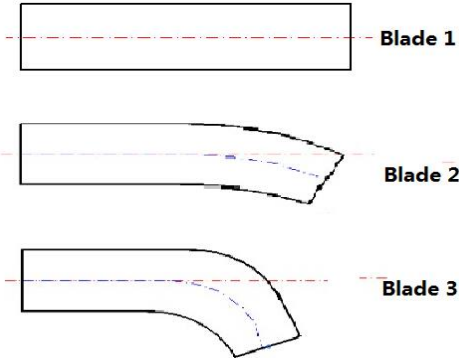


Figure 1 Three Blade Shapes With Different Curvatures

2.1 BEM Code

The commercial code BLADED is widely-used in wind turbine engineering. This code is based on BEM theory. BEM is the combination of momentum theory and blade element theory, where a blade is divided into strips of independent elements along the radius. Through a simple numerical iteration the aerodynamic loads are calculated. The computing time of BEM is short (only a few seconds for general calculation) because of the simplified model and the results are also very satisfactory with the use of empirical correction models[3-4]. The shortcoming of BEM method is that empirical models and tuning parameters limit the generality. And it may be expected that the accuracy and becomes less when the blades get more flexible.

2.2 Correction BEM Code

In [5] Ferede et all presents a modification to a standard BEM code in which the chord and twist distribution along a blade span are corrected for changes in the shape of the blade axis from initial straight line to a curved line as shown in figure 2. These corrections are then used as input for standard BEM formulation to calculate the aerodynamic loads.

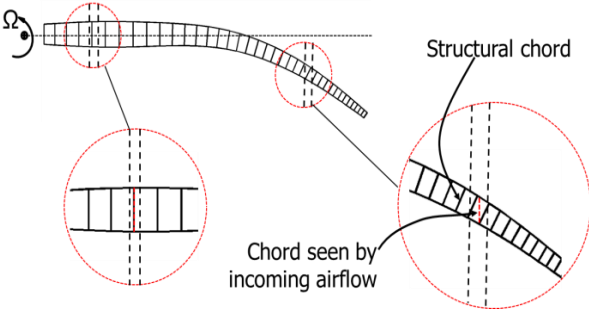


Figure 2: Plan-form Shape of Curved Blade

2.3 Panel Code

Vortex method simplified the vorticity distribution in the three-dimensional flow field of the wind turbine into line vortex or panel vortex, and calculate the aerodynamic loads by the attached geometry grids and different trailing vortex models. The results of panel method are with higher calculation

accuracy since it doesn't need experience constants, and the calculation efficiency is also much better compared with CFD method.

A 3-D unsteady multi-body panel method is developed by Dixon [6] that can model arbitrary geometries directly. The method has been specifically designed so that it can handle the blade-wake interactions and viscous wake effects. This code is further developed at TU Delft for horizontal axis wind turbines.

3. Results

The angle of attack was calculated and compared for three blade shapes, shown in figure 1. For the straight blade, as shown in figure 3, the results from the panel code and the correction BEM code agree with that from BLADED very well, and thus the accuracy and reliability of these two codes are verified. But with the increase of the curvature of the blades, the difference among the three codes gets larger, which can be seen in figure 4 and figure 5.

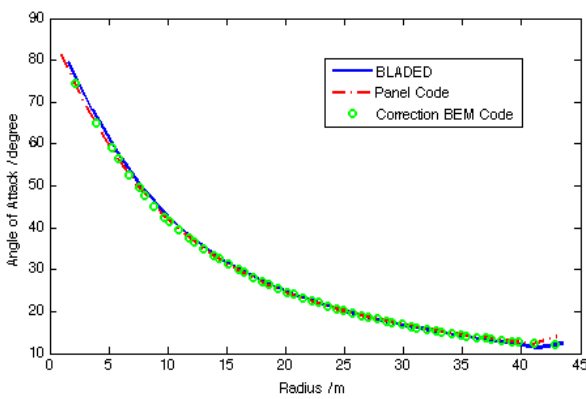


Figure 3 Results of Blade 1

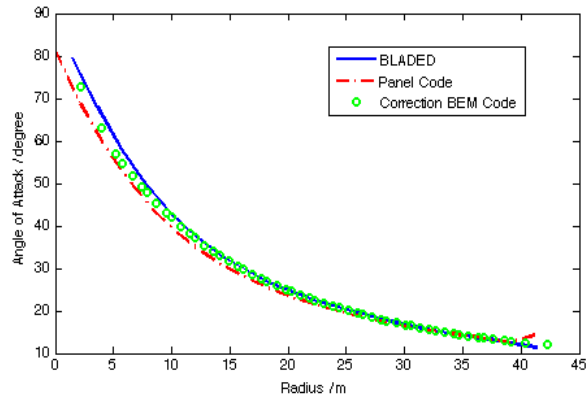


Figure 4 Results of Blade 2

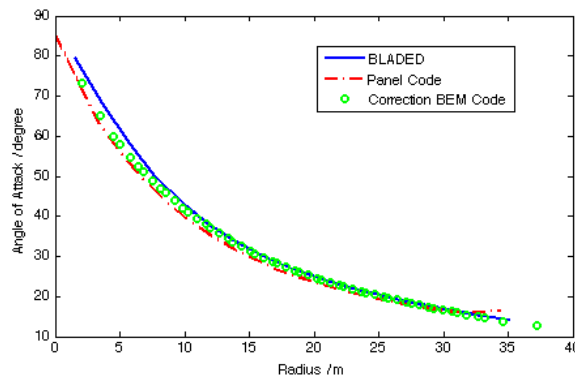


Figure 5 Results of Blade 3

Figure 6 to figure 8 show that the results of different blade shapes from BLADED are the same. The results from correction BEM code change a little since the difference between real structural data and the aerodynamic data needed is considered in this code. The results from panel code are expected to be the most accurate because the aerodynamic performance changes with the blade shape, as might be expected.

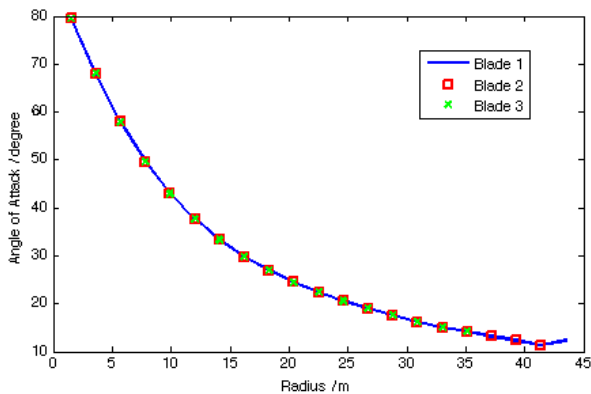


Figure 6 Results of BLADED

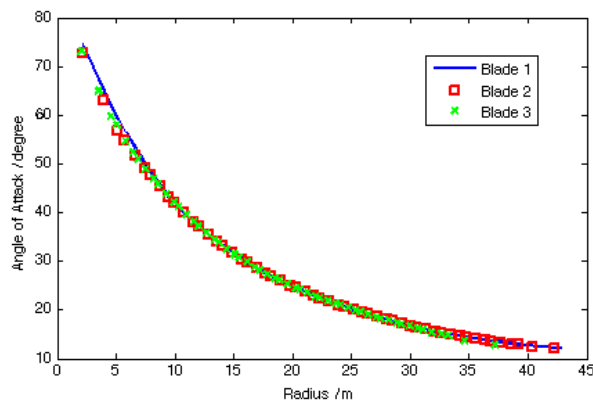


Figure 7 Results of Correction BEM Code

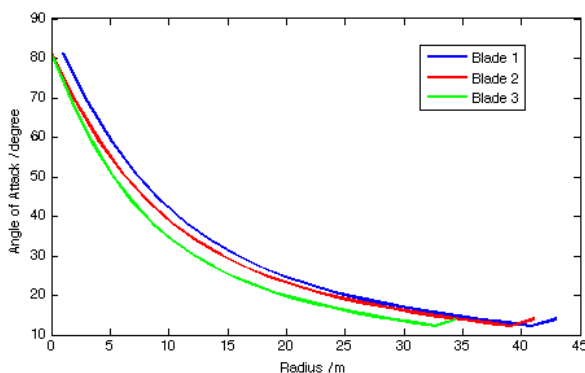


Figure 8 Results of Panel Code

4. Conclusion

The results show that the accuracy of BEM code decreases when the deformation of the blades increases. The correction to BEM seems to improve the result of the standard BEM formulation for moderately low curvatures. From the three methods, the panel code corrects most accurately for changes in blade shape (i.e. curved blade axis, coning effect, etc...). However, the computational time is significantly larger than the other two methods making it less suitable for aeroelastic optimization purposes.

For optimization purposes, the best method should meet the requirement that it can calculate the aerodynamic characteristics of flexible blades with the accuracy close to panel method and the computational time should be in the same order of magnitude as BEM. An extended lifting line method seems to be a good alternative and will be studied in the future work.

References

- [1] Y. Li, 2013. "Status of Large Scale Wind Turbine Technology Development Abroad". Applied Mathematics and Mechanics.
- [2] Z. Sheng, C. Li, H. Ren, X. Liu. 2012. "Investigation on the aerodynamic performance of large wind turbine blade based on CFD". Journal of Harbin Engineering University.
- [3] M.O.L. Hansen, J.N. Sørensen, 2006. "State of the art in wind turbine aerodynamics and aeroelasticity". Progress in Aerospace Sciences.
- [4] Hansen, M., 2008. "Aerodynamics of Wind Turbines". Second edition.
- [5] Ferede E, Pereira R, Abdalla M, van Bussel, G.J.W. , 2014. "Effect of Aeroelasticity on Blade Planform Optimization of Stall Controlled HAWT". Science of Making Torque from Wind.
- [6] K. R. Dixon, 2008. "The Near Wake Structure of a Vertical Axis Wind Turbine". Master thesis, Aerospace Engineering at Delft University of Technology.

Hybrid aerodynamic analysis of wind turbines

M. Schwarz¹, B. Stoevesandt², J. Peinke¹

¹ForWind, University of Oldenburg, Carl von Ossietzky Str. 9, 26129 Oldenburg, Germany

²Fraunhofer IWES, Ammerländer Heerstr. 136, 26129 Oldenburg, Germany

michael.schwarz@forwind.de

ABSTRACT

In order to reduce the cost of energy for wind power plants, the prediction of aerodynamic loads needs to be improved. Progress has not to be made exclusively towards higher accuracy, but in fact towards a higher efficiency, meaning the ratio of accuracy versus computational effort.

An established approach are Blade Element Momentum (BEM) calculations. These demand low computational effort and have been applied in industry successfully. BEM simplifies and neglects several physical effects and accounts for these assumptions with correction models. Computational Fluid Dynamics (CFD) is a different approach with a higher demand for computational power. Compared to BEM it relies on less simplifications and takes into account more physical effects.

Different strategies to couple BEM and CFD can be formulated and shall be investigated in the course of this study. The aim is to develop a coupling approach that combines the advantages of both methods in order to enable more accurate aerodynamic analysis at lower computational costs.

INTRODUCTION

Aerodynamics strongly influence the loads acting on a wind turbine and are therefore closely coupled to the cost of energy. Although several years of research have been dedicated to this topic, the correct prediction of aerodynamic performance remains a challenge for engineers and researchers.

Modern wind industry often relies on Blade-Element Momentum (BEM) calculations, which have a long tradition in aerodynamics. This simplified approach towards rotor aerodynamics has been improved by correction models and delivers acceptably accurate force predictions, demanding a low computational effort. On the one hand, the low computational costs are the main advantage of BEM theory. On the other hand, this computational efficiency comes along with several assumptions and simplifications, wherefore important details of rotor aerodynamics like three-dimensional flow effects are not captured.

A method that delivers detailed and high resolution of the entire flow field is constituted by Computational Fluid Dynamics (CFD). Currently though, due to it's high demand for computational power, CFD is not used as a stand-alone approach towards wind turbines. Although CFD simulations are computationally expensive, airfoils can be simulated within an acceptable time frame. A further advantage of CFD is it's flexibility. Generally, any kind of flow field can be investigated. Experimental studies in comparison, are limited to the constraints given by wind tunnels (e.g. maximal Reynolds number or geometry).

It is the main goal of this research project to investigate possibilities to combine the advantages of both BEM and CFD in order to generate a more efficient hybrid approach towards wind turbine aerodynamics.

Some specific coupling approaches discussed in this examination are

- i) CFD generated airfoil polars
- ii) CFD aided extrapolation of airfoil polar data
- iii) inclusion of specific physical phenomena, like the varying angle of attack under non-uniform inflow conditions, into airfoil polar data via CFD.

METHODS

The two approaches of BEM and CFD will shortly be outlined in the following.

BEM – Blade-Element Momentum theory

BEM is a combination of blade element theory and momentum conservation considerations, formulated by Glauert (Ref. [1]). A wind turbine (WT) blade will be regarded as consisting of different sections, so called 'blade elements'. Each of these elements is assumed to have an independent aerodynamic behavior. Based on momentum conservation and a stream tube model, an iterative process can be derived that allows the calculation of aerodynamic forces, acting on each section. The overall rotor torque and thrust are then to be found as integral quantities, by summing up each blade-element's normal, or tangential forces, respectively. Figure 1 (Ref. [2]) shows the lift, drag, normal and tangential force increments acting on a blade element.

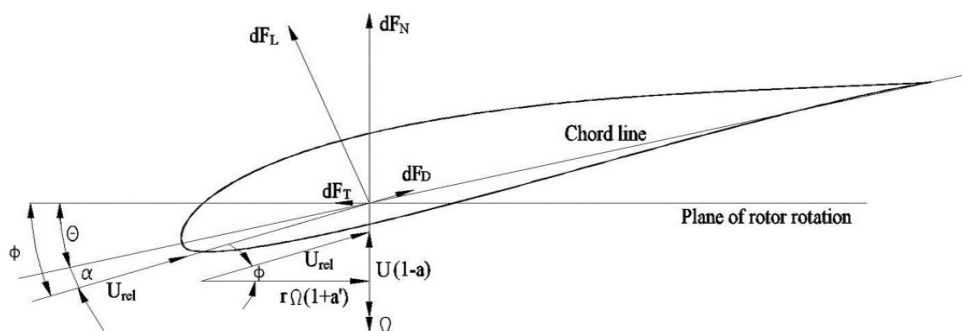


Figure 1: Blade Element, (Ref. [2])

This approach implies severe simplifications, as for instance the radial velocity component of the flow along the blade is assumed to be zero at any time and position. This is in contradiction with observations. In order to account for some of the simplifications, several models based on empirical and analytical considerations have been developed. These address different physical effects like root or tip losses or the effect of stall delay. A modern representative of these models is given by the stall delay model proposed by Bak et al. (Ref. [3]).

CFD - Computational Fluid Dynamics

CFD is a numerical approach to solve equations, governing a fluid's flow, most commonly the Navier-Stokes Equation (NSE). Several methods to approach the NSE exist. Widely used are Reynolds-Averaged Navier-Stokes (RANS) computations. These require so called 'turbulence models' in order

to gain mathematical closure. The modeling of turbulence is a complex challenge. Several models have been formulated, none of them being able to address a wide range of flow problems with constantly good results. For airfoil simulations with Reynolds numbers around 10^6 , the Shear Stress Transport (SST) model proposed by Menter (Ref. [5]) delivers good results in the pre-stall regime, while the prediction of flow fields around airfoils in stall condition still remains a challenge. This is not only the case for this particular turbulence model, but for RANS in general, if the separation point is unknown a priori, as it is in most design processes.

Another numerical approach towards the NSE is given by Large Eddy Simulations (LES). LES approaches turbulence with less modeling, wherefore it's ability to predict turbulent flows correctly is significantly better compared to RANS. Unfortunately, the better performing LES approach implies a significantly higher demand for computational power. Detached Eddy Simulations (DES), a compromise between RANS and LES, will be investigated within this project regarding it's suitability as a general approach towards airfoil simulations.

The advantages of CFD are it's flexibility and resolution of the entire flow field. Figure 2 exemplarily shows the resolution of the relative pressure field in Pa around a DU91-W2-250 airfoil at an angle of attack (AOA) of six degrees at a Reynolds number of 10^6 .

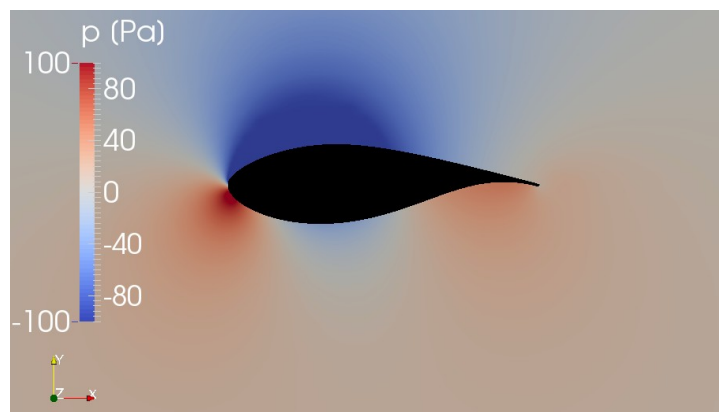


Figure 2: Pressure field around airfoil with CFD

COUPLING APPROACH

In general, different ways to couple BEM and CFD can be formulated. A straightforward, but synergetic method is to generate airfoil polar data within a CFD framework and use these as a basis for BEM calculations. The obvious advantage is that no costly and time consuming experimental studies need to be conducted, in case the CFD ansatz is validated. Nowadays, one is able to produce airfoil polar data within one or two days on a modern personal computer, depending on the approach.

Often potential flow based tools, e.g. XFOIL (Ref. [6]), are used to generate airfoil polar data. Potential flow neglects vorticity and is therefore unable to predict wakes and wall bounded flows at higher Reynolds numbers. Conclusively, CFD is more accurate than these methods.

Another advantage of this approach is the possibility to circumvent polar extrapolation methods. Since AOA around 90° can occur within BEM calculations (for instance when a stand-still design load case is considered), often polar data is extrapolated to 360° by assumptions based on flat plate considerations. A well known method has been proposed by Viterna and Corrigan (Ref. [7]). Due to problems related to blockage, wind tunnel investigations usually do not include AOA this high. CFD is generally able to calculate these

high angles and compared to extrapolations, offers a more accurate prediction of the aerodynamic performance. In the course of this study, established extrapolation techniques will be investigated. Furthermore, CFD generated polars allow to implement other flow problems into the polar data. WTs often face non-uniform flow velocity fields, as for instance in yawed condition or when facing sheared wind fields. Non-uniform inflow leads to a varying AOA, which again can lead to dynamic stall. This kind of flow can be simulated with a CFD airfoil simulation and for instance be communicated towards the BEM code in form of time averaged lift and drag coefficients. Similarly, turbulent inflow conditions can be used for airfoil simulations. The turbulent flow will lead to an aerodynamic behavior, different from the performance at steady, uniform inflow.

An alternative way to couple CFD and BEM is to analyze parts of wind turbine blades within a full CFD approach, while the remaining parts of the blade are calculated in a BEM framework. Typically, the root and tip region are envired by complex flow fields, wherefore it is more challenging to calculate the aerodynamic performance of these regions accurately. Approaching these regions with CFD, while calculating the remaining part of the blade in a BEM framework should in theory be more accurate than a pure BEM calculation, while still being computationally less demanding than full rotor CFD simulations. On the other hand, this method is in danger of decomposing the flow field and separating physical correlations. Additionally, BEM models and CFD investigations have to be consistent. For example, physical effects resolved by CFD must not be accounted for by BEM models within the same calculation, as this would mean to account for one effect twice.

OUTLOOK

Currently, the framework for CFD polar generation is in development. An automated process has been designed and is now in the testing phase. The simulation of airfoils operating in stall condition, still remains a key challenge. Different turbulence modeling approaches will be carried out in order to find the optimal setup. As a future step the connection to the BEM code will be established. Additionally, hybrid BEM/CFD techniques for challenging WT operation modes as in yawed condition, will be developed. A concept how to account for the effects in yawed condition is in discussion.

REFERENCES

- [1] H. Glauert, "The Elements of Aerofoil and Airscrew Theory", Cambridge University Press, 1926
- [2] Q. Song et al., "Design and Testing of a New Small Wind Turbine Blade", J. Sol. Energy Eng., 2014
- [3] C. Bak et al., "Three-dimensional corrections of airfoil characteristics based on pressure distributions", Proceedings of the EWEC, 2006
- [4] OpenFOAM project webpage: <http://www.openfoam.com>
- [5] F. Menter, "Two-equation eddy-viscosity turbulence models for engineering applications", AIAA Journal Vol 32, 1994
- [6] XFOIL webpage: <http://web.mit.edu/drela/Public/web/xfoil/>
- [7] L. Viterna et al., "Fixed pitch rotor performance of large horizontal axis wind turbines", NASA, Lewis Research Center , 1982

UNSTEADY AERODYNAMICS OF AIRFOILS FOR SMALL HAWT AT LOW REYNOLDS NUMBERS

D. Holst¹, G. Pechlivanoglou², C. N. Nayeri¹, C. O. Paschereit¹

¹TU Berlin, Institute of Fluid Mechanics and Technical Acoustics, David.Holst@TU-Berlin.de

²SmartBlade GmbH

ABSTRACT

Small wind turbines are often built up in aerodynamic unfavorable areas, e.g. next to obstacles. This results in complex wind conditions with lower wind speeds and high turbulence. The flow conditions are less predictable, i.e. considering a daily basis, they are more variable and intermittent [1]. Furthermore, there are design constraints to small wind turbines, like a simple structure, a compact design and portability [2]. The knowledge of the aerodynamic performance at low wind speeds is crucial to a proper estimation of the energy yield and thus the economic justification of the entire turbine [1]. Other studies have shown that for instance improving the starting performance can increase the annual energy yield by up to 40% [3].

The project this work belongs to concentrates on understanding the unsteady behaviour of airfoils for small wind turbines at low wind speeds and consists of several parts and experiments. This paper gives a short overview on the challenges of low Reynolds aerodynamics and presents the measurement setup for the dynamic testing. This implies the wind tunnel setup as well as a brief summary of planned measurement techniques. The subsequent parts of the project are finally outlined.

LOW REYNOLDS AERODYNAMICS

Low Reynolds airfoils are investigated in several areas. They are used for small wind turbines as well as unmanned-air-vehicles, micro-air-vehicles or bird-/insect-flight [4]. The Reynolds number of a small horizontal axis wind turbine (sHAWT) ranges from very low numbers while starting to the order of 100-thousands. While starting large turbines benefit from active pitch systems, sHAWT often have fixed pitch. Therefore their blades experience high angles of attack (AoA) near 90° and a higher pitch angle would improve the starting behavior but decreases maximal power [5]. This results in a compromise between fast startup, therefore better low wind speed performance, and maximal power, but longer idling periods. The tip area is optimized for power output and the root area for starting torque [2] and structural strength, e.g. using blunt trailing edges [6].

The airfoil's laminar boundary layer often separates before turbulent transition. In this case the transition happens within the free shear layer and the separated turbulent shear layer often reattaches forming a laminar separation bubble [7] as shown in figure 1. Such a bubble can affect the performance of an airfoil and therefore sHAWT profiles have to be insensitive to laminar separation bubbles [2]. At very low flow speeds the separated laminar shearlayer stays detached [8], the lift immediately drops and this results in a sharp stall. Stall regulated turbines however depend on a smooth stall behavior. A high lift to drag ratio is favorable to maximize power output [2] but the risk of flow separation increases if the adverse pressure gradient on the suction side grows [6]. The lift to drag ratio depends on the Reynolds number as figure 2 depicts. The graph is based on a XFOIL simulation of a low Reynolds profile.

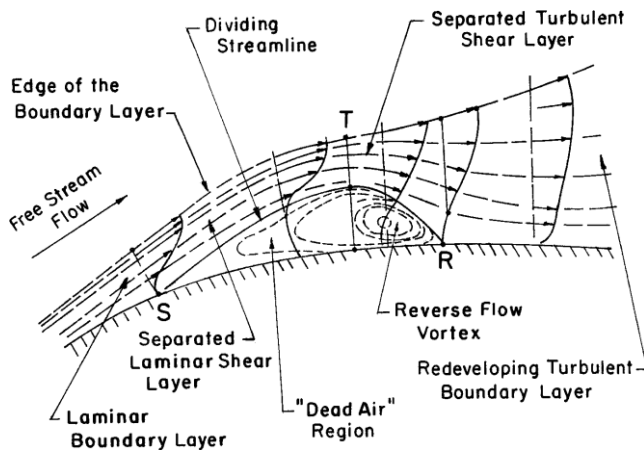


Figure 1: Laminar separation bubble [7]

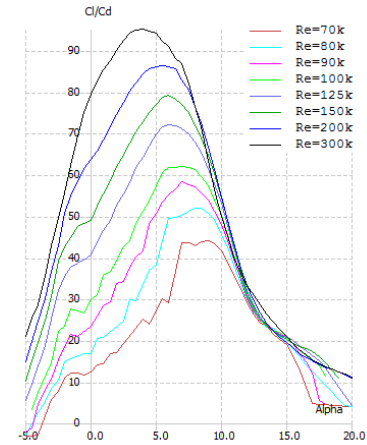


Figure 2: C_l/C_d – Re dependency

The wind characteristics in front of a sHAWT are often hard to know because they are often located in urban areas or next to obstacles, e.g. houses. The inflow is therefore high turbulent, intermittent and more variable than the inflow of large turbines. Figure 3 shows a time series of a wind velocity measurement at an airport done by Liu [9] without any obstacles next to the setup. Nevertheless velocity fluctuations of $\pm 25\%$ are evident and they imply a variation in Reynolds number as well as a fast change in the AoA. The unsteady wind field leads to unsteady aerodynamic phenomena, e.g. lift overshoot because of dynamic stall or delayed stall because of the higher turbulence. The airfoil can go through all the dynamic stall regimes even if the AoA is below the static stall angle [9].

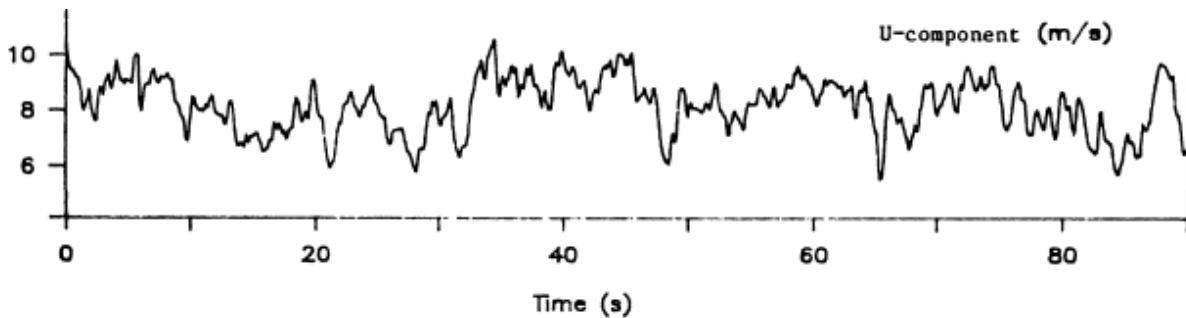
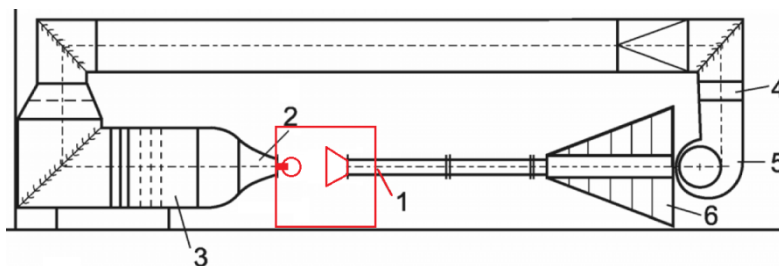


Figure 3: Time series of wind measurements (0.1s averages) at Ellensburg airport (mean: 8.2 m/s) [9]

The International Energy Agency stated in their longterm research and development needs for wind energy [10] that a better understanding of turbulent flows is crucial to a better prediction of wind turbine performance. Especially the prediction of annual energy yield of small wind turbines is difficult because the power curves are often not reliable. A study of Simic et. al. [11] revealed that 15 out of 43 powercurves provided exceed the Betz limit. Several research topics are necessary to improve the performance, proper design tools known from large scale turbines [12], airfoil aerodynamics and flow control in different Reynolds regimes [13, 14, 15]. The project this work belongs to focuses on the investigation of the dynamic effects of sHAWT airfoils.

MEASUREMENT SETUP

The measurements will be conducted in the closed loop laminar wind tunnel of the chair of fluid dynamics at the Institute of Fluid Dynamics and Technical Acoustics (ISTA), TU Berlin as sketched in figure 4. The tunnel was optimized for low turbulence flow to study laminar turbulent transition. Nevertheless, a new open measurement section was built to study airfoils at high angles of attack. Figure 5 shows a CAD of the measurement section which can be sealed and darkened for particle-image-velocimetry (PIV) measurements. The resulting jet has a maximal velocity of $U_{max}=25$ m/s and still a turbulence level of $Tu < 1\%$. A collector is used to reduce the losses within the closed loop setup. The airfoil mounting, magnified in figure 6, is directly attached to the nozzle and includes the support for the servo motor (not shown). The motor is able to handle one command per 20ms and controls the angle of attack. This ensures the possibility of fast changes in angle of attack. We investigate airfoil sections with an aspect ratio of two and a chord of 0.14m. The setup is designed to measure forces and



1. New measurement section
2. Nozzle
3. Settling chamber
4. Cooler
5. Radial fan
6. Silencer

$$U_{max} = 20 \text{ m/s}$$

$$Tu < 1\%$$

Figure 4: Sketch of the wind tunnel

surface pressure within an angle range of 360° synchronous and time resolved up to a rate of 2kHz. The cylinders between the mounting bracket and the splitterplates include the measurement equipment. We can use up to 60 pressure sensors and a two component balance. Hot-wire measurements are used to quantify the velocity fluctuations and PIV yields the field information. We are able to synchronize all hardware and additionally trigger the measurements based on airfoil position in realtime.

The measurement signals are digitized by an 16bit A-D converter using a sampling rate of up to 100kHz. The system control is based on a 80MHz realtime controller manufactured by National Instruments which monitors the system state, controls the angle of attack servo and does the position triggering. Additional A-D converters can be synchronized with the realtime system so that we can synchronously read more than 100 analogue channels.

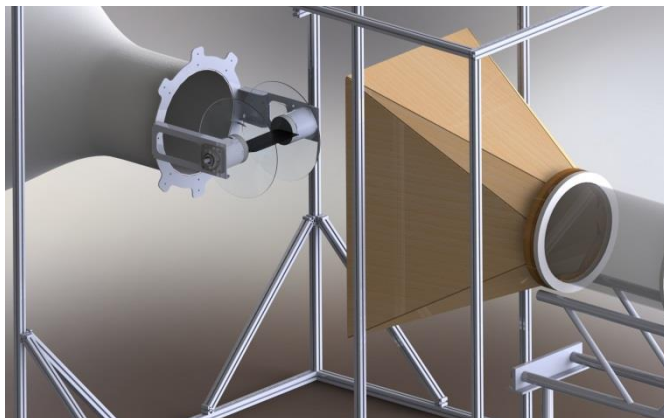


Figure 5: CAD of new open test section

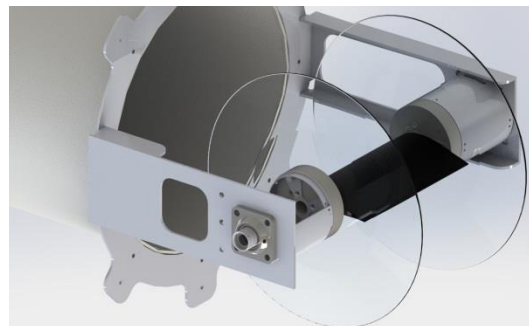


Figure 6: Airfoil mounting

FUTURE PLANS

The static performance of well known low Reynolds profiles will be investigated in the next step to validate the measurement setup against literature. Flow visualizations will be used to validate a good flow around the airfoil and minimize the interaction between airfoil and splitter plates. Afterwards we will investigate the airfoil's dynamic behavior at low wind speeds, like dynamic stall, the influence of turbulence, or the possibilities to control the airfoil performance.

We will finally compare the results of 2D airfoil measurements against measurements of the institute's research turbine. The turbine has a rotor diameter of 3m and was funded by the German Science Foundation (DFG) within the research project *Experimental assessment of active flow control techniques for wind turbines with a wind tunnel demonstrator*. The results are used to validate the transferability of 2D measurements into a rotating system.

REFERENCES

- [1] A. Peacock, D. Jenkins, M. Ahadzi, A. Berry and S. Turan, "Micro wind turbines in the UK domestic sector," *Energy and Buildings*, vol. 40, no. 7, pp. 1324-1333, 2008.
- [2] R. K. Singh and M. R. Ahmed, "Blade design and performance testing of a small wind turbine rotor for low wind speed applications," *Renewable Energy*, vol. 50, no. 50, pp. 812-819, 2013.
- [3] S. Worasinchai, G. L. Ingram and R. G. Dominy, "Effects of Wind Turbine Starting Capability on Energy Yield," *Journal of Engineering for Gas Turbines and Power*, vol. 134, no. 4, pp. 42603-42603, 2012.
- [4] Y. Zhou, M. Mahbub Alam, H. X. Yang, H. Guo and D. H. Wood, "Fluid forces on a very low Reynolds number airfoil and their prediction," *International Journal of Heat and Fluid Flow*, vol. 32, no. 1, pp. 329-339, 2011.
- [5] C. Mayer, M. E. Bechly, M. Hampsey and D. H. .. Wood, "The starting behaviour of a small horizontal-axis wind turbine," *Renewable Energy*, vol. 22, no. 22, pp. 411-417, 2001.
- [6] R. K. Singh, M. R. Ahmed, M. A. Zullah and Y.-H. Lee, "Design of a low Reynolds number airfoil for small horizontal axis wind turbines," *Renewable Energy*, vol. 42, no. 42, pp. 66-76, 2012.
- [7] H. P. Horton, "Laminar Separation Bubbles in Two and Three Dimensional Incompressible Flow," 1968.
- [8] T. J. Mueller and J. D. DeLaurier, "Aerodynamics of Small Vehicles," *Annual Review of Fluid Mechanics*, vol. 35, pp. 89-111, 2003.
- [9] H.-T. Liu, "Unsteady Aerodynamics of a Wortmann FX-63-137 Wing in a Fluctuating Wind Field," 1987.
- [10] IEA Wind, "Long-Term Research and Development Needs for Wind Energy for the Time Frame 2012 to 2030," 2013.
- [11] Z. Simic, J. G. Havelka and M. B. Vrhovcak, "Small wind turbines - A unique segment of the wind power market," *Renewable Energy*, vol. 50, no. 50, pp. 1027-1036, 2013.
- [12] G. Pechlivanoglou, G. Weinzierl, I. T. Masmanidis, C. N. Nayeri, T. P. Philippidis and C. O. Paschereit, "Utilization of Modern Large Scale HAWT Blade Design Techniques for the Development of Small HAWT Blades," in *Proceedings of the ASME Turbo Expo 2014, June 16-20, Düsseldorf, Germany*, 2014.
- [13] O. Eisele, G. Pechlivanoglou, C. N. Nayeri and C. O. Paschereit, "Flow Control Using Plasma Actuators at the Root Region of Wind Turbine Blades," in *Proceedings of DEWEK 2010, 17-18 November 2010, Bremen, Germany*, 2010.
- [14] O. Eisele, G. Pechlivanoglou, C. N. Nayeri and C. O. Paschereit, "Experimental Investigation of Dynamic Load Control Strategies using Active Microflaps on Wind Turbine Blades," in *EWEA 2011 (European Wind Energy Association), Brussels, Belgium, 14-17 March*, 2011.
- [15] D. Holst, A. B. Bach, C. N. Nayeri and C. O. Paschereit, "Influence of a Finite Width Micro-Tab on the Spanwise Lift Distribution," in *Proceedings of the ASME Turbo Expo 2013, June 3-7, San Antonio, Texas, USA*, 2013.

CFD Coupled with WRF for Wind Power Prediction

E. Leblebici^{1,2}, G. Ahmet^{1,2}, I.H Tuncer^{1,2}

¹METU, Aerospace Engineering Department

²METU Center of Wind Energy

enginl@ae.metu.edu.tr

gahmet@ae.metu.edu.tr

tuncer@ae.metu.edu.tr

ABSTRACT

The objective of the current study is to predict the daily wind power production estimation for a region of interest accurately. To do so, 3D unsteady Navier-Stokes solutions coupled with a mesoscale weather prediction model (WRF) are to be utilized using the open source CFD software OPENFOAM. Unstructured grids are used to discretize the complex terrain of interest. High resolution (1.5 arcsec) ASTER GDEM topographical data is used to create terrain following grids in order to capture the viscous effects which dominates the flow characteristics at the surface layer of the atmosphere where majority of the wind turbines reside. WRF solutions can be obtained using the real time weather prediction data ECMWF provides for a region of interest. Spatially and time varying boundary conditions are to be interpolated both in time and space from the WRF solutions and updated for each cell. In previous study, this procedure was done using FLUENT as a Navier-Stokes solver but higher grid resolutions could not be performed due to the fact that Fluent cannot be run in the parallel mode in the presence of a UDF that implements the time dependent boundary conditions from a table of data, and serial computations with the total number of cells exceeding 10^7 become prohibitively resource demanding. As OPENFOAM is an open source software, it is thought that this problem could be overcome. In this study, steady and laminar OPENFOAM solutions are done using spatially varying boundary conditions and are compared with WRF and FLUENT.

INTRODUCTION

Accurate predictions of unsteady rural and urban atmospheric flow fields have a wide range of usage such as micro-site selection for wind farms and pollution tracking, each of which are of current research topics with several examples in literature. [1,2] As wind farms consisting of a large number of wind turbines have a high initial investment cost, wind farm siting must be given a significant importance. [3,4] Low resolution wind energy potential atlases have the necessary statistical information for macro-siting of wind farms but lack the precision for the micro-siting. Therefore; high resolution, more accurate wind field information may be needed for micro-siting in order to improve the power output of a wind-farm.

Bowen(2004)[5] in a Risø-R Report states that Botta et al (1992)[6], Bowen and Saba (1995)[7], Reid (1995)[8] and Sempreviva et al (1986)[9] experiences in the operation of commercial wind farms (Lindley et al., 1993[10]) have confirmed that effects from the local complex terrain on the site characteristics of each turbine have a significant influence on the output (and perhaps even the viability) of a wind energy project. F.J.Zajackowski et.al.[11] compares Numerical Weather Prediction Models (NWP) and Computational Fluid Dynamics (CFD) simulations. They conclude that NWP can take radiation, moist convection physics, land surface parameterization, atmospheric boundary layer physics closures, and other physics into account, but wind flow features finer than 1 km are not

captured by the turbulence physics of such models. CFD simulations, however, have proved to be useful at capturing the details of smaller scales due to a finer scale topography, and details around urban features such as high-rise buildings.

WRF is a fully compressible, Eulerian, η -coordinate based, nest-able, non-hydrostatic, numerical weather prediction model with a large suite of options for numerical schemes and parameterization of physical processes[12].

Mostly used wind assessment tools use linearized models. Although these models are very powerful for smooth terrains, CFD based tools are needed for the complex terrains such as wind energy plant projects in Turkey. Therefore CFD based wind assessment tools (like WindSim, Meteodyne, WAsP-CFD) are getting more and more popular all over the world. On the other hand most of CFD software use fictitious flowfields. These flow fields are created just by using different uniform velocity inlet pressure outlet boundary conditions as seen in Figure 1. Starting from the zero degree, this software rotates uniform inlet and outlet boundary conditions till 360 degrees. For each case, boundary conditions are defined as follows. Each sector means a different simulation. Using these fictitious flowfields they correlate whole domain with the observation data. Therefore, observation is a must. For the projects which cannot provide observation data, meteorological data serie, so called virtual met-mast data, can be used in these commercial software as observation data.

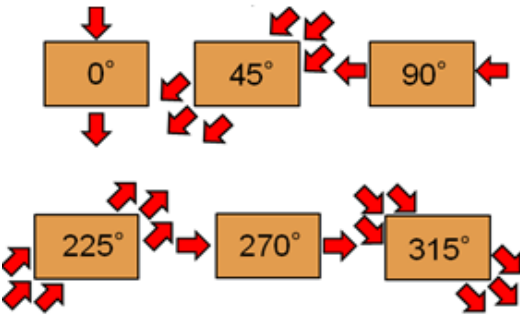


Figure 1: Linearized models BCs

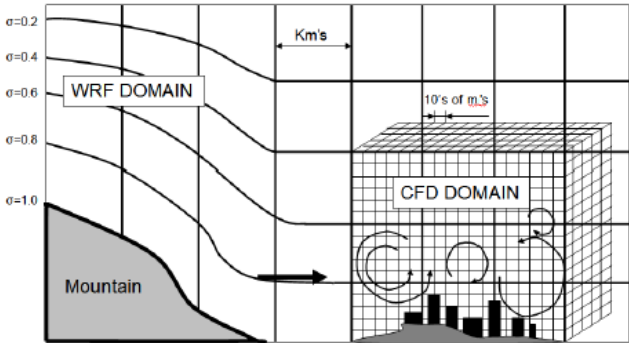


Figure 2: Coupling WRF and OPENFOAM

The main objective of this study is to obtain atmospheric flow solutions using OPENFOAM coupled with WRF. A high resolution topographical modeling along with turbulence models OPENFOAM provides, might make the solution more accurate in the vicinity of the ground level. Moreover, using the WRF weather prediction data as unsteady and spattially varying BCs for the CFD solution may prove to be one of the most realistic representation for the atmospheric flowfield.

Unlike other methodologies, in this study, observation data is not a must. Spatially varying boundary conditions taken from WRF can be defined in the CFD code, not only on one point like commercial tools but on whole of CFD domain boundaries.

In previous study [13] , the complete (unsteady, turbulent) procedure was done using FLUENT as a Navier-Stokes solver but higher grid resolutions could not be performed due to the fact that Fluent cannot be run in the parallel mode in the presence of a UDF that implements the spatially varying time dependent boundary conditions.

METHOD

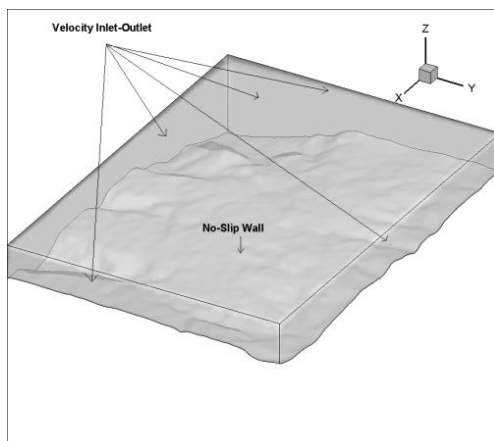
In this study, a coupled flow solution methodology with an atmospheric weather forecast software, WRF, and OPENFOAM, an open source Navier-Stokes solver, is developed. WRF produces a low

resolution, unsteady atmospheric weather forecast data, which provides the unsteady and spatially varying boundary conditions for the flow solutions obtained with OPENFOAM on terrain fitted, high resolution unstructured grids.

Unsteady WRF solutions are first obtained over the geographical domain of interest. The local terrain data is downloaded automatically from UCAR (University Corporation of Atmospheric Research) server via WRF. The time dependent initial and boundary conditions for the WRF solution are obtained from ECMWF (European Centre of Medium Range Weather Forecast). The unsteady boundary conditions needed for the OPENFOAM solution at its domain boundaries, which fall into the larger scale WRF domain, are then extracted from the WRF solution at 5 minute time intervals.

In computational grids for CFD solutions, the high resolution terrain topography is generated using the data obtained from ASTER GDEM, which is a product of METI and NASA, worldwide elevation at 1.5 arc-sec resolution which is approximately 30 meters. The vertical and horizontal grid resolution on the ground for the terrain fitted unstructured grids is about 25 meters. These grids also resolve the atmospheric boundary layers and stretch up to about 2200 meter altitude.

As for boundary conditions, region of interest is modelled as seen in Figure 3. Side and top surfaces are modeled as spatially varying velocity inlet-outlet whereas the topography is obviously modelled as a no-slip wall. The approach for utilizing the velocity inlet-outlet is to specify the velocity components from WRF solution if the flow is going into the domain. If the flow is going out of the domain, only the pressure is specified at the boundaries from WRF results.



For coupling between WRF and OPENFOAM, high resolution spatially varying boundary conditions for the OPENFOAM are extracted from low resolution WRF results. But in order to do so, first WRF coordinate system (latitude-longitude) (degrees) should be converted to UTM (northing-easting) (meters). Also, correct interpolation of WRF results for the face centers in OPENFOAM boundaries must be handled adequately. WRF results are converted to UTM and interpolated at OPENFOAM boundaries' face centers trilinearly in space.

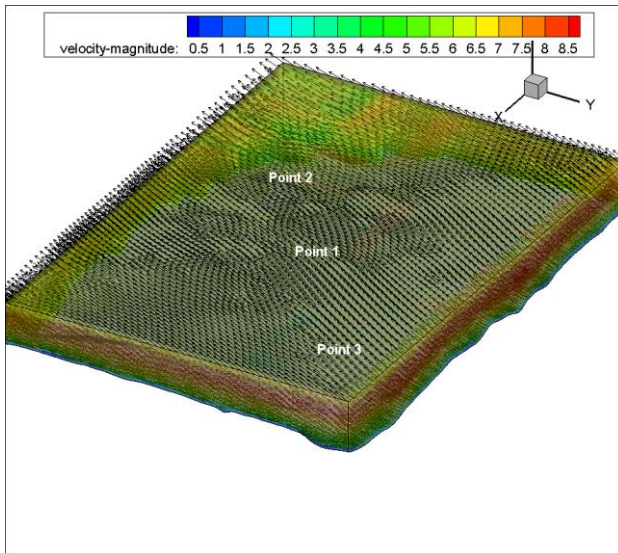
Using these profiles for each face centre at the boundary inlet-outlet type BC for flow velocity components and outlet-inlet type BC for pressure is used collectively.

Figure 3: Boundary Conditions

PRELIMINARY RESULTS

In this study, laminar steady atmospheric flow solutions coupled with WRF and an open source Navier-Stokes solver OPENFOAM are carried out around MUT region in MERSIN/TURKEY on high resolution unstructured grids. The simulation was done for 04.04.2010 at 00:00 GMT0. The objective of this preliminary study is to verify which approach for the BCs is more accurate with respect to WRF results.

In order to assess and understand which method is better with respect to WRF results, vector graph for the flowfield is given along with 3 control points on which the velocity profiles will be compared for FLUENT, OPENFOAM and WRF in Figure 5.



The choice of these 3 control points are made in order to observe the flow characteristics when flow is going into the domain (Point3), out of the domain (Point 2) and in the middle of the domain (Point 1) where the effects of spatially varying BCs will be smaller. As seen in Figure 5; at Point 1 and 3, velocity magnitude values for FLUENT and OPENFOAM matches WRF on the top of the domain which was expected since at both points, the wind is into the solution domain whereas for Point 2 abrupt differences between all of the FLUENT, WRF and OPENFOAM results are observed. Moreover, OPENFOAM solution for Point 2 doesn't match the top of the domain. The reason for that is the air is flowing out of the domain at the top for Point 2.

Figure 4: Vector Graph and Control Points

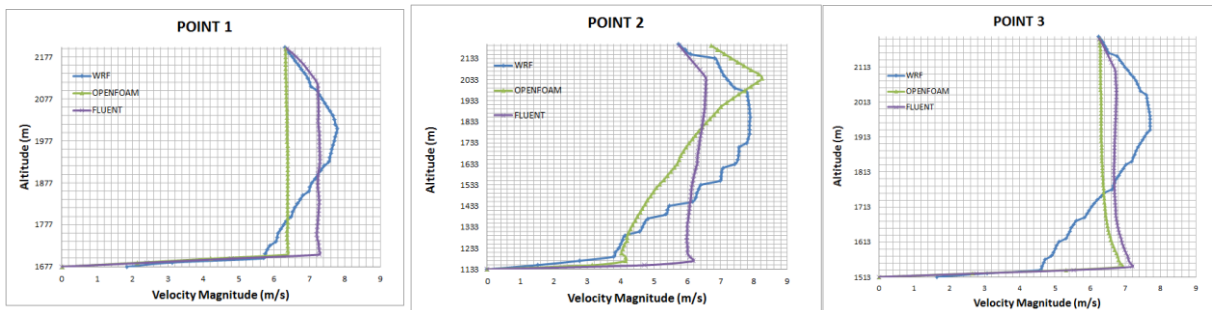


Figure 5: Velocity profiles for WRF, OPENFOAM, FLUENT at Control Points

Also, it is seen that both FLUENT and OPENFOAM failed to capture the variation in the atmospheric boundary layer assuming the WRF results are correct. For Point 1 and 3, FLUENT seems to be more successful for the higher altitude regions whereas for Point 2, OPENFOAM could be considered better in terms of accuracy. It is important to note that velocity inlet type boundary condition for FLUENT forces the value of the velocity whether the flow is into or out of the domain, allowing only changes in the tangential components of the velocity with respect to the face of the boundary. Also, the preliminary simulations are laminar so the results might be inconclusive. Another important drawback of the results presented is that the buoyancy is neglected and the solutions are carried out with incompressible flow assumption. This assumption might be the reason for not capturing the velocity profile of WRF.

FUTUREWORK

The most important addition to this work is making the solutions unsteady. In order to do so, ability to extract boundary condition profiles at specific time intervals is attained. The remaining part is to modify the solver to read two adjacent BC profiles according to the solution time and update each faces' boundary conditions at every time step for which the research is ongoing. Also, as mentioned before all the preliminary results are obtained with laminar flow assumption. So, different turbulence models should be tried out or implemented into OPENFOAM. Moreover, the process should be parallelized in order to reduce the computational time required for prediction. In addition, grid dependence studies and throughout inspection of the results are of significant importance.

REFERENCES

- [1] Cochran, B.C., Damiani, R.R., 2008, "Harvesting Wind Power from Tall Buildings", Wind Power 2008, (Houston, Texas).
- [2] Politis, E.S., Chaviaropoulos, P.K., 2008, "Micrositing and classification of wind turbines in complex terrain", European Wind Energy Conference and Exhibition Brussels, (Belgium).
- [3] Damiani, R., Cochran, B., Orwig, K., Peterka, J., 2008, "Complex Terrain: A Valid Wind Option?", American Wind Energy Association.
- [4] Derickson R.G., Peterka J.A., 2004, "Development of a Powerful Hybrid Tool for Evaluating Wind Power in Complex Terrain: Atmospheric Numerical Models and Wind Tunnels," American Institute of Aeronautics and Astronautics
- [5] Anthony J. Bowen nad Niels G. Mortensen, 2004, "WAsP prediction errors due to site orography," Riso National Laboratory, (Denmark, Roskilde).
- [6] Botta, G., Castagna, R., Borghetti, M. and Mantegna, D., 1992, "Wind analysis on complex terrain - The case of Acqua Spruzza," Jour. Wind Eng. Ind. Aerodyn. 39 pp 357-66.
- [7] Bowen, A.J. and Saba, T., 1995, "The evaluation of software for wind turbine siting in hilly terrain," 9th International Conference on Wind Engineering, (India)
- [8] Reid, S.J., 1995, "Modelling of channelled winds", BWEA Conference, (Warwick, UK), pp 391-6
- [9] Sempreviva, A.M., Troen, I. and Lavagnini, A., 1986, "Modelling of wind power potential in Sardinia", European Wind Energy Association Conference and Exhibition, (Rome Italy).
- [10] Lindley, D., Musgrove, P., Warren, J. and Hoskin, R., 1993, "Operating experience from four UK wind farms", 15th BWEA Annual Wind Energy Conference, (York, UK), p 41-45.
- [11] Frank J.Zajaczkowski, SueEllenHaupt, KerrieJ.Schmehl, 2011, A preliminary study of assimilating numerical weather prediction data into computational fluid dynamics models for wind prediction, Journal of Wind Engineering and Industrial Aerodynamics 99 pp 320-329.
- [12] William C. Skamarock, Joseph B. Klemp, Jimy Dudhia, David O. Gill, Dale M. Barker, Michael G. Duda, Xiang-Yu Huang, Wei Wang, Jordan G. Powers, 2008, "A Description of the Advanced Research WRF Version 3", National Center for Atmospheric Research, (Boulder, Colorado, USA)
- [13] E. Leblebici, G. Ahmet and .H. Tuncer, 2013, Atmospheric Turbulent Flow Solutions Coupled with a Mesoscale Weather Prediction Model, Eccomas special Interest Conference, 3rd South-East European Conference on Computational Mechanics, (Kos Island Greece)

AERODYNAMIC MODELLING FOR EQUAL FIDELITY AEROELASTIC ANALYSIS

T. Hegberg^{*}, R. De Breuker, G. van Bussel

Delft University of Technology, Section Aerospace Structures and Computational Mechanics and Section Wind Energy
Delft, The Netherlands

^{*}e-mail: t.hegberg@tudelft.nl

ABSTRACT

Fast analysis of composite blade aeroelastic loading could be achieved with low fidelity aeroelastic models that use sophisticated nonlinear beam elements for the blade structural analysis. For the equal fidelity aeroelastic model the aerodynamic model should consist of a limited amount of aerodynamic panels in spanwise and chordwise direction. Since wind turbines operate in unsteady conditions it is of great importance that unsteady aerodynamic models are used for the blade. The unsteady aerodynamic model is linearised around a geometrically nonlinear steady aeroelastic equilibrium solution, which means that large blade deformations are taken into account [1]. To be able to represent the blade by a limited amount of aerodynamic panels in the unsteady case as well, as a start Weissinger's method [2] is used together with the adaptations proposed by van Holten [3] for the steady aerodynamic model.

For the steady case it appeared that the higher-order lifting-line theory up to the first order of the reciprocal of the aspect ratio, is similar to a numerical method according to Weissinger valid for straight, yawed and curved elliptical wings [4]. For the verification of the numerical results, the analytical results from the curved lifting line theory [4] and [5] were used. For the wind turbine blade, the wake is modelled as a prescribed, cylindrical wake and circulation distributions along blade span. The normal and tangential force distributions are calculated as a function of the blade spanwise coordinate. The 3D blade circulation distribution and blade loadings are satisfactory compared with 2D results.

The numerical unsteady aerodynamic model calculates unsteady blade loads using an aerodynamic mesh in spanwise and chordwise direction of the blade. The wake is assumed to be

cylindrical and has a mesh distribution based on the step in azimuth divided by the angular rate of the rotor blade. The idea is to minimize the number of chordwise elements in order to approximate the lifting line case to reduce calculation time. The unsteady results are compared to the dynamic inflow model from the blade element momentum theory to verify whether a single bound vortex is sufficient for verification.

INTRODUCTION

For fast aeroelastic analysis and equal fidelity modeling of wind turbine blades the aerodynamic model considered consists of a limited number of aerodynamic panels in spanwise and, for the unsteady case, in chordwise direction across the blade. First, the steady aerodynamic model is considered. For this model, the blade is represented as a single lifting vortex. Numerically this is done by using Weissinger's method together with the adaptations proposed by van Holten [3]. It is investigated whether Weissinger's method gives similar results as higher order lifting line theory. If so, it is allowed to use Weissinger's method as numerical method for the steady aerodynamic case. The results from Weissinger's method will be compared with the lifting line results generated by Guermond [4]. For the unsteady it is questionable whether to use Weissinger's method since the unsteady wake should be modeled using multiple aerodynamic wake panels. For that part, a panel code is used for the unsteady aerodynamics in which the equations are linearised around a steady, nonlinear aeroelastic equilibrium case. Furthermore, it is necessary to use a limited number of aerodynamic panels in chordwise direction on the wind turbine blade, in line with the development of the wake. The dynamic inflow approach is used as a verifica-

tion of the unsteady panel code results.

STEADY AERODYNAMIC MODELLING

For the steady aerodynamic model Weissinger’s method has been used. Theoretically, this method looks like the matching of two velocity fields: the far field is represented by the velocity field generated by the lifting vortex and the near field is built by imposing the flow tangency condition at the three-quarter chord position for the local two dimensional situation. The matching of both velocity fields is inherently included within the numerical solution procedure which is nothing more than solving a system of linear equations. The results are checked using the generalized lifting line theory that is also valid for yawed, swept, and curved wings as described in reference [4]. The blade types used for the verification of the results are indicated in figure 1:

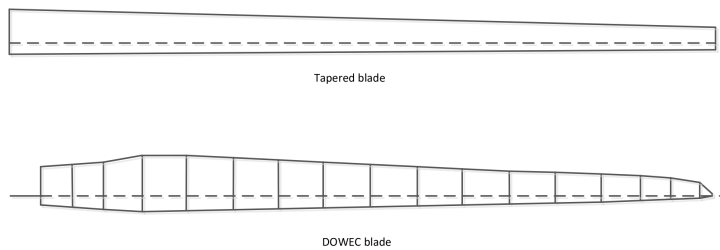


FIGURE 1. Blade shapes used

The circulation distribution for the DOWEC blade is shown in figure 2. The circulation distributions follow the planform of the blade as should be expected.

For the normal and tangential force per blade segment figure 3 shows the result for the DOWEC blade:

From this figure it is clear that the two dimensional results are higher than the three dimensional results, this indicates the correct modelling of the finite blade, furthermore, the shape of the normal and tangential force distributions look satisfactory.

UNSTEADY AERODYNAMIC MODELLING

The unsteady aerodynamic model is a linear panel code casted into a continuous time state space method to solve the equations in the time domain. A linear unsteady case is superposed to a nonlinear static aeroelastic solution. Since the number of aerodynamic panels in the wake is significant higher than the panels on the lifting surface, the chordwise distribution of panels over the bound vortex surface is chosen to be limited. Locally, at the lifting surface, each aerodynamic panel must satisfy the kinematic boundary condition $(\mathbf{V}_{aero} + \mathbf{V}_{struct}) \cdot \mathbf{n}$, where linearisation gives $\mathbf{n} = (\cos \theta_0, 0, -\sin \theta_0) d\theta$, θ_0 is the local blade

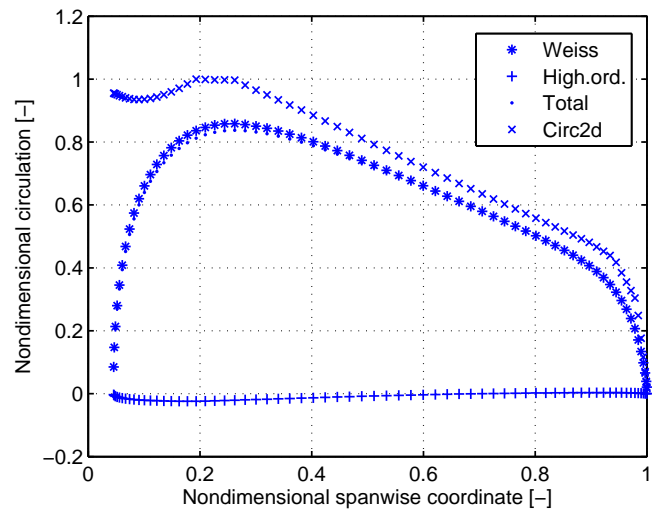


FIGURE 2. Circulation distribution for the DOWEC 63 meter blade, wind velocity 10 m/s

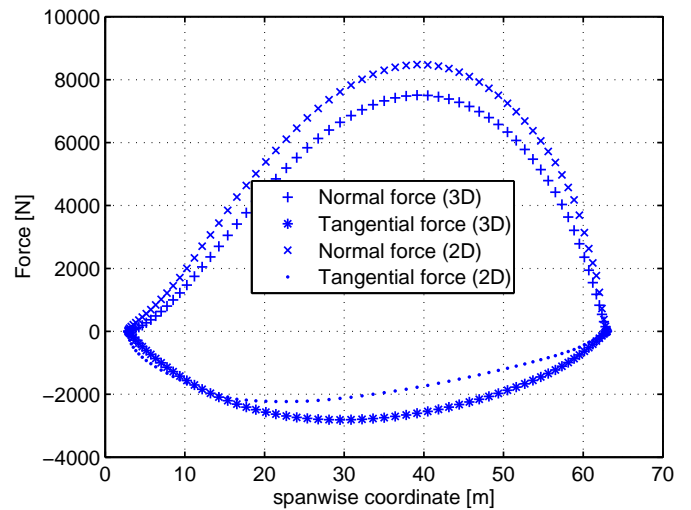


FIGURE 3. Normal and tangential force distribution for the DOWEC 63 meter blade, wind velocity 10 m/s

pitch angle and $d\theta$ is the perturbation twist angle. The aerodynamic velocity vector indicates the inflow velocity for each aerodynamic panel as $\mathbf{V}_{aero} = (\Omega r; 0, V_\infty)$ and the structural velocity vector indicates the velocities due to elastic deformations. The wake behind the wind turbine blade is modelled as a prescribed cylindrical wake, where the expansion is omitted. Furthermore, the Kelvin-Helmholtz theorem is applied, which means that closed vortex rings move with the local air velocity. The Kutta condition must be met at the trailing edge of the blade.

For a correct physical result it is important to include several revolutions in the wake. Leishman [6], suggests that six revolutions should be sufficient to include into the wake development.

RESULTS

For verification of the unsteady results the dynamic inflow approach will be used. Dynamic inflow alters the steady momentum balance into a time dependent momentum equation. It shows that after a disturbance in induction factor a the wake will behave approximately as a first order ODE:

$$a + \tau_w \dot{a} = \begin{cases} a_{\text{BEM}} & \text{for } C_T \leq C_{T,\text{TURB}} \\ a_{\text{TURB}} & \text{for } C_T > C_{T,\text{TURB}} \end{cases} \quad (1)$$

where a is the axial induction factor, τ_w the time constant for induction recovery, C_T the thrust coefficient according to momentum theory and the subscript TURB indicates the turbulent wake. Realising that the dynamic behaviour of the induction factor will be similar to that of the aerodynamic loads, the possibility exists to compare the unsteady aerodynamics from the panel code to that of the dynamic inflow model. Dynamic inflow modeling in blade element momentum codes is important especially at rapid blade pitch changes, vortex codes implicitly show such dynamic behaviour.

Holierhoek [7] suggests a choice of $\tau_w = 4 \frac{R}{U_\infty}$ where R is the blade radius and U_∞ is the undisturbed wind velocity. For the turbine blade used the time constant becomes, for normal operation, $\tau_w = 25.2$ seconds. For lower wind speeds the time constant increases which indicated a slower reaction of the wake; for high wind velocities the wake responds quicker. This should all be visible in the panel code results.

The unsteady loads are caused by a rigid collective change in angle of attack, equal for each blade element. This can be interpreted as a blade collective pitch input. Since the input for the state space system is still the first derivative of the angle of attack [8], the pitch change alters the angle of attack at an arbitrary blade element as $\alpha = \phi - \theta$, in which α is the local angle of attack of the blade segment, ϕ indicates the inflow angle and θ represents the blade pitch angle. From this it becomes clear that a collective pitch change still causes a distribution in angle of attack change across the blade.

Figures 4 and 5 show the results of the panel code for a single blade. The dynamic behaviour seems to be dependent on the spanwise coordinate. Near the blade root, figure:unsteady2, the recovery looks like first order behaviour, but a peak appears when moving in the direction of the blade tip, figure:unsteady3. The settling time for the unsteady aerodynamic load of the panel code is about 25 seconds, that is equal to the ratio $4 \frac{R}{U_\infty}$. However, in reference [7] it is stated that this recovery

time should be four times as large, of course defined for a three-bladed rotor. In the panel code a single-bladed rotor is analysed, which explains the difference. It is expected that a multi-bladed rotor generates better results for the time constant because the wake is more dense as can be concluded for one-bladed wakes for very low wind velocities: the vortex sheets are closer to each other, which results in an increase in time for the wake to recover.

Furthermore, figures 4 and 5 show the numerical behaviour of the change of angle of attack within a infinitesimal time interval, which is explained in Katz and Plotkin [9]: the discrete time step causes the difference between the analytical and the numerical model. However there is a difference between the time constants, it is still a fact that the panel code shows slow adjustment of the unsteady aerodynamic load. Considering the behaviour of the code it could be said that the unsteady aerodynamics is modelled adequately for attached flow conditions.

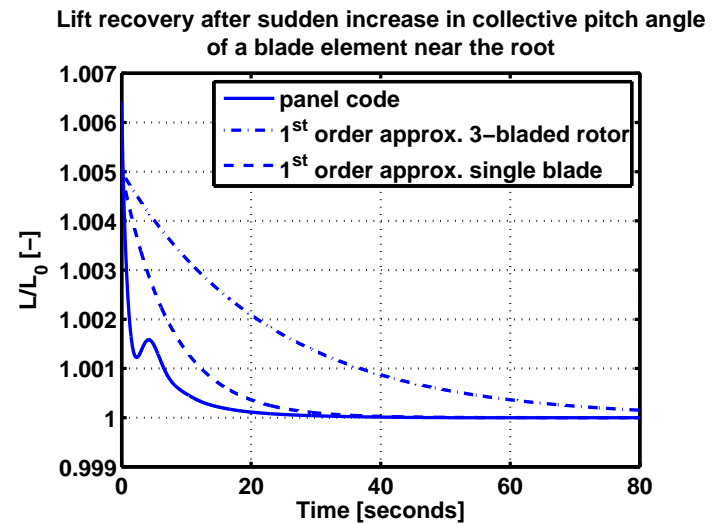


FIGURE 4. Development of aerodynamic load on a wind turbine blade root section after a sudden increase in collective pitch angle

The number of chordwise panels is varied to verify whether it has a significant influence on the unsteady aerodynamics results. It was found that there is no significant influence on the recovery time of the aerodynamic loads. This can be explained as follows: the wake contains multiple aerodynamic panels that have a significant influence on the blade loading in comparison with the bound vortex panel distribution in chordwise direction.

CONCLUSIONS AND FUTURE WORK

During this work, an unsteady aerodynamic panel code was developed for a single wind turbine blade. It was verified already

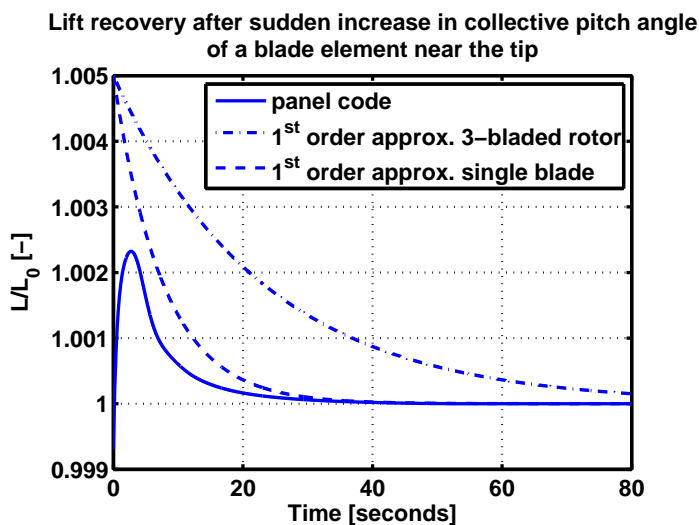


FIGURE 5. Development of aerodynamic load on a wind turbine blade tip section after a sudden increase in collective pitch angle

that the steady aerodynamic behaviour is acceptable. The unsteady model has been subjected to a step on the collective pitch of the blade and it was concluded that the recovery time towards a steady aerodynamic load was approximately a factor of 3 à 4 too high. This can be explained by realising that a one-bladed wake was generated. For a two-bladed or three-bladed rotor the vortex sheets are closer to each other which means that the blade loads need more time to recover. This behaviour shows that such unsteady behaviour is implicitly present in vortex models, which is a significant advantage. From this all, it is clear the unsteady model performs satisfactory.

In the near future a frequency analysis will be done as well. This analysis assumes a harmonic gust and should give results that are similar to Sears' problem [6]. A study will be done on the number of panels in chordwise direction and the influence of the frequency response. If the sensitivity of chordwise panels and Sears' function is negligible, the chordwise number of panels can be minimised which is a great advantage for calculation effort.

Furthermore, a possibility for a free wake solution will be studied, because the structure of the panel code is such that the aerodynamic calculations are very efficient; this could also allow some iterative inclusion of dynamic stall behaviour of the blade.

REFERENCES

[1] Hegberg, T., De Breuker, R., and van Bussel, G., 2013. "Nonlinear static aeroelastic design case studies of large offshore wind turbine blades". In Premier EWEA Wind Energy Event 4-8 February 2013.

[2] Weissinger, J., 1947. The lift distribution of swept-back wings. Tech. Rep. NACA-TM-1120.

[3] van Holten, T., 1976. "Some notes on unsteady lifting-line theory". *Journal of Fluid Mechanics*, **77**, pp. 561–579.

[4] Guermond, J.-L., 1990. "A generalized lifting-line theory for curved and swept wings". *Journal of Fluid Mechanics*, **211**, pp. 497–513.

[5] Hegberg, T., De Breuker, R., and van Bussel, G., 2013. "Higher order lifting line theory for equal fidelity aeroelastic analysis of wind turbine blades". In 9th PhD Seminar on Wind Energy in Europe 18-20 September 2013.

[6] Leishman, J. G., 2002. "Challenges in modelling the unsteady aerodynamics of wind turbines". *Wind Energy*, **5**, pp. 85–132.

[7] Holierhoek, J., 2008. *Aeroelasticity of Large Wind Turbines*. Ipskams Drukkers.

[8] Mohammadi-Amin, M., Ghadiri, B., Abdalla, M. M., Haddadpour, H., and De Breuker, R., 2012. "Continuous-time state-space unsteady aerodynamic modeling based on boundary element method". *Engineering Analysis with Boundary Elements*, **36**, pp. 789–798.

[9] Katz, J., and Plotkin, A., 2001. *Low-Speed Aerodynamics*, second ed. Cambridge University Press.

AERODYNAMIC DAMPING OF WIND TURBINES UNDER CONSTANT AND TURBULENT WIND

S. Schafhirt, M. Muskulus

Norwegian University of Science and Technology (NTNU),
Department of Civil and Transport Engineering, 7491 Trondheim,
sebastian.schafhirt@ntnu.no, michael.muskulus@ntnu.no

ABSTRACT

Aerodynamic damping is a crucial factor in the analysis of offshore wind turbines, especially for the fatigue assessment. Several methods have been proposed in previous studies to determine the aerodynamic damping ratio and showed good agreement for constant wind speeds below rated. In this paper the damping behaviour of an offshore wind turbine with jacket support structure is analyzed in nonlinear time-domain simulations in order to determine an aerodynamic damping ratio under constant and turbulent wind. Results show that the aerodynamic damping ratio is highly underestimated by previous approaches.

INTRODUCTION

Offshore wind turbines (OWT) are highly dynamic and tightly coupled systems and subject to nonlinear effects from aerodynamic and hydrodynamic loading. A simulation in time-domain is, therefore, required to obtain reliable and accurate results [1]. However, time-domain simulations are computationally demanding and time-consuming, especially for OWT with multi-member support structures such as tripods and jackets. A reduction in time and effort to obtain accurate results would be welcome and will be crucial for the future success of OWT with complex support structures.

A calculation in frequency-domain or the speed up of time-domain simulations by replacing the aerodynamic calculation by a simplified, computationally more efficient method are possible ways to reach this goal. The latter can be achieved by decoupling the rotor dynamics. In this decoupled model the rotor-nacelle-assembly (RNA) is entirely removed and aerodynamic loads are included by precalculated time-dependent forces and moments at tower top. Besides the reduction in simulation time, the possibility to use general FEM-software is an additional benefit of this method. However, the decoupling of the rotor does not capture the dynamic interactions between the RNA and support structure. The most important dynamic interaction is the aerodynamic damping [2]. Studies have been performed where a linear damper was introduced to account for the aerodynamic damping and it has been shown that this method gives reasonable results for wind speeds below its rated value [3].

Van der Tempel and de Vries [4] described a frequency-domain approach for the load calculation of OWT and highlight the importance of the aerodynamic damping, especially for fatigue damage assessment. In this approach aerodynamic damping needs to be added to the damping in the transfer function. A relatively rough estimation has been used to account for the aerodynamic damping in the study by van der Tempel and de Vries. They used a uniform ratio for all wind speeds, but pointed out that the damping ratio has to be calculated for each wind speed to obtain more reliable results.

Several studies investigated methods to determine the aerodynamic damping ratio under constant and turbulent wind theoretically [2][5][6]. It has been shown that approaches for constant speed turbines and for variable speed turbines below rated wind speed provide good results, but do not match with empirically obtained results for variable speed turbines operating above rated wind speed [7].

AERODYNAMIC DAMPING UNDER CONSTANT WIND

Among the methods proposed by Kühn [2], the analysis of the transient decay of free vibrations of the structure is the simplest and most straight forward method. A time-domain simulation has to be

performed, where a force is applied at tower top until the structure reaches a static equilibrium. The force is released afterwards and the free vibration response is recorded. The system damping ratio can now be calculated with

$$\xi = \frac{\Lambda}{\sqrt{4\pi^2 + \Lambda^2}}, \quad (1)$$

where the logarithmic decrement Λ is defined in terms of the i -th and $(i+n)$ -th peak of the response as

$$\Lambda = \frac{1}{n} \ln \left(\frac{u_i}{u_{i+n}} \right). \quad (2)$$

The damping ratio ξ calculated in Eq. (1) describes the system damping ratio. It is a linear combination of damping ratios from different sources, such as soil, water, and air. The contribution from these sources has to be subtracted from the system damping to obtain the aerodynamic damping. Hence,

$$\xi_{\text{aero}} = \xi_{\text{system}} - \xi_{\text{other sources}}. \quad (3)$$

This method has been tested with the OC4 reference jacket [8] and the well-known NREL 5-MW baseline wind turbine on top [9]. The flexible multibody simulation tool, FEDEM Windpower (Version R7.0.4, Fedem Technology AS, Trondheim), was used for the time-domain analysis of the OWT. A force of 1 MN has been applied at tower top to displace the turbine in wind direction until it reached a static equilibrium. After the force has been released the free vibration response of the tower top in wind direction has been recorded until the vibration was no longer detectable. The simulation was performed in still water and with different constant wind speeds, between 3 m/s and 24 m/s. A simulation without wind has been carried out in order to determine the system damping ratio without aerodynamic damping. Calculating the logarithmic decrement and using Eq. (1) and (3) led to $\xi_{\text{other sources}} = 1\%$, which corresponds to the value given in [8].

After the damping ratio from other sources has been determined, the system damping ratio has been calculated by analysing the dynamic behaviour of the wind turbine under constant wind. Examples of free vibration decays for four different wind speeds are shown in Figure 1.

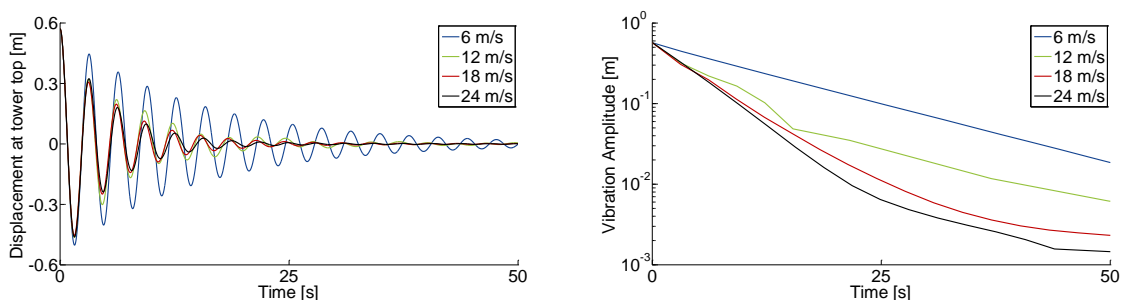


Figure 1: Free vibration decay at tower top for below and above rated wind speeds

It can be seen that the vibration amplitude does not decrease logarithmically for the wind speeds above its rated value. This effect is caused by the pitch mechanism, which is activated due to the motion of the tower top. This motion leads to small changes in the relative wind velocity experienced by the blades. The pitch angle is changed to keep the rotor speed constant. However, it takes a certain time until the pitch controller has balanced out the fluctuations, which leads to a nonlinear decay curve. Figure 2 and Figure 3 shows the fluctuations of the pitch angle for a wind speed of 12 m/s and 18 m/s. The 5th until 15th peak of the response is used to calculate the logarithmic decrement in order to neglect the fluctuations of the pitch angle. A second set of simulation was, therefore, performed with a deactivated pitch mechanism. The pitch angle was set to a fixed value which corresponds to its value for a steady wind field. This led to small variations in the rotor speed during the vibration of the tower top, since the controller was still active. However, the effect is of smaller magnitude and can be neglected. The deactivated pitch mechanism led to a logarithmically decay of the vibration on tower top (not shown). The first ten peaks are used to calculate the logarithmic decrement.

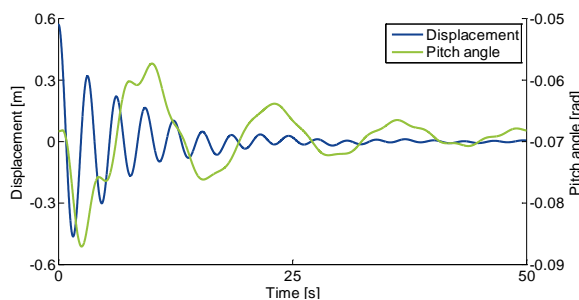


Figure 2: Free decay for 12 m/s

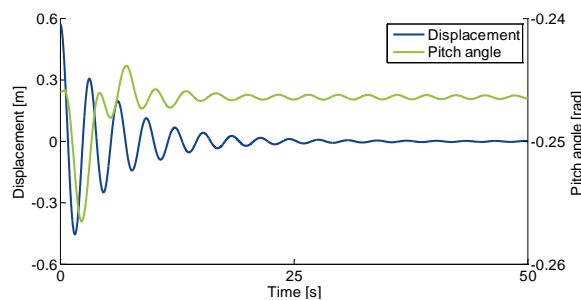


Figure 3: Free decay for 18 m/s

AERODYNAMIC DAMPING UNDER TURBULENT WIND

The aerodynamic damping under turbulent wind can be determined in a similar manner to the method used for constant wind. A simulation of the entire OWT in still water and under turbulent wind with a turbulence intensity of 10% was performed for different wind speeds between 3 m/s and 24 m/s. A time step of 0.01 seconds was selected for the simulation. Each 400 seconds a loading with a magnitude of 1 MN has been applied for the duration of one time step at tower top. A second set of simulations has been performed for the same wind speed range with the same wind field but without the pulse loadings. The time history response of the tower top displacement in wind direction was subtracted from the time history response with 27 pulse loadings. The difference in the response is regarded as the deterministic part of the free vibrations in a turbulent wind field [2]. Figure 4 shows the damping behaviour for one out of the 27 pulse loadings for a wind speed of 20 m/s. Again, the logarithmic decrement is calculated using the first ten peaks of the response. The damping ratios determined with this method are plotted over the wind speed in Figure 5. Each dot of the plot stands for the dynamic behaviour of one pulse loading. Hence, the figure shows 27 dots per wind speed.

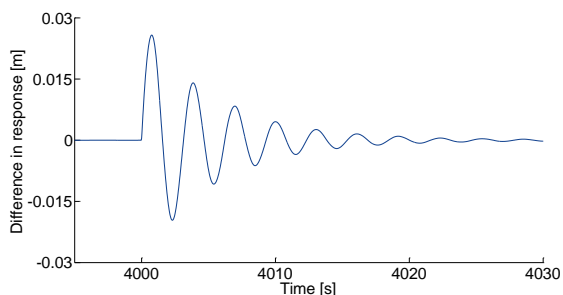


Figure 4: Response for 20 m/s turbulent wind

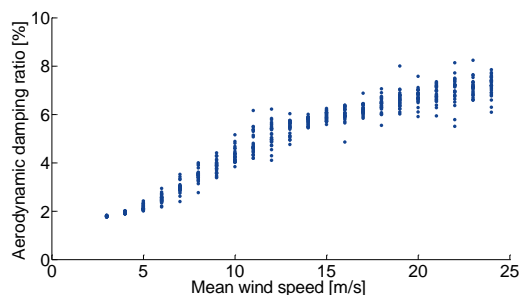


Figure 5: Damping ratio for turbulent wind

RESULTS AND DISCUSSION

The dynamic behaviour of an OWT has been analysed under turbulent as well as constant wind. The latter has been done with an active as well as a deactivated pitch mechanism. The damping ratios obtained by these calculations are shown in Figure 6. The figure also shows the closed form method proposed by Kühn [2]. An almost linear behaviour for wind speeds below its rated value for both constant and turbulent wind can be seen. This is in accordance with Kühn's closed form method and other empirical and theoretical approaches presented in previous studies [2][5][6][7]. It is also shown that the pitch mechanism, which is active for wind speeds above its rated value, highly influences the damping behaviour of the turbine. The damping ratios for constant wind with fixed pitch angle and for turbulent wind is further increasing, while the damping ratios for constant wind and active pitch mechanism follow the trend of the theoretical approach. The relatively low damping ratio for 12 m/s is caused by fluctuations of the pitching angle, which have not been removed completely. The increase of the aerodynamic damping ratio for higher wind speeds was also observed by Salzmann [7]. He compared the response spectra of a time-domain simulation with the response spectra obtained in the frequency-domain and changed the aerodynamic damping ratio in steps of 0.5% until the resonance

peak of the frequency-domain matched the results from the time-domain simulation. Other theoretical approaches by Garrad [5] or Van der Tempel [6] are closer to Kühn's closed form method [7].

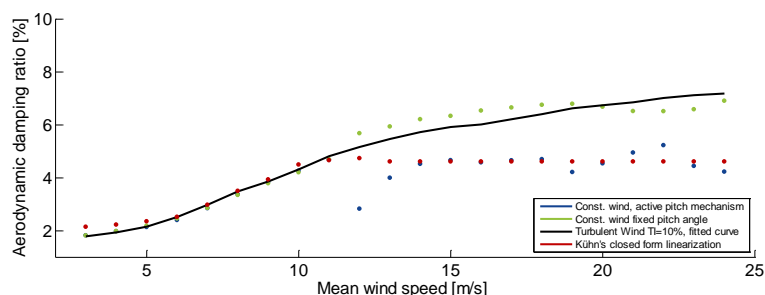


Figure 6: Aerodynamic damping ratio for constant and turbulent wind

CONCLUSION AND FURTHER WORK

The importance of aerodynamic damping is clear and different studies investigated empirical and theoretical approaches to determine an aerodynamic damping ratio. It has been shown that these methods provides good results for below rated wind speed, but highly underestimate the aerodynamic damping for variable speed turbines operating above rated wind speed, where controller actions have to be taken into account. Further study is required to identify the aerodynamic damping ratio in dependence on pitch angle and turbulence intensity.

ACKNOWLEDGEMENTS

Support by the Norwegian Research Centre for Offshore Wind Technology (NOWITECH FME, Research Council of Norway, contract no. 193823) is gratefully acknowledged.

REFERENCES

- [1] F. Vorpahl, H. Schwarze, T. Fischer, M. Seidel, J. Jonkman (2013). „Offshore wind turbine environment, loads, simulation, and design”, *WIREs Energy Environ*, 2, 548-570.
- [2] M. Kühn (2001). *Dynamics and Design Optimization of Offshore Wind Energy Conversion Systems*, PhD Thesis, Wind Energy Research Institute, TU Delft, The Netherlands.
- [3] M.C. Ong, E.E. Bachynski, O.D. Økland, and E. Passano (2014). “Dynamic Response of a Jacket-Type Offshore Wind Turbine using decoupled and coupled Models”, *Proc ASME 2014 33rd Int Conf Ocean Offshore Arct Eng*, San Francisco, CA, USA, OMAE, 10 pp.
- [4] J. van der Tempel and W. de Vries (2005). “Frequency Domain Calculation of Offshore Wind Turbine Response to Wind and Wave Loads”, DUWIND, *Proc Copenhagen Offshore Wind Conference*, 11 pp.
- [5] L.L. Freris (1990). *Wind Energy Conversion Systems*, Prentice Hall, Englewood Cliffs, New Jersey.
- [6] J. van der Tempel (2000). *Lifetime Fatigue of an Offshore Wind Turbine Support Structure*, PhD Thesis, Wind Energy Research Institute, TU Delft, The Netherlands.
- [7] D.J. Cerda Salzmänn and J. van der Tempel (2005). “Aerodynamic Damping in the Design of Support Structures for Offshore Wind Turbines”, *Proc Offshore Wind Energy Conference, Copenhagen*, Denmark, 9 pp.
- [8] F. Vorpahl, W. Popko, and D. Kaufer (2011). „Description of a Basic Model of the “UpWind Reference Jacket” for Code Comparison in the OC4 Project Under IEA Wind Annex XXX”, Technical Report, Fraunhofer Institute for Wind Energy and Energy System Technology IWES, Bremerhaven, Germany, 19 pp.
- [9] J. Jonkman, S. Butterfield, W. Musial, and G. Scott (2009). “Definition of a 5-MW Reference Wind Turbine for Offshore System Development”, Technical Report NREL/TP-500-38060, National Renewable Energy Laboratory, Golden, CO, 75 pp.

The Low Induction Rotor

Peter Mills, Peter Jamieson and David Infield

Dept. of Electronic and
Electrical Engineering
University of Strathclyde
Glasgow, UK

Abstract—Maximising wind turbine annual energy yields whilst minimising additional loading is a key consideration especially in offshore environments. Additional blade loads result in higher loadings on the hub, tower and foundations, hence resulting in additional overall turbine costs and potentially reduced availability. The basic principles of the design of a low induction rotor were investigated in this project whilst accounting for the effects on loads, rotor diameter and power output. The project objective was to produce a rotor design that for a given wind speed maximises the energy capture but without increasing the bending moments. Load reduction is particularly applicable to offshore wind turbines where access for maintenance is a significant issue. A small reduction in efficiency of power capture would be worth an increase in availability. The intention is to increase the power generated whilst keeping the loads constant.

I. INTRODUCTION

Both GH Bladed and the theoretical calculations used are based on blade element momentum (BEM) theory. The Lanchester-Betz limit is the theoretical maximum for the power coefficient of 0.593 achieved for an axial induction of 1/3 [1]. By optimising the rotor for values of axial induction less than 1/3 theoretically the thrust and bending moments can be reduced considerably without causing a substantial reduction in efficiency. The rotor radius is increased to increase the power output so that the maximum bending moments are the same as the base case for axial induction of 1/3. The rotor is scaled up so that the power should theoretically increase whilst the rotor diameter is scaled such that the loads are kept constant. The objective of the scaling of the rotor diameter is to increase the power harnessed from the wind field, while still retaining the same out of plane bending moment. Turbines designed for high wind speed sites will be studied. These turbines have larger rotor diameters to increase the swept area in order to make up for the power lost by having lower induction. Lower induction rotors are slightly less optimum but the drop in thrust is more significant. For offshore wind turbines the cost of the rotor is a relatively small proportion of the overall cost of construction and operation of an offshore wind farm. Infrastructure costs including foundations, substations and transmission are larger. Therefore increasing the annual energy yield a small amount by increasing the swept area will allow more effective utilisation of this infrastructure [2].

II. INTERACTION OF KEY LOADS WITH AXIAL INDUCTION AND ROTOR DIAMETER

The thrust coefficients reduce to a greater degree than the power coefficients for values of axial induction between 1/3 to 0.2 Figure 1. Therefore by reducing the axial induction the

loads can be reduced significantly at the expense of a small reduction in efficiency.

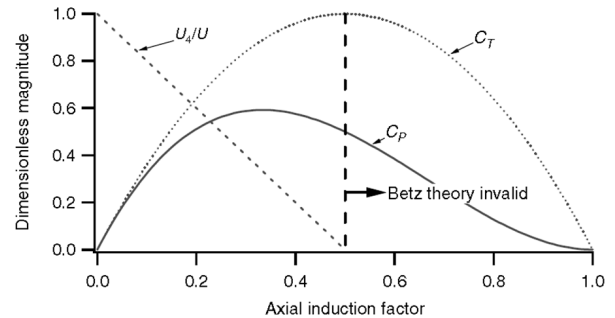


Fig. 1. Variation of performance coefficients (C_P) and thrust coefficients with axial induction factor (C_T) [3]

TABLE I. GENERAL CHARACTERISTICS OF ROTOR AND TURBINE

Characteristics of rotor and turbine	Value	Units
Rotor diameter	100	m
Number of blades	3	
Hub height	81.11	m
Control	Pitch regulated Variable speed	
Radial position of root station	1.33	m
Cut-in and cut-out wind speeds	4 - 25	m/s
Blade length	48.7	m

III. OPTIMISATION FOR AXIAL INDUCTION OF 0.2

A wind speed range of 4 to 15 m/s with a step size of 0.1 m/s was defined for steady loads calculations. The upper value of 15 m/s was chosen to be above rated wind speed. The angle of attack is equal to the flow angle of the resultant velocity to the rotor plane minus the inclination of the local blade chord to the rotor plane. The values for angle of attack, lift coefficients and drag coefficient were selected on the basis of giving the maximum lift to drag ratio see (Table II). Optimisation for fixed axial induction was undertaken using these values which were fixed for the blade span. Aerofoil selections were also fixed to simplify the model being used.

TABLE II. VALUES USED FOR OPTIMISATION CALCULATIONS WITH MAXIMUM LIFT TO DRAG RATIO

Angle of attack α	4
Lift Coefficient C_L	0.876
Drag Coefficient C_D	0.007
Lift Drag ratio k	125.14

An axial induction factor of 0.2 was chosen as the target optimisation value. Formula in [4] were used. The values for optimisation are shown in Table II. A tip speed ratio of 9 was

used for optimisation as this gives the maximum coefficient of performance (C_{Pmax}). Values for distance along blade, chord and twist were extracted from the original Bladed model for which the turbine details are summarised in Table I. The radial distance is equal to the distance along the blade plus the root length minus a correction factor (0.08016 m). The radius fraction (x) is the radial distance out of the total distance. The original rotor has a rotor radius (R) of 50m.

The tangential induction factor, a' is calculated using the equation:

$$a' = \frac{(\lambda^2 k^2 x^2 + 2\lambda kx - 4ak(\lambda x - k(1-a)) + 1)^{0.5} - (\lambda kx + 1)}{2 \cdot \lambda \cdot k \cdot x} \quad (1)$$

Prandtl tip factor is calculated using:

$$F = \frac{2}{\pi} \arccos \left[\exp \left\{ -\frac{(1-x)B\lambda}{2(1-a)} \right\} \right] \quad (2)$$

The non-dimensional lift distribution is calculated using:

$$\Lambda = \frac{8\pi a(1-a)}{B\lambda(1+a)\sqrt{(1-a)^2 + \lambda^2 x^2(1+a)^2}} \cdot \frac{F}{\left(1 + \frac{(1-a)}{k\lambda x(1+a)}\right)} \quad (3)$$

The new optimised blade chord is then calculated from:

$$c = \frac{\Lambda R}{C_L} \quad (4)$$

The optimum blade twist:

$$\theta(x) = \text{atan} \left(\frac{2}{3\lambda x(1+a)} \right) - \alpha_0 \quad (5)$$

IV. COMPARING LOADS

The in-plane and out-of-plane blade root bending moments were compared. The out-of plane bending moments are the most important as they have the biggest impact on loads and hence costs of the turbine. The thrust forces were also compared. Figure 2 shows the variation of out of plane blade root bending moments for the two cases of axial induction of 0.2 and 1/3. Table III shows the maximum out of plane bending moments that are used for up-scaling calculations in Section 5.

TABLE III. MAXIMUM OUT OF PLANE BLADE ROOT BENDING MOMENTS, MY (kNm)

Induction (a)	Hub Wind Speed (m/s)	Maximum out of plane moments (kNm)
1/3	11.6	3290.64
1/5	13.3	2629.42
	Ratio	1.25

V. UP-SCALING

A. First Iteration up-scaling

The rotor was up-scaled so that the out-of-plane bending moments were kept constant with the objective of increasing the overall power output. The turbine optimised for an axial induction of 0.2 was up-scaled by increasing the rotor radius and linear dimensions. The bending moments (M) are proportional to the radius cubed (R^3). Hence the cube of the

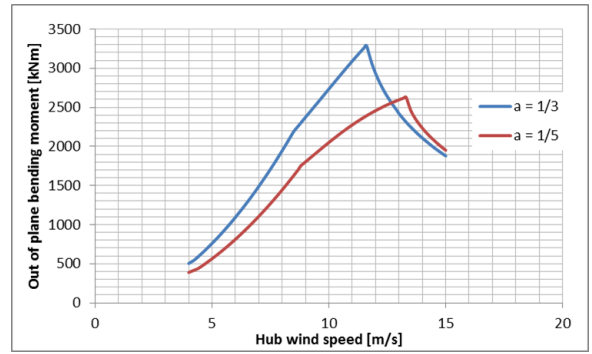


Fig. 2. Out of plane bending moments

ratio of the radius is equal to the ratio of the out of plane blade root bending moments. The intention is to have a larger rotor diameter and more power whilst keeping the loads on the turbine constant.

$$R_1 = R \left(\frac{M_{0.333}}{M_{0.200}} \right)^{\frac{1}{3}} \quad (6)$$

Where:

R_1 = new rotor radius

R_{base} = Original rotor radius = 50 m

$M_{0.333}$ = Maximum out-of-plane bending moment for $a = 1/3$

$M_{0.200}$ = Maximum out-of-plane bending moment for $a = 0.2$

The most important linear dimensions were scaled by a factor of 107%. The dimensions that were scaled included: distance along the pitch axis, blade chord, hub vertical offset, root length, blade root diameter and the rotor diameter (see Table IV). The root length needs to be increased so that the first blade station is in the required location. Note that the modified values displayed are values in the Bladed file produced. Values are rounded and the rotor diameter is slightly greater than 107 m because it is based on the blade stations entered.

TABLE IV. LINEAR DIMENSIONS SCALING

	Original	Modified
Hub vertical offset (m)	2.11	2.2577
Root Length (m)	1.33	1.4231
Blade Root Diameter (m)	2.684	2.87188
Nominal rotor diameter (m)	100	107.146

Total hub height was left constant so as not to change wind shear effects more than necessary. The overhang and nacelle geometry were also left the same. The distance along pitch axis values is increased by 107% - this automatically increases the rotor diameter. The new chords which had been optimised for $a = 0.2$ are up-scaled by 107%. The twist values are left the same.

B. Second Iteration Up-scaling

The out of plane bending moments for the 1st iteration up-scaling (up-scaled) of the turbine optimised for an axial induction factor of 0.2 did not successfully scale the bending moments so as to reproduce those of the axial induction of 1/3 case. For this reason a second iteration up-scaling (rescaled) was performed on the design for an axial induction of 0.2 Table

V. This achieved approximately equal out of plane bending moments see Figure 8.

TABLE V. COMPARISON OF MAXIMUM OUT OF PLANE BENDING MOMENTS (K NM)

Axial induction	Maximum Out of Plane Bending Moments (k Nm)
1/3 (Base case)	3290.64
0.2 Up-scaled (1st iteration)	3114.41
0.2 Rescale (2nd iteration)	3248.47

VI. NON CONSTANT INDUCTION

The effects of varying the axial induction factor linearly over the rotor diameter whilst maintaining an area average of 0.2 were investigated for two cases were considered. One case study involved an axial induction factor of 20% less at the blade tip which corresponds to a tip axial induction factor of 0.16. The other case was for a tip axial induction factor of 20% more (0.24). Figure 3 shows the annual energy yield gain for the non-constant induction designs and the 0.2 rescaled case (see section V-B) as a factor of the design for an axial induction of 1/3.

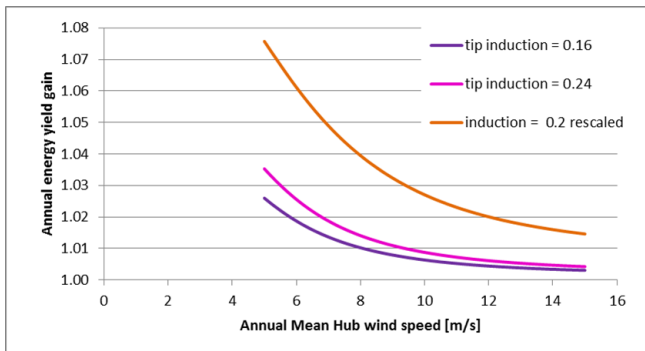


Fig. 3. Annual energy yield gain for non-constant induction designs relative to induction of 1/3 case

VII. EVALUATION

A. Energy and Loads

Reducing the induction from 1/3 to 0.2 increases the annual energy yield by approximately 0.4 KWh. The maximum thrust is also reduced by about 1.4 kN (see Table VI). The maximum thrust is significant as the turbine will need to be designed to cope with maximum thrust loadings. The turbine reaches the rated power of just over 3 MW at slightly lower wind speeds for the lower induction cases hence the power gain see Figure 5.

TABLE VI. THE EFFECT OF AXIAL INDUCTION ON ANNUAL ENERGY YIELD AND THRUST FOR AN ANNUAL MEAN WIND SPEED OF 9 M/S

	1/3	0.25 Up-scaled	0.2 Rescaled
Annual energy yield [KWh]	13.11	13.35	13.54
Thrust force [kn]	281.92	278.87	280.48

B. Finding best axial induction between $a = 0.2$ and $a = 1/3$

Graphs for the up-scaled $a = 0.25$ design have been compared to the second iteration up-scaling of the $a = 0.2$ design (rescaled) and the $a = 1/3$ base case. The annual energy yields for the up-scaled design with an axial induction of 0.2

and 0.25 compared to the design optimised for $a = 1/3$ as a base case are given in Figure 4. The annual energy yield for the axial induction of 0.2 design is consistently the highest. The annual energy yield for the 0.250 design is consistently between those of the 0.2 and 1/3 designs. This shows that the up-scaled low induction rotor has a higher annual energy yield. The increase in annual energy yield compared to the $a = 1/3$ case can be seen in Figure 5. There is a significant gain from optimisation, comparisons of the percentage gain of annual energy yield is shown in Table VII.

TABLE VII. ANNUAL ENERGY YIELD PERCENTAGE GAIN COMPARED TO ANNUAL MEAN HUB WIND SPEED

Increase in annual energy yield (%)	5 m/s	10 m/s	15 m/s
Induction 0.2	7.5	3	1.5
Induction 0.25	4	1.5	1

The power curves indicate that the lower induction cases have slightly greater power output below rated. As the gain is relatively small the power gain is illustrated in Figure 6. The in-plane bending moments are greater for the up-scaled lower induction cases compared to axial induction of 1/3. This is displayed in Figure 7. The out-of-plane bending moments were scaled so that the maximum moments were the same. Figure 8 shows that this has been achieved. The thrust forces were marginally lower for the up-scaled lower induction cases than that of the induction of 1/3 case.

Between radial distances of 30-40 m the axial induction is approximately constant, which is consistent with the objective. For the up-scaled case the axial induction in the region is about 0.25. The reason for the rescaled case being above 0.2 should be investigated in future work. Lower values of axial induction have lower maximum performance coefficients. The lower axial induction cases have maximum performance coefficients at higher tip speed ratios see Figure 9. This is a limitation of the study.

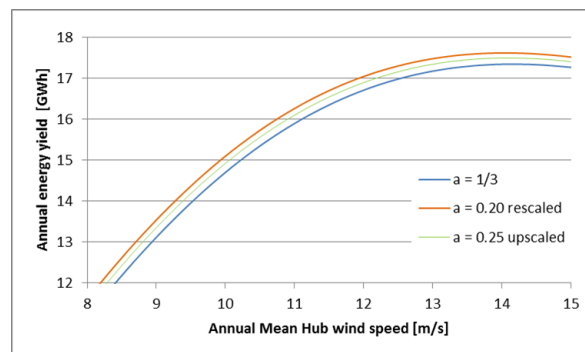


Fig. 4. Annual energy yield [KWh]

VIII. CONCLUSION

There is a significant gain from optimisation. The design for an induction of 0.2 gives higher annual energy yield than for the 0.25 design. This is true across the range of annual mean wind speeds. The induction of 0.25 design gives results between for the induction 0.20 and 1/3 cases. The accuracy of the calculations should be considered, however given that Bladed calculations should be consistent it is assumed the differences are significant. Reducing the axial induction does

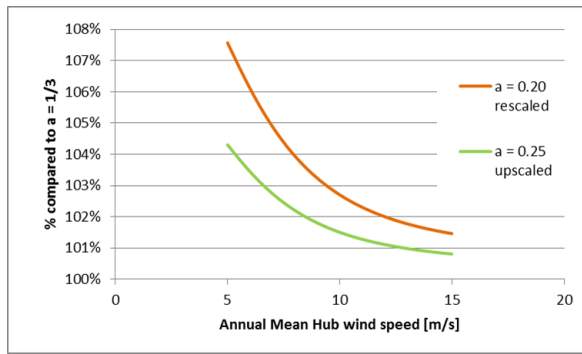


Fig. 5. Annual energy yield gain relative to case for axial induction (a) of $\frac{1}{3}$

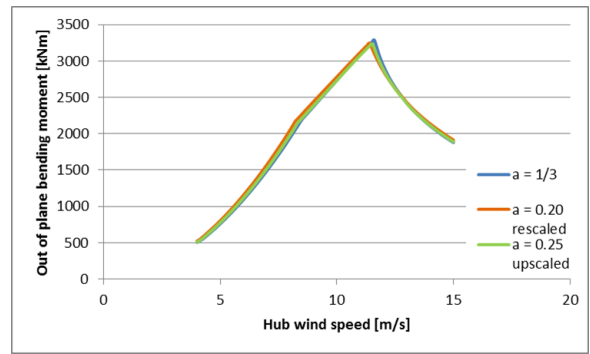


Fig. 8. Out of plane bending moment

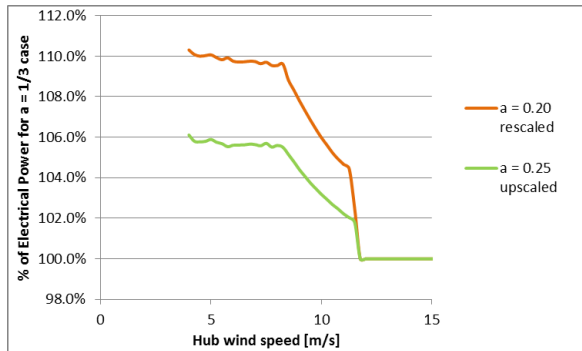


Fig. 6. Power gain

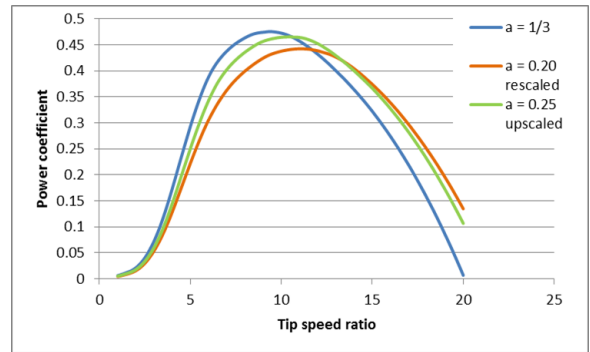


Fig. 9. Power coefficients

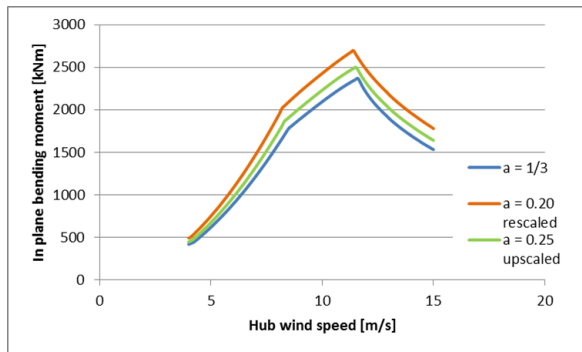


Fig. 7. In plane bending moment

increase the power output. Turbine costs are 30% of the total capital expenditure of an offshore project [4] and blades cost are around 18% [4]. Therefore the total value of the blades is about 5%. For the axial induction factor of 0.25 case the rotor diameter has been increased by 104%. As an approximation this gives an increase in overall project expenditure of about 0.2%. For the axial induction factor of 0.20 design the rotor diameter is increased by 107%, estimated additional capital expenditure for the project is about 0.4%. These approximations have been scaled for the increase in rotor diameter including cost resulting from increased blade loadings. However the rotor diameter has been increased without increasing the bending moments so the actual blade cost increase should be lower than this. For a wind speed of 10 m/s the increase in annual

energy yield is about 1.5% for the 0.25 design and about 3% for the 0.2 design. For the 10 m/s wind speed case the two lower induction rotor designs are equal improvements on the axial induction of 1/3 design.

Future work should look at other values of axial induction between 1/3 and 1/5. The effects of non-constant induction could also be further investigated including the effects of non-linear induction variation. Further investigations would need to be carried out to establish the cost of the increased rotor diameter to substantiate if the overall cost of energy is reduced. In conclusion the low induction rotor design gives increased annual energy yield and preliminary estimates suggest that this design has significant potential to reduce the cost of energy.

ACKNOWLEDGEMENT

Support from the UK's Engineering and Physical Sciences Research Council is gratefully acknowledged.

REFERENCES

- [1] T. Burton, *Wind Energy Handbook*. John Wiley & Sons Inc, May 2011. [Online]. Available: <https://www.dawsonera.com:443/abstract/9781119992721>
- [2] J. B. P.K. Chaviaropoulos, "Moving towards Large(r) Rotors Is that a good idea?" 2013.
- [3] J. F. Manwell, J. G. McGowan, and A. L. Rogers, *Wind energy explained: theory, design and application*. John Wiley & Sons Inc, Sep. 2010. [Online]. Available: <https://www.dawsonera.com:443/abstract/9780470686287>
- [4] P. Jamieson, *Innovation in Wind Turbine Design*. Chichester, UK: John Wiley & Sons, Ltd, Aug. 2011. [Online]. Available: <http://doi.wiley.com/10.1002/9781119975441>

Aerodynamic Performance Losses due to Ice Buildup in Wind Turbines

O. Yirtici¹, I. H. Tuncer¹, S. Ozgen²

¹METUWIND–METU Center for Wind Energy, oyirtici@ae.metu.edu.tr,
tuncer@ae.metu.edu.tr ²Middle East Technical University, sozgen@ae.metu.edu.tr

ABSTRACT

Ice accretion on blades modifies the blade profile and alters the aerodynamic characteristic of the blades and the wind turbine. The objective of this study is to determine performance losses on a wind turbine due to the formation of rime or glaze ice. The analysis is based on the Blade Element Momentum approach in order to predict the energy production of the wind turbine. The sectional aerodynamic loads are evaluated with a Navier-Stokes solver using the iced blade profiles. Currently, the iced blade profiles are predicted with a ice accretion prediction methodology based on extended messenger model. The preliminary results show that the aerodynamics performance losses heavily depend on the modified leading edge profile due to ice formation. The predicted performance degradation is significantly higher for the glaze ice formation than that of the rime ice.

I. INTRODUCTION

Atmospheric icing causes power losses since ice accretion on blades changing the aerodynamic characteristics and create instrument or controller errors on the wind turbines. The amount of wind power losses depend on the amount of ice accumulation on the blades, blade design and turbine control. Since the global wind resource is found in cold climate regions and mountainous areas, wind power loss prediction take an important role on the estimation of the annual energy production of the turbine. Wind power loss happens when either turbines are shut down or icing occur on blades depends on icing severity. In common, two kind of icing severity is defined in wind turbines. While heavy icing is described as a icing on blades happen many weeks during a year, in light icing severity icing on blades occur few days in a year. Ice accretion over rotating blades build up mostly on the leading edge of the blades and can cause critical unbalanced loads on the wind turbine. This situation enlarge material fatigue, bring down the operational life of the turbine. Also icing on wind turbine causes ice throw and ice fall of wind turbine and makes the noise louder. In the horizontal axis wind turbine, aerodynamic performance losses are similar to that observed by wings and helicopter rotors under icing conditions [1]. In order to maximize energy production from the turbine which is operating under icing conditions performance losses needed to be predicted.

In this study, a Navier-Stokes solver with ice accretion prediction module will be used to predict the power production of the wind turbine by using BEM approach to estimate performance losses due to ice buildup in wind turbine blades. In the future, ice accumulation will be predicted for each blade sections for a given flow conditions, then a Navier-Stokes solver will be used to compute aerodynamic coefficient to calculate power production of the selected wind turbine by using the BEM approach.

II. ICING

Icing is formed when the supercooled droplets impinge on the any kind of surface such as wing, propeller or turbine blade. These droplets can stay in a liquid state even at temperatures as low as -40 °C. Temperature, liquid water content, droplet size and surface size of iced-up body are basic factors affecting icing. Temperature influences the type and intensity of ice. Liquid water content determines the severity of icing, type and shape. Droplet size indicates the type and rate of icing. Surface size of iced-up body determines the rate of ice accretion. Droplets may freeze instantly and form rime ice on the surface or run downstream and freeze later forming glaze ice structure. Rime, glaze and mixed ice are three type of ice formed in the air.

Rime ice typically forms at temperature from 0 °C down to -40 °C. This kind of ice has milky, opaque appearance with smooth shapes, tends to grow into the airstream, and can be easily removed by de-icing or prevented by anti-icing systems since it is friable. It is usually occurs at low airspeed, low temperature and low liquid water content. Glaze ice occurs at temperatures between 0 and -6 °C. Glaze ice has transparent appearance with irregular shapes like horns and hard to remove by de-icing systems. It is occurs at high airspeed, high temperature and high liquid water content when a fraction of the water droplets freezes upon impact while remainder droplets run back along the surface and freeze downstream. An example to the rime and glaze can be seen in Figure 1. Mixed icing is a combination of rime and glaze ice. It occurs in layers from rime to glaze ice.



Figure 1: Rime ice (left) and Glaze ice (right) [2]

III. METHOD

Ice accretion prediction involves complex physics comprising aerodynamics, heat transfer and multiphase flow, which are all time dependent and involve geometric deformation. The numerical method employed in this study predicts the ice accretion on aerodynamic surfaces as a result of water droplets hitting on the surface iteratively. It employs the general methodology for the simulation of ice accretion on airfoils, which is based on the successive calculation of air flow, water droplet trajectories, collection efficiency, heat transfer balance and accreted ice. In order to determine the flow field velocity components for droplet trajectory calculations, a panel method is used. Droplet trajectories are computed by using a Lagrangian approach to obtain the collection efficiency distribution around the airfoil. To determine the thickness of the ice, the convective heat transfer coefficients are determined by using the two-dimensional Integral Boundary Layer equation and the thermodynamic balance is achieved with the Extended Messinger model. More information about this ice prediction code can be found in References [3,4]. The present solver is written in Fortran programming language. The Navier-Stokes equations are discretized by second order accurately cell centered finite volume method and solved explicitly by using Runge-Kutta dual time integration technique. Fluxes are computed with upwind methods. The numerical simulations are performed in parallel environment using domain decomposition and PVM library routines for interprocess communications. Further information about present solver can be found in Reference [5].

IV. PRELIMINARY RESULTS

A . Estimation of Power Production by using BEM Tool

NREL untwisted and untapered wind turbine is used to estimate power production. The geometry information and power curve of the NREL phase II wind turbine are given in the reference [6]. Iced airfoil shape is taken from the study of Brillembourg D. [7] for case 1 at the radial location A. Clean and iced S809 airfoil shapes and power curve comparison of the NREL phase II wind turbine for clean and iced airfoils can be seen in Figure 2.

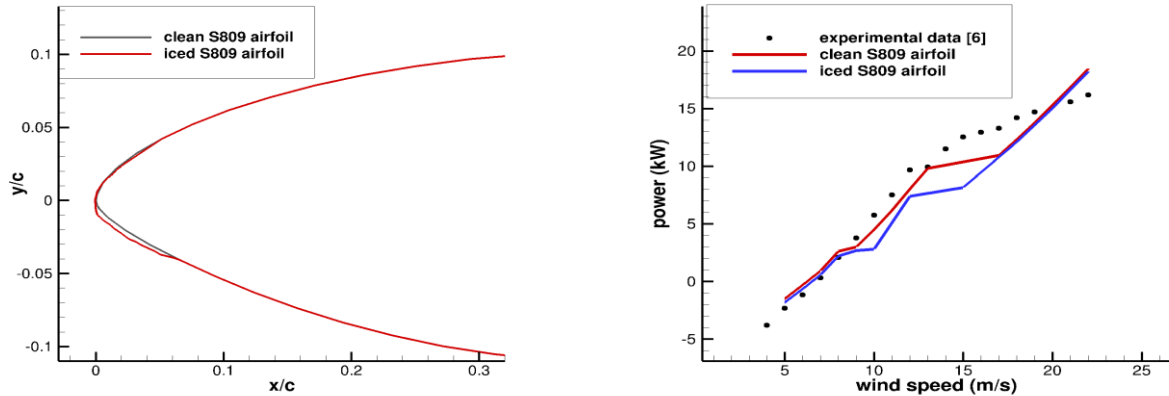


Figure 2: Clean and iced S809 airfoil shapes (left), Power curve comparison for NREL Phase II wind turbine (right)

It is seen from Figure 2 that for the clean airfoil sections, BEM analysis results agree well with test data for low wind speeds, but in high wind speeds performance prediction is poor since XFOIL could not compute aerodynamic coefficients correctly (at high speeds blade sections encounter high angle of attacks) .Still, It can be seen clearly that ice accretion decrease the performance of the wind turbine.

B.Performance Losses for Rime and Glaze Ice

Ice accretion over NACA 0012 airfoil is predicted for both rime and glaze ice. The obtained results are compared against experimental and numerical studies performed by da Silveira et al.[8]. Thegeometric and flow conditions in the reference study are presented in Table 1.

Table1: Geometric characteristics and flow conditions used in the calculations

Variables	Values for rime ice	Values for glaze ice
Ambient temperature, T_a	-30.5 °C	-6.7 °C
Freestream velocity, V_∞	93.8 m/s	58.1 m/s
Airfoil chord ,c	0.5334 m	0.5334 m
Liquid water content, ρ_a	1.05 g/m ³	1.3 g/m ³
Droplet diameter, d_p	20 μ m	20 μ m
Exposure time, t_{exp}	372 s	480 s
Ambient pressure, p_∞	92610 Pa	95610 Pa
Angle of attack, α	4.0 °	4.0 °
Humidity	100 %	100 %

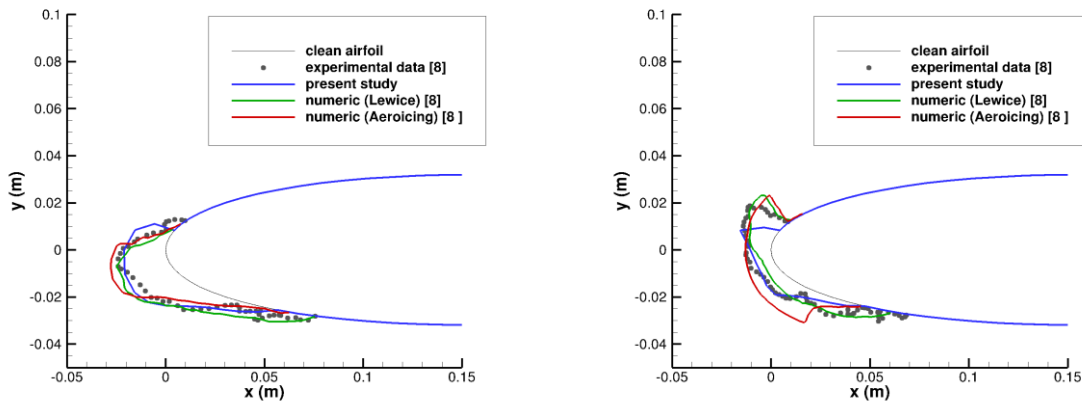


Figure 3: Comparison of ice shape predictions for rime (left) and glaze (right) ice

In Figure 3, obtained ice shapes are compared with those obtained numerically by Lewice and Aeroicing respectively. It is observed that all the predictions agree fairly well with the experimental

data for rime ice case. Present solver estimate the upper horn less than others for the glaze ice case. Time step, splash and break up effects are the informations which are missing in the study of da Silveira et al.[8] may cause this discrepancy. Figure 4 shows close up views of solution domain for the glaze ice case.

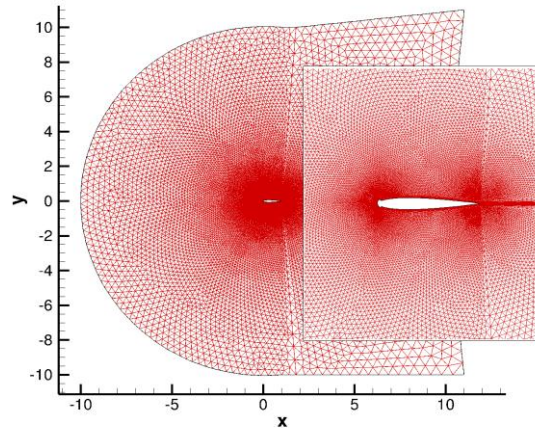


Figure 4: Detailed view of the solution domain

Table1: Aerodynamic coefficients for clean and icing airfoils

	C_L (rime ice)	C_D (rime ice)	C_L (glaze ice)	C_D (glaze ice)
Clean airfoil	0.2206	0.00349	0.2214	0.00378
Iced airfoil	0.2144	0.01070	0.2168	0.01675

The aerodynamic load coefficients are given in Table 2. A significant increase in the drag coefficient and a decrease in the lift coefficient are observed. Ice accumulation on the airfoil gives rise to pressure fluctuations and this causes an increment in drag and a decrement in lift coefficient. Obtained preliminary results are analyzed and commented. It is seen that the amount of aerodynamic performance losses depends on the kind of ice shape. For glaze ice, predicted performance degradation is observed to be more than rime ice. The next step will be implementing the Blade Element Momentum method to the present solver for predicting energy production losses of the wind turbine.

REFERENCES

- [1] Jasinski, S. Noe, M. Selig and M. Bragg, "Wind Turbine Performance under Icing Conditions", ASME, vol.120, pp.60-65, 1998.
- [2] J.F. Corbett, "Predicting Icing Losses", [http://www.windpower.org/download/06/JFC/Icing losses 20110401.pdf](http://www.windpower.org/download/06/JFC/Icing%20losses%20110401.pdf), last visited on November 2014.
- [3] S. Ozgen, M. Canibek, "Ice Accretion Simulation on Multi-Element Airfoils using Extended Messinger Model", Heat Mass Transfer, Volume 45, Issue 3, pp 305-322, 2008.
- [4] S. Ozgen, M. Canibek, "In Flight Icing Simulation with Supercooled Large Droplet Effects", 7th Int. Conference on Heat Transfer, Fluid Mechanics and Thermodynamics, Antalya, Turkey, 2010.
- [5] O. Yırtıcı, "Detached Eddy Simulation of Turbulent Flow on 2D Hybrid Grids", <https://etd.lib.metu.edu.tr/upload/12615002/index.pdf>, Msc Thesis, METU, 2012.
- [6] J. G. Schepers et al, Final Report of IEA Annex XVIII: Enhanced Field Rotor Aerodynamics Database, Energy Research Centre of Netherlands, Technical Report ECN-C-02-016, February 2002.
- [7] D. Brillembourg, "Wind Turbines Under Atmospheric Icing Conditions – Ice Accretion Modeling, Aerodynamics, and Control Strategies for Mitigating Performance Degradation", Msc Thesis, The Pennsylvania State University, 2013.
- [8] da Silveira Rafael A., Maliska Clovis A., Estivam Diego A., "Aircraft Icing Simulation using Navier-Stokes and Potential Flow Simulation for the External Aerodynamics", the 10th Brazilian Congress of the Thermal Sciences and Engineering, Rio de Janeiro, Brazil, 2009.

IMPLEMENTATION OF PASSIVE CONTROL STRATEGIES THROUGH SWEEPED BLADES

C. Pavese¹, T. Kim¹

¹DTU, Wind Energy Department, Roskilde, cpav@dtu.dk, tkim@dtu.dk

I. Introduction

The purpose of this study is to define guidelines for the benchmarking of wind turbines that use passive control methods to reduce extreme and fatigue loads on the structure. Passive control techniques can be divided in two branches: changes of the blade geometry and tailoring the material properties with blade layups. The objective of the current investigation involves exclusively the first type.

The core of the concept behind the passive control methodology considered in this study is to create a coupling between flapwise bending toward the tower and torsion towards feathering. This coupling has the capability to mitigate loads due to a decrease in the angle of attack. This beneficial effect is achieved changing the geometry of the blade creating a backward swept shape.

Information concerning the positive and negative effects on the loading of a wind turbine with swept blades can be found in literature [1] [2] [3] [4]. For example, the parametric study carried by Verelst and Larsen [2] provided a clear picture related to the quality of the load variation generated by the use of different swept blade configurations. Knowledge regarding an accurate estimation of the quantity of these load variations is missing. The reason is the differences in power output between the baseline and passive-controlled wind turbines. The geometrical bend-twist coupling effect reduces the angle of attack, and this reduction is responsible for a decrease in power output below rated wind speed. Hence, in order to properly quantify the load variations, the benchmarking has to be based on wind turbines with comparable power curves.

This study uses a simple method to provide the benchmarking of turbines with swept blades, with power curves comparable to a baseline with unswept blades. The method is based on a study conducted by Hansen [3]. In order to compensate the power loss below rated wind speed, new minimum pitch angle settings for the controller are evaluated. The swept blades are therefore pitched further towards stall with respect to the baseline blade in order to achieve similar power outputs.

The paper provides guidelines for this type of benchmarking with the final purpose of isolating the effects on the loading brought by the use of geometrical passive control methodology.

A comparison of wind turbines with various swept blades is reported. Results and methods to improve and better isolate passive control effects to quantify load variations are discussed.

II. Model

In this investigation, two in-house aeroelastic codes have been used: the linear aero-servo-elastic model for open- and closed-loop eigenvalue and frequency-domain analysis HAWCStab2 [3] and the nonlinear aeroelastic model for response in time domain HAWC2 [5] [6] [7].

The DTU 10 MW Reference Wind Turbine (RWT) [8] is used as a baseline for the current study.

As previously introduced, three different swept geometries are considered. All the properties of the wind turbines related to aerodynamic characteristics of the blade are kept the same for all the configurations analysed.

The sweep geometries are described by the following shape function:

$$s = \left\{ a \frac{z}{R_0} - b \left(\frac{z}{R_0} \right)^c, 0, z \right\}^T \quad z \in [0; R_0]$$

where s is the pitch axis as function of the blade length, z is the coordinate along the pitch axis of the blade, $R_0 = 89.166 \text{ m}$ is the blade length in hub-coordinate system, a is a linear term for forward sweep added to compensate an otherwise large steady torque moment and b is the term for the backward sweep, which curve exponent is determined by c .

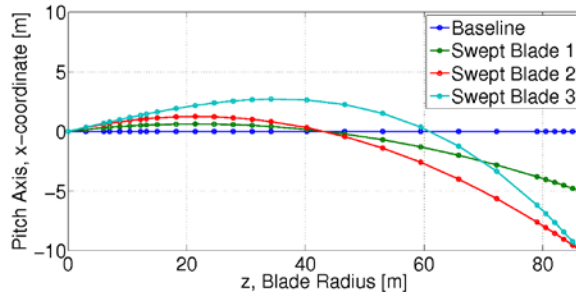


Figure 1: Pitch axis x-coordinate for the baseline and the backward swept blades

The pitch axes of the blade along the span for three different swept configurations are plotted in Figure 1, whereas the parameters for the different configurations are:

- Swept Blade Level 1 : $a = 5, b = 10, c = 2$
- Swept Blade Level 2 : $a = 10, b = 20, c = 2$
- Swept Blade Level 3 : $a = 10, b = 20, c = 3$

A fair benchmarking has to be based on wind turbines with comparable power curves. New minimum pitch angle settings are calculated using HAWCStab2. The aim is to compensate the reduction of the angle of attack below rated wind speed pitching the backward swept blades toward stall. Figure 2 shows the power curves of the baseline and the turbines with swept blades. The lower plot shows the relative error in percentage between the baseline and the three sweep levels. The dashed lines represent the difference in power curves when all the configurations have the same minimum pitch angle (zero degree) below rated wind speed. The solid lines shows the relative error when new minimum pitch angles have been used. The power losses have been significantly reduced and the maximum error is around 2%.

This simple method for obtaining comparable power curves has an important downside: pitching the full blade below rated wind speed might push the part of the blade closer to the root to operate in stall condition. The coupling between flapwise bending toward the tower and torsion towards feathering produces a reduction of the angle of attack in the region of the blade closer to the tip. The angle of attack closer to the root is significantly less influenced by the coupling effect. Hence, when the backward swept blades are forced to pitch further toward stall below rated wind speed, the lift coefficient of the airfoils closer to the root, which work already at high angles of attack, approaches dangerously the stall region.

Lift coefficients along the blade span of the different DTU 10 MW RWT configurations used for the current benchmarking have been constantly monitored, to make sure that all the swept-blades wind turbines used for this study kept a behavior comparable to the baseline.

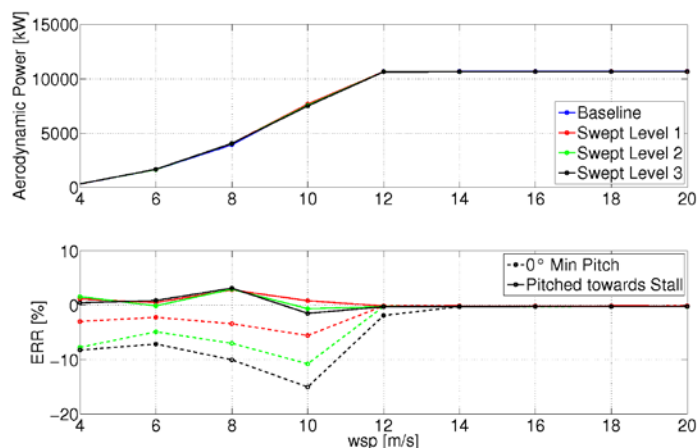


Figure 2: wind turbines Power Curves, Upper Plot - Relative Error between the power curves with comparison between configurations using same minimum pitch angles and HAWCStab2 new pitch settings below rated wind speed

III. Results

The load case used for the benchmarking consist of 10 minute simulations with turbulent wind speed from 4 m/s to 26 m/s (single turbulence seed is considered), tower shadow and no wind shear. Extreme and fatigue loads acting on the wind turbines are computed. Two sets of simulations have been run: one where the minimum pitch angle below rated wind speed is kept equal (zero degree) for all the configurations, and the other one where a new minimum pitch angle has been selected for each of the cases to minimize the discrepancies between the power curves.

Extreme blade root flapwise bending moment for the different sweeps are reported in Figure 3. The upper plot shows the values of this particular load for the different blade configurations. One bar (blue color) denotes the blade root flapwise bending moment for the set of simulations where the minimum pitch angles have been kept equal despite the blade geometry. The other bar (in red) shows the extreme blade root flapwise bending moment for wind turbine configurations with comparable power curves.

The lower plot shows the variation registered between the extreme loads calculated with and without taking into account wind turbines with similar power outputs. The maximum discrepancy in load variation from the baseline registered for the highest sweep level implemented with respect to extreme blade root flapwise moment is around 10%.

The maximum blade root torsional moment, shown in Figure 4, increases dramatically when a swept geometry for the blades is introduced. A similar effect on the extreme load variation seen from Figure 3 is reported. Torsional loadings are overestimated when a common pitch setting is used for all the configurations.

The extreme blade root flapwise bending and torsional moment are computed for wind speeds close to the rated. Therefore, the change in the minimum pitch angle below rated wind speed, introduced to compensate the power loss observed in wind turbines with backward swept blades, is responsible for the load variations observed between the two sets of simulations. Hence, a benchmarking without compensating the power losses of passive controlled wind turbines below rated wind speed brings to an overestimation of the extreme load alleviations due to the use of backward swept blades.

Life time (20-years) equivalent fatigue loads for the blade root flapwise bending moment (Figure 5) and for the blade root torsional moment (Figure 6) have been reported. Weibull distribution is considered. No relevant discrepancies between fatigue loads computed for the two sets of simulations are observed. For the blade root moments, the loading introduced by the action of the pitch actuator has the most relevant impact on the life time fatigue load, shadowing eventual effects due to a benchmarking done without considering turbines with lower power curves below rated wind speed.

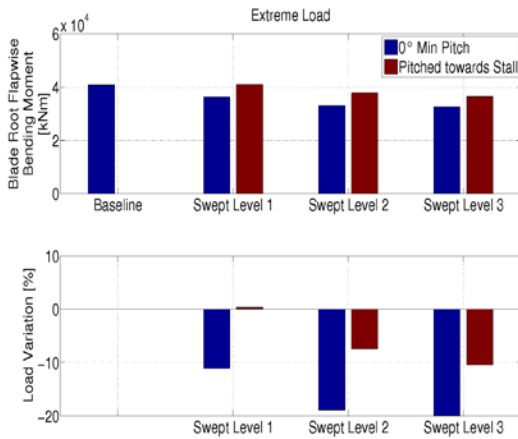


Figure 3: Extreme blade root flapwise bending moment. Load variation with respect to the baseline (lower plots) according to the configurations using the same minimum pitch angles (blue) and new pitch angles (red).

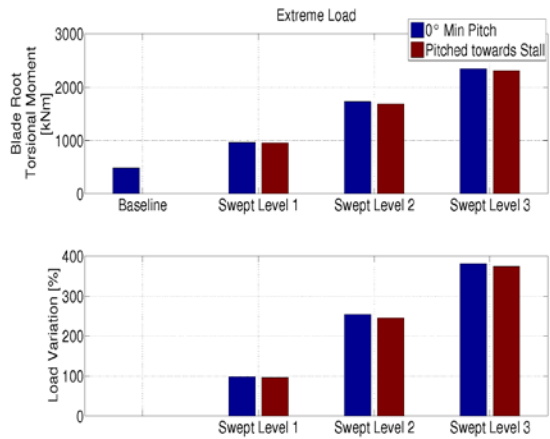


Figure 4: Extreme blade root torsional moment. Load variation with respect to the baseline (lower plots) according to the configurations using the same minimum pitch angles (blue) and new pitch angles (red).

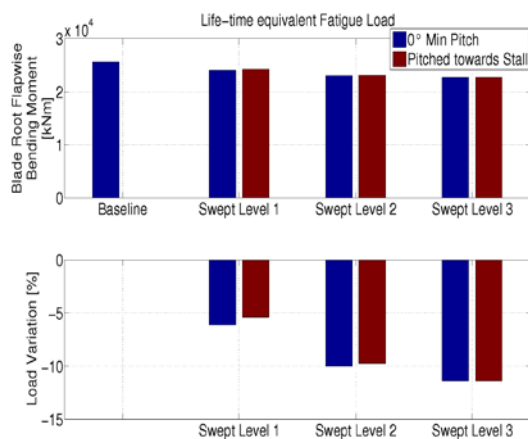


Figure 5: LTE Fatigue blade root flapwise bending moment. Load variation with respect to the baseline (lower plots) according to the configurations using the same minimum pitch angles (blue) and new pitch angles (red).

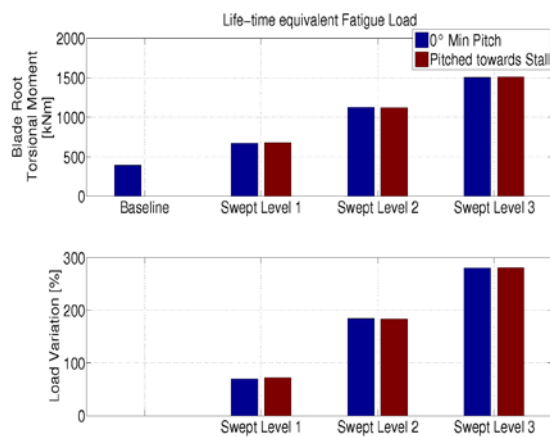


Figure 6: LTE Fatigue blade root torsional moment. Load variation with respect to the baseline (lower plots) according to the configurations using the same minimum pitch angles (blue) and new pitch angles (red).

The wind turbines with the backward sweep shapes chosen are characterized by excessive extreme and fatigue blade root torsional moments. Different changes in blade geometry must be investigated in order to overcome this issue.

It is important to remark that this type of benchmarking have to be based on wind turbines that produce the same power output below rated wind speed. The risk is a significant overestimation of the beneficial and negative effects brought by the use of geometrical bend-twist coupling. A load analysis that takes into account excessive discrepancies in the power curves cannot be trusted to evaluate the potential of passive control strategies.

IV. Conclusions

The current study showed the importance of providing definite guidelines for the benchmarking of wind turbines that use geometry-type passive control. Results have been reported with the purpose of comparing different configurations of wind turbines with backward swept blades. Main difference between the sets of simulations proposed was the implementation of a simple scheme able to provide the benchmarking with wind turbines characterized by comparable power curves. If the wind turbines used for the benchmarking produce less power below rated wind speed than the baseline, the beneficial load alleviations brought by the passive control method chosen can be overestimated. In order to give a correct estimation of the load variations brought by the passive control methodologies isolating its effects, the recommendation is that the benchmarking has to be based on wind turbines with similar power curves.

References

- [1] T. D. Ashwill, "Passive Load Control for Large Wind Turbines," in *48th AIAA Meeting, Orlando, Florida*, 2010.
- [2] D.R.S. Verelst, T.J. Larsen, "Load Consequences when Sweeping Blades - A Case Study of a 5 MW Pitch Controlled Wind Turbine," Risø-R-1724(EN), Risø DTU, August 2010.
- [3] M. H. Hansen, "Aeroelastic Properties of backward swept blades," in *49th AIAA Meeting, Orlando, Florida*, 2011.
- [4] M. Zuteck, "Adaptive Blade Concept Assessment: Curved Planform Induced Twist Investigation," Sandia, 2002.
- [5] T.J.Larsen, A.M.Hansen, *How 2 HAWC2, the user's manual*, Roskilde, Denmark: June 2013, June 2013.
- [6] Larsen, T.J., Aagard Madsen, H., Larsen, G.C. and Hansen, K.S., "Validation of the dynamic wake meander model for loads and power production in the Egmond Aan Zee wind farm," *Journal of Wind Energy*, vol. 16(4), no. doi:10.1002/we.1563, pp. 605-624, 2013.
- [7] Kim, T., Hansen, A.M., and Branner, K., "Development of an Anisotropic Beam Finite Element for Composite Wind Turbine Blades in Multibody System," *Journal of Renewable Energy*, vol. doi:10.1016/j.renene.2013.03.033, pp. 59:172-183, 2013.
- [8] C. Bak, F. Zahle, R. Bitsche, T. Kim, A. Yde, L.C. Henriksen, A. Natarajan, M.H. Hansen, "Description of the 10 MW Reference Wind Turbine," DTU Wind Energy Report-I-0092, Roskilde, Denmark, July 2013.
- [9] T.D. Ashwill, G. Kanaby, K. Jackson, M. Zuteck, "Development of Swept Twist Adaptive Rotor (STAR) Blade," in *48th AIAA, Orlando, Florida*, 2010.

Integrated aero-structural optimization of wind turbine rotors

P. Bortolotti¹, C.L. Bottasso¹

¹Technische Universität München, Wind Energy Institute
Boltzmannstr. 15, 85748 Garching b. München, Germany
Mailing address, pietro.bortolotti@tum.de

Abstract

The present work describes two methodologies for the integrated aero-structural optimization of wind turbine rotors. Pursuing the idea of a holistic approach to the optimization problem, the two methods aim at minimizing the cost of energy by performing high-fidelity simulations that allow the accurate description of all the operative conditions experienced by a wind turbine. The two methods are applied to a conceptual 10 MW wind turbine model and the results prove good consistency. The optimized rotor design shows higher rotor solidity and higher maximum chord. This allows to achieve a higher structural efficiency without meeting with large losses in terms of annual energy production.

1. Introduction

The design of wind turbine systems is a complex engineering activity that typically aims at delivering the lowest possible Cost of Energy (CoE). The inherent multi-disciplinarity of the design activity and the intricate couplings amongst design variables render the problem extremely challenging [1]. The present work describes an integrated aero-structural optimization of wind turbine rotors that includes the aerodynamic shape optimization, the evaluation of the relevant load conditions and the optimal sizing of the structural configuration, considering the mutual couplings between the various sub-disciplines and simultaneously accounting for the presence of several design constraints.

In the public literature several studies describe procedures for a combined aerodynamic and structural design optimization process. Large efforts are for example currently being conducted at the U.S. National Renewable Energy Laboratory (NREL) with analyses of the influence of different figures of merit during the optimization process [2]. An important study has also recently been released by Ashuri et al. [3], where a trade-off between model accuracy and computational costs is investigated to reach the minimum CoE. A global reduction of the CoE is then reported thanks to an optimal coupling between rotor aerodynamic performance and rotor and tower structures. In the public literature other studies are also available and they mainly differentiate for level of fidelity of the models used [4-7]. The current work fits in this framework of research by aiming at developing integrated aero-structural optimization procedures using high-fidelity models and it aims at continuing past efforts towards the holistic optimization of wind turbines [1].

The paper is organized as follows. After the introduction reported in Sect. 1, Sect. 2 describes the structure of the two algorithms. Sect. 3 is then devoted to the presentation of the results, while the paper is closed by Sect. 4, where the main conclusions of the study are presented.

2. Structure of the optimization algorithms

This section aims at presenting the main structure of the two aero-structural optimization algorithms. Here only a short description is reported, while interested readers can find more details and the formal description of the algorithms in [8].

2.1. Pre-Assumed Aerodynamic Shape algorithm

The first approach, hereafter named PAAS (Pre-Assumed Aerodynamic Shapes), consists of three consecutive steps. First, a family of rotor aerodynamic shapes is created by optimizing the chord distributions of the blades to get the maximum Annual Energy Production (AEP) for different values of solidity σ and maximum chord c_{\max} , which are introduced as constraints throughout the optimization

process. The twist distribution is also obtained in the same optimization process to maximize the AEP. Second, each of these configurations goes through a subsequent structural optimization. Eventually, the global optimum solution is the one producing the lowest CoE. Assuming that the family of blades describes a representative field of solution, this procedure allows for a good identification of the global minimum.

The PAAS approach offers a very robust and reasonably fast tool to understand the global behavior of the CoE. The main drawback of the PAAS approach is related to the fact that it heavily relies on the analyst's skills. The good identification of the minimum for the CoE is indeed function of the choice of the values for σ and c_{max} . No guarantee is present on the correctness of this selection. Moreover, to this day the process is not fully automated and it requires the manual creation of the family of blades and the subsequent running of the structural optimization loops. Given these pros and cons, the PAAS approach is seen as a very useful initial tool, but the need for a more accurate and automated method is highlighted.

2.2. External Aerodynamic/Internal Structure algorithm

The second optimization strategy, hereafter called EAIS (External Aerodynamic Internal Structure), is implemented having an automatic optimization routine evaluating the chord variables through the CoE. The cost function of this outer loop includes the blade structural optimization, which internally minimizes blade mass, evaluates the AEP and eventually computes the CoE. This EAIS algorithm is currently run thanks to the function `patternsearch` of the MATLAB Global Optimization Toolbox [9]. `patternsearch` offers a robust tool for the non-linear constrained optimization process, without requiring continuity and differentiability of cost functions. This is an important feature that allows to explore the solution space relaxing the continuity and linearity assumptions assumed in the problem. In EAIS, the handling of the twist optimization variables is separated from the one of the chord variables. This is found to be necessary because of the very low sensitivity of the CoE in respect to the twist. The twist is therefore found by a separate optimization routine, which aims at maximizing the power coefficient of the wind turbine in control region II.

Compared to the PAAS approach, the EAIS optimization tool offers a fully automated procedure that can explore the space of solutions more effectively and more accurately. Moreover, it does not rely on any a-priori choice of the aerodynamic parameters and the optimization algorithm can impose variations to the chord based on the downstream variations of the CoE. The main drawback of this tool compared to the PAAS approach is the higher computational cost.

3. Results and discussion

The PAAS and the EAIS strategies have been tested using as initial guess the baseline reference wind turbine developed during the European project INNWIND [10]. The main characteristics of this conceptual wind turbine model are briefly reported in Sect. 3.1. The reference model is then used to benchmark the optimization results, presented and discussed in Sect. 3.2. Before the concluding remarks, Sect. 3.3 faces the future developments that are planned for the rotor design tools.

3.1. Baseline configuration

The reference wind turbine chosen in this project is the INNWIND 10 MW. Some global data of the wind turbine are listed in Table 1. Full details can be found in [10].

Data	Value
Wind regime	IEC Class 1A
P_{rated}	10 MW
Rotor diameter	178.3 m
Hub height	119.0 m

Table 1: Main data of INNWIND 10 MW

Regarding the rotor aerodynamic properties, the blades have a c_{max} equal to 6.21 m and σ equal to 4.66%. For the rotor structure, each blade has two spar caps and two straight webs, while a third web runs at 87% of the chord. Trailing edge, leading edge and root area have extra composite reinforcements. For the optimization process, it is decided to select chord and twist variables at 4 stations uniformly distributed along the span of the blade. The structure is instead parameterized for a total of 72 thickness variables. Non-structural masses, as sandwich core, adhesive, resin uptake and paint, are also modelled for a correct blade mass estimation. The list of considered dynamic load cases (DLC) prescribed by the international standards includes DLC 1.1, 1.2, 1.3, 2.1, 2.3, 6.1, 6.2 and 6.3. The rotor of the baseline configuration has the active constraints of minimum tower clearance and fatigue lifetime.

3.2. Optimum aero-structural configuration

The results from the PAAS and EAIS approaches show good correlation. The PAAS approach scans the space of solutions with different sets of values for σ and c_{max} . An interpolation using cubic splines is then run on the σ and c_{max} values and a minimum for the CoE is assumed to exist at σ equal to 5.32% and c_{max} equal to 7.4 m. Assuming these values as active constraints, a new optimal aerodynamic shape is generated and subsequently the structural optimization loop is run. This produces the optimal solution named PAASOpt. The optimum from the EAIS approach, marked EAISOpt, follows the trend indicated by the PAAS results and is able to achieve a slightly better compromise between structural efficiency and power production. Fig. 1 reports four diagrams showing the behavior of the baseline design, the PAASOpt and the EAISOpt for the distributions along blade span of chord, twist, spar cap thickness and skin thickness. Table 2 shows the advantages of the two optima in terms of blade mass, AEP and CoE compared to the baseline configuration. Although the two methods produce results with similar trends, the EAIS method shows a greater ability to optimize the blade design at the price of higher computational costs.

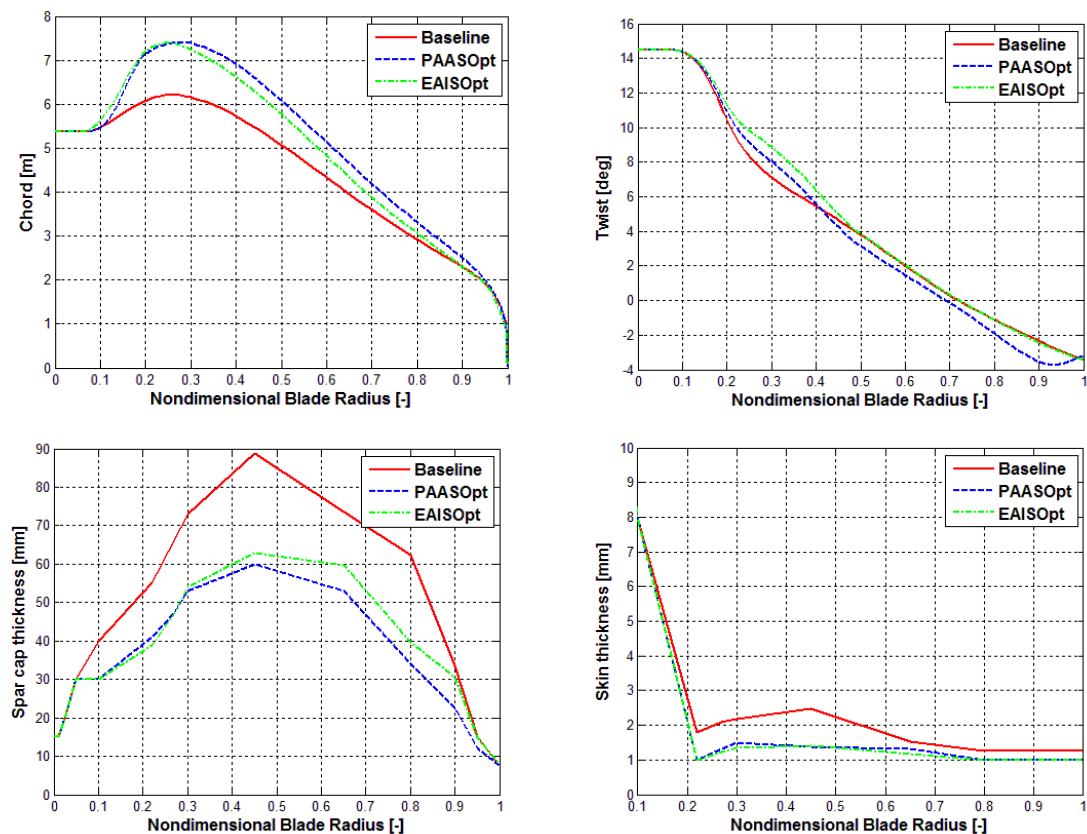


Figure 1: Comparisons between baseline design and aero-structural optima for chord distribution (top left), twist distribution (top right), spar cap thickness (bottom left) and skin thickness (bottom right)

Data	% difference from baseline	
	PAASOpt	EAIsopt
Design method		
Blade max chord	+ 19.2	+ 19.2
Rotor solidity	+ 14.3	+ 10.9
Blade mass	- 6.73	- 8.32
AEP	- 0.17	- 0.14
CoE	- 0.19	- 0.29

Table 2: Summary of results from aero-structural optimizations

3.3. Next developments

This project shows that the aero-structural approach allows to obtain the best compromise between structural and aerodynamic efficiency, but the advantages in term of CoE are very limited. In order to obtain a more remarkable reduction of CoE, the parameters that define the wind turbine configuration must be included into the design procedure. For this reason, the future work must focus on parameters that define the rotor but that also heavily affect the global wind turbine configuration, such as rotor radius, rotor cone angle, blade pre-bend and nacelle up tilt angle. Low induction rotor solutions will also be investigated.

4. Conclusions

This work shows two methodologies for the integrated aero-structural optimization of wind turbine rotors. Each approach is based on high fidelity simulation environments that allow accurate aero-servo-elastic simulations, where all the fundamental physical effects are taken into account. These two methodologies are applied to a conceptual 10 MW wind turbine and show good agreement and promising reductions in terms of CoE. These advantages are produced thanks to variations in rotor solidity and maximum chord to achieve a better trade-off between rotor structure, which is made lighter, and aerodynamic performance, which is not depressed significantly.

References

- [1] Bottasso, C.L., Campagnolo, F., Croce, A., “Multi-disciplinary constrained optimization of wind turbines”, *Multibody System Dynamics*, vol.27 (2012) pp. 21-53.
- [2] Ning N.S., Damiani R., Moriarty, P.J.: Objectives and constraints for wind turbine optimization, 51st AIAA Conference, January 2013
- [3] Ashuri T., Zaaier M.B., Martins J.R.R.A., van Bussel G.J.W., van Kuik G.A.M.: Multidisciplinary design optimization of offshore wind turbines for minimum levelized cost of energy. *Renewable Energy*, 68, 893–905 10.1016/j.renene.2014.02.045 (2014)
- [4] Fischer G.R., Kipouros T., Savill A.M.: Multi-objective optimisation of horizontal axis wind turbine structure and energy production using aerofoil and blade properties as design variables. *Renewable Energy*, 62, 506-515, 10.1016/j.renene.2013.08.009 (2014)
- [5] Bottasso C.L., Croce A., Sartori L., Grasso, F.: Free-form design of rotor blades. *Proceedings of The Science Of Making Torque From Wind*, Copenhagen, June 2014
- [6] Maki K., Sbragio R., Vlahopoulos N.: System design of a wind turbine using a multi-level optimization. *Renewable Energy*, 43, 101-110 DOI: 10.1016/j.renene.2011.11.027 (2012)
- [7] Vesel Jr. R.W., McNamara J.J.: Performance enhancement and load reduction of a 5 MW wind turbine blade. *Renewable Energy*, 66, 391-401 DOI: 10.1016/j.renene.2013.12.019 (2014)
- [8] Bottasso, C.L., Bortolotti, P., Croce, A., Gualdoni, F., “Integrated aero-structural optimization of wind turbine rotors”, *Multibody System Dynamics*, In preparation for submission
- [9] Matlab. The MathWorks Inc., 3 Apple Hill Drive, Natick, MA 01760-2098, USA, www.mathworks.com
- [10] C. Bak, F. Zahle, R.Bitsche, T. Kim, A. Yde, L.C. Henriksen, P.B. Andersen, A. Natarajan and M.H. Hansen, “Design and performance of a 10 MW wind turbine”, *J. Wind Energy*, To be accepted

Design of a Model Floating Wind Turbine to Measure the Coupled Response to Wind and Wave Action

Conor Gilmour
University Of Strathclyde
Glasgow, Scotland
Conor.gilmour@strath.ac.uk

Steven Martin
University Of Strathclyde
Glasgow, Scotland
Steven.martin@strath.ac.uk

Sandy Day
University Of Strathclyde
Glasgow, Scotland
Sandy.day@strath.ac.uk

Abstract—This project investigates how to better scale wind turbine rotors in order to build more representative scale models of offshore floating wind turbine systems. Previous experiments have designed models with the goal of maintaining the Froude number and mass distribution. The blade chord Reynolds number drops by several orders of magnitude in such models, this is partially corrected by increasing the wind speed. However doing this increases the drag on the platform significantly and as such the model is limited in its usefulness. The aim of this project is to address the issue of the Reynolds number deficit by radically redesigning the rotor such that the coefficient of thrust of the rotor is representative of a full scale system.

I. INTRODUCTION

Wave tank modelling is a well established practice and is invaluable in the design of offshore vessels. One of the main scaling methodologies employed in wave tank testing is Froude Scaling [1]. The Froude Number is a dimensionless quantity that can be defined as the ratio of a body's inertial to gravitational forces. In the construction of a model this number is kept constant. Such scaling methodology works very well for models where wind speed isn't as important as, say, in a floating wind turbine. To correctly Froude scale the wind we divide it by the square root of the geometric scale factor. This is sufficient for vessels where aerodynamic effects are not significant. In the case of a floating wind turbine however there are forces exerted on the platform due aerodynamic performance of the rotor, these are dependent on the Reynolds Number which in turn is dependent on wind speed. Froude scaling the wind correctly has an adverse effect on the Reynolds Number and increasing the wind speed to try and increase the Reynolds Number will introduce unrealistic drag effects on the platform.

The aerofoils of a full scale turbine are designed to operate in conditions where the Reynolds Number (Re) is $\sim 10^7$. At model scale this figure drops to $\sim 10^4$. The aerofoils were never designed to operate in these conditions and as such the performance of the rotor and therefore the effects of the wind on the vessel are not representative of the real situation. This investigation aims to devise a way to correctly model the thrust and the vessel's resulting overturning moment on a Froude scaled model by redesigning the turbine rotor to

operate in the low Reynolds number environment. Offshore floating wind turbines are operating in a highly unsteady environment. It is a structure which has six degrees of freedom and its motion is highly complex and non-linear. For this reason the analysis below only takes into account the turbine's response in the steady state. The performance of the model is designed to match as closely as possible to that of the prototype in the steady state, this should ensure that performance of the model in the unsteady state is as representative as possible. It must be noted that to achieve the required performance from the model it need to look like the prototype. One is free to vary the shape of and number of the blades in order to achieve the desired results. The investigation is performed using Xfoil to generate lift and drag data for various aerofoils and CCBlade, a purely aerodynamic BEM (Blade Element Momentum) package, to calculate the coefficient of thrust.

II. BACKGROUND

The NREL 5 MW Baseline Wind Turbine, which this report is based upon, has blades composed of NACA and Delft aerofoils [3] which operate at Re of $\sim 10^7$. Their performance is incredibly poor at model [1] scale where we have Re of $\sim 10^4$. At high Re the flow over the aerofoil is laminar with an orderly transition to turbulent near the leading edge. The flow remains attached over the full length of the chord of a typical aerofoil resulting in lift which increases with angle of attack. In this state drag is minimal prior to stall. At low Reynolds number, the flow over such an aerofoil has the potential to separate close to the leading edge, this is known as a laminar separation bubble, it has the effect of increasing the drag and destabilising the lift performance. There are several options which can be implemented to attempt to reduce the effect of transitional flow:

1. Trip the flow
2. Redesign the rotor

Tripping is accomplished by artificially introducing turbulence to the flow as it passes over the aerofoil [4]. Turbulent flow is

much more likely to resist the formation of the laminar separation bubble. When the flow surrounding the aerofoil is laminar the boundary layer can easily expand but the erratic nature of the turbulence resists this and there is no laminar separation bubble we therefore see improved lift and reduced drag characteristics. Roughening the surface of the leading edge with, for example, a strip of sand paper should induce this effect. All results presented assume tripped flow. There are aerofoils specifically designed to operate at low Re; these are typically very thin with a thickness ratio of around 8% whereas aerofoils operating at high Re can be in excess of 18%. The thickness will dictate the pressure on either side of the aerofoil and therefore the lift. On the thicker aerofoils flow will only remain attached if the Reynolds number is large enough. If we can redesign the rotor with blades that use more suitable aerofoils we can model the thrust and thus the overturning moments correctly

III. AEROFOILS

There is a vast array of aerofoils, they each have their own characteristics and operate optimally within a specific range of conditions. As already stated the aerofoils of the full scale turbine are completely inappropriate for use at model scale. In the past the development of low Re aerofoils was driven by model aircraft enthusiasts [5] and there was little industrial interest. However the current interest in UAEs which operate in a similar Reynolds environment is reinvigorating development of this niche technology.

A. Lift and Drag plots

Aerofoils experience both lift and drag when subject to an incoming airflow. Ideally we should see that lift increases fairly linearly with angle of attack until stall. Drag varies like a bathtub i.e. some drag at low angle of attack dropping to be negligible as the angle increases before increasing quickly as the aerofoil begins to stall.

In Figure 1 we see the lift and drag coefficients plotted against angle of attack for one of the aerofoil sections used in the NREL 5MW Baseline turbine (DU25) at high Re. The effect of the low Reynolds number environment is obvious from Figure 2. Lift becomes erratic and reduced

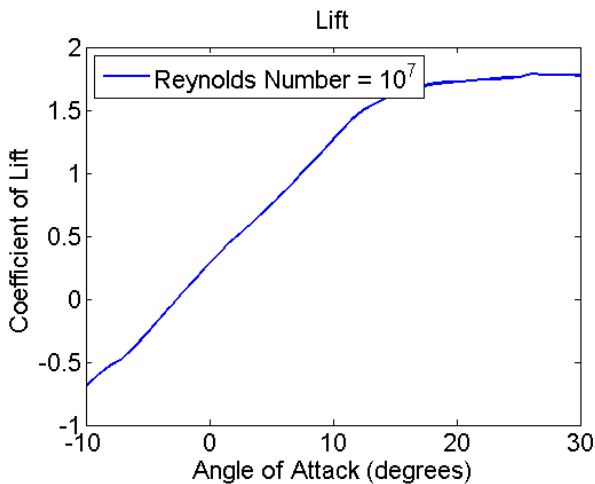


Figure 1 Lift coefficient against angle of attack for DU25 aerofoil in high Re environment

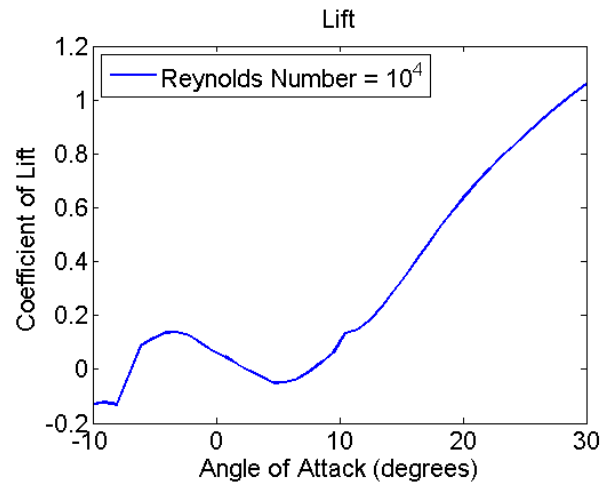


Figure 2 Lift coefficient against angle of attack for DU25 aerofoil in low Re environment

while drag is around an order of magnitude higher between 0 and 10 degrees of angle of attack. The same plots for a low Re specific aerofoil (RG15) are shown in Figure 3. We see that a marked improvement over the DU25 blade at low Re although it is still not as good as the DU25 blade in a high Re environment. There are a great many such aerofoils available and several will be tested. (NB: Drag plots are omitted in this

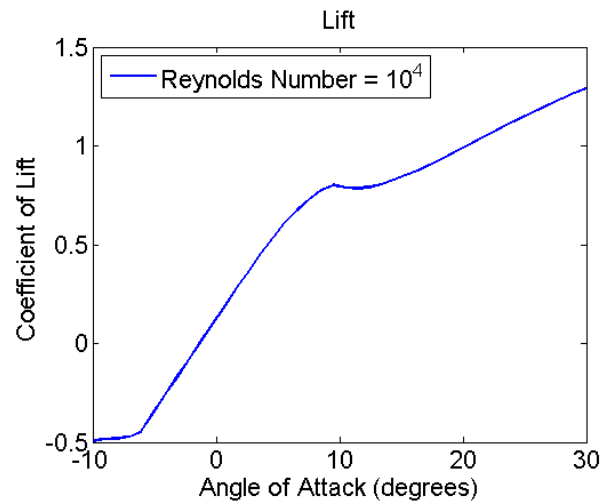


Figure 3 Lift coefficient against angle of attack for RG15 aerofoil in low Re environment

version of the paper)

Figure 4(a) clearly illustrates the problem dealt with in this investigation. We see how low the thrust coefficient of the Geometrically scaled model compares to the prototype. This, as discussed above is due to operation in the low Re environment. The blades are not generating enough lift and so the performance is incredibly poor. Unfortunately, scaling the turbine geometrically but changing the aerofoil profile does not produce the desired thrust as shown in Figure 4(b). We see a significant improvement but Re is still very low in this situation, lower than the ideal operating range of the low Re specific aerofoils. as a result a series of atypical design approaches are investigated.

IV. SCALED TURBINE PERFORMANCE

A. Blade Number

There are several ways in which the rotor thrust can be increased. The simplest way being to add more blades. This produces an improved result with regards to thrust modelling as we can see in Figure 5 but is not really a suitable solution. An accurately scaled rotor would have a mass in the region of 200g which is near impossible to achieve with three blades let alone five. It is necessary to correctly scale the mass in order to model to gyroscopic forces. There is also the issue of solidity. Solidity affects, among other things, the axial induction factor of the wind turbine so in increasing this significantly one is changing the fundamental dynamics of the turbine [6]. Increasing the solidity effects how the thrust is

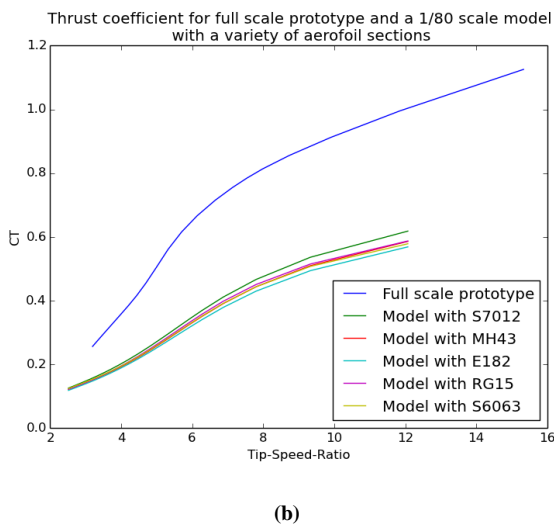
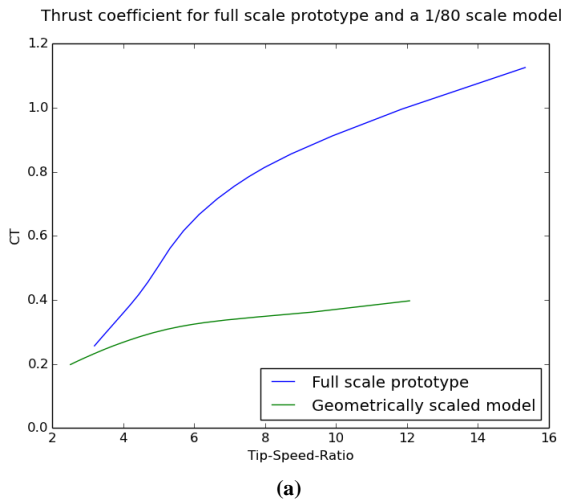


Figure 4 Geometrically scaled model and model with a variety of low Re aerofoils

being generated. With higher solidity, more of the thrust is being generated by drag as opposed to by lift. We want the thrust to be generated by drag and lift in the correct proportions and this necessitates keeping the solidity the same for model and prototype. This is important because a floating

turbine is a moving structure so it is seeing a continually varying angle of attack and therefore a fluctuating coefficient of lift, this implies an erratic coefficient of thrust which will not be correctly represented if the thrust is induced by pressure on the rotor.

B. Blade Geometry

One can also increase the chord length of the blades [7]. The Reynold's number will be scaled by whichever factor one

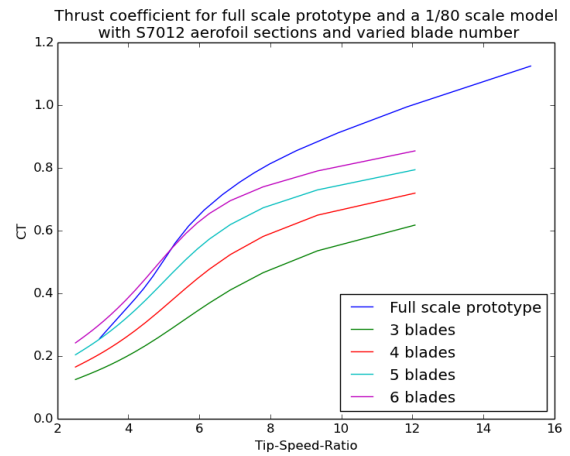


Figure 5 Coefficient of Thrust plotted against TSR for a variety of blade numbers

chooses. This will yield promising results with respect the thrust but has the problems of increased mass and solidity. Another approach to this problem is to remove half of the blade and increase the chord length of the remaining half to match the solidity of the original turbine as illustrated by Figure 6. The specifics of the design of the half blade are open to question, particularly where it changes from stem to blade. Large discontinuities of the blade would result in poor real world performance due to three dimensional aerodynamic effects not accounted for by the code, like the circulating flow

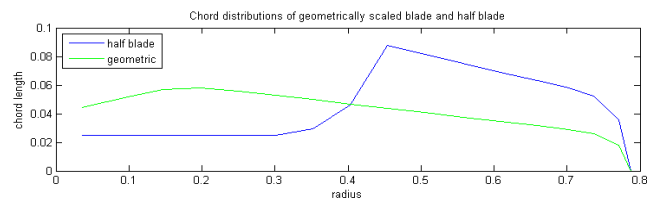


Figure 6 Modified and original chord profiles

along the length of the blade. Here, one would imagine that the best shape for lowest drag would be an ellipse, like the tip. It was noted however that small extensions of the aerofoil area here significantly increased the performance of the model so the thrust coefficient was higher than that of the prototype. It was also noted that the actual shape of the blade (with solidity constant) had very little bearing on the performance of the model. This leads to the conclusion that structural performance and the need to keep the mass low without adding much more material will drive the design of this section. The nearest examples of rotors in this configuration are those of helicopter tails. These seem, upon visual

inspection, to have a similar basic shape as the design discussed here. We see in Figure 7 that this new half blade geometry shows a marked improvement over the previous design. We also note that at higher TSRs the improvement is much reduced. This can be attributed to the angle of attack being reduced as the rotor spins more quickly.

C. Twist

Turbine blades are designed with a twist. This is to ensure that the angle of attack is consistent across the whole blade since apparent wind speed is the result of contributions from the freestream wind speed and the radially varying tangential velocity of the blade. Keeping this constant angle of attack is important at full

scale both structurally and for smooth power delivery. Angle of attack of a wind turbine blade is the angle the apparent wind speed makes with the plane of the rotor minus the twist; by reducing the twist we increase the angle of attack and as such should be able to generate the necessary extra lift. This investigation is not primarily concerned with achieving a constant angle of attack; we therefore have the freedom to vary the twist to achieve the best results. Figure 7 shows the effect of modifying the twist of the half blade. It is found that dividing the twist by 4 along the length of the blade results in a thrust curve that matches very closely with that of a prototype.

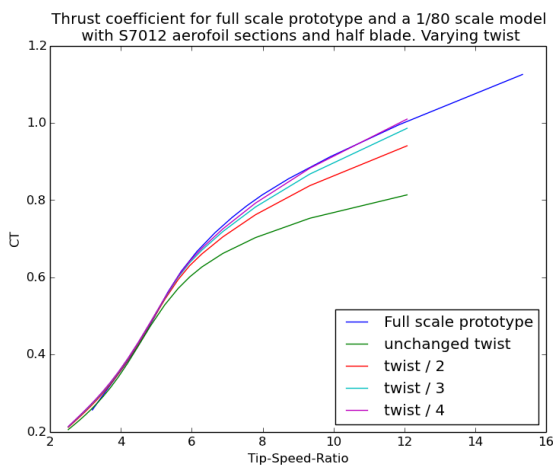


Figure 7 Performance of Model with modified chord profile and modifications to the twist

D. Error Analysis

The code used performs the analysis using 2 dimensional aerodynamics, it was also necessary to extrapolate data generated from Xfoil for use across a greater range of angles of attack. This means that in all likely-hood the thrust coefficient of a real model will not be precisely what is shown on the above graphs. It is possible to augment the data for lift and drag. The coefficient of drag can be increased significantly with little effect on the model performance. Changing the lift however has a more pronounced effect. Figure 8 shows how the turbine behaves when the coefficient of lift is reduced by 20% and the coefficient of drag in

increased by 50%. It is clear from figure 8 that the performance is reduced but it is still a significant improvement over the performance in 4(a). This implies that a model turbine designed as recommended by this analysis should generate good results in spite of less than perfect modelling conditions, manufacturing defect and analytical errors.

V. CONCLUSION

This investigation aimed to address one of the major issues associated with the modelling of floating offshore wind

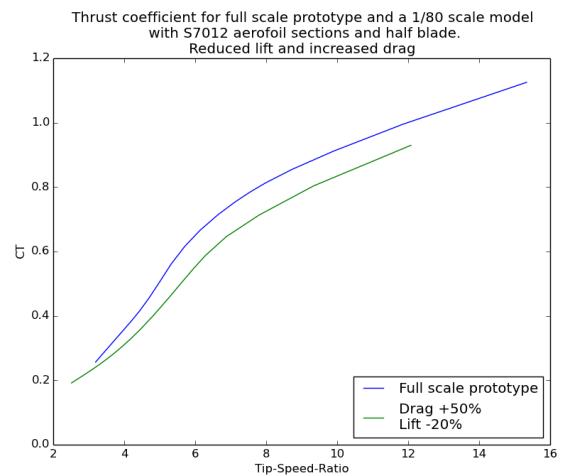


Figure 8 Some rudimentary error analysis for the modified blade with twist/4

turbines. The forces exerted on the platform by the turbine must be modelled correctly. By far the most significant force is that of the thrust exerted on the turbine rotor which is responsible for a large overturning moment. Ideally we want to scale this correctly along with the gyroscopic loading associated with the rotating disc. The latter is dealt with by Froude scaling the mass of the rotor and maintaining the TSR. The former must be dealt with by designing a rotor with blades with the correct lift characteristics. This was achieved by redesigning the blade to maximise to Reynolds Number. The half blade design doubles the Reynolds number everywhere and using the more appropriate S7012 aerofoil makes the best use of the low Reynolds environment. Tripping the flow eliminates the laminar separation bubble and as such increase the lift. Finally decreasing the twist increases the angle of attack lifting the trust at high TSRs and producing a thrust coefficient which matches that of a prototype across an extensive range of TSRs.

REFERENCES

- [1] H. R. Martin et al. Methodology for wind-wavebasin testing of floating offshore wind turbines. *Journal of Offshore Mechanics and Arctic Engineering*, 2012.
- [2] I. Prowell, A. Robertson, J. Jonkman, G.M. Stewart, and A.J. Goupee. Numerical prediction of experimentally observed behavior of a scale model of an offshore wind turbine supported by a tension-leg platform. Technical Report NREL/CP-5000-57615, National Renewable Energy Laboratory, Golden, CO, January 2013. To be presented at the 2013 Offshore Technology Conference Houston, Texas May 6 9, 2013.

- [3] J. Jonkman, S. Butterfield, W. Musial, and G. Scott. Definition of a 5-mw reference wind turbine for offshore system development. Technical report, National Renewable Energy Laboratory, 2009.
- [4] Ashok Gopalarathnam Benjamin A. Broughton Bryan D. McGranahan Michael S. Selig. Design of low Reynolds number airfoils with trips. *Journal of Aircraft*, 40(4):768-775, 2003.
- [5] Philippe Giguere and Michael S Selig. Low Reynolds number airfoils for small horizontal axis wind turbines. *Wind Engineering*, 21(6):367-380, 1997.
- [6] T. Burton, N. Jenkins, D. Sharpe, and E. Bossanyi. *Wind Energy Handbook*. Wiley, 2011.
- [7] Erik-Jan de Ridder et al. State of the art model testing techniques for floating wind turbines.
- [8] Easy composites, carbon rod. <http://www.easycomposites.co.uk/Category/pultruded-carbon-bro-tube-1m.aspx>.
- [9] Solid solutions low density rigid foam. <https://secure.solidsolutions.com.au/datasheets/>

EXPERIMENTAL METHODS FOR THE OPTIMAL DESIGN OF SMALL WIND TURBINES

N. Bartolini¹, F. Castellani¹, A. Garinei², R. Pignattini¹

¹University of Perugia, Department of Engineering, Via G. Duranti 93 – 06125 Perugia (ITALY),
nicola.bartolini@studenti.unipg.it

²DMII, Università degli Studi Guglielmo Marconi, Roma 00193, Italy a.garinei@unimarconi.it

ABSTRACT

The design of small wind turbines (SWT) is very often developed through a pragmatism rather than a theoretical approach. The small size of these systems allows a fast and cheap prototyping and usually technicians simply try the best solutions without understanding the principle of operation.

In the present work a new experimental approach is proposed in order to quickly characterize and define the optimal design parameters for different types of small wind energy converters and to validate numerical methods used for the design.

Two different kinds of tests of the key components as well as the overall wind conversion system are proposed:

1. measurements on the electrical generator test rig;
2. wind tunnel test.

Results demonstrate that this kind of experimental activity can give very useful information for strongly improving the performances of the system and for a validation of all the design methods.

INTRODUCTION

Optimal design of small wind energy converters can be defined using numerical tools [1] in a very detailed way. Anyway it could be difficult to define the optimal electrical load curve [2,3] for operation because of the fixed blade pitch and the wide range of rotational speed. Measurements on the electrical generator test rig are fundamental in order to define the efficiency of all the components of the energy conversion chain: electrical generator, power conversion systems etc.... Wind tunnel tests (fig.1) are as well fundamental to finally verify the aerodynamic efficiency of the rotor and to optimize the coupling of mechanical and electrical devices.

In the present work, results of the characterization of different kinds of wind turbines with a rotor diameter of up to 2 m and a rated power of 1.5 kW are discussed.



Figure 1: Wind tunnel test for torque and electric power measurements.

The wind turbines can be roughly classified according to their dimensions in terms of rotor swept area; turbines with a rotor swept area between 2 m^2 and 200 m^2 are considered small wind turbines [2]. For this kind of wind energy converters a substantial market exists mainly for remote applications or systems suited to supply energy for residential consumption [4]. With the growth of energy production from renewable sources, in recent years there have been considerable investments by national

governments, especially in northern Europe, just in respect to the installation of small wind turbines [5]. This kind of machines can have very different design frames, starting from the rotational axis arrangement. Vertical axis turbines (VAWT) present some benefits especially for small sizes (typically quieter, no yaw control needed for variable wind direction), but the horizontal axis turbines (HAWT) had a greater development, on research fields too, from when it became accepted that they were more efficient at large scales [6]. Another design variable is the number of blades to use, depending on the desired efficiency of the turbine and on the production costs. Usually, increasing the number of blades increases the total efficiency [7], but the complexity of the machine is higher. The level of output power is generally low because of their small size and for this reason the total cost of the entire system has to be as low as possible. To reach these objectives, the use of non-conventional design approaches can be helpful, as well as the use of fast, cheap and universal experimental methods for the final design characterization and optimisation.

EXPERIMENTAL METHODS

This work focuses on some experimental methods exploitable to evaluate the performances of single parts of the system as well as the entire chain of energy conversion. The first method is focused on the evaluation of the efficiency of electrical generators with respect to the rotational speed and the electrical load. The test rig includes an inverter-controlled electrical engine (4 kW) that provides the mechanical power in input to the generator through a shaft, instrumented with an optical speed sensor and a torque meter. The generator provides in output a triphase electrical current, connected with a rectifier. In the DC circuit, the values of tension and intensity are measured to evaluate the electrical power obtained. Tests are performed for different kinds of permanent magnet gearless generators, which are compact and specifically designed for this kind of application. Using this method, the power output and the real efficiency of generator and rectifier is evaluated from values of mechanical and electrical power measured in working conditions; during this test the electrical power is dissipated on a rheostat.

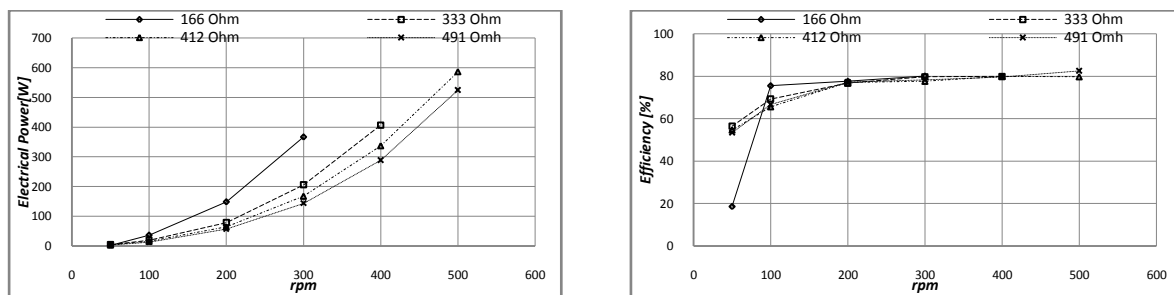


Figure 2: Experimental data for electrical power in output and efficiency for the generator

The efficiency of the system (η_s) is defined as:

$$\eta_s = \frac{P_{out}}{P_{in}}$$

where P_{in} is the mechanical power in input and P_{out} is the electrical power in output obtained in the DC circuit:

$$P_{in} = \omega_m T_m P_{out} = V_{DC} I_{DC}$$

where ω_m is the rotational speed of the engine, T_m is the torque on the shaft, V_{DC} and I_{DC} are the values of tension and intensity of the current. The trend of the electrical output power and the efficiency of a 500W electrical generator is shown in figure 2; in this case, for rotational speeds between 200 and 500 rpm (the rated rotational speed of the generator is 450 rpm), the efficiency is almost constant around 80%, with a weak dependence from the electrical load value (the outlier value at 50 rpm for 166 Ω is due to instability in continuous operation). Contrariwise, the electrical power in

output is strongly influenced by the rotational regime; for low values of resistance, the power output is higher at low rotational speeds, but the stability of the system is not ensured for high rotational speeds. It is because lower is the resistance in the circuit, higher is the value of current intensity, reaching the upper permitted limit. This kind of results is very helpful to choose the optimal load value for different rotational speeds, to generate an optimal load curve for the inverter used to convert the electrical power for the grid.

Another experimental test involves the electrical components previously described connected to the small wind turbine in operation in the wind tunnel. In this way is possible to evaluate the performances of the entire system, considering the aerodynamical, mechanical and electrical coupling.

The test is used to characterize the performance with a fixed incoming wind speed (power coefficient C_p versus speed ratio λ). The power coefficient is defined:

$$C_p = \frac{P}{\frac{1}{2} \rho A v^3}$$

Where ρ is the air density, A is the area swept by the rotor, v is the incoming wind speed and P is the mechanical power out from the turbine:

$$P = \omega_m T_m$$

The coefficient λ is the ratio between the speed of the tip section and the incoming wind speed.

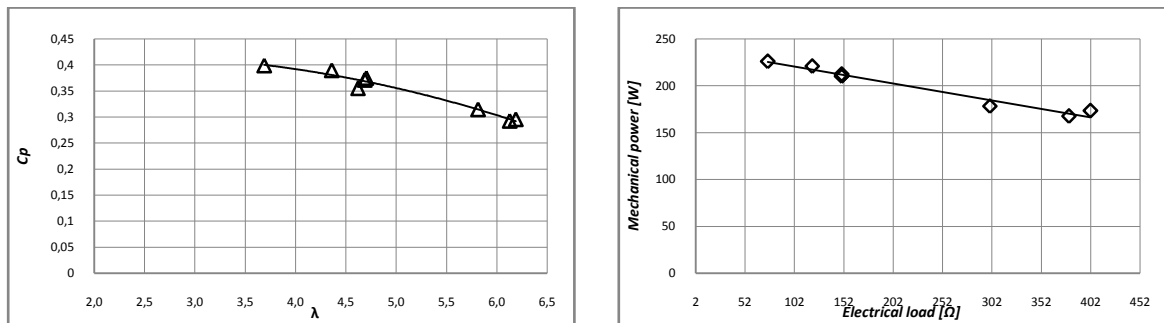


Figure 3: Experimental characteristic curve of the turbine and mechanical power in output with respect to the electrical load (fixed wind speed)

This kind of test is really useful to tune up the load curve in function of the rotational regimes and to compare the experimental results with the numerical simulations in term of global efficiency. Important informations are given about the stability of the turbine for different operating points.

In the last proposed test, the aerodynamic stall is experimentally investigated[8]. Numerically, knowing the characteristics of the used profile, it is possible to have informations about the pitch angle where the this phenomenon occurs. This method includes wind tunnel tests with flow visualization using wool threads and video acquisition. At first this kind of test was performed with only a single blade vertically mounted in the center of the wind tunnel test room. Even if this situation is quite far from the real operation conditions of the blade this test was useful to develop the image post-processing tool in order to finally do this measurement triggering the video acquisition of the complete rotor during the operation of the turbine. The used support permits the variation of the rotational angle of the blade. Wool threads are applied in the suction surface of the blade; when the air flow reaches a stable speed value, if aerodynamic stall is not present the wool threads remain attached to the surface without oscillatory motions. Contrariwise, when the phenomenon appears, there is a deattachment of the fluid from the surface of the blade and vortices are generated, that leads to an oscillatory motion of the threads. Because of the warpage of the blade, may occur operating conditions where a section of the blade is under stall with the onset of instable vibrations, but the rest of profiles are regularly working. The aim of this method is to provide a clear image that shows the behaviour of the wool threads, indicative about the presence of the phenomenon. To do this, an high-speed camera is used to observe the behaviour of the threads; the acquired frames are processed by a dedicated software, able to filter the images, isolate the threads and generate binary images. All the frames of the single video

are then analyzed to build a single image that show the threads activity for the test. Three tests are conducted at the same wind speed, varying the rotational angle of the entire blade. In the first test, the pitch angle of the tip section is 0 degrees and from the numerical data, is predictable to have no stall phenomena. In the second test the angle is increased to 10 degrees, and a stall area near the tip section is expected. The angle is increased again to 30 degrees and in all the blade the stall is expected, except for the section near the root of the blade.

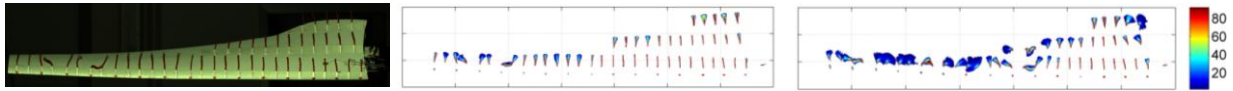


Figure 4: Blade with wool threads (a), activity of threads for rotational angle of 20° (b) and 30° (c)

The elaborate images confirm the expected behaviours of the stall phenomenon with respect to the angular rotation of the blade.

RESULTS

The first described test permits to evaluate the general behaviour of the generators, in terms of efficiency and electrical power output. Usually the informations provided by the manufacturer are not exhaustive with regards to the operating under different electrical loads and this test is useful to reach optimal load curves for the generator in order to increase the total efficiency for the system. The second test is useful to evaluate the behaviour of the mechanical-electrical coupling, providing indications on the stability of the operating points. The experimental characteristic curve of the machine is obtained, to compare with the expected results from the design process. The third test provides useful informations with regard to the behaviour of the aerodynamic stall that can appear on different sections of a twisted blade. The images confirm the data obtained from the numerical simulations for the analysed blade.

CONCLUSIONS

The experimental methods proposed in this work, have the aim to provide useful informations for the optimization of the system in terms of power output and efficiency. Not less, results for the validation of the numerical models used in the design process are provided. One of the main characteristics of these methods is the cheapness and the speed to earn useful results. This allow to marginally affect the final cost of the product; this can be fundamental for the development of small wind turbines.

REFERENCES

- [1] D. Marten, "QBlade e Guidelines v 0.6", (2012), TU Berlin
- [2] D. Wood, "Small wind turbines." Springer Berlin Heidelberg, 2011.
- [3] Hsiao, Fei-Bin, Chi-Jeng Bai, and Wen-Tong Chong. "The Performance Test of Three Different Horizontal Axis Wind Turbine (HAWT) Blade Shapes Using Experimental and Numerical Methods." *Energies* 6.6 (2013): 2784-2803.
- [4] Adam Mirecki, Xavier Roboam, Member, IEEE, and Frédéric Richardeau. "Architecture Complexity and Energy Efficiency of Small Wind Turbines", *IEEE Transactions On Industrial Electronics*, Vol. 54, No. 1, February 2007
- [5] Jorund Buen, "Danish and Norwegian wind industry: The relationship between policy instruments, innovation and diffusion", *Energy Policy*, Volume 34, Issue 18, December 2006, Pages 3887–3897
- [6] Robert Howell, Ning Qin, Jonathan Edwards, Naveed Durrani, "Wind tunnel and numerical study of a small vertical axis wind turbine", *Renewable Energy* 35 (2010) 412–422
- [7] Wilson, Robert Elliott, Peter BS Lissaman, and Stel N. Walker, "Aerodynamic performance of wind turbines." Corvallis, Oregon: Oregon State University, 1976.
- [8] Nigel Swytink-Binnema, David A. Johnson, "Novel Image Analysis Method for Blade Aerodynamic Performance on Operational Turbine". *Journal of Physics: Conference Series* 524 (2014).

“

Aerodynamic Control

”

FLAPS FOR WIND TURBINE APPLICATION: NOISE SOURCE LOCALIZATION ON A TEST AEROFOIL

Carl Robert Brand*, J.R. Seume

ForWind - Center for Wind Energy Research, Leibniz Universität Hannover
Institute of Turbomachinery and Fluid Dynamics - TFD
Appelstr. 9, 30167 Hanover, Germany
Email: Brand@tfd.uni-hannover.de, Seume@tfd.uni-hannover.de

ABSTRACT

Wind turbine rotors are exposed to unsteady wind conditions such as gusts and the atmospheric shear layer. These unsteady conditions cause highly dynamic loads on rotor blades, which significantly reduce wind turbine operation time. Blades with trailing edge flaps applied have the potential to significantly reduce these critical loads. However, the flaps can potentially generate an additional sound source on the blades. In an experimental set-up, a test aerofoil with a flap will be investigated to study the sound characteristic at the flap using a microphone array and a beamforming algorithm. The development of the acoustic test set-up is presented in this paper. Starting with the basic set-up presentation, the activities and applied methods to develop a suitable acoustic set-up are described. A proof of the applications is demonstrated by a Monte Carlo Simulation. The results show significant enhancement of the two acoustic map's key characteristics.

NOMENCLATURE

s = Acoustic energy
 t = Time
 M = Total microphone number
 p = Sound pressure
 \vec{x} = Coordinate vector

Greek

$\vec{\alpha}$ = Wave vector
 τ = Time delay

Subscript

m Microphone index

Abbreviations

RMS Root mean square
MLW Main lobe width

INTRODUCTION

During operation, unsteady wind conditions and the atmospheric shear layer cause high dynamic loads on wind turbine rotors. These high loads can lead to long-term blade failure, and to non-reparable wind turbine breakdown. Trailing edge flaps can potentially reduce these critical loads significantly [1]. However, experimental investigations of aerofoils with flaps for aviation applications show significantly higher global sound emissions [2]. Specifically the turbulent, unsteady flow around the flap side edge causes additional sound sources, emitting noise in ranges which are audible to humans. Consequently, these additional sound sources can also emerge when using flaps on wind turbine rotors.

Wind turbine acoustics is a major issue in the industry, for several reasons. Firstly, wind turbine operators must adhere to statutory sound emission requirements [3]. Exceeding these limits will lead to a withdrawal of permission to operate, causing

*Address all correspondence to this author.

large financial losses. Secondly, the turbines acceptance by local residents depends significantly on the level of sound emitted. Furthermore, wind turbine sound has been shown to disturb the nearby fauna.

Consequently, the acoustic properties of an aerofoil with a trailing edge flap for wind turbine applications must be investigated. An experimental test set-up has therefore been designed at the Institute of Turbomachinery and Fluid Dynamics. A microphone array will be used to identify the sound sources at the flap. Using post-processing, an acoustic flap map will be generated. The map quality is reliant on the microphone arrangement in the array, which can be improved through an optimization process [4]. To this end, a synthetic sound source localization process and an optimization algorithm are linked. The implementation and a demonstration are presented in this paper.

The paper is organized as follows: firstly, the experimental test set up is presented and then secondly, the microphone array sound sources localization technique is introduced. The major focus of this paper is on the array design process. The process for an optimal microphone array design is described. A proof of the process is demonstrated by Monte Carlo Simulation results. Finally, a conclusion and an outlook on further work are given.

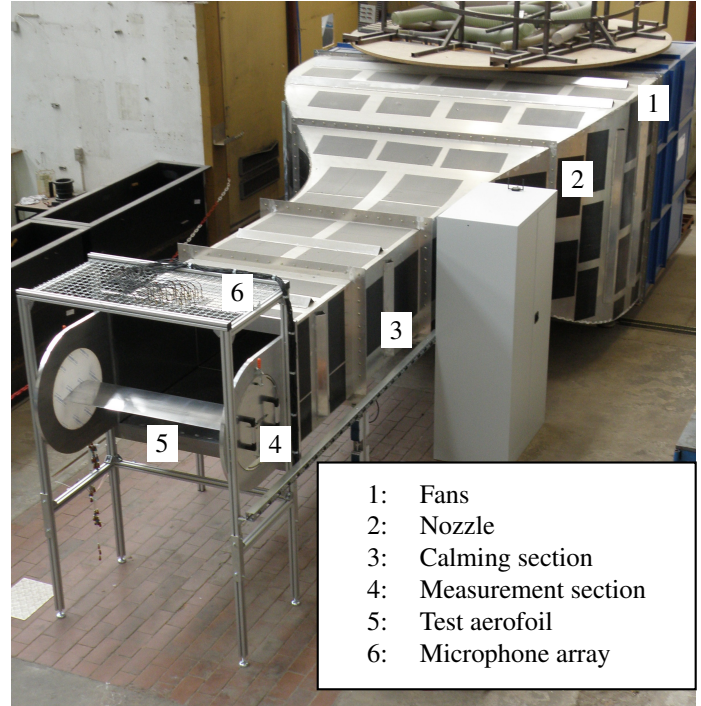


FIGURE 1. Wind tunnel test rig

TEST SET-UP

The experimental sound source localization will be performed in a wind tunnel test set-up (cf. Fig. 1). The tunnel is an open jet wind operated by two high-power fans. A nozzle is placed downstream and accelerates the flow up to 25 m/s. In order to decrease flow turbulence, a 3 m inflow section is set between the nozzle and the measuring section, which is built in an open configuration with a cross-section of 1.2 m x 0.8 m. This section consists solely of plugs for measurement equipment and a plug for the test aerofoil. The test aerofoil is placed in the open jet core stream in the measurement section. During operation, the angle of attack is adjusted manually.

A DU-W-180 geometry is used as the basic profile for the smart blade test aerofoil (cf. Fig. 2). The smart blade span length is 1.2 m and the chord length is 0.3 m. The flap is mounted at the trailing edge and has a length of 30 % of the chord length. The flap hinge point is set to 50 % of the relative aerofoil thickness. The trailing edge flap is adjusted with an electronic controller.

A microphone array will be used to localize the sound sources on the test aerofoil. The microphone array consists of 32 single microphones and is placed outside of the stream in the measurement section. It is arranged to scan the sound sources on the aerofoil flap suction side. The microphones are sampled with an external data acquisition system. Additionally, the post-processing source localization (beamforming) is performed using external devices.



FIGURE 2. Test aerofoil with trailing edge flap

BEAMFORMING

Microphones are usually used to sample the sound emitted by an object, such as the test smart blade. However, a single microphone records only the global sound pressure in front of its diaphragm. Therefore a single microphone is not able to identify the sound source direction. When several microphones are combined in an array and the sound pressure field is recorded simultaneously, the sampled data can be processed to establish directionality in the array and therefore the sound source direction can be identified. The physical background of this directionality is as follows [5]: The microphones are placed at different positions in the array. As the sound waves arrive at each microphone at a different time due to the different propagation length

between the source and the microphone, the time difference is dependent on the sound source position relative to the array position. In post-processing, these time lags are used to identify the sound source position in front of the array. This post-processing method is called beamforming.

The most commonly used beamforming method is the delay and sum algorithm. A sound source scan grid is defined in front of the microphone array. Then, the microphone array is focused consecutively at each point on the grid and the array output power

$$s(t) = \sum_{m=1}^M p_m(t - \tau). \quad (1)$$

is calculated. Additionally, each microphone signal $p_m(t)$ must be shifted by the time τ so that the time delay due to the different sound propagation time is compensated for. Finally, the shifted signals of each of the M microphones are summed.

The calculated array output power represents the acoustic energy at each grid point, and is used to identify the sound sources in the grid: A high acoustic energy value at a grid point indicates a sound source at this position. In contrast, areas with low acoustic energy indicate an absence of sound sources in this section.

Different acoustic sources emit sound in different frequency ranges. To take the frequency-dependency into account, the delay and sum algorithm must be performed in the frequency domain. The microphone signals are therefore Fourier transformed into the frequency domain to allow the generation of an acoustic energy map for each frequency bin.

In Fig. 3 an example acoustic energy map for a discrete frequency is shown. The two dimensional surface plot represents the acoustic energy in a layer, in front of the array. The color denotes the acoustic energy amount in the unit dB .

The main sound source is clearly recognizable and is located in the middle of the acoustic map. However, there are also high acoustic energy areas, which do not belong to real acoustic sound sources. These unwanted artifacts are caused by inaccuracies in the determined time shift of the microphone signals in the delay and sum algorithm.

A one-dimensional acoustic map pattern is shown in Fig. 4. The main sound source (called the main lobe) is clearly visible. A unwanted artifact (denoted as side lobe) is also visible on the right side of the main lobe. Furthermore, the two qualities of an acoustic map are depicted in Fig. 4 [5]. The main lobe width (MLW) represents the main lobe extent and is measured as 3 dB below the maximum. A large main lobe of a dominant sound source covers the main lobes of nearby weaker sources. Consequently, the main lobe width must be minimized. The energy level between the main lobe and the first side lobe is denoted as the dynamic D . This quality must be maximized so that the side

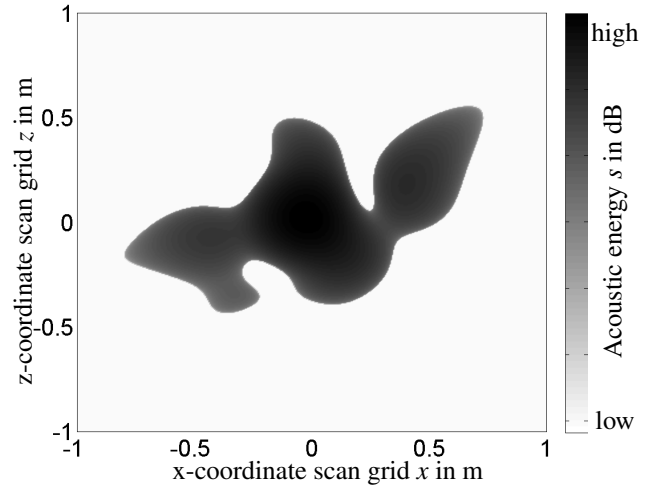


FIGURE 3. Example acoustic energy map

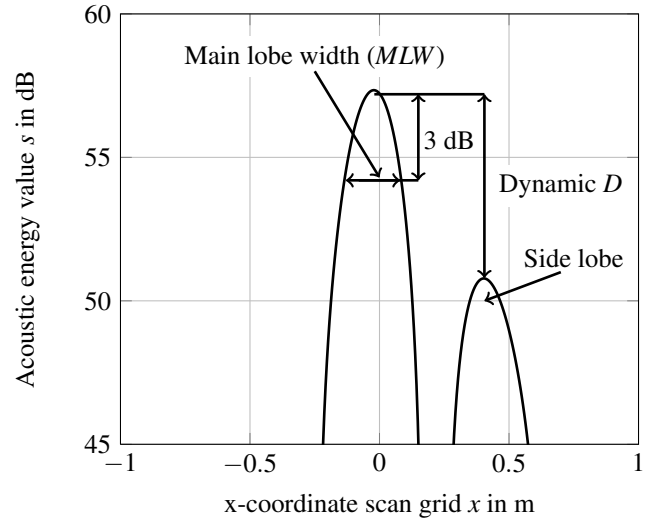


FIGURE 4. One-Dimensional acoustic map profile

lobes are not misinterpreted as additional main lobes of other sources. In addition, a small dynamic D can cover main lobes of weaker sound sources.

The main lobe width MLW and the dynamic D depend on the frequency and the microphone arrangement in the array [4]. Therefore when the frequency range of interest is known, a microphone arrangement optimization can be performed to increase the acoustic map quality.

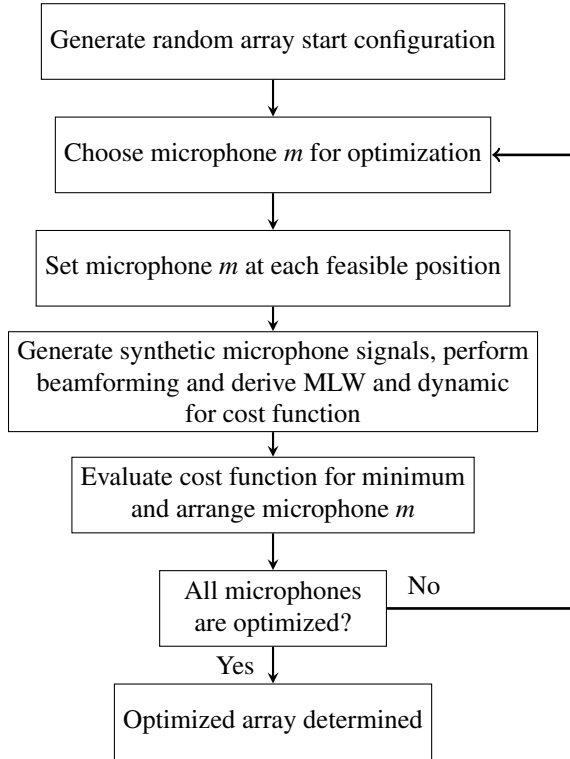


FIGURE 5. One-factor-at-a-time optimization process for array applications

OPTIMIZATION OF MICROPHONE ARRANGEMENT

The smart blade is applied with a trailing edge flap. Previous experimental flapped aerofoil investigations for aircraft applications identified a sound source at the flap which emits sound in the 2,500 Hz frequency range [6]. This frequency is used as a first assumption for the sound source frequency at the smart blade flap. With an initial assumed value, the microphone arrangement optimization at the array can be performed.

The arrangement optimization is an iterative computer based process (cf. Fig. 5). First, an initial arrangement is generated based on a random normal microphone distribution. The initial array solution considers provided boundary conditions such as the maximum array dimension. The generated microphone arrangement serves as a starting configuration for the following one-factor-at-a-time optimization algorithm.

The algorithm consecutively optimizes the position of each microphone in the array. The microphone is therefore placed in turn at each feasible position, and the synthetic array microphone signals are calculated with:

$$p_m(\vec{x}) = \exp(i\vec{\alpha} \cdot \vec{x}). \quad (2)$$

Equation 2 describes an incoming plane wave at the microphone coordinate \vec{x} . The wave frequency and the arrival direction are represented by the wave vector $\vec{\alpha}$. The computed synthetic signals are used as input data for the beamforming processing, based on the delay and sum algorithm in the frequency domain. The *MLW* and dynamic *D* are derived from the generated acoustic map.

The optimal position of a single microphone in the array is found when the *MLW* is minimized and the dynamic is maximized. To identify the optimal microphone position *m*, the cost function

$$w_m = MLW + \frac{1}{D_m} \quad (3)$$

for each feasible microphone position *m* is calculated. Finally, the microphone position *m* is chosen as where the cost function is minimized. The algorithm then optimizes the arrangement of the next microphone.

At the end of the optimization process an optimal microphone arrangement for a fixed map frequency has been determined. However, the level of map enhancement depends on the initial starting configuration as it is generated by a random process. In addition, the synthetic microphone signals (cf. Eq. (2)) do not include noise. To take this into account, noise is superimposed onto the synthetic signals sampled with the test-rig. Furthermore, the optimization process is repeated multiple times to ensure an optimal arrangement.

RESULTS

A Monte Carlo Simulation (200 replications) is performed to demonstrate the optimization algorithm. A synthetic sound source ($f = 2500$ Hz) is placed in front of the array. The distance to the array is 0.7 m.

The *MLW* and the dynamic enhancements are presented in Fig. 6 and 7. As previously described, the enhancement levels depend on the generated random starting configuration which is visible in the range. Nevertheless, both qualities are significantly enhanced during the optimization process. The average *MLW* enhancement is 0.07 m. Two separated blocks are visible for the dynamic enhancement in Fig. 7. The left block (range: 10...20 dB) represents the optimization results in which side lobes are still present; however the dynamic level is significantly enhanced. The right block (range: 45...60 dB) indicates the results in which the side lobes are eliminated. Over all, the average dynamic enhancement is 39.63 dB.

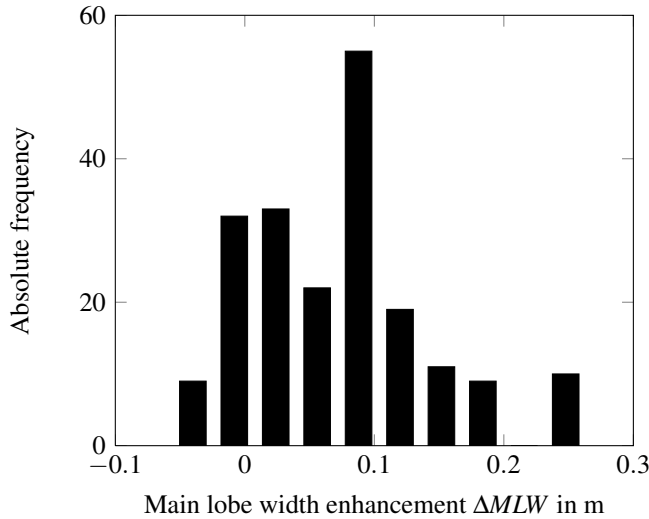


FIGURE 6. Monte Carlo Simulation results for the main lobe width enhancement

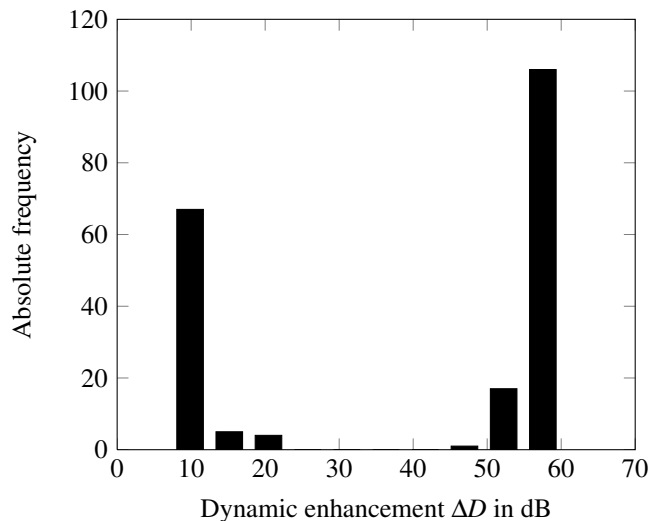


FIGURE 7. Monte Carlo Simulation results for the dynamic enhancement

CONCLUSION

Beamforming is a suitable method to locate sound sources. In the context of trailing edge flaps for wind turbine applications, the method will be used to study the acoustic flap characteristics. An experimental set-up with a test aerofoil and a microphone array is designed. However, the microphone arrangement in the array must first be optimized, in order to improve the sound flap map quality. A synthetic beamforming process therefore linked with a one-factor-at-a-time-algorithm in which a cost function is minimized. The cost function contains the MLW and the dy-

namic which are the acoustic map's key characteristics. A Monte Carlo Simulation shows that both quantities were significantly improved. Therefore the generated acoustic map based on the optimized array arrangement is of a higher quality in order to allow the easier location of the sound sources on the aerofoil flap.

In future work, additional optimization algorithms will be implemented and tested. Furthermore, the optimization process will be extended for a frequency range.

ACKNOWLEDGMENTS

The present work is funded within the framework of the joint project Smart Blades (0325601A/B/C/D) by the German Federal Ministry for Economic Affairs and Energy (BMWi) under decision of the German Federal Parliament.

REFERENCES

- [1] Ortega Gomez, J., Balzani, C., and Reuter, A., 2014. Evaluation of the possibility of replacing pitch control by active trailing edge flaps in wind turbines. *EWEA 2014 Annual Event* (Barcelona, Spain).
- [2] Fink, and Schlinker, 1980. "Airframe noise component interaction studies". *J. Aircraft*, **17**, pp. 99–105.
- [3] Bundesministerium fuer Umwelt, N. u. R., 1998. Technische Anleitung zum Schutz gegen Laerm TA Laerm.
- [4] Sijtsma, 2004. Experimental techniques for identification and characterisation of noise sources.
- [5] Johnson, D., 1993. Array signal processing : concepts and techniques. Upper Saddle River, NJ.
- [6] Koop, 2005. "Aktive und passive Stroemungsbeeinflussung zur Reduzierung der Schallabstrahlung an Hinterkantenklappen von Tragfluegeln". PhD thesis, Technische Universitaet Berlin.

NUMERICAL INVESTIGATION OF AN AIRFOIL WITH MORPHING TRAILING EDGE FOR LOAD REDUCTION

T. Wolff*, J.R. Seume

ForWind - Center for Wind Energy Research, Leibniz Universität Hannover
Institute of Turbomachinery and Fluid Dynamics - TFD
Appelstr. 9, 30167 Hanover, Germany
Email: Wolff@tfd.uni-hannover.de, Seume@tfd.uni-hannover.de

ABSTRACT

The average length of wind turbine rotor blades has been increasing throughout the last few decades. Higher stresses arise, especially at the blade root, due to the longer lever arm. One way to reduce unsteady blade-root stresses caused by turbulence, gusts, or wind shear is to actively control the lift in the blade tip region. One promising method involves airfoils with morphing trailing edges to control the lift and consequently, the loads acting on the blade. This study investigates the steady and unsteady aerodynamic behavior of a typical thin wind turbine airfoil equipped with a morphing trailing edge. Two-dimensional Reynolds-Averaged Navier-Stokes (RANS) simulations were carried out to determine an optimal trailing edge geometry. The defined geometry was then used to investigate the unsteady aerodynamic behavior of the deformable trailing edge, using time-resolved simulations with a deformable grid. The phase shift between the trailing edge motion and the lift coefficient was analyzed for different angles of attack and velocities of the trailing edge motion. The results show an increase in phase shift with increasing velocity of the trailing edge motion and with decreasing angle of attack. At the highest angle of attack, the phase shift is negative.

NOMENCLATURE

a = speed of sound
 c = chord length
 c_d = drag coefficient

c_l = lift coefficient
 k = reduced frequency, $(\omega \cdot c)/(2 \cdot U)$
 Ma = Mach number, U/a
 p = calculation order
 Re = Reynolds number, $(U \cdot c \cdot \rho)/\mu$
 U = freestream velocity
 t = thickness
 t^* = non-dimensional time
 y^+ = non-dimensional wall distance

Greek

α = angle of attack
 β = deflection angle of the deformable trailing edge
 η_{flap} = flap effectiveness parameter, $(\partial c_l / \partial \beta) / (\partial c_l / \partial \alpha)$
 μ = dynamic viscosity
 ρ = density
 ϕ = phase shift
 ω = frequency of the trailing edge motion

Subscripts

fte flexible part of the trailing edge
rte rigid part of the trailing edge
te trailing edge

Abbreviations

GCI Grid Convergence Index
RANS Reynolds-Averaged Navier-Stokes

*Address all correspondence to this author.

INTRODUCTION

During the last few decades, the length of wind turbine rotor blades increased in response to the demand for higher power generation per wind turbine, according to Kaldellis and Zafirakis [1]. Complex flow environments with wind shear, turbulences, and gusty wind conditions cause high unsteady loading on increasingly long and slender rotor blades, see Kelley et al. [2]. Due to the longer lever arm which accompanies longer blades higher stresses arise, particularly at the blade root. One way to reduce these blade-root stresses is to reduce the forces acting near the blade tip region, achieved by reducing the lift coefficient in this region. Airfoils with morphing trailing edges applied to the outer blade region of the wind turbine are a promising method to actively control the lift coefficient and consequently the loads acting on the blade, see Barlas and van Kuik [3].

The application of trailing edge flaps and deformable trailing edges on wind turbine blades is inspired by existing applications on aircraft wings and helicopter blades, though with different control objectives. Studies of trailing edge flaps and deformable trailing edges applied to wind turbine blades have already been carried out, including numerical and experimental investigations. The wind tunnel tests carried out by Pechlivanoglou et al. [4] showed that the lift of a wind turbine airfoil can be directly controlled by adaptive trailing edge geometry. Pechlivanoglou et al. [4] indicate, however, that it is not always possible to reach a lift-to-drag-ratio equal or close to zero, which is necessary for a shut down, or for wind conditions in which the rotor is just idling. Therefore, the deformable trailing edge cannot be used as the sole control system. Troldborg [5] carried out extensive simulations in order to derive an optimal trailing edge geometry using the 2D incompressible RANS solver EllipSys2D. In addition to the parameter study based on steady-state simulations, transient flow phenomena were investigated by means of simulations of harmonic pitch oscillations and/or oscillatory motions of the deformable trailing edge. In conclusion, Troldborg's work suggests that a curved trailing edge with a relative chord length between 5% and 10% is a good compromise between the ability to control the lift and the actuator power needed to deflect the trailing edge. In addition, Wolff et al. [6] investigated the optimal geometry and unsteady behavior of a fully flexible trailing edge. They found an optimal flexible trailing edge length of 20% of the chord length.

In order to reduce the unsteady loads on wind turbine rotor blades caused by turbulent inflow conditions and gusts, the present study is mainly focused on designing optimal deformable trailing edge geometry for the DU08-W-180-6.5 airfoil, and analyzing the effect of the actively deformed trailing edge on the flow characteristics. First, two-dimensional computations are carried out to evaluate the trailing edge's effectiveness in terms of the coefficients of lift and drag. Second, unsteady phenomena, i.e. the phase shift between trailing edge deflection and lift coefficient, are investigated using time-resolved simulations of the

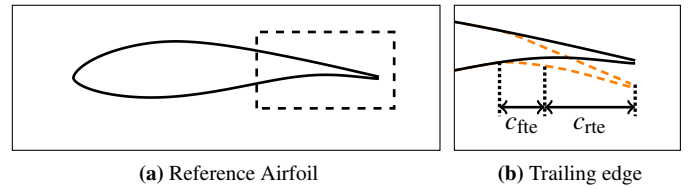


FIGURE 1. Geometry of the DU08-W-180-6.5 airfoil; undelected trailing edge (—); $\beta = 10$ deg deflected trailing edge ($c_{rte} = 0.2$, - - -)

actively deflected trailing edge using a deformable grid approach.

AIRFOIL GEOMETRY

The present study investigated the DU08-W-180-6.5 airfoil designed at the TU Delft [7]. This is a typical thin airfoil, which can be used in the outer part of modern wind turbine blades. Deformable trailing edges are particularly desirable in this region because they have a large impact on the blade root bending moments. The reference DU08-W-180-6.5 airfoil, which is shown in figure 1a, has a thickness-to-chord ratio of $t/c = 18\%$ and has a relative blunt trailing edge of height $t_{te}/c = 0.65\%$. In the present study, all simulations were conducted with a normalized chord length of $c = 1$ m. In contrast to Wolff et al. [6], the flexible trailing edge was realized by combining a flexible and a rigid part. The rigid part starts at the trailing edge and its length in the upstream chordwise direction was varied between $c_{rte} = c_{te}/c = 0.05$ and $c_{rte} = 0.2$ in steps of $\Delta c_{rte} = 0.05$. The rigid part is followed in the upstream chordwise direction by a flexible part of $c_{fte}/c = 0.1$ length. The deflection angles chosen ranged from $\beta = -10$ deg to $\beta = 10$ deg in steps of $\Delta\beta = 5$ deg. A positive deflection angle describes a deflection to the pressure side and a negative deflection angle describes a deflection to the suction side.

NUMERICAL MODEL

Flow Solver

The aerodynamic design code FLOWer, developed by the German Aerospace Center (DLR), German universities, and Airbus Germany [8], is used for the numerical simulations. FLOWer solves the two- and three-dimensional Reynolds-averaged Navier-Stokes equations using structured multi-block meshes and a finite-volume approach. The convective fluxes are discretized by a central discretization scheme according to Jameson [9]. The closure problem of the Reynolds equations is solved by substituting the Reynolds-stress tensor by a two-equation SST $k-\omega$ turbulence model [10]. All boundary layers are assumed to be fully turbulent.

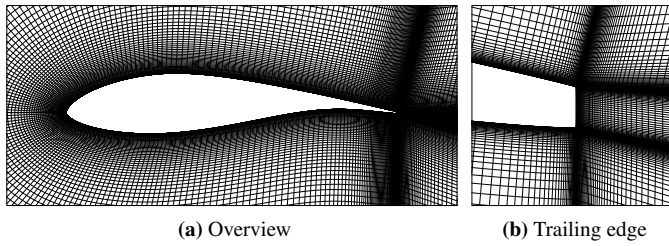


FIGURE 2. Computational grid around the airfoil and detailed view on the trailing edge grid with undeflected trailing edge

The time-resolved simulations use a second-order accurate implicit dual-time stepping scheme. A deformable grid approach, which uses linear interpolation to interpolate between given meshes, is used to simulate the morphing trailing edge. A non-dimensional time step of $t^* = 1$ is used for the parameter studies. The non-dimensional time step for the simulations with actively deformed trailing edge was decreased to $t^* = 0.5$ to accurately resolve the trailing edge motion in time.

Mesh

The computational region includes the two-dimensional airfoil surrounded by a C-H-grid (see figure 2), with a radius of $50 \cdot c$ to ensure that there are no reflecting influences from the boundaries. The first cell distance normal to the airfoil surface was defined to be small enough so that the dimensionless wall distance equals $y^+ \approx 1$. The boundary layer region is resolved with 48 cell layers in the direction normal to the airfoil surface. The whole mesh consists of approximately 85.000 nodes. A grid convergence study (GCI) has been conducted in accordance with the ASME V & V 20 Committee [11] to determine the discretization error. The results for a conservative calculation order of $p = 1$ show a GCI for the used grid of $GCI_{c_1} = 0.9\%$ concerning the lift coefficient c_1 and $GCI_{c_d} = 4.7\%$ concerning the drag coefficient c_d .

Boundary Conditions

The airfoil surface is defined as a no-slip wall, and the boundary of the computational region is set as a farfield boundary. The Reynolds number is chosen as $Re = 7.31 \cdot 10^6$ and the Mach number as $Ma = 0.236$. The turbulence intensity is set to 1% to ensure stable simulations. The angle of attack is varied between $\alpha = -12$ deg and $\alpha = 12$ deg during the parameter analysis. Simulations with six different angles of attack in the range between $\alpha = 0$ deg and $\alpha = 10$ deg are performed for the investigations with actively deformed trailing edges. Three different reduced frequencies k are examined for each angle of attack in order to describe the trailing edge motion. According to Hansen [12], flutter can occur in wind turbines at a reduced

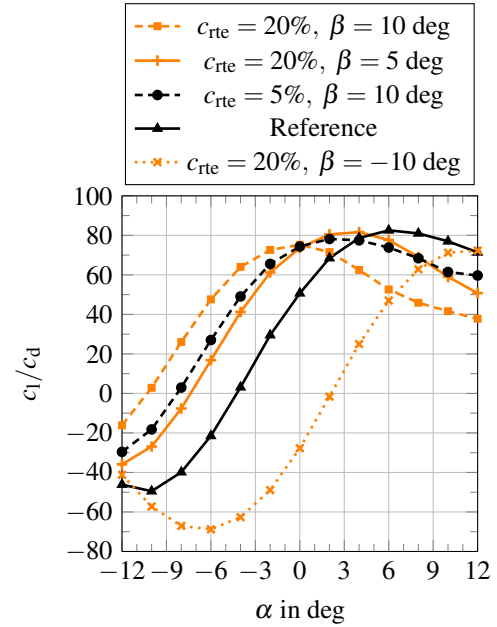


FIGURE 3. Lift-to-drag ratio c_1/c_d plotted against the angle of attack α for a variation of deflected trailing edges

frequency $k \ll 1$. Thus, values between $0.1 < k < 0.2$ have been chosen in a similar range to Troldborg [5]. The higher the reduced frequency, the faster the trailing edge motion and the better the ability of the trailing edge motion to react to unsteady flow conditions. The trailing edge motion is simulated described by a cosine-curve, starting from $\beta = 0$ deg and with an amplitude of $\beta = 10$ deg.

PARAMETER STUDY

A parameter study of the deformable trailing edge has been carried out and is described in this section. Firstly, the effects of the relative trailing edge length c_{rte} and the deflection angle β on the lift and drag coefficients are discussed. Secondly, the effectiveness of the flap is evaluated by considering the sensitivity of the lift coefficient with respect to the angle of attack α and the deflection angle β .

Lift and Drag Coefficients

The lift-to-drag ratio c_1/c_d is plotted against the angle of attack α for different trailing edge configurations in figure 3. The flow deviation increases if the deflection angle β is positive and decreases if the deflection angle β is negative. This leads to higher (positive deflection) or lower (negative deflection) lift coefficients and lift-to-drag-ratios, respectively (see figure 3). An increase in the size of the deflected trailing edge c_{rte} amplifies these effects.

The effect of the deflected trailing edge on the lift-to-drag ratio is shown in figure 3. The increased lift caused by positive trailing edge deflections increases the lift-to-drag ratio in comparison to the reference airfoil at angles of attack between $\alpha = -12$ deg and approximately $\alpha \approx 3$ deg. The increased drag that accompanies a positively deflected trailing edge (as a larger cross section is perpendicular to the flow direction) at positive angles of attack causes a decreasing lift-to-drag ratio at angles of attack $\alpha \gtrsim 3$ deg.

Flap Effectiveness Evaluation

To evaluate the deformable trailing edge's effectiveness, several aspects have to be considered. Most importantly, the deflected trailing edge must generate the desired amount of additional or reduced lift to actively control the loading. Additionally, low drag and a high lift-to-drag ration are required. In theory an optimal geometry could be found for every angle of attack, however this is not a realistic target. Instead, as a compromise the angle of attack with the highest lift-to-drag-ratio of the reference airfoil ($\alpha = 6$ deg, see figure 3) was used to determine the optimal geometry. This angle of attack is normally used as the control value for the pitch regulation and therefore it is the most common operating condition.

The discussion in the section above shows that the deformed trailing edge changes the lift sufficiently while achieving a high lift-to-drag ratio. The flap effectiveness parameter η_{flap} defined by Troldborg [5] describes the sensitivity of the lift coefficient to changes of the deflection angle, normalized by the change of the lift coefficient by changing the angle of attack (see nomenclature). In figure 4 it is shown that the flap effectiveness parameter η_{flap} increases for negative trailing edge deflections as the morphing trailing edge increases in length. For a deflection angle of $\beta = 10$ deg, a maximum in the flap effectiveness occurs at $c_{rte} = 15\%$. The flap effectiveness just slightly increases from $c_{rte} = 15\%$ to $c_{rte} = 20\%$ for a deflection angle of $\beta = 5$ deg. This is due to an increasing area of flow separation caused by the trailing edge deflection. Therefore, it is not recommended to use trailing edges with a rigid deflected length longer than 15% of the chord length.

UNSTEADY BEHAVIOR OF THE ACTIVELY DEFORMED TRAILING EDGE

The time-resolved simulations with the trailing edge motion using a deformable grid approach are described in this section. The analyzed phase shift ϕ plotted in figure 5 is the delay between the trailing edge motion and the change in lift coefficient. First, a Fourier analysis of the dynamic lift coefficients oscillation is performed to calculate its phase. Afterwards, the difference between the phase of the lift coefficients oscillation and the trailing edge oscillation is calculated to determine the phase shift.

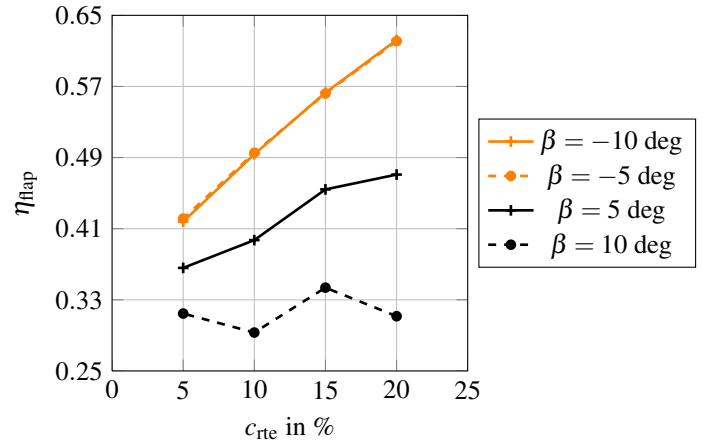


FIGURE 4. Effectiveness of the deflected trailing edge η_{flap} plotted against the relative chord length of the rigid trailing edge part c_{rte} for four deflection angles at $\alpha = 6$ deg

It can be observed that the phase shift increases with increasing reduced frequency to an asymptotic value, and with decreasing angle of attack. The increase due to the increased reduced frequency takes place because of the inertia of the flow. The flow cannot trace the trailing edge's motion exactly and this effect is then exacerbated when the trailing edge moves faster.

The lift change caused by the trailing edge deflection is greater at lower angles of attack compared to higher angles of attack. If it is assumed that the duration of the trailing edge motion stays the same for different angles of attack, then the lift must change faster at lower angles of attack. The gradient of the lift depending on the deflection angle decreases with an increasing angle of attack. This can be observed in figure 5 where the phase shift decreases with increasing angle of attack. A negative phase shift appears at the highest angle of attack. The reason for this is the flow separation, which is induced by the trailing edge deflection. The lift coefficients maximum is reached before the maximum of the trailing edge deflection because of the flow separation.

CONCLUSIONS

Two-dimensional numerical investigations have been performed on a wind turbine blade's airfoil with a deformable trailing edge. These investigations included a parameter study of several deflection angles and relative chord lengths of the morphing trailing edge, as well as time-resolved simulations which included a dynamic trailing edge deflection with different reduced frequencies.

Actively deformed morphing trailing edges significantly affect the lift coefficient and the stall behavior of an airfoil, depending on the geometry (size and deflection angle) of the deformed

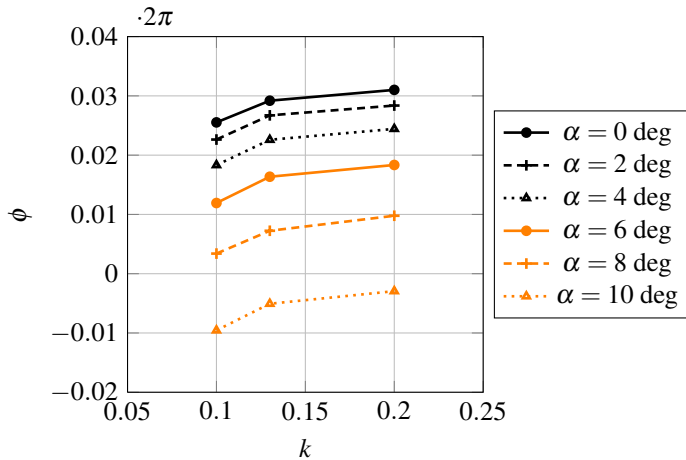


FIGURE 5. Phase shift ϕ plotted against the reduced frequency k for different angles of attack, $c_{rte} = 20\%$, $\hat{\beta} = 10$ deg

trailing edge. The change in lift increases with deflection angle and an increase in length of the morphing trailing edge. The lift gained by deflecting the trailing edge shows a maximum for a morphing trailing edge of $c_{rte} = 15\%$ with respect to the chord length of the airfoil. For larger relative chord lengths, the increase in flow separation caused by the deformable trailing edge decreases the flap effectiveness. Thus, for the present airfoil a length of $c_{rte} = 15\%$ is the optimal length of the morphing trailing edge. However, this is not general and for every specific airfoil a compromise between lift gain, aerodynamic force acting on the trailing edge, and stall behavior has to be found. Furthermore, structural aspects and ease of manufacture need to be taken into account.

A phase shift between the trailing edge motion and lift coefficient was observed during the deformable grid simulations. This phase shift increases with the reduced frequency to an asymptotic value. The faster the trailing edge moves, the smaller the change in phase shift. In addition, the phase shift increases with decreasing angle of attack and becomes negative at the highest angle of attack because of the flow separation. The phase shift has to be taken into account during the controller design as it represents the delay between the moving trailing edge (actuator) and the dynamic lift coefficient (control parameter).

In future work, simulations with combined motion of the pitch and deformable trailing edge are planned. These simulations will be used to define the operating points at which the deformable trailing edge system is less effective (e.g. angles of attack near stall). At these points the pitch system is more effective.

ACKNOWLEDGMENTS

The present work is funded within the framework of the joint project Smart Blades (0325601A/B/C/D) by the German Federal Ministry for Economic Affairs and Energy (BMWi) under decision of the German Federal Parliament. The authors appreciate the German Aerospace Center (DLR) for providing FLOWer. The authors thank the Leibniz Universitaet Hannover IT Services (LUIS) for the computational resources provided.

REFERENCES

- [1] Kaldellis, J. K., and Zafirakis, D., 2011. The wind energy (r)evolution: A short review of a long history. *Renewable Energy* **36**, pp 1887-901.
- [2] Kelley, N., Hand, M., Larwood, S., and McKenna, E., 2002. The NREL large-scale turbine inflow and response experiment - Preliminary results. *ASME Wind Energy Symp.* (Reno, Nevada). WIND2002-64 pp 412-26.
- [3] Barlas, T. K., and van Kuik, G. A. M., 2007. State of the art and perspectives of smart rotor control for wind turbines. *J. Phys.: Conf. Ser.* **75**, 012080.
- [4] Pechlivanoglou, G. K., Wagner, J., Nayeri, C. N., and Paschereit, C. O., 2010. Active aerodynamic control of wind turbine blades with high deflection flexible flaps. *48th AIAA Aerospace Sciences Meeting* (Orlando, Florida). AIAA 2010-644.
- [5] Troldborg, N., 2005. Computational study of the Riso-B1-18 airfoil with a hinged flap providing variable trailing edge geometry. *Wind Engineering* **29** (2), pp 89-113.
- [6] Wolff, T., Ernst, B., and Seume, J. R., 2014. Aerodynamic behavior of an airfoil with morphing trailing edge for wind turbine applications. *J. Phys.: Conf. Ser.* **524** 012018.
- [7] Timmer, N., and van Rooij, R., 2009. *Summary of the delft university wind turbine dedicated airfoils*. Tech. rep. TU Delft.
- [8] Kroll, N., and Fassbender, J. K., 2002. *MEGAFLOW - Numerical flow simulation for aircraft design*. Springer, Berlin.
- [9] Kroll, N., Radespiel, R., and Rossow, C. C., 1995. Accurate and efficient flow solvers for 3D applications on structured meshes. *AGARD R-807*, pp 4.1-4.59.
- [10] Menter, F., 1994. Two-Equation Eddy-Viscosity Turbulence Models for Engineering Applications. *AIAA Journal* **32**, pp 1598-1605.
- [11] ASME V & V 20 Committee, 2009. *Standard for verification and validation in computational fluid dynamics and heat transfer*. The American Society of Mechanical Engineers, New York, USA.
- [12] Hansen, M. H., 2007. Aeroelastic Instability Problems for Wind Turbines. *Wind Energy* **10**, pp 551-577.

CFD studies of a 10 MW wind turbine equipped with active trailing edge flaps

E. Jost¹, A. Fischer¹, Th. Lutz¹, E. Krämer¹

¹University of Stuttgart, Institute of Aerodynamics and Gas Dynamics (IAG),
e.jost@iag.uni-stuttgart.de

ABSTRACT

The active trailing edge flap concept is a very promising approach to reduce the dynamic loading of large wind turbines. Over the last years it has been widely researched with different methods as e. g. engineering models making use of the blade element method. The aim of the authors' work is to further analyse the concept in a high fidelity Computational Fluid Dynamics (CFD) environment. Therefore, this article gives an overview on different possibilities to realise actively deflecting flaps in CFD. Three different concepts, one based on the CHIMERA technique and two based on grid deformation, have been examined in 2D and a numerical setup for 3D simulations has been investigated.

1. Introduction

One of the main focus points of today's wind energy research is the accurate determination and reduction of the turbine loads. This is caused by the ambition to realise bigger turbines with higher power output to achieve a lower cost of energy. Many current research projects concentrate on the development of 10 MW turbines. One example is the european-funded INNWIND.EU project, which examines the generic DTU 10 MW reference wind turbine [1]. The realisation of these large turbines is very challenging since simple up-scaling is hardly possible. As described in [2], power, thrust, aerodynamic and centrifugal forces as well as the rotor mass rise disproportionately with the rotor radius. Applied on current market turbines, up-scaling will lead to big, heavy weight rotors which is undesirable because of many economic and technical reasons. It is therefore necessary to develop new concepts in the aerodynamic, structural and controller design of these large turbines. One of the main aerodynamic challenges is to reduce the dynamic loading caused by tower shadow, atmospheric boundary layer or turbulent inflow. As shown by several scientists, e.g. Barlas [3], active trailing edge flaps (ATEF) constitute a very promising approach for these matters. The majority of them researched the technology with the use of blade element or free vortex methods. The aim of this work is to investigate the ATEF concept with CFD. Two dimensional simulations of the NACA 64₃618 have been performed to evaluate the different possibilities to enable active flaps in CFD. Additionally to the trailing edge flap (TEF) the airfoil is equipped with a leading edge flap (LEF) to validate both cases. Furthermore three dimensional simulations were conducted on the DTU 10 MW RWT in a 120 degree model. The basic principle behind ATEFs is very simple. Deflecting flaps attached to the rear of a profile are able to influence the lift coefficient for a given angle of attack. A change in the incoming wind speed leads to a variation of the angle of attack and thereby an alleviation or increase of lift resulting in the turbine loads. Active trailing edge flaps counter this effect with the attempt to keep the lift constant by adapting the flap deflection to the current wind condition.

2. Realisation of active flaps in the CFD code FLOWer

The simulations were performed with the compressible Navier-Stokes solver FLOWer which was developed at the German Aerospace Center [4]. FLOWer is a block structured code based on finite volume formulation. The implementation of the CHIMERA technique for overlapping meshes [5] in addition to the Dual-time-stepping method for time-accurate simulations allow flow computations around moving or rotating bodies as e.g. wind turbines. In FLOWer, active devices like flaps can be realized in two different ways, through grid deformation and based on the CHIMERA technique. So far, two different types of grid deformation algorithms are implemented, the first based on hermite polynomials [6] and in a newer code version one based on radial basis functions [7]. In the following they are described in detail and referred to as CHIMERA flap, HP flap (hermite polynomials) and RBF flap (radial basis functions). For simplification the functioning is shown on an airfoil only equipped with TEF. The geometry of wind turbine flaps differs to those commonly used in aviation as the flap is

directly hinged to the airfoil and moving in a circle-formed chamfer. There is no gap between the main and the flap part of the airfoil.

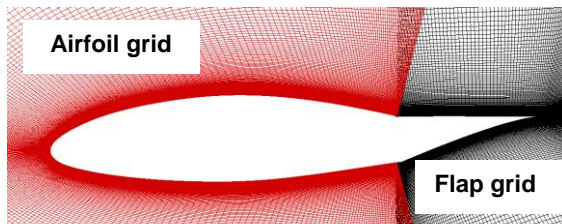


Figure 1: CHIMERA flap

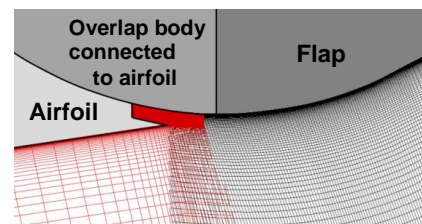


Figure 2: Gap closing CHIMERA flap

The modeling based on the CHIMERA technique requires the use of two completely separate grids for the airfoil and flap part. These grids are overlapped and holes are cutted out of the airfoil grid where the flap is located and respectively to the flap grid where it connects to the airfoil. Figure 1 shows the final computational grid. The small gap between airfoil and flap, that is created through the separation into two different grids, is closed like it is shown in figure 2. This is necessary to avoid flow through the split which can affect simulation results. Figure 2 also shows how the airfoil is extended with an overlap part to achieve an accurate CHIMERA interpolation. A obvious disadvantage of the CHIMERA flap is the elaborate grid generation process already in 2D. In addition, two grids lead to a higher amount of cells and therefore longer computation time.

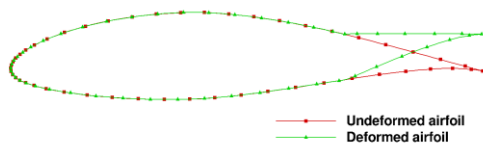


Figure 3: Undeformed and deformed surface

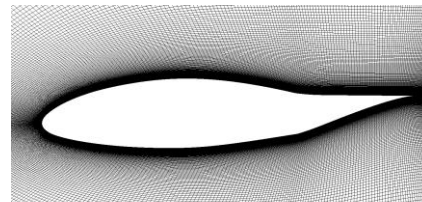


Figure 4: Deformed computation grid

The basic principles of the two possibilities based on grid deformation, the HP flap and the newer RBF flap, are identical. First, the deformed surface is obtained by rotating the flap part of the surface around a defined hinge point. Figure 3 shows the undeformed original surface in addition to the deformed surface with flap deflection. Based on these surfaces the deformation of the simulation grid is computed as illustrated in figure 4. The difference of the two options results from the deformation algorithm and is their variability concerning grid topology. The HP algorithm calculates the deformation of the nodes based on their i,j,k -index of the structured grid. It is therefore necessary to stick to certain restrictions regarding the block structure. In the RBF algorithm the deformation is computed based on x,y,z coordinates and independent of grid topology. Both algorithms needed adaption to achieve accurate results in the transition region from airfoil to flap. In figure 5, the issue is shown exemplarily on the RBF algorithm with the lower side of the airfoil displayed. The problem is that the rotation results in a gap in the surface discretization. For good results the local node distribution had to be adjusted by the use of two sided stretching functions [8] like it is shown in figure 5b. The HP version showed the same issue in a similar manner and was therefore also adapted.

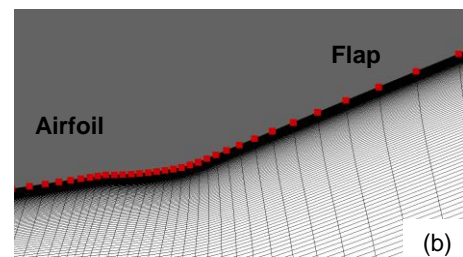
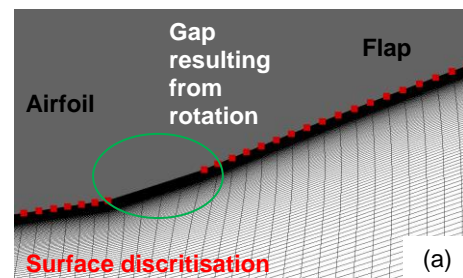


Figure 5: RBF grid before (a) and after (b) redistribution

In general a modeling based on grid deformation is favorable in comparison to the CHIMERA approach. A smaller amount of cells (approx. 130,000 in a 2D case) and grids and no CHIMERA intersection near the airfoils surface are major advantages concerning simulation time and accuracy.

3. 2D results single trailing edge flap case and combined leading/trailing edge flap case

The implementations have been tested in a single TEF case and in a combined LEF/TEF case for which measurement data is available. The data was obtained by Lambie [9] who researched a self-adapting camber concept. The HP algorithm was only investigated in the TEF case as no LEF implementation has been made so far. Up to now the implementation is also not planned because of the major grid topology restrictions that the algorithm needs. The CHIMERA flap and the RBF flap have been simulated for both cases as it is shown in figure 6 and 7.

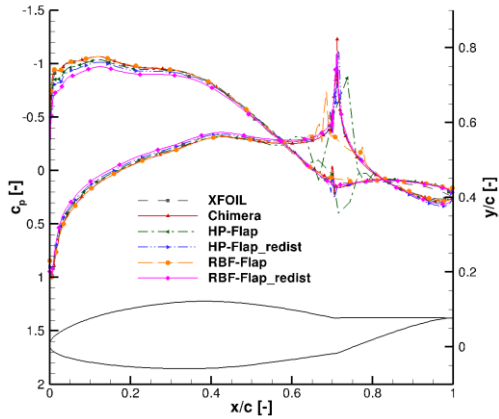


Figure 6: c_p single TEF case ($\alpha=8.455^\circ$, $\beta_{TEF}=14.63^\circ$)

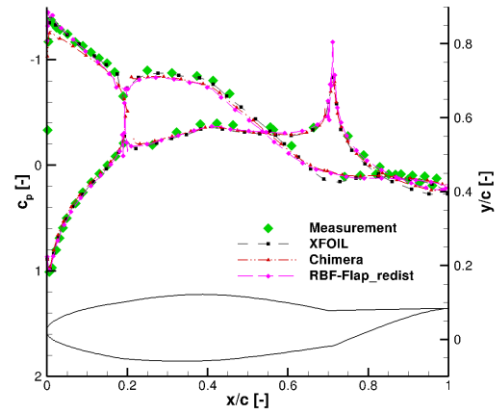


Figure 7: c_p LEF/TEF case ($\alpha=9.07^\circ$, $\gamma_{LEF}=-5.61^\circ$, $\beta_{TEF}=15.98^\circ$)

The notation ‘_redist’ indicates the redistributed version of the deformation algorithms. For comparison a xfoil-simulation is also shown. A good accordance can be seen in all cases but the undistributed deformation cases where there are strong fluctuations in the transition areas from airfoil to flap. This is because of the minor grid quality as it has been explained in chapter 3. Further results can be found in [10] and [11].

4. 3D Simulation in a 120 degree model of the DTU 10 MW RWT blade

As the RBF flap offers the needed flexibility regarding grid generation and is easier to handle than the CHIMERA flap with respect to the setup, it has been chosen for the first 3D simulations with static flap deflection. The main objective of the simulation was a first functionality test to examine the numerical setup and the grid deformation in 3D. Since so far the redistribution algorithm is not available in 3D, special focus has been put on the computation grid. Figure 8 shows a TEF deflection of 10 degrees extending from approx. 82 % to 95 % rotor radius with 10 % chord wise length. The gaps between the flap part and the main part of the rotor blade are kept closed to ease this first computation. Another reason is that as the simulation has been made with a timestep corresponding to 2° azimuth, unsteady gap effects cannot be resolved.

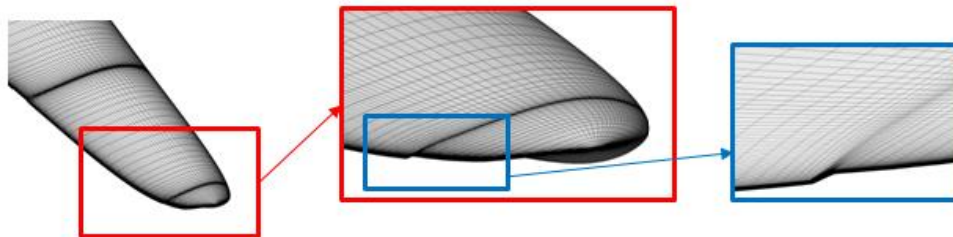


Figure 8: DTU 10 MW RWT 3D surface grid

The computation setup consists of 4 different meshes, background, spinner, nacelle and blade, which sum up to approx. 23.7 million grid cells. In this case the blade is highly resolved with 201 nodes around the airfoil and 261 in spanwise direction to adapt to the flap deflection. As turbulence model the Menter SST was used and to accelerate convergence the MultiGrid method was applied. The simulation was carried out at rated wind speed of 11.4 m/s and 9.6 rpm which leads to a Reynolds

number of 6.15 million. In total about 50,000 CPUh were required to achieve a converged solution. In figure 9 results of the simulation are displayed in form of a λ_2 vortex visualization. The blade tip vortex as well as the vortex caused by the change of circulation because of the flap deflection (red circle) can be clearly seen. The flap reduces the aerodynamic power is reduced from 11.02 MW to 10.86 MW and the rotor thrust is increased from 1.77 MN to 1.89 MN. This unintended power reduction is caused by a high drag coefficient resulting from a too large TEF deflection angle. But since the simulation was run with the purpose of a functionality test a large deflection is reasonable.

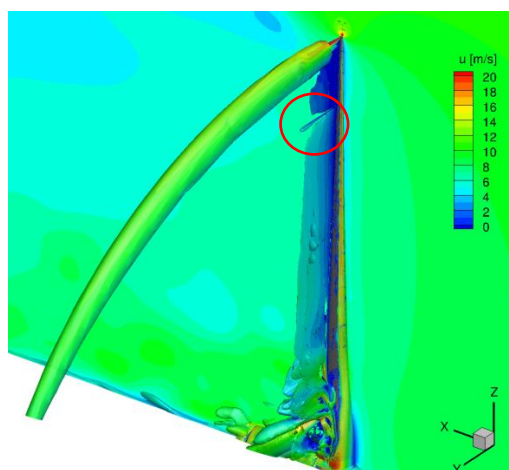


Figure 9: λ_2 vortex visualisation

5. Conclusion and Outlook

This article gives an overview over different possibilities to realise ATEFs in CFD. A modeling based on grid deformation is regarded favorable as less grid cells are needed and a higher accuracy is ensured than with the CHIMERA approach. In order to determine actual load variations on the examined 10 MW turbine full 3D simulations including tower and atmospheric inflow are planned for the future. As the tower shadow has the most pronounced influence, this will be the first focus point for a simulation with active flaps. Since it is possible to evaluate loads during simulation runtime, control concepts can also be applied. For the beginning the flap deflection will be implemented as function of the blade azimuth.

6. Acknowledgements

For providing their resources the authors gratefully thank the *High Performance Computing Center Stuttgart* and the AVATAR project for funding.

REFERENCES

- [1] C. Bak; F. Zahle; R. Bitsche; T. Kim; A. Yde; L.C. Henriksen; P.B. Andersen; A. Natarajan, M.H. Hansen; "Design and performance of a 10 MW wind turbine"; *J. Wind Energy*; To be accepted
- [2] R. Gasch; J. Twele; "Windkraftanlagen"; Vieweg+Teubner; 7.Auflage ; ISBN 978-3-8348-1460-9; 2011
- [3] T. Barlas; "Active aerodynamic load control on wind turbines"; PhD thesis; TU Delft; 2011
- [4] N. Kroll; J. Fassbender; "MEGAFLOW – Numerical Flow Simulation for Aircraft Design"; Springer Verlag Berlin/Heidelberg/New York; ISBN 3-540-24383-6; 2002
- [5] J.A. Benek; J.L. Steger; F.C. Dougherty; P.G. Buning, Arnold Engineering Development Center; Arnold AFS TN.; "Chimera: A Grid-Embedding Technique"; Defense Technical Information Center; 1986
- [6] K.-H. Hierholz; S. Wagner; "Simulation of Fluid-Structure Interaction at the Helicopter Rotor"; ICAS 98 Proceedings; International Council of the Aeronautical Sciences; Stockholm; Sweden; and AIAA; Reston, VA; 1998
- [7] M. Schuff; P. Kranzinger; Manuel Keßler; E. Krämer; "Advanced CFD-CSD coupling: Generalized, high performant, radial basis function based volume mesh deformation algorithm for structured, unstructured and overlapping meshes"; 40th European Rotorcraft Forum; Southampton; UK; September 2014
- [8] M. Vinokur; "On One-Dimensional Stretching Functions for Finite-Difference Calculations"; *Journal of Computational Physics* 50; p. 215 – 234; 1983
- [9] B. Lambie; "Aeroelastic Investigation of a Wind Turbine Airfoil with Self-Adaptive Camber"; Doctoral thesis; TU Darmstadt; 2011
- [10] K. Busse; "Numerische Untersuchung eines Profils mit gekoppelter Vorder- und Hinterkantenklappe unter Verwendung der Chimera-Technik"; Bsc. Thesis; Universität Stuttgart; May 2014
- [11] M. Bühler; "Numerische Untersuchung und Optimierung des Modells für Hinter- und Vorderkantenklappen im Strömungslöser FLOWer"; Bsc. Thesis; Universität Stuttgart; October 2014

Wake Flow Model for Wind Farm Control

*T. Ahmad, P.C. Matthews, B. Kazemtabrizi

Durham University UK, School of Engineering and Computing Sciences tanvir.ahmad@durham.ac.uk

Abstract --- A wake flow model for wind farm control strategies is presented using the Jensen wake flow model. Wind speed in the vicinity of each turbine is calculated and a correction factor is applied for calculating power in the wind. A separate turbulence model is used for calculating turbulence intensity in the wind farm. A modified version of the Jensen model is presented by varying the value of wake decay coefficient which varies with the change in turbulence. The goal of this work is to develop a wake flow model which is sufficiently accurate and faster enough to be used in a wind farm controller for load and power optimisation.

I. INTRODUCTION

Wind Turbines are installed together in wind farms to take advantage of economy of scale. A wind farm has to produce maximum possible energy with a number of turbines and minimum spacing between them [1]. However, installing turbines together creates aerodynamic interactions in the form of wake effects. Wakes negatively influence the affected turbines as these turbines have lesser wind speeds for electricity production. This results in power losses which can reach up to 40% in full wakes [2]. Wakes also increases turbulence intensity which increases the mechanical loads on the turbines shortening their life time and increasing operation and maintenance costs [3]. This paper shows how these wake losses can be controlled with coordinated control by optimising the power and loads in a wind farm.

II. COORDINATED CONTROL

A coordinated control can be used to increase the efficiency and reliability of the wind farm. If the upstream turbine is de-rated so that the decrease in produced power is less than the increase in shadowed turbines powers, there will be an overall increase in farm output whilst decreasing mechanical loads [4]. Decreasing loads will increase wind farm life and will reduce cost of energy, which will be helpful in making wind energy competitive with conventional energy sources. Figure 1, presents a preliminary comparative analysis of a simple array of two 6MW wind turbines, quantifying the benefits of a coordinated control strategy. In the first case, the array is operated with the traditional greedy approach. Though upstream turbine is almost producing 6MW - its maximum - the farm output is 10.1MW. However, in the second case – when the upstream turbine is de-rated by 12.16% to produce 5.27MW - the farm output is 10.39MW. This represents a net increase of 2.87% in total farm output. .

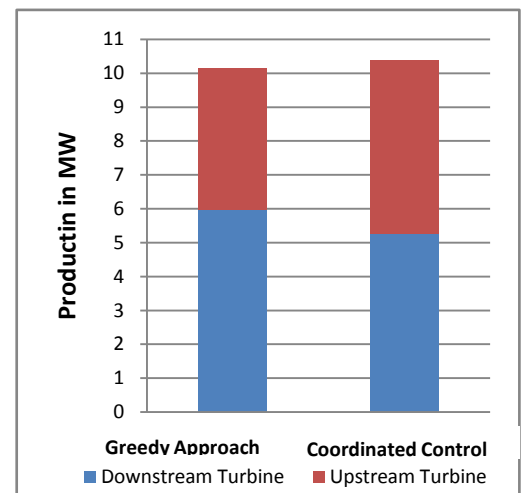


Figure 1: Greedy Approach vs Coordinated Control

One of the requirements for a farm controller is a wake flow model which shall be able to calculate wind speed deficits and turbulence intensity in the wind farm. The wake flow model shall be accurate enough with very high processing speed. The processing speed should be in seconds as turbines are to be controlled in real time. Development of such a model is the aim of this paper. The choice of a suitable wake model depends upon the following three factors [5].

- The desired computational time
- Level of accuracy required
- Available wind modelling parameters

One of the key requirements of a farm controller is that it should do all the optimisation very fast (in seconds). If the optimiser is fast enough then the optimised reference can be communicated to individual turbines to take advantage of the coordinated approach. There is a trade-off between wake model computational efficiency and level of accuracy. High fidelity CFD models, such as SOWFA and Eddy viscosity models can represent the wind farm and wake flow in more detailed way with accurate results but the processing time is very high as these models have to present all the wind turbines and turbulence in the wind farm [6].

Table 1: Comparison of Wake Models for Farm Control [8]

Model	Processing Time	Accuracy	Feasibility
Park Model	5 seconds	Low	Most suitable for feedback control
DWM	8 minutes	Medium	Not feasible
Actuator Disk	25 seconds	Medium	Invalid in far wake region
SOWFA	30 hours	High	Computationally very expensive

The processing can take days and even weeks [6]. On the other hand engineering models such as the Jensen model are less accurate but are computationally very efficient and suitable for real time feedback control systems [7, 8]. A study was conducted in [8] for assessing suitability of different wake models for optimal wind farm control strategies using a two turbine array. A summary of the results with comments are given in Table 1.

As computational efficiency is the primary requirement for this work, the Jensen model is used for wind deficit calculation. The Jensen model cannot calculate the turbulence intensity inside the wind farm. Turbulence intensity is important for farm controller as it can be used to calculate turbine loads. Therefore, the original Jensen model is modified in this paper by adding a turbulence model into it.

III. JENSEN WAKE MODEL

The Jensen wake model is the simplest but precise and reliable wake flow model and has been widely used for wind A farm control because of very high computational speed [8, 9]. The Jensen model is a practical tool as long as mean energy production rather than velocity field is area of interest [10]. This model is only valid for far wake regions (3D or more) [11] and the ideal wind flow is considered i.e. frictionless and incompressible [9, 10].

Farm controller requires speed deficits in far wake areas as turbines are not installed in the near wake region. The main assumption is that wake expands linearly behind the rotor starting with a diameter equal to the rotor diameter [9, 10]. The model follows law of conservation of momentum [10].

$$\pi r_0^2 u_T + \pi (r^2 - r_0^2) u_0 = \pi r^2 u \quad (1)$$

$$r = r_0 + kx \quad (2)$$

$$k = 1 / [2 \ln (z / z_0)] \quad (3)$$

Where u_0 is free stream wind speed, r_0 is rotor radius of upstream turbine, r is wake diameter at distance x and k is the decay coefficient which depends upon hub height “ $z = 40\text{m}$ ” and roughness length of the terrain “ z_0 ” as shown in equation (3) [5]. k is kept constant throughout the wind farm in the original model [10]. The wind speed in the wake is determined by the following equation (4).

C_T is the thrust coefficient.

$$u = u_0 \left[1 - \left(\frac{1 - \sqrt{1 - C_T}}{\left(1 + \frac{kx}{r_0}\right)^2} \right) \right] \quad (4)$$

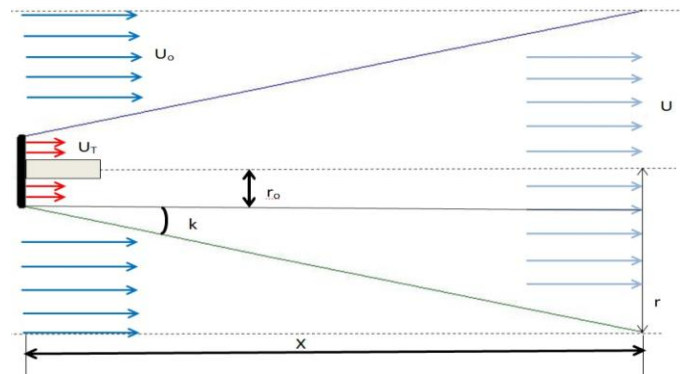


Figure 2: Jensen Wake Flow Model

This basic single wake flow model is extended to multiple and partial wakes in [5, 9, 10]. This modification is used in this paper for adding multiple wakes on downstream turbines. The wake decay coefficient determines how quickly the wake expands. A typical value for the wake decay coefficient in small offshore wind farm is $k = 0.05$ and larger offshore farms it is $k = 0.04$, for onshore the recommended value is $k = 0.075$ [3, 12]. Value of k shall be high for unstable conditions than stable conditions and the existing values shall be re-evaluated for getting accurate results.

One of the shortcomings of the Jensen model is that it cannot be used for turbulence intensity calculation [10]. Turbulence and hence wake decay coefficient k remains constant as the wind flows through the wind farm. But the turbulence intensity varies with the wind deficit in the farm. Determining turbulence intensity is important for farm optimisation as it will be used for calculating additional loads due to wakes.

IV. TURBULENCE MODEL

Turbulence intensity is the measure of overall turbulence. One of the negative effects of wakes is increased turbulence on the downstream turbines. The downstream turbine fatigue loads may increase up to 80% due to increased turbulence levels [13]. Therefore, reducing turbulence intensity and hence fatigue loads is also one of the primary objectives in farm optimisation. As Jensen model is unable to calculate turbulence intensity, a separate turbulence model from [3, 14] is used in this paper. This turbulence model can be used with single, multiple and partial wakes.

Turbulence intensity can be found with the following equation (5). =

$$I = I_0 (1 + \alpha) \exp \left(- \left[\frac{\theta}{\beta} \right]^2 \right) \quad (5) \text{ Where } \beta = 25/x \text{ [deg]} \quad (6),$$

$$\alpha = \sqrt{\left(I_w / I_0 \right)^2 + 1} - 1 \quad (7), \quad I_w = 1 / \left(1.5 + 0.3x / \sqrt{U_0} \right) \quad (8)$$

Where x is the distance between wake creating and wake affected turbine. β is the characteristic width of the wake. I_w is the wake added turbulence and I_o is the ambient turbulence. The average of farm generated turbulence \bar{I} can be found by the following equation (9) [14].

$$\text{Average Farm generated Turbulence} = \bar{I} = \frac{1}{2} \left(\sqrt{I^2 + I_o^2} + I_o \right) \quad (9)$$

V. MODIFICATIONS

As already mentioned that Jensen model does not take turbulence into account for wake calculation. Therefore the value of k remains constant throughout the wind farm. Inclusion of atmospheric stability (turbulence) in the Jensen model is not that simple [15]. One possible solution is to adjust the parameters in the model to match the observed data [15]. The value of k depends upon the hub height and length of surface roughness as shown in equation (3). We have modified the value of z_o by replacing it with modified values of turbulence from equation (9). The \bar{I} in equation (9) is first divided into different bins, then based on those bins a scaling operation is performed for calculating a new value of z_o . The modified model will use a reduced, increased or equal value of \bar{I} as z_o . This way value of k varies as the wake moves through the wind farm. At the same time, multiple and partial wakes are used to get more accurate results. The wake behind the rotor still remains linear but the wake expansion varies according to the value of k . This way the turbulence effect is included in the wind speed deficit calculation. The model used in [9] is used as a benchmark for calculating the value of k . WindPro software is used in [9] for calculating the effect of turbulence on value of k .

The basic aim of this model is to be used for optimising load and power in a wind farm. To get the power in the wind accurately, a correction factor is applied. The correction factor is important as power in the wind is proportional to cube of the wind speed. The following formula is used for equivalent wind speed for power calculation [9].

$$U_{power} = \sqrt[3]{u_0 \left(1 - \sqrt{\sum_{k=1}^{i-1} \left(1 - \frac{u_{k,i}}{u_0} \right)^2} \right)^3} \quad (10)$$

VI. RESULTS & DISCUSSION

A single row array of 5 wind turbines is considered for analysis. Turbines are similar in size with blade length of 30m. Ambient turbulence intensity I is 0.14, coefficient of thrust C_T is 0.4 and spacing between the turbines is 7D. The

Table 2: Modified Jensen Model Results

Free stream speed = 15 Ambient Turbulence= 0.14	T2	T3	T4	T5
Effects by Turbine1 k	14.15 .0707	14.62 .0713	14.86 .0929	14.91 .0931
Effects by Turbine2 k	x	13.54 .0931	13.9 .0931	14.01 .0932
Effects by Turbine3 k	x	x	12.97 .0932	13.31 .0932
Effects by Turbine4 k	x	x	x	12.42 .0932
Multiple wakes effects	14.15	13.5	12.69	11.76
Wind speed for power calculation	14.05	12.93	12.36	12.2
Turbulence Intensity	0.169	0.186	0.187	0.188

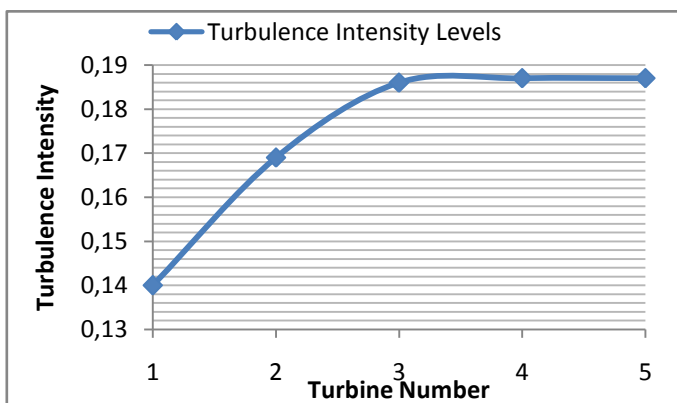


Figure 3: Turbulence Intensity in the wind farm

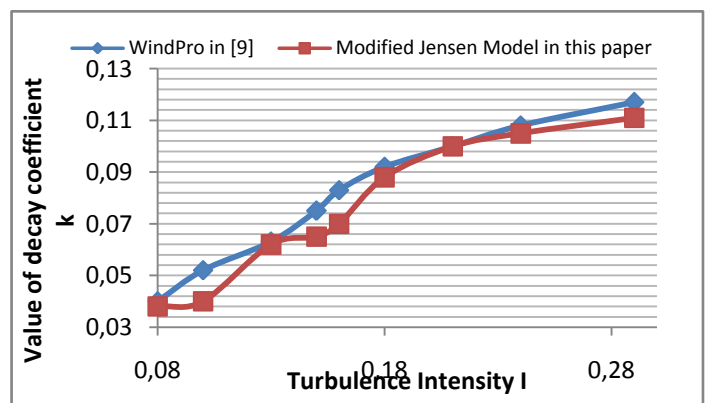


Figure 4: Variation of k with Turbulence Intensity

results are given in Table 2. This table shows the effects of each upstream turbine on downstream turbines. The downstream turbines are in full wakes. Then wind speeds at each turbine for calculation are given. The first row shows the effect of first turbine on the four downstream turbines. The second row shows the effects of second turbine on downstream turbines and so on. Multiple wakes are superimposed according to the method given in [9, 10]. The final row shows the turbulence intensity in the vicinity of each turbine. It can be seen in Figure 3 that turbulence intensity increases inside the array. The value of k is not constant. It changes as the wind flows through the wind farm. This change of value depends upon the turbulence and is almost in agreement with the results from WindPro software in [9] as shown in Figure 4. The wind speed is decreasing down the farm, which increases the turbulence intensity. As

mentioned, the basic aim of this model is to be used in a farm controller for power and load optimisation. Hence a correction factor was applied to the wind speed in table 2 as per equation 10. The difference in speeds for wake flow and power (because of the correction factor for power) can be seen in Figure 5.

VII. CONCLUSIONS AND FUTURE WORK

A dynamic wake flow model for wind farm control was presented in this paper. The Jensen model was modified for accumulating multiple and partial wakes. A separate turbulence model is used for calculating turbulence intensity. The surface roughness length is linked to the turbulence intensity in the wakes. This way the wake decay coefficient varies as the wind flows through the wind farm. A correction factor is used for calculating power in the wind. This model can be used for developing wind farm controllers and optimising loads and power in a wind farm.

The next step in this research will be to design an optimiser which will optimise power and loads in the wind farm. The optimiser shall be computationally efficient and accurate. Our farm optimiser will be based on Particle Swarm Optimisation (PSO). This technique is inspired by the flocking of birds and schooling of fish [16]. PSO is a population based technique where particles search through the solution space communicating and cooperating with each other. PSO is fast, robust and easy to implement optimisation method. It has a very high success rate for finding high quality solution for complex optimisation problems. This optimiser will be connected to the wake flow model developed in this paper for load and power optimisation in a wind farm.

The model can be used for different wind speeds in a single simulation. However, when the wind direction is changed, a new simulation has to be run with a new set of (x, y) coordinates for farm geometry. In the future work wind direction will be included in the model. The turbulence bins and mathematical operators used for calculation of decay coefficient will be selected with a continuous function.

REFERENCES

- [1] Moskalenko, N., K. Rudion, and A. Orths. Study of wake effects for offshore wind farm planning. in *Modern Electric Power Systems (MEPS), 2010 Proceedings of the International Symposium*. 2010. IEEE
- [2] Sanderse, B., S. Pijl, and B. Koren, Review of computational fluid dynamics for wind turbine wake aerodynamics. *Wind Energy*, 2011. **14**(7): p. 799-819
- [3] ALI, M. and J. Milanovic, Probabilistic assessment of wind farm energy yield considering wake turbulence and variable turbine availabilities
- [4] Adaramola, M. and P.-Å. Krogstad, Experimental investigation of wake effects on wind turbine performance. *Renewable Energy*, 2011. **36**(8): p. 2078-2086
- [5] González-Longatt, F., P. Wall, and V. Terzija, Wake effect in wind farm performance: Steady-state and dynamic behavior. *Renewable Energy*, 2012. **39**(1): p. 329-338
- [6] Fernandez, L.M., J.R. Saenz, and F. Jurado, Dynamic models of wind farms with fixed speed wind turbines. *Renewable Energy*, 2006. **31**(8): p. 1203-1230
- [7] Johnson, K.E. and N. Thomas. Wind farm control: addressing the aerodynamic interaction among wind turbines. in *American Control Conference, 2009. ACC'09.2009*. IEEE
- [8] Annoni, J., et al. Evaluating Wake Models for Wind Farm Control. in *American Control Conference, Portland, OR, USA. 2014*
- [9] Choi, J. and M. Shan, Advancement of Jensen (Park) wake model. EWEA conference, 2013
- [10] Katic, I., J. Højstrup, and N. Jensen. A simple model for cluster efficiency. in *European Wind Energy Association Conference and Exhibition. 1986*
- [11] Beaucage, P., et al. Overview of six commercial and research wake models for large offshore wind farms. in *Proceedings of the European Wind Energy Association Conference, 2012*
- [12] Gaumont, M., et al. Benchmarking of wind turbine wake models in large offshore wind farms. in *Proceedings of the Science of Making Torque from Wind Conference, 2012*
- [13] Adaramola, M. and P.-Å. Krogstad, Experimental investigation of wake effects on wind turbine performance. *Renewable Energy*, 2011. **36**(8):
- [14] Frandsen, S. and M.L. Thøgersen, Integrated fatigue loading for wind turbines in wind farms by combining ambient turbulence and wakes. *Wind Engineering*, 1999. **23**(6): p. 327-340
- [15] Peña, Alfredo, and Ole Rathmann. "Atmospheric stability- dependent infinite wind- farm models and the wake decay coefficient." *Wind Energy* (2013).
- [16] Kennedy, J. and R. Eberhart. Particle swarm optimization. in *Proceedings of IEEE international conference on neural networks. 1995*. Perth, Australia

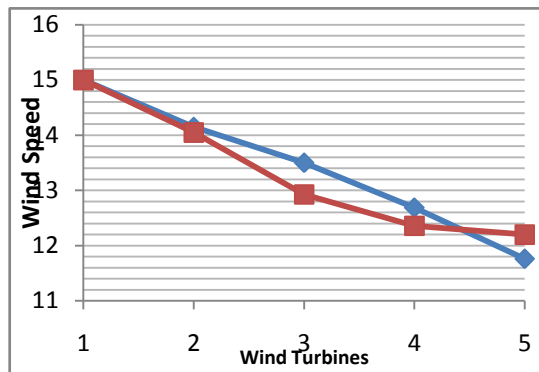


Figure 5: Wind Speed at different Turbines

Effects of Tip-Injection on the Flow Downstream of a Model Wind Turbine Rotor Blade Tip

A. Abdulrahim¹, E. Anık¹, Y. Ostovan¹, O. Uzol¹

¹Middle East Technical University (METU), Department of Aerospace Engineering,
METU Center for Wind Energy (METUWIND), Ankara, Turkey

ABSTRACT

The present paper describes an experimental investigation of the effects of tip-injection on the near wake of a model wind turbine rotor just downstream of the rotor blade tips. Measurements have been conducted downstream of the rotor blade tip by measuring the instantaneous axial velocity using a single sensor hot-wire driven by a Constant-Temperature Anemometry (CTA) system. In addition, Particle Image Velocimetry (PIV) measurements have also been conducted downstream of the rotor blade tip. The experiments are carried out by placing a specially designed wind turbine rotor at the exit of an open-jet wind tunnel facility. The model wind turbine consists of a 3-bladed rotor of 0.95 m diameter. The rotor blades are non-linearly twisted and tapered with NREL S826 airfoil profile all along the span. The nacelle, hub and the blades are specifically designed to allow pressurized air to pass through and get injected from the blade tips while the rotor is rotating. As shown in the mean velocity magnitude and turbulence intensity plots the trajectory of the tip vortex and the near wake flow characteristics have been significantly influenced by injection. It appears that the injection causes increased diffusion and mixing downstream of the rotor. Furthermore, the injection seems to increase the width of the wake region due to quicker diffusion of the vortex trajectory. The flow field is now occupied by a highly turbulent region that occupies wider areas as one propagates downstream.

INTRODUCTION

Tip injection is an Active Flow Control (AFC) technique aimed at controlling the leakage/vortex characteristics at the blade tips as well as the size, vorticity and turbulence characteristics of the tip vortex. This technique has been widely investigated in various applications such as fixed wings [1] [2], helicopter rotors [3], turbomachinery blades [4] [5], as well as wind turbines [6]. Studies have shown that tip injection increases the total lift generated from a wing/blade because of the increase in the effective span due to reduced leakage at the blade tip.

EXPERIMENTAL SETUP

The experiments are conducted in an open-jet wind tunnel facility with 1.7 m jet exit diameter shown in Figure 1a. The maximum velocity reached by this tunnel is 10 m/s and the average turbulence intensities at the jet centerline are around 2.5 %.

The model wind turbine used in the experiments consists of a 3-bladed rotor with non-linearly twisted and tapered blades that have an NREL S826 profile all along the blades. The model wind turbine is equipped with a torque transducer and a load sensor to measure the torque and thrust applied on the turbine rotor. The turbine rotor is driven by an AC servo motor to control the rotational speed of the rotor. The nacelle, hub and the blades are specially design to allow pressurized air to pass through and get injected from the blade tips while the rotor is rotating. Figure 1 shows the test setup used in the experiments as well as the measurement planes for the CTA and PIV systems.

Mean axial velocity magnitude and turbulence intensity data are collected on the measurement plane shown in Figure 1b. The measurement plane is a 20 cm x 20 cm grid with step sizes of $\Delta x=1$ cm $\Delta y=0.2$ cm. The CTA system is controlled by an NI DAQ system through a LabView program. Data have been collected at a sampling rate of 5 kHz for 4 seconds at each grid point. Direction of flow is from left to right marked by the solid black arrow shown in Figure 1b. The position $y/R=1$ marks the blade tip. The PIV measurement plane is an 8 cm x 12 cm grid. The PIV system consists of a 30 mJ Litron Nd: YLF laser and a Phantom V640 camera with a maximum resolution of 2560x1600 pixels at a frequency of 1.5 kHz (4 megapixels at full resolution). Moreover, a smoke generator has been used

for flow seeding. Data have been collected at 742 Hz with 20 μ s time separation between each laser pulse.

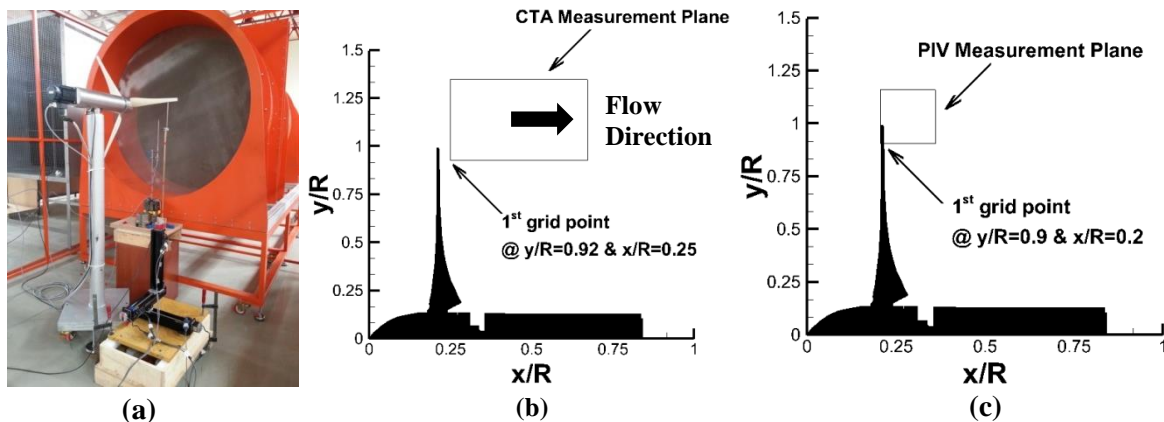


Figure 1: (a) Open-jet facility & model wind turbine, (b) CTA measurement plane, and (c) PIV measurement plane

RESULTS AND DISCUSSIONS

Constant Temperature Anemometry (CTA) Measurements

Figures 2 & 3 show the velocity magnitude and turbulence intensity plots both for the baseline as well as the injection cases. The experiments have been conducted at a wind speed of 5 m/s and for a Tip Speed Ratio (TSR) of 5. The flow rate exiting the blade tips was obtained by measuring the velocity at the tip using a Pitot-Static probe while the turbine is stationary. Injection Momentum Ratio (R_M), which is defined as the ratio of the total momentum of injected air to the momentum of air going through the rotor disk has been used as an indicator of the amount of injection used during the tests. The tip injection velocity variation from blade to blade is less than 5 %.

As shown in the mean velocity magnitude and turbulence intensity plots the trajectory of the tip vortex is clearly depicted in the baseline case. When one applies tip injection, the entire flow field downstream of the blade tip is occupied by a highly turbulent zone. The injection affects the tip vortex trajectory due to enhanced mixing and quicker diffusion. It appears that the tip vortex is pushed radially outwards due to injection. Figure 4 shows line distributions of velocity and turbulence intensity along the radial direction at $x/R=0.27R$ downstream of the blade tip. These plots illustrate some of the arguments presented previously in a more quantitative manner. Near the blade tip region ($y/R=1$), there is a sharp change in velocity distribution for the baseline case. Having tip injection modifies this region significantly. The momentum of the jet exiting from the blade tips generates a peak in the velocity distribution and the transition region from the rotor wake to the freestream conditions occupies a wider area when injection is applied. The turbulence intensity variation shows also dramatic changes near the tip due to injection. The tip jets when mixing with the oncoming freestream seem to generate substantial increase in local turbulence levels showing almost 4-5 times more turbulence intensity at the peak of the distribution. Note that the turbulence intensity variations as well as the axial velocity nicely converge onto each other for the baseline and injection cases away from the tip region within the wake and freestream zones.

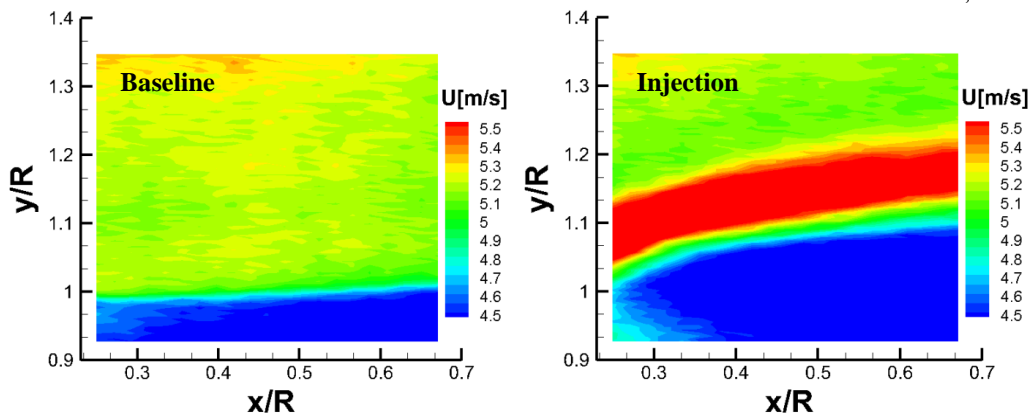


Figure 2: Velocity magnitude distributions downstream of blade tip region @ $U_\infty=5$ m/s & TSR=5: Baseline case (left), and Injection case (right) @ $R_M=1.3\%$

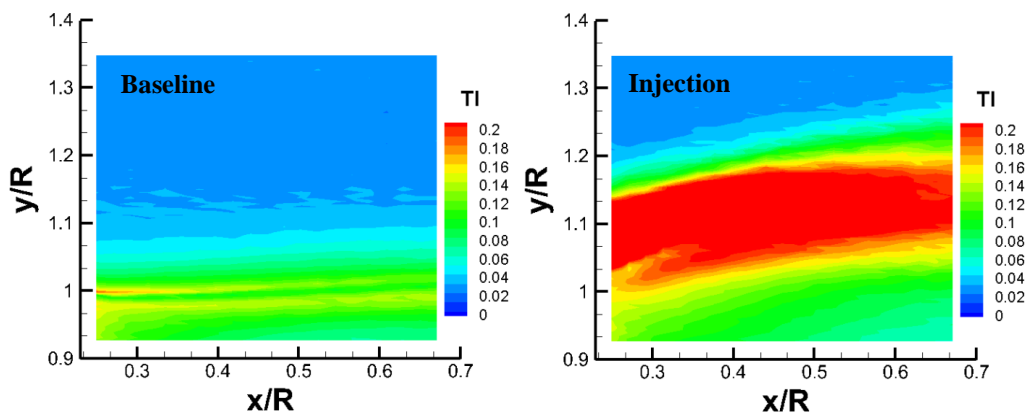


Figure 3: Turbulence intensity distributions downstream of blade tip region @ $U_\infty=5$ m/s & TSR=5: Baseline case (left), and Injection case (right) @ $R_M=1.3\%$

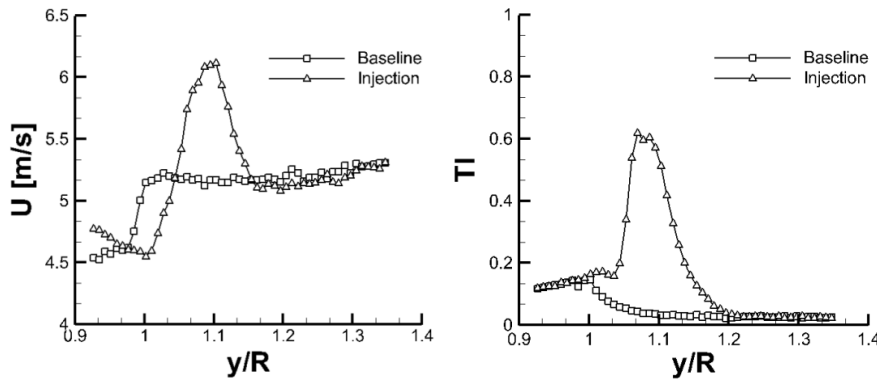


Figure 4: Velocity (left) and turbulence intensity (right) variations along radial direction at $U_\infty=5$ m/s & TSR=5

Particle Image Velocimetry (PIV) Measurements

Figure 5 presents the velocity magnitude and the vorticity magnitude contour plots resulted from the PIV measurements. Although, the measurement plane used for the PIV experiments is different from the CTA measurement plane, we still can observe the similarity in the flow field behavior. From the PIV measurements one can observe the remarkable differences that injection has posed on the flow field downstream of the blade tip as compared to the baseline case. This is clearly presented in the velocity magnitude plots. Another remarkable difference appears in the vorticity magnitude plots, the baseline case shows the tip vortex trajectory to be consistent for a typical model wind turbine. However, for the injection case the entire tip vortex trajectory is completely influenced by injection

and presents different flow field behavior. This difference consists of the generation of two vortex trajectories of same magnitude but opposite direction. Therefore, more investigation is being carried out to understand the behavior of the flow field downstream of the rotor blade and the differences that injection imposes on the flow field.

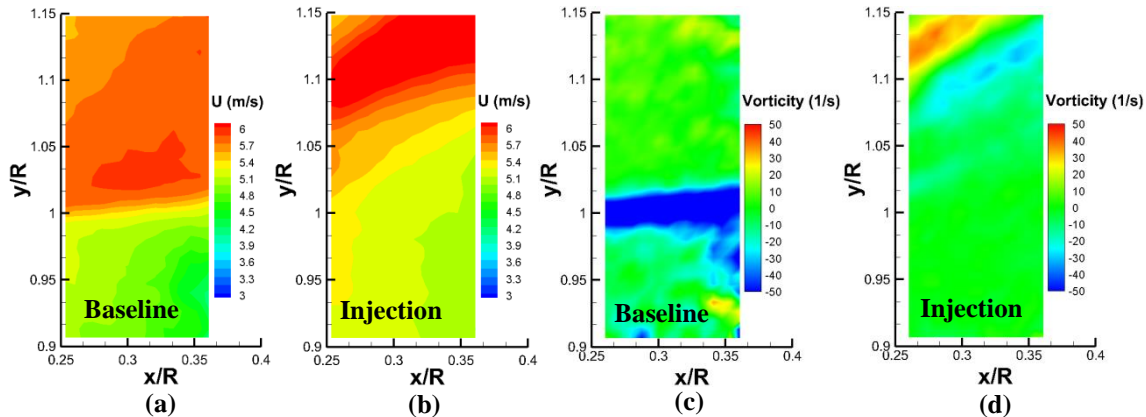


Figure 5: PIV measurements; (a-d) Velocity and Vorticity Magnitude plots @ $U=5$ m/s, $TSR=5$: (a,c) Baseline case (b,d) Injection case @ $R_M=1.3$ %

CONCLUSIONS

This paper summarizes the results of an experimental investigation of the effects of tip injection on the flow field downstream of the rotor blade tips. The entire flow field downstream of the blade tip has been significantly changed due to tip injection. This will have a major influence on the entire wake flow structure downstream of the rotor, which might have significant effects on successively arranged wind turbines in wind farms. Moreover, tip injection might result in diminishing the tip losses by reducing or totally eliminating the effects of tip vortices.

ACKNOWLEDGEMENT

This study is supported by the Scientific and Technological Research Council of Turkey (TÜBİTAK) under the grant number 112M105 as well as by METU Center for Wind Energy (METUWIND). Their support is greatly appreciated.

REFERENCES

- [1] Gursul, I., Vardaki, E., Margaris, P., Wang, Z., 2007, "Control of Wing Vortices Active Flow Control," Notes on Numerical Fluid Mechanics and Multidisciplinary Design pp. 137-151 Springer-Verlag Berlin
- [2] Mercan, B., Ostovan, Y., Doğan, E., Uzol, O., 2010, "Effect of Chord-wise Modulated Waveform Tip Injection on the Characteristics of the Tip Vortex," 40th Fluid Dynamics Conference and Exhibit, Chicago, Illinois
- [3] Vasilescu, R., 2004, "Helicopter Blade Tip Vortex Modifications in Hover Using Piezoelectrically Mounted Blowing," PhD Thesis, Georgia Institute of Technology, USA
- [4] Mercan, B., Ostovan, Y., Uzol, O., 2011, "Effect of Waveform Tip Injection on Tip Leakage Characteristics of a LPT Blade," 11th International Conference on Fluid Control, Measurements and Visualization FLUCOME 2011-Paper No. 202, December 5-9 2011, National Taiwan Ocean University, Keelung Taiwan
- [5] Mercan, B., Doğan, E., Ostovan, Y., Uzol, O., 2012, "Experimental Investigation of the Effects of Waveform Tip Injection in a Low Pressure Turbine Cascade," *ASME Turbo Expo 2012* Copenhagen Denmark
- [6] E. Anik, A. Abdulrahim, Y. Ostovan, B. Mercan, O. Uzol, 2014 "Active control of the tip vortex: an experimental investigation on the performance characteristics of a model turbine", The Science of Making Torque from Wind (TORQUE2014), 17-20 June, 2014 Copenhagen, Denmark

Determining the Wind Speed Distribution within a Wind Farm considering Site Wind Characteristics and Wake Effects

T. Ahmad, C.J. Smith, P.C. Matthews, C.J. Crabtree, B. Kazemtabrizi

Durham University, School of Engineering and Computing Sciences, tanvir.ahmad@dur.ac.uk,
c.j.smith2@dur.ac.uk

ABSTRACT

This paper introduces a wind speed model for simulating the distribution of wind speeds within a wind farm. The model combines a macro scale wind speed time series (WSTS) model based on a continuous Markov process with a wake flow model, based on the Jensen model, to produce wind speeds upwind of every wind turbine. This model has been designed for use in the testing of turbine coordinated control algorithms and for use in detailed reliability analysis. An example analysis was carried out to investigate the Annual Energy Not Produced (AENP) due to wake effects on a single string wind farm. It was found that the wakes accounted for a 20.2% reduction in energy production compared to the wakeless scenario, highlighting the need to model these wake effects.

I. INTRODUCTION

The stochastic nature of the wind and effect of wakes from upstream wind turbines provides unique fuel characteristics for wind farms. For reliability analysis of offshore wind farms the need to capture these characteristics is paramount, as the wind resource affects the power available to each wind turbine at any given time. By including wind resource characteristics and wake effects in the farm, the effect of failed assets and farm layout on Levelised Cost of Energy (LCoE) can be more accurately quantified. The modelling of these wind speed characteristics is also essential for evaluation and testing of coordinated control algorithms. The variations in wind speed will affect the performance of wind turbines when operated with coordinated control.

To produce the distributed wind speeds within a wind farm that are suitable for both reliability assessment and the testing of coordinated control algorithms, work on reproducing wind speed time series (WSTS) based on original wind speed data [1] has been combined with a wake flow model developed in [2].

This paper outlines the characteristics of this combined wind speed model. Section II gives details on the WSTS model and wake flow model, and how the models are combined to produce a whole farm model. Section III outlines an example analysis that this whole farm model can be used for. Section IV details the results of the example analysis and important conclusions from this analysis for reliability analysis and coordinated control, and Section V summarises the key findings from this paper.

II. WHOLE FARM WIND SPEED MODEL

This section outlines the key components of the whole farm wind model; the WSTS model for determining the macro-wind speed at given time period, the wake flow model which is based on the Jensen model, and how the two models are combined.

Firstly, to decide what model to use to generate the WSTS, the metrics in [1] were used to assess the quality of the model. The metrics are designed to determine the quality of the WSTS for reliability analysis, so here it has been assumed that the WSTS will also be adequate for use in testing the coordinated control algorithms. The results in [1] have determined that of the models tested so far, a continuous Markov Process model is the most appropriate for this whole farm wind speed model. The specific details of this model can be found in [1].

Secondly, a wake flow model has been developed in [2]. The model is based on Jensen wake flow model [3] with some modifications. In the original Jensen model [3], the wind flow is assumed to be ideal with the same turbulence intensity in the whole wind farm. In this model, the wake decay coefficient varies according to the turbulence intensity in the wind farm. This way the effect of turbulence is incorporated for calculating wind speed deficits. A correction factor is applied to the wind speeds for power as power is directly proportional to the cube of wind speed. Wind direction is considered to be parallel to the array of turbines and therefore the turbines are in full wakes. The effects of multiple wakes are considered on downstream turbines. Details of this model can be found in [2].

The two models were combined to produce the whole farm wind model. A look-up table (LUT) was produced, which shows the wind speed deficit at every wind turbine for every macro-scale wind speed experienced at a site. A WSTS is

produced for the site for a given period of time from the WSTS model. Using this WSTS and the LUT of wind speeds, a WSTS was produced for each wind turbine in the farm for the life time of the farm.

For this whole farm wind model, there are some simplifying assumptions. Firstly, it has been assumed that macro-wind speed for the whole site remains constant in a given time period, and the only variation is due to the turbines' wakes effects. The wind direction also remains constant, and faces the front of the farm.

Therefore, a whole wind farm model has been produced by combining a WSTS model based on a continuous Markov Process with a wake flow model that is based on the Jensen model, considering the effects of multiple wakes.

III. ILLUSTRATION

This Section details an example analysis carried out using this whole farm wind model. The Annual Energy produced (AEP), Annual Energy Not Produced (AENP) and annual revenue loss over the lifetime of a wind farm were calculated for both wake and wake-less scenarios.

To calculate the AEP due to wake effects, the energy produced at each turbine is computed for wake-less and wake scenarios using (1).

$$E_{T(i)} = \sum_{k=1}^{N-1} 0.5C_p\rho\pi r^2 u_{t,T(i),k}^3 (t_{k+1} - t_k) \quad (1)$$

Where $E_{T(i)}$ is the energy produced by turbine i in the array (Wh), k is the time array step, N is the total number of time array steps, C_p is the coefficient of power, ρ is the air density (kg/m^3), r is the blade length (m), $u_{t,T(i),k}$ is the equivalent velocity at turbine i at k (m/s), and t_k is the time at k (hours). The equivalent velocity is calculated by modifying the actual wind speed with limits to represent the cut-in, cut-out and rated wind speeds (2).

$$u_t = \begin{cases} 0, & u < u_{in} \\ u, & u_{in} \leq u < u_{rated} \\ u_{rated}, & u_{rated} \leq u < u_{out} \\ 0, & u \geq u_{out} \end{cases} \quad (2)$$

Where u is the actual wind speed (m/s), u_{in} is the cut-in wind speed (m/s), u_{rated} is the rated wind speed (m/s), and u_{out} is the cut-out wind speed (m/s). The AEP is calculated by dividing by the simulation time.

The energy not produced (ENP) is calculated using (3).

$$ENP = N_T E_{T(1)} - \sum_{i=1}^{N_T} E_{T(i)} \quad (3)$$

Where N_T is the number of turbines.

AEP and AENP are calculated by dividing by the number of simulation years. To calculate annual revenue loss, the AENP for this multiplied by both £140/MWh and £100/MWh, representing current and future strike prices [4].

To carry out this analysis, a model wind farm was required. The wind farm in this example was a single string of 5 wind turbines in a row, in line with the wind direction, with 7 diameter (7D) array spacing. The performance parameters of the turbine and characteristics of the air are detailed in Table 1.

Parameter	Value	Parameter	Value
N_T	5	C_p	0.36
Distance between turbines	420 m	u_{in}	4 m/s
r	30 m	u_{rated}	13 m/s
Wind farm lifetime	25 years	u_{out}	25 m/s
Coefficient of thrust (C_t)	0.4	ρ	1.225 kg/m^3

Table 1: Wind farm and wind turbine operating parameters.

For this analysis, the original wind speed data was taken from the meteorological mast at the Egmond aan Zee wind farm site [5]. The data used was wind speeds from a height of 70 m, at 10 minute intervals from 01/07/2005 to 30/06/2006, and has been cleaned to produce a complete data set. This data set was used as the data to develop the continuous Markov process transition rate matrix. A 25-year WSTS was produced to simulate the wind profile over the lifetime of the farm.

It has been assumed that the turbines have perfect reliability for this analysis, and that the propagation time of wake effects in the farm are negligible compared to the sampling time of the WSTS. Therefore, the wake effects are assumed to occur simultaneously at all wind turbines.

The example analysis investigates the energy and revenue loss of a 5 turbine string array wind farm due to wake effects with unidirectional wind speed over a 25 year life time using the combined WSTS-wake flow model.

IV. RESULTS AND DISCUSSION

This section presents the results of this example analysis. Table 2 details the results of the energy analysis, Figure 1 gives an example trace of the WSTS for each of the turbines for a month, and Figure 2 shows the distribution of energy production and energy loss throughout the wind farm.

Parameter	Value	Parameter	Value
AEP	23.39 GWh	AENP (percentage of AEP wakeless)	20.2%
AEP (wakeless)	29.32 GWh	Annual revenue loss (current)	£0.83M
AENP	5.93GWh	Annual revenue loss (future)	£0.59M

Table 2: Results of example analysis.

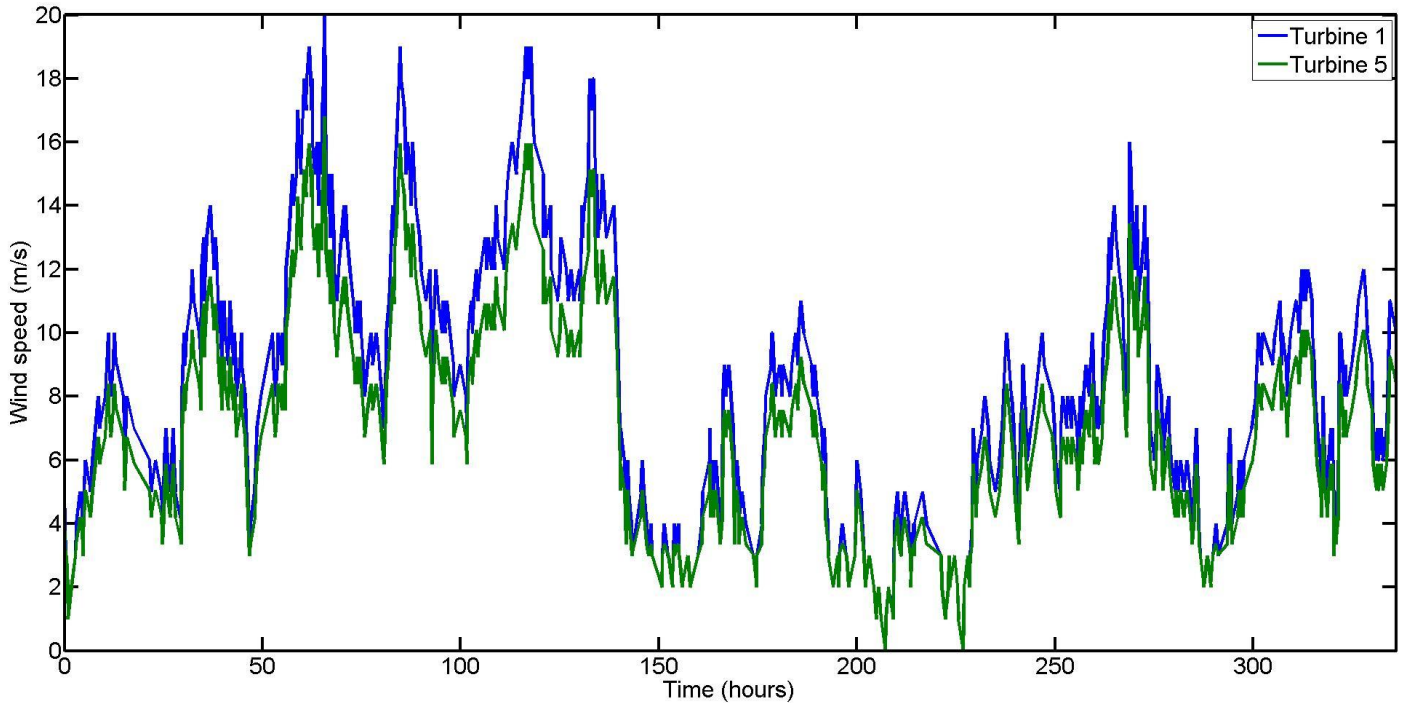


Figure 1: WSTS for 2 weeks for turbines 1 and 5.

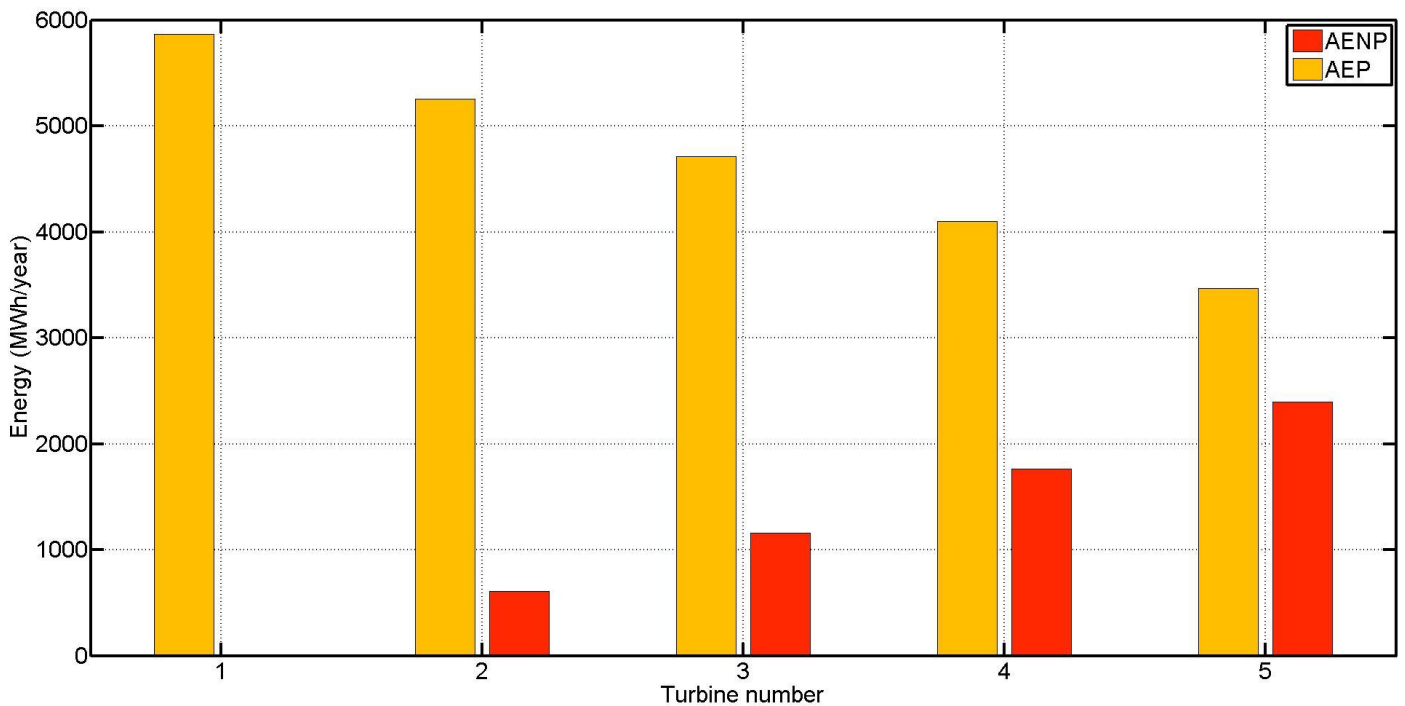


Figure 2: Distribution of energy production and energy loss throughout the wind farm.

Table 2 reveals that the effect of wakes has a large impact on the energy output of the wind farm, with the wakes accounting for a 20.2% reduction in energy production when compared to the wakeless scenario. These results are in line with the values found in[6]. Figure 2 shows that this energy loss, as expected, increases with array length. Interestingly, the wake effects on turbine 5 cause a 40.8% reduction in turbine 5's energy production. This is due to cumulative effect of each of the wakes of the turbines in front of turbine 5. Indeed, Figure 1 displays a significant reduction in wind speed from turbine 1 to turbine 5, particularly at high winds. This has the greatest impact when the wind speed is reduced from the rated wind speed to a much lower speed. Therefore, there is potential for a reduction in energy extraction at the leading turbines to increase the overall energy production of the wind farm by increasing the wind speeds at the downwind turbines.

In reality, a single string wind farm with the turbines in a row would be positioned so that the turbine wakes did not shadow downwind turbines in the prevailing wind direction and therefore the AENP due to wakes would be lower than described. However, an array of wind turbines with a number of strings in a grid will suffer similar magnitude wake losses, depending on current wind direction and distance between turbines. To adapt this model for a grid of turbines, the distribution of wind speeds across the front of the wind farm needs to be investigated.

These results provide two key conclusions. Firstly, the impact of wakes on energy production and annual revenue loss in even a simple wind farm highlight the potential benefits coordinated control can bring to a wind farm operator. By controlling the wind turbines in the array to maximise energy extraction by minimising wake effects, an increase in annual revenue can be achieved for a small investment and design change. This whole farm wind speed model can be used to quantify these potential benefits once the algorithms are developed. The transitions between wind speeds can also test the robustness of the co-ordinated control algorithms.

Secondly, the results highlight the importance of including wake effects in reliability analysis. Neglecting to accurately portray wake effects in the wind farm can lead to an over-estimation of the energy production of a wind farm by a significant margin. In turn, the effect of a failure of a wind turbine may be over-estimated; a failure of a downwind turbine will be lower than that of an upwind turbine, and the reduction in energy production due to failure of an upwind turbine could be smaller than anticipated due to the improved performance of the downwind turbines. This combined whole farm wind speed model can provide the basis for such a reliability analysis.

The AENP for this 5 turbine wind farm was 20.2% due to wakes, with a significant impact on turbine 5's energy production. This highlights the need to model wake flows both in reliability analysis and the testing and evaluation of coordinated control algorithms. The model developed in this paper is able to carry out these analyses.

V. CONCLUDING REMARKS

This paper introduces a wind speed model for a whole wind farm that combines a macro scale WSTS model with a wake flow model to generate the 10 minute average wind speeds at every wind turbine in a farm for the life time of the farm. The WSTS model is based on a continuous Markov process that has been tested for its suitability, whilst the wake flow is based on a modified Jensen model with varying turbulence intensity. The wake flow model produces a LUT of wind speeds at every time interval. A WSTS is produced for the upwind turbine in the array, and the LUT used to produce the wind speeds for each of the downwind turbines.

An example analysis was carried that investigated the AENP due to wake effects on a single string, 5 turbine example wind farm, with the wind always facing parallel to the string direction. It was found that the AENP was 5.93GWh; a 20.2% reduction in energy production compared to a wakeless scenario. This high AENP highlights the large impact wakes can have on the energy production of a farm.

The whole farm model allows for more accurate calculation of energy production in the farm in reliability analysis. The wind farm model can also be used to test the robustness of coordinated control algorithms and quantify their benefits on the farm energy production. In future, the model will be expanded to include the distribution of wind speeds across the front of an entire wind farm, the effect of turbine failures on wake interaction, and the modelling of wind direction.

REFERENCES

1. C.J. Smith, et al., *Modelling and Evaluation of Wind Speed Time Series for Reliability Analysis of Offshore Wind Farms*, in *10th EAWC PhD Seminar on Wind Energy in Europe*. 2014: Orléans, France.
2. T. Ahmad, P.C. Matthews, and B. Kazemtabrizi, *Wake Flow Model for Wind Farm Control*, in *10th EAWC PhD Seminar on Wind Energy in Europe*. 2014: Orléans, France.
3. N.O. Jensen, *A note on wind generator interaction*. 1983.
4. E. Davey and A. Nimmo. *Offshore Wind Cost Reduction, Pathways Study*. 2012; Available from: <http://www.thecrownestate.co.uk/media/305094/offshore-wind-cost-reduction-pathways-study.pdf>.
5. Noordzeewind. *Noordzeewind: Reports & Data*. 2014; Available from: <http://www.noordzeewind.nl/en/knowledge/reportsdata/>.
6. M.S. Adaramola and P.Å. Krogstad, *Experimental investigation of wake effects on wind turbine performance*. *Renewable Energy*, 2011. **36**(8): p. 2078-2086.

FEEDBACK CONTROL OF BLADES TRAILING EDGE FLAPS FOR BLADE ROOT LOAD MITIGATION

R. Ungurán¹, M. Kühn¹

¹ForWind – University of Oldenburg, Research Group Wind Energy Systems, Germany,
robert.unguran@forwind.de

ABSTRACT

Within the ongoing evolution of increasing rotor diameter and hub height of wind turbines the importance of load reduction is getting more in the focus of research. Therefore, various new control concepts are under development in present. However, the current control strategies have some limitations regarding the load reduction and rotor speed control due to the limited pitch actuators dynamics and lack of information about the approaching inhomogeneous wind field in advance. To resolve the above-mentioned problems different approaches can be taken. The individual pitch control (IPC) [1] has the potential to reduce the blade root bending moments, it can also wear and tear the pitch system and has a relatively slow reaction due to the considerable mass moment of inertia of large blades. Hence, lightweight movable trailing edge flaps are considered one option to provide good prospects for fatigue and extreme loads reduction of very large blades [2][3].

The dynamic loads on the rotor blades and tower are mainly caused by turbulence, wind shear and skewed or wake-induced inflow. Their impact can be reduced by controlling the blades pitch or the movable trailing edge flaps angles individually. The first phase of the present PhD project deals with feedback control. Hence, two control concepts are realized where the feedback of the blade root bending moment is used as the control input. In the first concept the blades pitch angles are used only to regulate the generator speed, while the control of the movable trailing edge flaps angles focuses on the reduction of loads varying with the rotational frequency (1P) and its high harmonics (nP). In the second concept the blade pitch angles are controlled individually to mitigate the 1P load components, whereas the trailing edge flaps are employed to alleviate the higher harmonics. As a result two feedback control concepts and simulation results are presented in respect to the load mitigation of a 7.5 MW reference wind turbine model.

SIMULATION SETUP

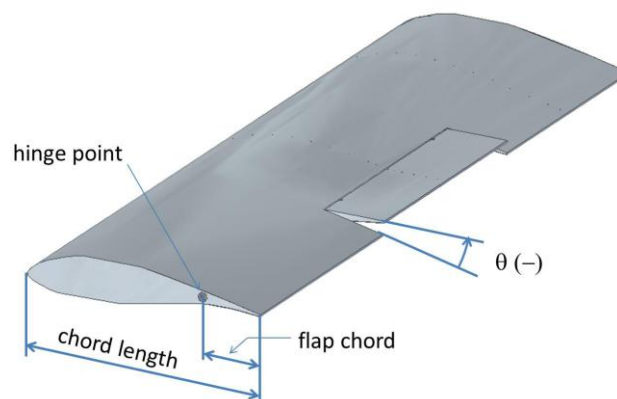


Figure 1: Movable trailing edge flaps (Figure: TFD, ForWind – Hannover)

This paper will present numerical simulations on the 7.5MW onshore reference turbine developed within the Smart Blades project, which is a coordinated cooperative project of the German Aerospace Center (DLR), Fraunhofer IWES and ForWind Hannover and Oldenburg. The results are based on the HAWC2 aeroelastic simulation software. An aerodynamic model of the flaps [4] is implemented into HAWC2, which gives the possibility to study and control the movable trailing edge flaps.

The study is based on 4m long trailing edge flaps. It is placed between span 72 m and 76 m on the 80 m length blade. The length of the trailing edge chord is 20% of the blade chord length. The flap angle can vary between $\pm 10^\circ$. The parameters are based on the findings of [5].

CONTROL DEVELOPMENT

Van Engelen [1] presented the use of individual pitch control for reducing the loads around the rotational frequency and multiple of it. A similar method is used for the development of individual pitch and trailing edge flaps control for the 7.5MW reference turbine. Beside the baseline control (BLC), three additional control loops are added: a control loop for the individual pitch control around 1P, two control loops for trailing edge flaps control around 1P and 2P. Also it is assumed that the blade root bending moments can be measured, hence this can be used as the control input as seen on Figure 2. For transferring the time variant control problem to a linear time invariant form, the Coleman transformation [6] is applied. This means the blade root bending moments are transformed from rotating reference frame to fixed reference frame, by creating artificial tilt and yaw signals.

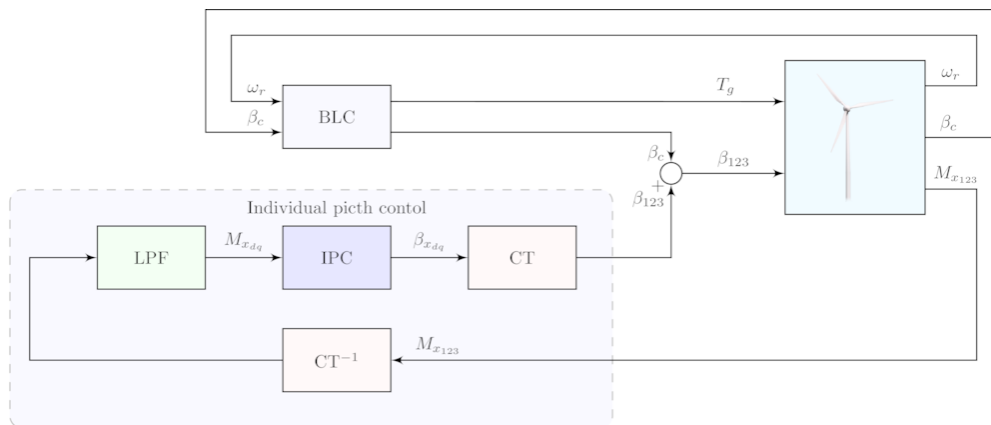


Figure 2: Control block, individual pitch control included

By applying the Coleman transformation the 1P is modulated to 0P, and the higher harmonics are modulated to 3P and multiples of 3P. Therefore, a low pass filter around and beyond 3P is necessary to eliminate the influences of the higher harmonics. The same approach can be applied [4] for higher harmonic control development.

Within the study two control concepts were developed for loads reduction. In the first case individual pitch control was developed for reducing the 1P load, the trailing edge flaps control for 2P load alleviation. In the second case only the trailing edge flaps were controlled to reduce the 1P and 2P loads.

TIME DOMAIN SIMULATION RESULTS

Time-domain simulations were performed with five control cases:

1. reference case: only the collective pitch is activated
2. collective pitch and trailing edge flaps control around 1P
3. collective pitch and trailing edge flaps control around 1P and 2P
4. collective pitch and individual pitch control around 1P
5. collective pitch, individual pitch control around 1P and trailing edge flaps control around 2P

For comparison the design load case 1.2 from the IEC 61400-1 certification standard, with a mean wind speed of 13m/s and a turbulence intensity of 0.165 is used.

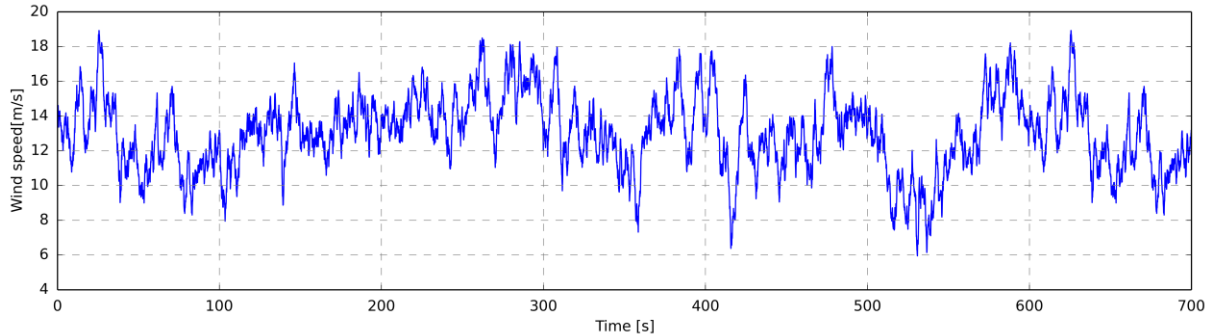


Figure 3: Horizontal wind speed at hub height

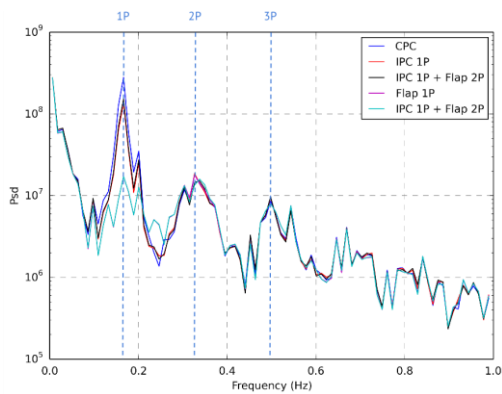


Figure 4: PSD of flapwise blade root bending moment

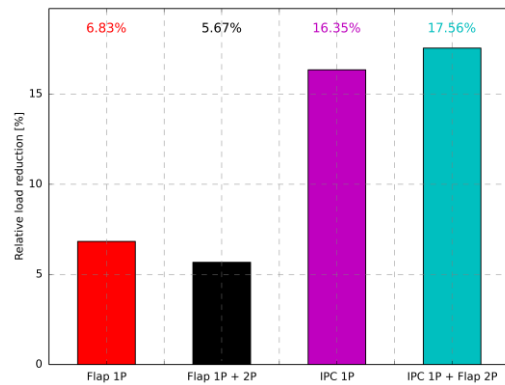


Figure 5: Reduction of DEL of blade root bending moment compared to reference case

Figure 4 shows the power spectra density of the flapwise blade root bending moments, where the 1P and 2P load reduction compared to the collective pitch control is clearly visible. Furthermore damage equivalent load (DEL) calculation was performed and the results are compared to the case when only the collective pitch control is activated. From the results on Figure 5, the maximum blade root bending moment reduction can be achieved by the activation of the individual pitch control on 1P and movable trailing edge flap control on 2P. In contrast, the minimum load reduction is achieved when the movable trailing edge flap controls are activated for both 1P and 2P. This is due to the use of the same actuator for different load reduction goals. Hence the reduction of the 2P loads leads to the increase of the 1P loads and the overall loads reduction is decreased.

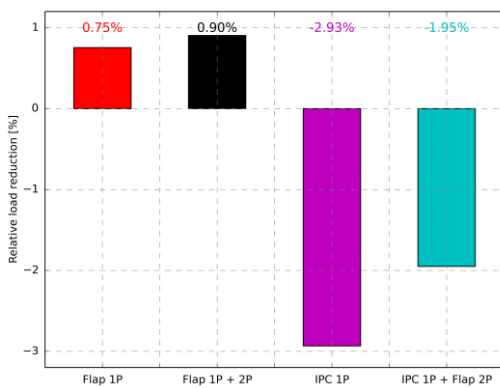


Figure 6: Reduction of DEL of tower bottom fore-aft bending moment compared to reference case

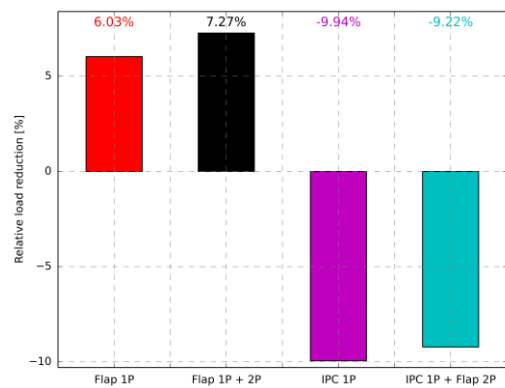


Figure 7: Reduction of DEL of tower bottom side-to-side bending moment compared to reference case

A different effect of the control concepts on the tower bottom side-to-side (Figure 6) and fore-aft bending moments (Figure 7) has been found. Here a load reduction is only observed if the trailing edge flap control is used without individual pitch control. The further investigation is required to eliminate the tower bottom excitations when the individual pitch control is activated.

CONCLUSION

Results clearly show the effect of the movable trailing edge flaps for load mitigation. Trailing edge flaps with a length of 5% of rotor span can reduce the blade root bending moment significantly. It is also visible that there is a positive effect on the tower bottom side-to-side and fore-aft moments when only the control of the movable trailing edge flaps is activated. The individual pitch and trailing edge flaps control were developed around one operation point, hence further improvements can be considered, like gain scheduling. The overall goal is the development of a robust H-infinity optimal control, where only the 1P load reduction will be considered by the control of the trailing edge flaps.

ACKNOWLEDGEMENT

This work is partially funded by the German Federal Ministry for Economic Affairs and Energy (BMWi). It is part of the Smart Blades project, which is a coordinated cooperative project between ForWind, the German Aerospace Center (DLR), and the Fraunhofer IWES

REFERENCES

- [1] T.G. van Engelen: “Design model and load reduction assessment for multi-rotational mode individual pitch control (higher harmonics control)”, Proceedings of the European Wind Energy Conference, Athens, Greece, 2006.
- [2] D. Castaignet, T. Buhl, N. K. Poulsen, J.J. Wedel-Heinen: “Model predictive control of trailing edge flaps on a wind turbine blade”, Technical University of Denmark, Risø National Laboratory for Sustainable Energy, 133 p., 2011.
- [3] M.A. Lackners, G.A.M. van Kuik: “A Comparison of Smart Rotor Control Approaches using Trailing Edge Flaps and Individual Pitch Control”, Wind Energy, Vol. 13, No. 2-3: 117-134, 2009.
- [4] L. Bergami, V. A. Riziotis, and M. Gaunaa. “Aerodynamic Response of an Airfoil Section Undergoing Pitch Motion and Trailing Edge Flap Deflection: A Comparison of Simulation Methods.” Wind Energy, 2014.
- [5] J. Ortega Gómez, C. Balzani and A. Reuter, “Evaluation of the possibility of replacing pitch control by active trailing edge flaps in wind turbines”, 2014, EWEA
- [6] R.P. Coleman, A.M. Feingold, and United States. National Advisory Committee for Aeronautics. “Theory of Self-excited Mechanical Oscillations of Helicopter Rotors with Hinged Blades.” National Advisory Committee for Aeronautics: Report. National Advisory Committee for Aeronautics, 1957.

Investigation of the derivation of the wind turbine dynamics from measured data

Luis Reguera
Wind Energy DTC
University of Strathclyde
Glasgow, UK
luis.reguera@strath.ac.uk

Prof. William Leithead
Dept. of Electronic and
Electrical Engineering
University of Strathclyde
Glasgow, UK

Dr. Julian Feuchtwang
Dept. of Electronic and
Electrical Engineering
University of Strathclyde
Glasgow, UK

Abstract—In this paper an explanation can be found of how to identify the aerodynamic torque dynamics of a wind turbine using only sampled data from the wind turbine sensors. Making use of techniques such as Gaussian processes the data can be not only filtered but also an inference of the values which have not been sampled can be obtained completing the aerodynamic torque dynamics.

I. INTRODUCTION

Wind turbine operators now have large fleets of machines that are out of warranty, including hundreds of the same model. In some cases the wind turbine performance is very poor due to control problems but, unfortunately, the manufacturers no longer provide the support required to rectify these problems. Consequently, there is a growing market for specialist control companies to provide control solutions. Unfortunately, no information is available concerning the original controller design, its code or the dynamic properties of the wind turbine. The best option is to by-pass the existing controller by a new Programmable Logic Controller (PLC) which will implement a new controller design. In order to do so, the dynamics of the wind turbine has to be identified using a set of sampled data measured directly from the wind turbine. These measures are the rotor speed, the pitch angle and the wind speed measured from the anemometer. A very brief explanation about Gaussian processing will be described as following. Afterwards, the studied case is presented and how this technique is used to do Gaussian regression and predictions about the aerodynamic torque. For the realisation of this paper a Gaussian process toolbox programmed in Matlab extracted from [1] has been used.

A. Bayesian Inference

Bayes' rules states that it is possible to relate the conditional probability of the output given the input ($p(y|x)$) knowing the conditional probability of the input given the output ($p(x|y)$). However, in order to progress in the dissertation, a model (named as \mathcal{D}) has to be incorporated in the process. This model will have the capability to be adaptable in function of the set of sampled data that it is being introduced in the calculation. I.e. if the set of sampled data represents the wind speed, a Weibull distribution would be a good model for this application since it is well known that the probability distribution of the wind

is very similar to this distribution [2]. The model selected will be adapted to the reality using sampled data. This adaptation process is based on the maximization of the model likelihood for every possible combination of the values k and λ (being these the parameters of the Weibull distribution). As example the adaptation process would based on (1) for the wind speed shown before.

$$\frac{\partial(\log p(\mathcal{D}|k, \lambda))}{\partial(k, \lambda)} = 0 \quad (1)$$

Once the model has been optimized it is possible to do predictions (or in a more general way inference) based on the trained model with some margin of uncertainty (or standard deviation). Obviously, this process is quite long and is not the objective of this paper although more information can be found in [1] and [3] for a deep analysis.

B. Gaussian process

Following with the example of the wind speed shown before, a Weibull distribution was chosen in that case because of the assumption that the wind speed distribution always responds to a distribution like that but, there will be cases where no assumption will be possible and then the amount of model options will be infinite. One model that can cope with this will be a non-parametric model that will be expressed as a joint probability distribution of infinite variables which every single one has a Gaussian distribution. The reason why the normal distribution is chosen is because it has some properties that will help the calculation of the predictions such as the cases of marginalizations and factorizations. Taking into account that a Gaussian distribution is defined by its mean vector and the covariance this can also be extended to a Gaussian process, where it will be fully specified by a mean function $m(x)$ and a covariance function ($\Lambda(x, x')$) or using math notation.

$$f(x) \sim \mathcal{GP}(m(x), \Lambda(x, x')) \text{ Indexes: } x \quad (2)$$

The training method (described before for parametric models), is renamed, if Gaussian processes is being used, as Gaussian Process prior model optimisation which produces as an outcome the parameters a, d and b of (??) that suit better to

the explanatory variable (the time in the previous example of the wind speed), the targeted values (the sampled wind speed following with the previous example) and also the maximum likelihood obtained with them. These parameters a, d and b are named as the hyperparameters of the Gaussian process and they have a crucial importance along the whole process. a is the average value of the Gaussian distribution, d is the length scale parameter of the process (it will explain how sensible is to changes of the explanatory variables) and b is the noise parameter. Once the hyperparameters have been obtained it is possible to calculate the prediction and standard deviation of the posterior joint probability for the Gaussian Process prior model.

II. 1ST PHASE: CLEANING THE DATA USING GAUSSIAN REGRESSION

The whole process to be carried out for the determination the wind turbine dynamics is explained as following. The data used for the identification is; The wind speed measured from the anemometer (U), the pitch angle (β) and the rotor speed (Ω). However, every measurement has been taken from transducers that inherently incorporate noise to the main signal contaminating the prediction of the dynamics prediction. Fortunately, the Gaussian processing can be used also to clean the data from this noise and this will be explained in the following section consisting the first phase of the process. Afterwards, once the data has been filtered, it is possible to find the torque characteristic in function of the tip speed ratio (λ) and the pitch angle.

A. Gaussian regression

Plotting the data it is possible to observe the noise that is coupled to the main signals for every single measurement although the source of these disturbance are different as it will be described later. However, thanks to the Gaussian process it is possible to make what is named as Gaussian regression which gives a similar result (but more discriminated) to a regular filtering.

Once the Gaussian process prior model has been trained and a set of hyperparameters have been obtained, the prediction function will need as input arguments: these cited hyperparameters, the explanatory variable (in this first phase it will be the time), and also the values of the input explanatory variable for which the prediction is required. If these two last parameters are the same, which will mean that the explanatory variable to be predicted will be the same than the one of the data to predict, the inference becomes regression. Taking into account that, when the maximum likelihood (eq. (1)) is computed in a unique single stochastic process, the length scales tends to be the slowest, (the one with the a longer length scale) which gives as net effect a result similar to filtering. This is the process followed in this first phase.

B. Cleaning data

Plotting the signal obtained from the rotor speed is possible to see (Figure 1) that there are three stochastic Gaussian

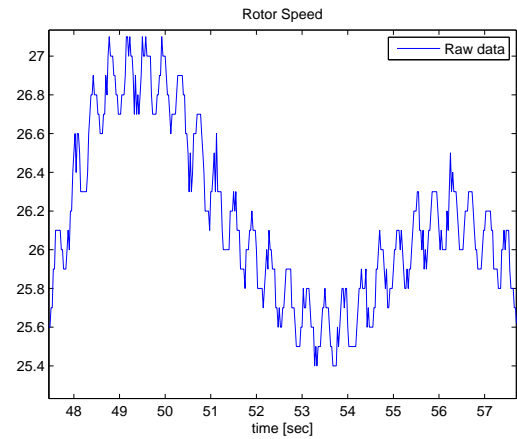


Fig. 1. Rotor speed signal data

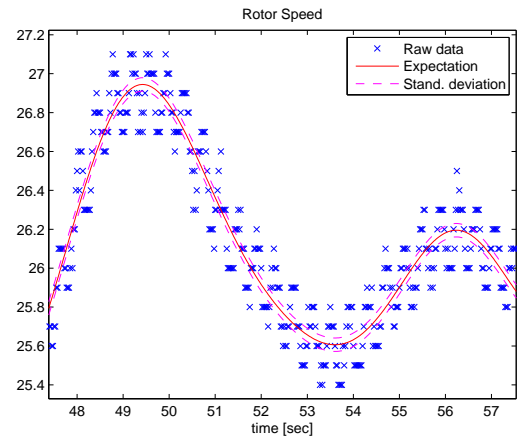


Fig. 2. Rotor speed signal data, expectation and standard deviation

processes with three different length scale for everyone. There is a slower stochastic process due to the changes of the wind speed, there is another faster due to the drive-train dynamics that interfere to the signal and there is another even faster that is due to the noise of the encoder used to measure this signal. Although everyone of them could be separately distinguished and identified to enhance the standard deviation (or uncertainty) of the predictions, the result with an unique length scale has been considered as satisfactory enough for the purpose of the paper since the slowest process can be clearly identified and selected (as it was described before). An excerpt of the rotor speed data with the expectation (signal already filtered) and the standard deviation (uncertainty over the prediction) can be found joint to the raw data in Figure 1. It is possible to see that the regression has been very successful and the undesired components have been removed.

Related to the wind speed, a plot of the raw signal can be found in Figure 3. In this case there are again three stochastic process but looking at the expectation obtained in Figure 4 the result is quite unsatisfactory since the fastest process has been removed but not the process due to the blades which has

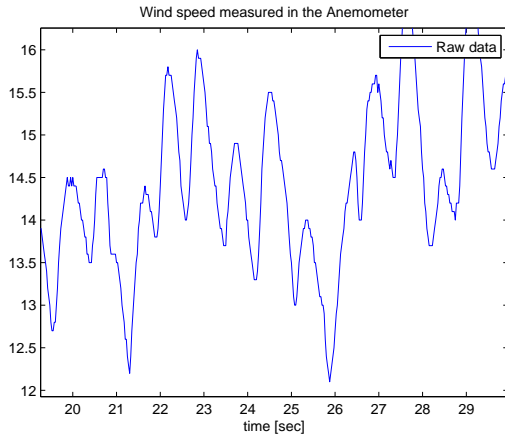


Fig. 3. Wind speed signal data

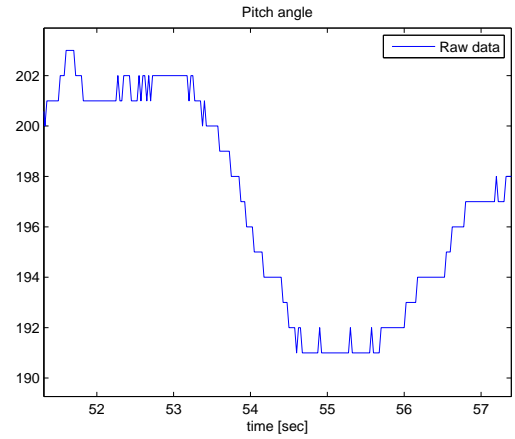


Fig. 5. Pitch angle data

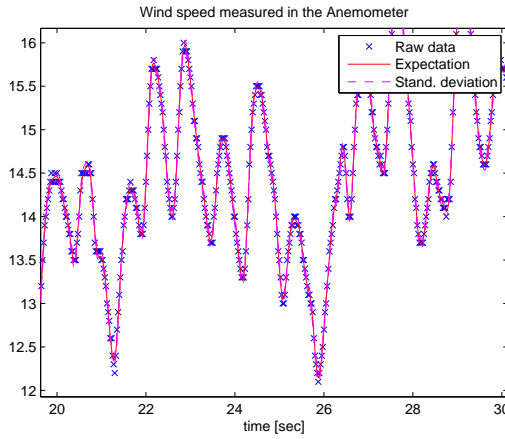


Fig. 4. Wind speed signal data, expectation and standard deviation

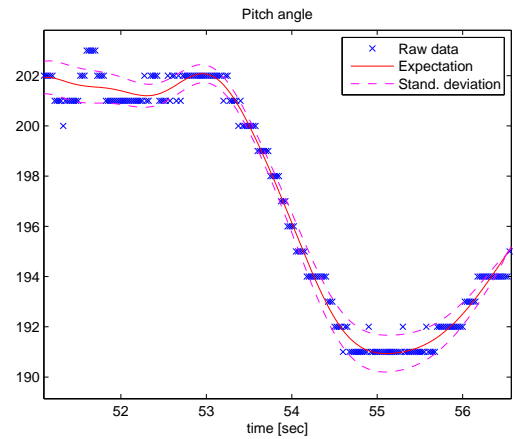


Fig. 6. Pitch angle data, expectation and standard deviation

been interpreted as the signal itself, staying in the expectation. However, this disturbance does not seem to affect much to the final result so, again, for simplicity reasons this has been considered enough for the purpose of the paper although a further investigation about how this disturbance affects to the final result can be done.

Finally, the last signal that has to be cleaned with Gaussian regression is the pitch angle. Again, a plot of the raw data can be found in Figure 5. The regression is effectively executed and plotted in Figure 6.

III. 2ND PHASE: OBTAINING THE TORQUE EXPRESSION

Once all the data is cleaned, an inference with the measurements can be done to obtain the torque. Although the instantaneously measured torque produced is not available, an scaled expression of it can be obtained using the rotor speed since, recalling the swing equation for generators, the difference of the electric torque and the mechanic torque will produce an acceleration in the rotor speed which will be proportional to the momentum of inertia of the generator (see (3)).

$$T_m - T_o = J\dot{\Omega} \quad (3)$$

Where T_m is the mechanical torque and T_o is the electrical torque. Assuming the last one is constant, the mechanical torque produced by the aerodynamic torque will be some unknown scalar (the momentum of inertia J) times the rotor acceleration. In other terms, a expression of the torque can be found using this equation although the numbers will not match with the real ones. Nonetheless, in order to control the system in the future it is more important to see how the system reacts rather than the exact numbers since these parameters could be added easily to the calculations later on. The extraction of the values for the rotor acceleration can and has been obtained through the use of Gaussian processing (more information in [4]).

However, the aerodynamic torque is a expression that relies on three variables, the effective wind speed (U), the pitch angle (β) and the rotor speed (Ω) ($T_m(\omega_R, \beta, U)$) but in order to facilitate its representation it can be presented as a function of the tip speed ratio (λ) and the pitch angle. This process

is explained as following. Knowing the algebraic expression of the torque produced by the wind in a wind turbine it can be combined with (3). Then, all the constants of the torque algebraic expression are substituted by a unique one and a expression of the coefficient torque can be found:

$$\frac{J\dot{\Omega}}{kv^2} = C_Q(\lambda, \beta) \quad (4)$$

Where $k = \frac{1}{2}\rho AR$ and ρ is the air density, A is the area covered by the rotor and R is the blade radius. Now, thanks to (4) the torque expression as a function of three variables has become a equation of only two facilitating the presentation of the data. Again, although the numbers will not match with the reality because there are scalars that have been ignored during the process, the shape and response of the aerodynamic torque characteristic can be obtained properly through the torque coefficient.

IV. 3RD PHASE: WIND TURBINE IDENTIFICATION

Having found the expression of the torque through the torque coefficient C_Q is possible to relate the values of C_Q with λ and β since the calculation of the tip speed ratio is well known.

$$\lambda = \frac{\Omega R}{U} \quad (5)$$

And R is another unknown constant that can be ignored for the purpose of this paper. The Gaussian process toolbox can be used to plot properly, but instead of doing Gaussian regression, Bayesian inference will be used with Gaussian processing to get as result a cleaner surface which can be more easily identifiable. It is important to remark that, before the Gaussian prior model is being built and the maximum likelihood process is going to begin, it is very recommendable to initialize the hyperparameters to some sensible values otherwise it will give as result a wrong inference that will produce, or wrong results, or excessive margins of confidence if random numbers are used as starting point [1].

Finally, the aerodynamic torque characteristic surface is plotted in Figure 7 in function of torque (although the torque coefficient has been used as index to relate it), the pitch angle and the tip speed ratio. 30 values for pitch angle and 30 values for the tip speed ratio have been used giving a combination of 900 points to be inferred.

The solid surface plotted in Figure 7 is the expected torque value for every single point and the two meshed grid are the uncertainty. It can be observed that in the regions where there is enough data, the standard deviation is narrowed giving more confidence to the inference. However, in the extreme sides of the surface, where there is an absence of data the expectation, the inference is not so confident and the values for the standard deviations are higher. According to the graph surface, the higher the tip speed ratio is, the lower torque will be obtained. This is possible, if the tip speed is higher than the optimal one. Taking into account that the set of data sampled has been taken close to the above rated operation of the wind turbine

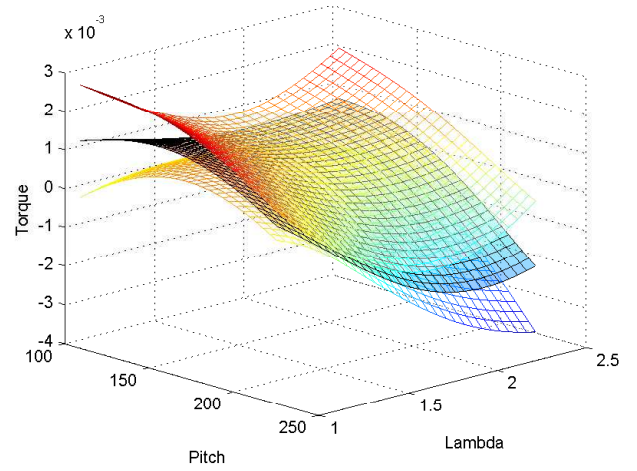


Fig. 7. Aerodynamic torque characteristic inferred

that use to operate in this region, the inference matches with the graph. If the application makes necessary to complete the surface along all the operative margins a set of sampled data containing these regions should have to be used and (added to the actual ones) to the training process. Regarding to the pitch angle, the inference seems to match with the reality since, when the pitching angle increase, the torque extracted from the wind is reduced for a fixed value of lambda.

V. CONCLUSIONS

Along this paper, it has been shown that it is possible to identify the aerodynamic torque using only sampled data, even if they are heavily contaminated by noise or they have not been taken appropriately, using Gaussian processes and Bayesian inference. These techniques have been proven as a very powerful technique not only for inference but also for filtering purposes using Gaussian regression. However, it is important to remark that they require a huge load of computation to be processed; higher with respect to the number of samples taken (a rough approximation is N^3 operations where N is the number of samples [1]).

REFERENCES

- [1] Non-linear dynamics identification using Gaussian process prior models within a Bayesian context. PhD thesis (2008). Keith Neo Kian Seng, Hamilton Institute, National University of Ireland. <http://www.hamilton.ie/keith/research.htm>
- [2] Wind Energy Handbook. Tony Burton, David Sharpe, Nick Jenkins, Ervin Bossanyi. Ed. Wiley
- [3] Gaussian Processes for Machine Learning. Carl Edward Rasmussen and Christopher K. I. Williams The MIT Press, 2006.
- [4] Identification of Nonlinear Systems by Combining Equilibrium and Off-Equilibrium Information. W.E. Leithead. Dept. of Electronics and Electrical Engineering, University of Strathclyde
- [5] Identification of aerodynamic and drive-train dynamics for a variable speed wind turbine. W.E. Leithead, F. Hardan, D.J. Leith. Hamilton Institute, National University of Ireland.

Controlling Large Wind Turbines – The Effect of Wind Turbine Size on Controller Design

C. Siddons, W. Leithead,

A. Stock, P. Jamieson

Department of Electronic and Electrical Engineering
University of Strathclyde, Glasgow, UK

D.Robb

Sgurr Control
Glasgow, UK

Abstract—Control system designers face increasing difficult challenges nowadays as the size of wind turbine continues to increase. The decreasing frequency of the fore-aft structural mode of the tower and its associated right half plane zero being a key reason which makes controller design so difficult. The need for an integrated design strategy incorporating both controller and turbine design is emphasized to help mitigate many of the problems encountered in controller design. The need for more advanced control techniques in order to achieve better performance characteristics is emphasized.

I. INTRODUCTION

Since wind energy came into prominence as a viable energy source, the size of wind turbines has steadily been increasing, best seen in figure 1. This change is most often observed in offshore environments, where the factors affecting the cost of energy differs to onshore turbines. EU legislation states that we must achieve a 20% reduction in carbon emissions by 2020 [1]; developing wind technology can play a major role in achieving this objective.

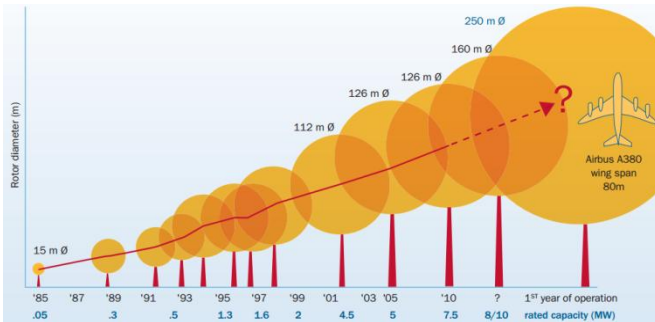


Figure 1: Timeline of size increases of wind turbines [2]

This increase in size has obvious advantages of greater power capture per turbine, but it also introduces additional challenges for the designers of the control systems. Modern controllers are required to maximise the power capture of the wind turbine, whilst simultaneously reducing the loads on the machine. Numerous techniques have been developed to achieve this beyond conventional control including: Co-ordinate control, phase advance design, individual blade/ pitch control (IPC/IBC), and advanced tower loops.

Co-ordinated control seeks to reduce tower loads, pitch activity, and also the impact of right-half plane zeros on the above rated controller design by making use of the generator excitation [3].

Phase advance aims to minimize the impact of sudden increases in wind speed around the switching point between above and below rated operation. Implementation means that

the blade pitching begins earlier preventing the turbine going into over-speed [4].

Individual blade/ pitch control seeks to reduce the unbalanced rotor loads by taking measurement of the root bending moment of each blade. IPC and IBC differ predominantly on how the pitch demand is sent. In IPC each pitch actuator takes a signal from the central controller which it directly acts on, IBC differs in that each actuator has its own controller in feedback with the blade moment. Each actuator/controller pair receives the same signal from the central controller [5].

Conventional control includes drive train filters, tower filters, a below rated controller and an above rated controller with gain scheduling. All turbines in this project have been developed using these techniques with the aid of an advanced Matlab toolbox developed by Sgurr Control and the associated guide (labs) document [6]. Models of the turbines for the control toolbox were calculated using the physical parameters from bladed models, the software could then be used to develop 3, 5 and 7MW controllers.

II. CONTROLLER DESIGN

The following conventional techniques were used to design controllers for each turbine.

A. Gain scheduling

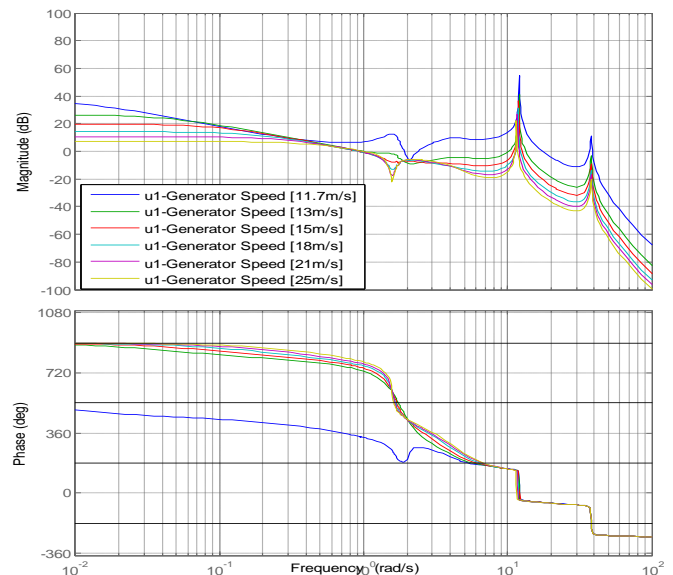


Figure 2: Gain scheduling on a 5MW controller showing the response between reference generator speed and actual generator speed.

The relationship between the aerodynamic torque, wind speed and blade pitch is highly non-linear, to compensate for this the technique of gain scheduling can be applied to linearize the system. Figure 2 below shows the effects of gain scheduling on the 5MW controller, it can be seen that there is a bunching around 0.6 rad/s of the magnitude response.

B. Drive train filter

A band-pass filter of the form shown in equation 1 was implemented at the frequency of the drive train, this had the effect of ‘raising’ the frequency range of the drive train so that a simple additional gain could be used to cancel out the drive train peak, minimizing the effect in other parts of the frequency response.

$$G_{dtr} = \frac{ks}{\left(s + \frac{\omega_0}{n}\right)(\omega_0 n)} \quad (1)$$

The ‘n’ in the equation above controls the width of the filter, of which a small allowance was made, as in reality the actual frequency of the drive train may differ to that of the modeled drive train. There also exists a slight variation in the drive train frequency over a range of wind speeds.

The drive train filter enabled a crossover frequency of 1 rad/s on all below rated controller designs, emphasizing its importance in wind turbine controller design.

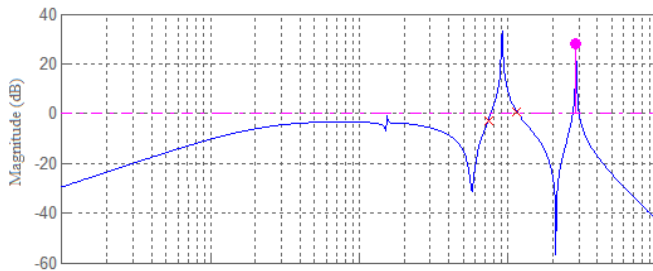


Figure 3: 7MW drive train filter design on an open loop, bode magnitude plot. The signal used is from torque demand to generator speed. Pole locations are shown as red crosses.

C. Tower filter

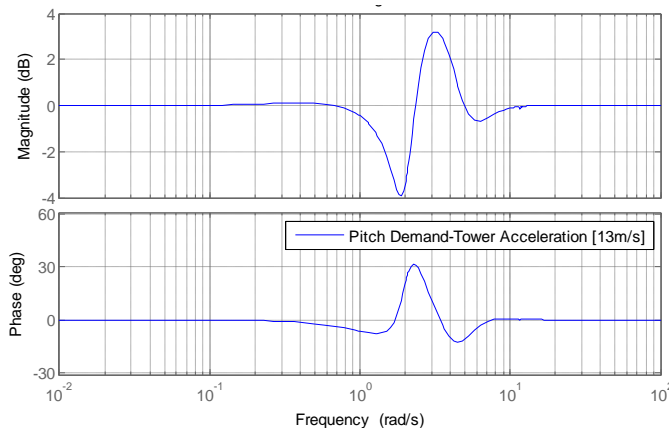


Figure 4: Sensitivity plot showing the attenuation and enhancement effects of a tower filter

The tower filters were designed with a very similar form to the drive train filter, except with an integrator included, as we are attempting to damp the tower velocity and not the direct measurement from the accelerometer.

Each of the tower filters designed were very sensitive to enhancing a right-half plane zero close to the tower frequency, therefore the gain had to be carefully adjusted so that it would not hinder the optimal design of the above rated controller.

D. Above rated controller

The above rated controller was designed first before the below rated, this had benefit of improved switching strategy dynamics (see section F). The above rated controller also makes use of gain scheduling techniques, as previously explained, to compensate for the non-linear relationships between pitch, rotational speed and aerodynamic torque. Typically the above rated controller would be of the form shown in equation 2, which is the transfer function used for the 7MW turbine.

$$C_{AR} = \frac{-7(s + 0.035)}{s(s + 2.4)} \quad (2)$$

The drive train and tower filters had to be adequately designed such that their respective functions would not interfere when attempting to maximise the performance of the controller. The overall aim of the design was to achieve a high frequency roll off and low frequency disturbance rejection- ideally a crossover frequency of 1 rad/s would be achievable. Offset free setpoint tracking is also an important requirement and is achieved through applying an integral in the transfer function.

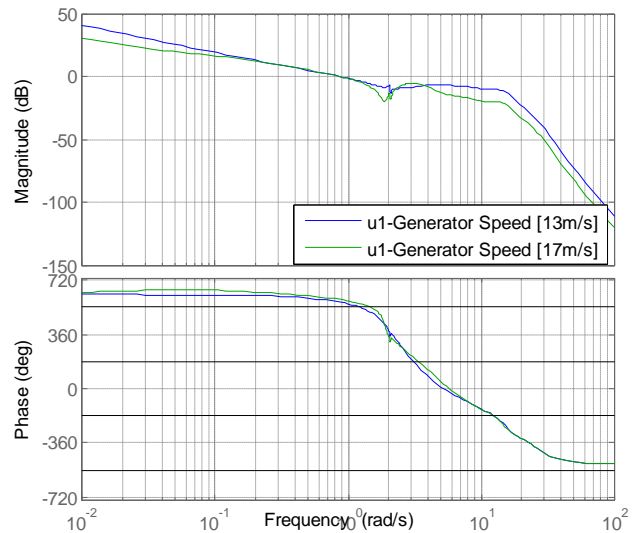


Figure 5: Open loop bode plot from reference generator speed to generator speed for the above rated 3MW controller.

A design wind speed of around 1m/s more than the rated wind speed was chosen in all controllers. This ensured that the controller was versatile enough to perform across the range of wind speeds, and also address some of the more challenging aspects of designing a controller close to rated wind speed. A

tradeoff between gain margins, phase margins and crossover frequency was always an issue in the design as later explained in section IV.

E. Below rated controller

The above rated poles and zeros are copied to the below rated controller for the benefit of switching dynamics. The drive train filter will heavily damp the first drive train mode, enabling a crossover frequency of 1rad/s in all cases. The controller will also include integral action like the above rated controller. The below rated controller as well as the above rated controller include negative gains to compensate for the physical characteristics of the turbine, the following example explains why this is: If ω_g exceeds ω_{set} then the controller will need to increase the generator excitation to decrease the rotor speed. The error signal in this case is negative, but a greater excitation is required. A negative gain therefore yields the desired response.

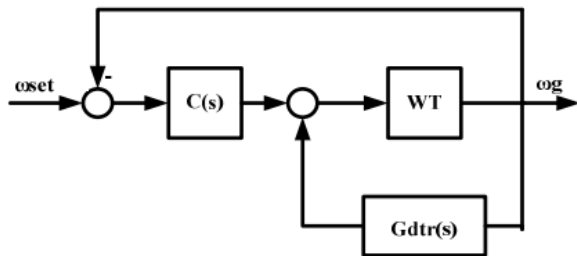


Figure 6: Below rated feedback loop with drive train filter

F. Switching Strategy

The Simulink model tested the switching properties of each controller; switching is achieved via a series of switches, gains and comparators. The switching simply determines which part of the controller is active at a particular time, the overall aim is also to minimize the transients when going from one mode to another. Such control strategies can be seen in figures 7 and 8 in the results section.

III. RESULTS

The fundamental properties of each controller’s design can be found in table 1. It can be seen that the general trend is that as the turbine increases in size, a crossover frequency close to 1 rad/s is much more difficult to achieve. None of the turbines achieved the ideal margins of 6dB of phase margin and 60 degrees of phase. Although this is far from ideal, it provides a good basis for comparison between the crossover frequencies of each controller, as seen below:

Table 1: Performance characteristics of the above rated controller of the scaled turbines

	Crossover Frequency (rad/s)	Gain Margin (dB)	Phase Margin (degrees)
3MW	0.85	3.6	33
5MW	0.6	3.4	38
7MW	0.35	3	32

The gain margins and phase margins are similar across the range of controllers, large variations however can be seen in the gain crossover frequency of each controller.

Each controller developed was tested in a Simulink model. This had the benefit of being able to monitor the generator speed, torque and pitch activity in response to a set wind field. Each wind field was produced was to a pre-defined average wind speed and turbulence intensity, applied to each wind turbine. This would test the effectiveness of the controller in response to a range of conditions[6].

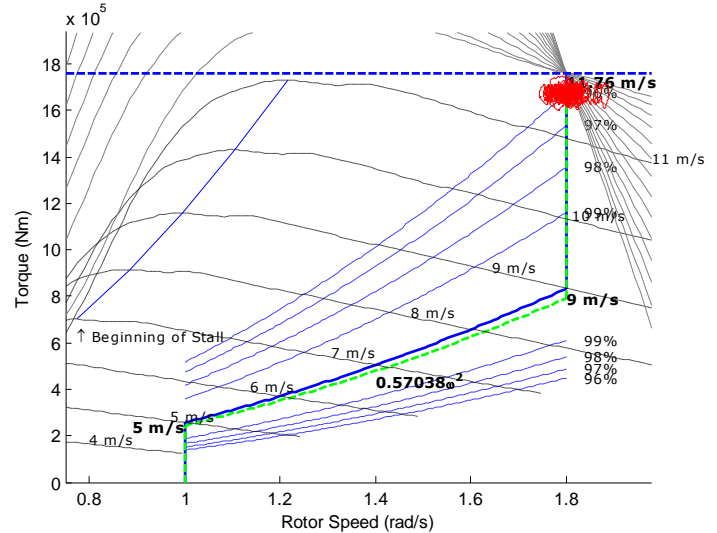


Figure 7: Operational strategy for the 3MW turbine showing a simulated average wind speed of 18m/s with 15% turbulence.

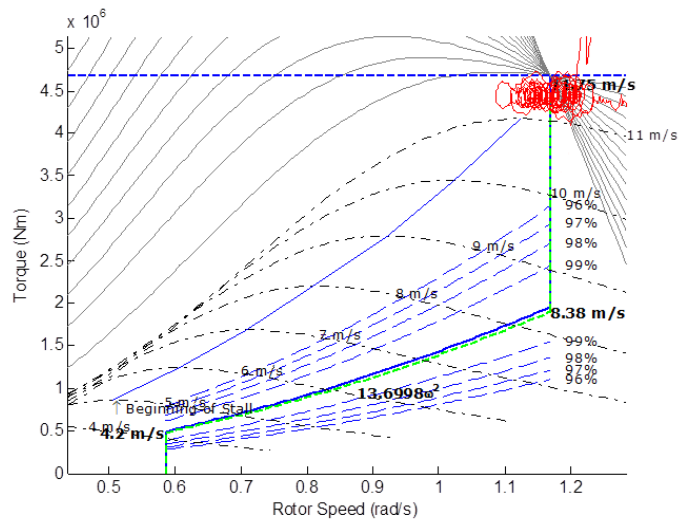


Figure 8: Operational strategy for the 5MW turbine showing a simulated average wind speed of 18m/s with 15% turbulence.

Figures 7 and 8 below demonstrate the disturbance rejection capability of the 3MW and 5MW turbines. It can be seen that the controller for the 3MW turbine can track the setpoint much more effectively than the 5MW controller- a direct consequence of the lower crossover frequency and thus poorer disturbance rejection in the 5MW controller.

IV. DISCUSSION

It was found that as the turbines got larger the performance criteria became much harder to achieve. Relevant open loop bode plots seen in figures 5 provides an example. Although it may be apparent from figure 5 that a better crossover frequency could have been obtained, this would come at the cost of the gain and phase margins. The presence of a non-minimum phase zero close to the tower frequency was difficult to design around, especially in the case of designing an effective tower filter.

The first drive train mode was found to be much more prominent in the larger turbines, however, this was effectively dealt with by the drive train filter.

At rated power, disturbance rejection was a major issue for the larger wind turbines, figures 7 and 8 shows this effect in a similar wind field. Testing was also conducted in a turbulence intensity of 30% for an average wind speed of 18 m/s. The larger wind turbines in this case were not able to stabilize.

It can be seen in figure 8 that the pitching is operating very close to the stall region, figure 9 shows a time series of the simulation. A significant drop in the wind speed can be seen at around 250 seconds, at this point a reduction in the rotor speed can also be seen and the blades would pitch back towards -1° . The reduced rotor speed would induce the blades into stall (i.e. to the left of the stall region)- a pitch regulated machine is not designed to do this and thus will become unstable.

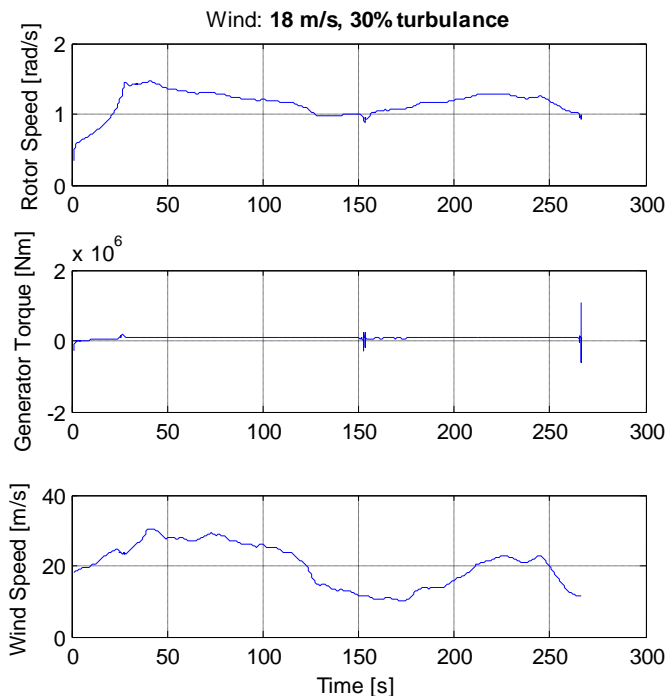


Figure 9: 5MW testing of the generator response

A key issue regarding this is the method by which the turbines were scaled- at no point along the scaling process was the controller design taken into account. DNV GL currently recommends that controller design takes place alongside the

wind turbines design; this they claim yields better turbine performance. These were the findings DNV GL's project FORCE[6].

The gearbox design of the larger machines appeared to be a very specific issue with the designed turbine. Scaling laws depict that as the low speed shaft input torque increases, it is more cost effective to scale the generator than the gearbox[9]. This does however have knock on for the operational strategy.

V. CONCLUSIONS AND RECOMMENDATIONS

Controller design becomes increasingly more difficult as the wind turbine becomes larger- the ability of the designer to achieve the desired performance characteristics is greatly hindered by the dynamics of the given plant.

Advanced control techniques such as IBC/IPC, phase advance and coordinated control would help the designer achieve greater margins and reduce many crucial areas where loading plays a role- an area which this project has not focused on and could be developed into future work.

The turbines used in this project were scaled versions of a 3MW turbine previously developed, the scaling process for these turbines did not take account of the controller design in the development phase. A holistic approach to the design of wind turbines, especially in the case of the 7MW turbine, may have helped to obtain better controller performance. Further research involving the design of a controller and turbine simultaneously can help devise a specific set of best practices for large wind turbine design.

REFERENCES

- [1] EU, "EU greenhouse emissions and targets," 9th July 2014. [Online]. Available: http://ec.europa.eu/clima/policies/g-gas/index_en.htm. [Accessed 22nd July 2014].
- [2] Upwind, "Design limits and solutions for very large wind turbines," European Wind Energy Association, 2011.
- [3] W. E. Leithead and S. Dominguez, "Coordinated Control Design for Wind Turbine Control Systems," in *EWEC 2006*, Athens, 2006.
- [4] A. -. P. Chatzopoulos, "Full Envelope Wind Turbine Controller Design for Power Regulation and Tower Load Reduction," PhD Thesis, University of Strathclyde, Glasgow, 2011.
- [5] Y. Han and W. E. Leithead, "Alleviation of Extreme Blade Loads by Individual Blade Control during Normal Wind Turbine Operation," in *EWEA Annual Event*, Copenhagen, 2012.
- [6] *SgurrControl Laboratories*, Glasgow: SgurrControl, 2014.
- [7] V. W. Neilson, "Individual Blade Control for Fatigue Load Reduction of Large-scaled Wind Turbines: Theory and Modelling," PhD Thesis, University of Strathclyde, Glasgow, 2010.
- [8] DNV GL, "Integrated approach to wind turbine structure will reduce cost of offshore wind by at least 10%," 11th June 2014. [Online]. Available: <http://dnvgl.com/news-events/news/project-force.aspx>. [Accessed 22nd July 2014].
- [9] P. Jamieson, *Innovation in wind turbine design*, Chichester: Wiley, 2011.

Clarifying the performance of coordinated control for large wind turbine loads

Daniel Danzerl, W.E Leithead, Hong Yu
Wind Energy CDT, University of Strathclyde, 50 George Street, Glasgow, UK
daniel.danzerl@strath.ac.uk

Abstract — one of the control objectives for large scale wind turbines is to reduce tower lifetime equivalent fatigue loads. The basic approach is to additively modify the pitch demand in response to a measurement of tower speed. An alternative and more effective approach is to employ coordinated control, whereby, both pitch demand and torque demand are modified in response to power and rotor speed. Some uncertainty has recently arisen regarding the most effective tuning for coordinated control when applied to 5MW+ wind turbines. Although coordinated control still performs very well the extent of the improvement over the basic approach needs to be clarified. The objective is to review coordinated control of tower loads on a large scale wind turbine and clarify its attainable performance.

Keywords: Tower fatigue load reduction, coordinated control, feedback, power coordinated control

I. INTRODUCTION

Wind turbines are often exposed to strong varying loads as a result of their exposure to high stochastic nature of the wind. Their effect on tower loads are a major concern. Variable speed wind turbine controller regime consists of below and above rated modes. At below rated mode, the controller's task is to regulate generator speed between its minimum and maximum values to maximise power output by using generator reaction torque. In the above rated mode, the objective is to modify the blade pitch angle to regulate generator speed whilst maintaining rated power output [7].

This paper focuses on the above rated mode where the control tasks are multivariable and regarded as the region at which the tower fore-aft motion has major contribution to the tower fatigue loads. The advent of structurally flexible multi-megawatt wind turbines in recent years has also brought about further control design issues and limitations. It relates to the influence of the tower dynamics on the performance of the control system. This involves the interactions of the tower fore-aft movements with the drive-train introducing a pair of right half-plane zeros (RHPZ) in the dynamics that link blade pitch angle to generator speed. The RHPZ becomes restrictive and hence tends to limit the control system's ability to regulate the generator speed through blade pitch control [10]. In this paper two schemes

of coordinated controller designs are reviewed as an approach to increase tower fore-aft load reduction whilst simultaneously reducing the pitch activity and circumventing the limiting right-half plane zeros.

II. CONTROLLER DESCRIPTION

The controller design adopted for this paper is a full envelope controller developed by [1] which has been fully validated. Its performance has been investigated using simulation in Garrad Hassan Bladed on a 5MW Supergen wind turbine model to assess coordinated control performance for tower load reductions. The make-up of the controller consists of global gain scheduling which addresses aerodynamic nonlinearities. The controller caters for the nonlinearities existing between the aerodynamic torque, the rotor speed as well as the pitch angle of the blades [4]. The idea is to change the controller parameters according to a set of local operating points. The controller consists of a drive train filter which is primarily designed to damp drive-train oscillations.

In the case of variable speed pitch regulated turbines; these turbines are prone to serious risks of damage as a result of vibrations of the drive train components. Such risks can be alleviated by implementing a band pass filter at the drive train frequency to regulate the torque based on the generator speed error. This causes drive train mode damping to be significantly increased and oscillations caused to the generator speed signal to be dramatically reduced [1]. The controller design also consists of a tower feedback loop (TFL) which aims at reducing the first tower frequency mode [1] and thereby increasing the aerodynamic damping of the tower [7]. An anti-wind up loop has been incorporated into the design which is in place to prevent the pitch rate from exceeding maximum limits. Pitch phase advance implemented in the design is to compensate for the response of the pitch actuator to sudden changes in wind speed which in some extreme cases may cause rotor over speeding.

III. TURBINE DYNAMICS

Standard design and convention to tower load alleviation has involved coupling of the generator speed and tower speed. This control approach has caused reduced effectiveness of not only the tower speed loop itself but also the generator speed loop. Dynamic interactions linking the

tower speed and the blade pitch demand of the wind turbine model is depicted in a Bode plot in **Figure 1**. From the figure, the first peak, at 2rad/s , corresponds to the tower mode, and the second peak, at 6rad/s , corresponds to the blade flap-wise mode [7]. It can be observed that there is 180° phase loss between the two modes. The blade flap mode magnitude is dependent on some parameters that are wind speed dependent, however the phase loss between the modes does not alter as the parameter values change. At the first tower mode frequency, there is presence of RHPZ as a result from interaction between the tower and drive train modes. They cause reductions in phase and stability margins of the system

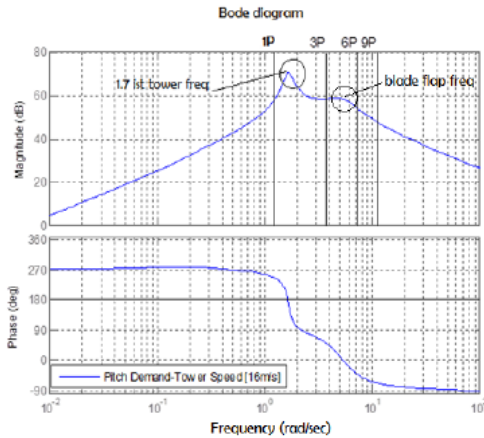


Figure 1 Blade Pitch Demand to Tower Speed [7][5]

Recently, new configurations for controller design system has emerged which involves an improved representation of the wind turbine dynamics and accommodation of the interaction of the two loops. This is the concept of coordinated control design systems. In the case of variable speed pitch regulated wind turbine this new controller regime has proven reliable and out-performs standard controllers.

IV. COORDINATED CONTROLLER DESIGN

Coordinated control design (CCD) is an innovative approach for the above rated regime which addresses challenges and issues concerning multi-megawatt wind turbines. The design overcomes limitations posed from the tower induced RHPZ to achieve a more effective generator speed control and further reductions in fatigue loads [7]

The design is based on a parallel path modification of the plant [3]. It uses both blade pitch and generator torque demand. Even though the basic design is quite similar to the conventional controller, the parallel path modification enables the RHPZ due to the tower to be counteracted and removed by coordinating the action between the torque and pitch controllers. Both controllers are active simultaneously and therefore coordinating the main controller task between them is possible. Additionally, the parallel path

modification is utilised to decouple the generator speed loop from the tower feedback loop in order to achieve more effective TFL control. In the CCD, a *PI* controller is combined with the parallel path modification to achieve the same bandwidth as the conventional controller. As would be expected in the absence of the RHPZ, the stability margins are improved. [7]. It also aims to reduce the pitch activity near the tower mode by using a notch filter, *Y*, centered at the tower frequency in the vicinity of the first tower mode and using a parallel path that splits the control of the generator speed between the pitch and torque demand. A coordinating transfer function, *X*, is used with the inverse of *Y* on the torque demand path to maintain the overall system dynamics which is shown in **Figure 2** shows the block diagram of this scheme [1].

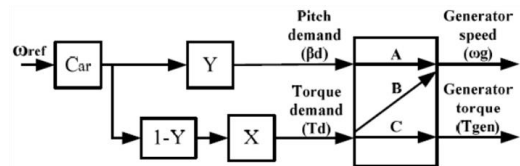


Figure 2 Block Diagram of Coordinated Controller Design [1]

The CCD transfer function is deduced based on Equation 1 [1]

$$C_{ar} * Y * A + C_{ar} * (1 - Y) * X * B \equiv C_{ar} * A \quad \text{Equation 1}$$

$$X = \frac{G_{pac} * A}{B}$$

The transfer function for coordinated control is given by [5]

$$X = \frac{3.536e14}{s^4 + 1015s^3 + 350250s^2 + 4.366e7s + 8.881e8} \quad \text{Equation 2}$$

$$Y = \frac{s^2 + 0.3s + 2.89}{s^2 + 0.6s + 2.89}$$

V. POWER COORDINATED CONTROLLER DESIGN

In the above rated operational mode, generator torque regulation is characterised by induced fluctuations to the output power and the torque hence requiring an improvement of the CCD to obtain a smooth power quality output. To address this, a power coordinated control design (PCC) is implemented which is an extension to the CCD design. In this design regime, instead of generator speed control, the controller will be regulating the output power and to maintain it. The block diagram is shown in Figure 3. [5]

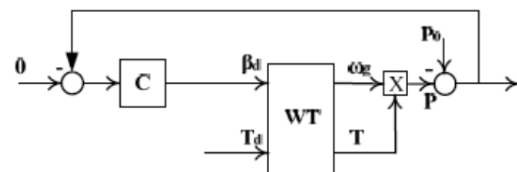


Figure 3 Power loop of system [1]

From the block diagram in **Figure 3**, it can be observed that there are very weak interactions between pitch demand angle and generator torque which means that perturbations in output power, arises almost entirely from perturbations of the generator speed. Hence by controlling the output power, the generator speed will also be controlled. It can be expressed in the following form [2];

$$\omega_1 T_{set} + (\omega_g - \omega_1)T + (T - T_{set})\omega_1 = P_0 + (\omega_g - \omega_1)T + (T - T_{set})\omega_1$$

Equation 3

ω_1 is defined as the rated speed, T_{set} is the rated torque and P_0 the rated power. The block diagram then becomes;

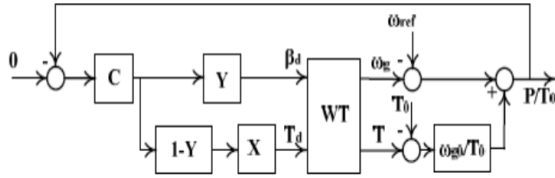


Figure 4 Reformed System [1]

Equation 4 shows the relation between the dynamics of the system for PCC design [5]

$$C_{ar} * Y * A + C_{ar} * (1 - Y) * X * \left(B + \frac{\omega_{set}}{T_{set}} \right) \equiv C_{ar} * A$$

$$X = \frac{G_{pac} * A}{B + \left(\frac{\omega_{set}}{T_{set}} \right)}$$

Equation 4

The transfer functions for the Power Coordinated Controller is given by [2]

$$Y = \frac{s^2 + 0.3s + 2.89}{s^2 + 0.6 + 2.89}$$

$$X = \frac{-2.042e14}{s^5 + 1200s^4 + 535180s^3 + 1.051 \cdot 10^8 s^2 + 7.672e9 + 1.148e9}$$

Equation 5

VI. RESULTS AND DISCUSSION - 5MW MODEL

The controllers have been compiled by [1] [5] in C++ appropriately for use in GH Bladed. Essentially all methods involved a feedback of the tower speed, which was based on measurements of the tower acceleration, which thereby increases the aerodynamic damping of the tower. The CCD and PCC have been implemented into the external controller in Bladed and simulations runs were made to produce various outputs to study dynamic behaviours of the wind turbine model under the various controller design strategies. These are shown seen in **Figures 5-9** below;

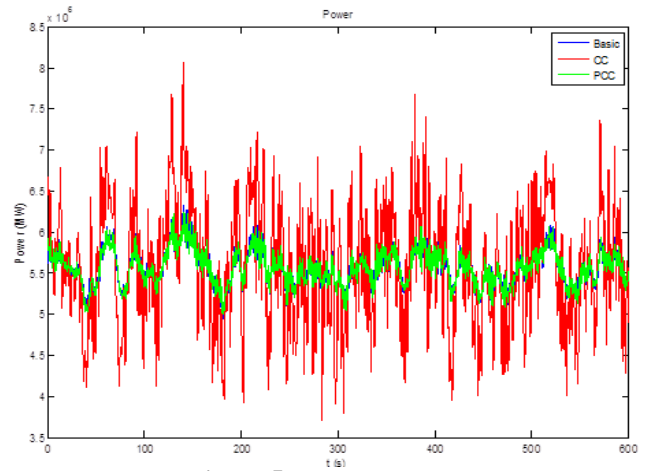


Figure 5 Generator Power

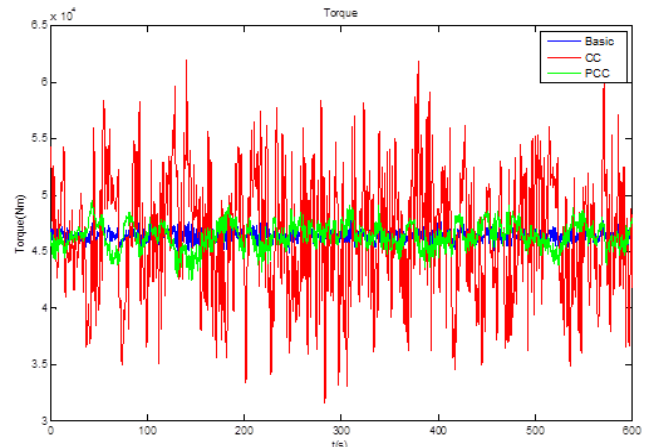


Figure 6 Generator Torque

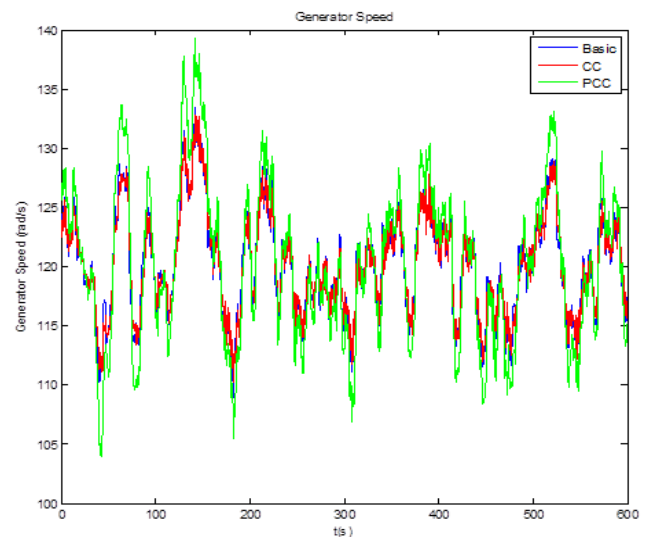


Figure 7 Generator Speed

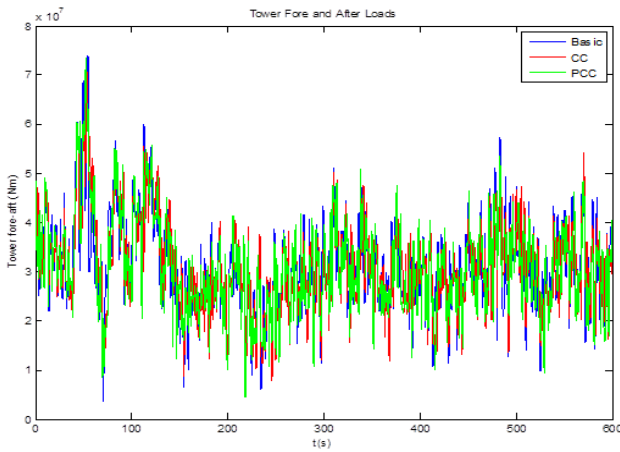


Figure 8 Tower Fore-Aft Loads

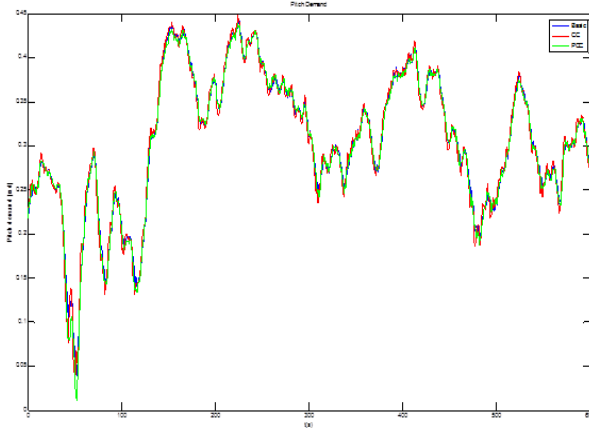


Figure 9 Pitch Demand

Damage equivalent loads (DEL) experienced by the tower in the above rated region have been investigated under the various controller strategies. This involved determining the number of cycles at different stress ranges using the rainflow counting method and applying these to the Wohler S-N curves for the particular material user Miner's rule [6]. **Figure 10 and 11** depicts tower load behaviours under the various controller strategies at 20% wind turbulence in the above rated region.

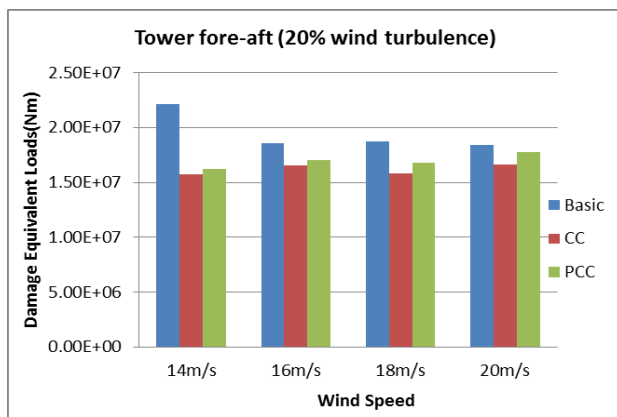


Figure 10 Tower fore-aft loads (20% turbulence intensity)

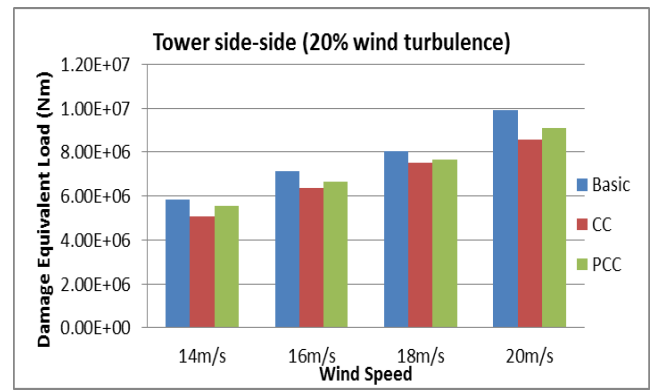


Figure 11 Tower side-side loads (20% turbulence intensity)

Figure 10 illustrates tower fore-aft DEL reductions under the various control strategies at the above rated region. It is observed that, coordinated control design demonstrated significant reductions in tower loads at lower wind speeds than at higher wind speed. Percentage reductions in DEL ranged from 32.4% at 14m/s to 9.61% at 20m/s. Power coordinated control reductions in DEL for tower fore-aft ranged from 28% to 3.32% at the same nominated wind speeds and turbulence intensities. The fore-aft mode and the side-to-side mode differ considerably as a result of the fore-aft mode being strongly damped, due to the aerodynamic damping of the wind turbine rotor. The side-to-side mode is a lightly damped, since there is almost no aerodynamic damping in normal conditions.

REFERENCES

- [1] Aristeidis – Panagiotis Chatzopoulos, Full Envelope Wind Turbine Controller Design for Power Regulation and Tower Load Reduction
- [2] D. I Hamilton, W.E Leithead, Applying Coordinated Control to Wind Turbines in Bladed, 2012
- [3] I. Horowitz, Synthesis of Feedback Systems. Academic Press, 1963.
- [4] I. Munteanu, A. I. Bratcu, N. A. Cutululis, E. Ceang, "Optimal Control of Wind Energy Systems", Springer, 2008
- [5] Saman Poushpas, W E Leithead, Application of Coordinated Control and Power Coordinated Control to a 5MW Supergen Wind Turbine
- [6] V. Veldkamp, "Chances in wind energy: a probabilistic approach to wind turbine fatigue design." Delft University, 2006.
- [7] W.E Leithead, Coordinated Control Design for Wind Turbine Control Systems
- [8] W.E Leithead, Controller Design for the Cancellation of Tower Fore-aft Mode in a Wind Turbine, 2005
- [9] W.E Leithead, Implementation of Wind Turbine Controllers
- [10] W.E Leithead, S Dominguez Analysis of Tower Blade interaction in the cancellation of the tower fore-aft mode via control

“

Wind, Turbulence

”

Simulation of wind turbines in complex terrain by means of direct CFD

C. Schulz¹, Th. Lutz¹, E. Krämer¹

¹University of Stuttgart, Institute of Aerodynamics and Gas Dynamics (IAG)
schulz@iag.uni-stuttgart.de

ABSTRACT

In order to improve predictions of wind turbine loads and power generation in complex terrain situations sophisticated numerical methods are needed as standard approaches reach their limits. In this article a numerical process chain for these kind of simulations is shown as well as several results of a complex terrain wind turbine simulation with a fully meshed turbine using a hybrid URANS/LES approach.

1 Introduction

In the expanding wind energy market onshore wind sites play an important role as many costumers do not want to take the high risks and costs of offshore wind parks. Nowadays non-occupied flat terrain sites are often rare and therefore the importance of wind energy in complex terrain steps more into focus. Another promising aspect is that topography often induces a speed-up resulting in a higher power output. Furthermore, the complex terrain influences the overall inflow conditions of the turbine significantly and interacts with the atmospheric boundary layer resulting in a change of loads, life time, power output and financial benefit compared to a flat terrain site. One of the key factors in these cases is the atmospheric turbulence, which needs to be better understood in order to improve predictions on wind turbine behavior [1]. Different numerical approaches have been made to do so. These vary regarding their basic idea as well as in their numerical complexity of wind turbine consideration. [5] describes briefly a couple of approaches like meso-micro-scale coupling or statistical down scaling. Looking at the turbine effects various modelling approaches are possible. They range from BEM (Blade Element Momentum) over actuator line and disk models to direct simulations of the turbine itself [3,5]. The latter require a fully resolved boundary layer and discretized blades. Hence, this type of simulation is the most complex and expensive but offers the ability to consider 3D dynamic stall effects and the interaction of turbine and atmospheric boundary layer without additional modeling like for other methods needed. This approach will be used in the described process chain.

2 Numerical Approach and Computational Details

A process chain to analyze the aerodynamics of wind turbines by means of CFD has been developed at the IAG [3]. It can be divided into two main parts. The first one is the commercial grid generation software Gridgen by Pointwise, Inc. supporting scripting capabilities and the automation of meshing. The second is the block structured flow solver FLOWer provided by the German Aerospace Center. Within FLOWer, different implementations have been made to account for atmospheric or generic inflow conditions with different spatial and temporal resolutions [3] and have been successfully tested for different operational cases [3,5,6,7]. This process chain has been extended for the current research to account for complex terrain. All grids used for the studies are represented as a full model being meshed with a fully resolved boundary layer. The different grids for the blades, nacelle, hub, tower and background are overlapped using the chimera technique implemented. For further details about the basic idea of this approach, the publications of [3,5,6] can be considered. The background grid has been divided into three parts. An even inflow region, a region of interest including the terrain data as well as the wind turbine and an extended downstream region to cover the subsiding of the main disturbances. Overall, a grid with a size of 1100 m x 400 m x 475 m has been used for the simulations. A position of special interest is the connection between the tower and the terrain data. The existing process chain had

to be modified to overcome the challenges occurring at that point. As described in [4,5] different problems can emerge if non adapted meshes are tried to connect using the chimera technique. Therefore, different adaptations have been analyzed and two showed reasonable almost identical results. In a first approach the tower foot has been adapted to create a surface equal to the terrain data. In a second one, the terrain data have been adapted to create an even plateau for the tower foot. For the presented data, the second approach has been used. The boundary conditions for the background grid has been chosen as displayed in “Fig. 1”. The studies have been performed using a Detached-Eddy-Simulation with a Spalart Allmaras turbulence model (DES97). For each time step 35 inner iterations have been performed using an implicit dual-time stepping method as temporal discretization. The convective fluxes have been reconstructed using a second order central differences Jameson-Schmidt-Turkel method. In order to obtain converged data the inflow field has been propagated through the whole domain ten times before the data evaluation has been performed. All simulations have been performed at *High Performance Computing Center Stuttgart (HLRS)* with AMD Interlagos processors. The test cases required about 100,000 CPUh in total.

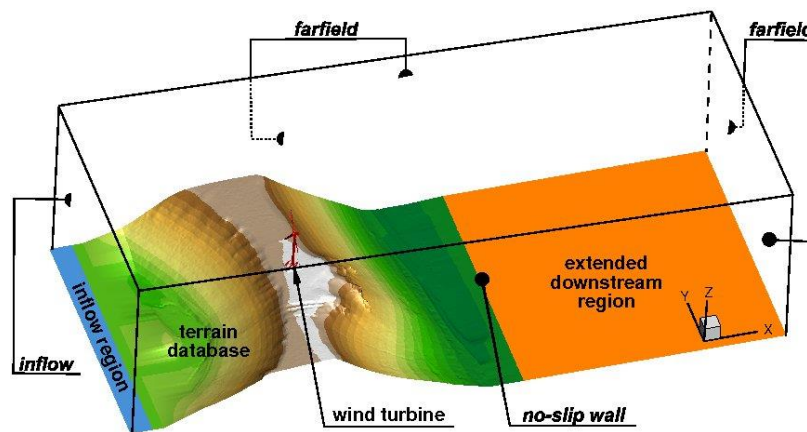


Figure 1: General computational setup

3 Test Cases

The studies have been done using a stepwise setup for the simulation. First of all, a baseline simulation (*CaseA*) of the turbine with uniform inflow in flat terrain was done and validated against manufacturer data. In *CaseB* turbulent inflow has been added to the simulation to study the interaction between turbine and atmospheric boundary layer. In *CaseC* the terrain without turbine but with turbulent inflow has been simulated to develop prediction models for later turbine behavior in a terrain situation. Finally, *CaseD* included the turbine into the setup of *CaseC* and made it possible to study the interaction between terrain, turbine and atmospheric boundary layer directly and to evaluate the prediction models developed for *CaseC*. For all turbine simulations a *kenersys K110 2.1MW* turbine has been used having a hub height of 95 m, a rotor diameter of 109 m operating under 12.81 RPM and a mean inflow speed at hub height of 11.01 m/s. Because of the limited space of this article, only some of the test cases can be shown in detail. For more detailed results the work of [5] and [7] can be considered.

4 Results

“Fig. 2” shows the vortex structure visualization of *CaseD* by means of a λ_2 -iso-surface. The coloring of the surface is done using the relative velocity $v_{rel} = \sqrt{u^2 \cdot v^2 \cdot w^2} / u_\infty$. A thin vortex layer at the slopeside of the windward side of the hill indicates a speed-up of almost two compared to the freestream velocity. In contrast, at the lee side the flow is retarded and massively separated showing three dimensional vortex structures. The existence of the speed-up and the separations is also proven by *CaseC*, which is not shown here. As the power output of a wind turbine is proportional to the cubic of the mean wind speed a closer look at the vertical velocity profiles can provide further information. In

“Fig. 3” the profiles of the flat terrain case and on top of the hill are compared and drawn as a function related to the height above ground. The profile of *CaseC* is taken at the designated turbine position. The black dot and the black T’s symbolize the hub position of the turbine as well as the blade area. The velocity in *CaseC* is significantly reduced up to a height of 25 m. Above this height a uniform speed increase of about 20 percentage points can be seen. This gives reason to expect a power augmentation when siting the turbine at this hill. Leaving mean values and talking about fluctuations leads to

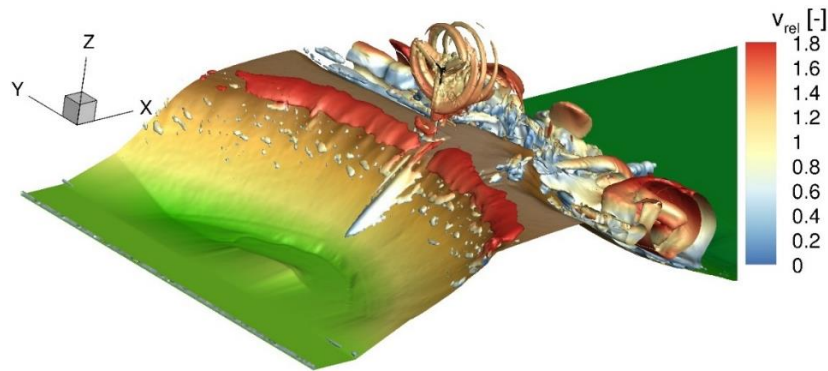


Figure 2: Vortex structures of *CaseD* visualized using a λ_2 -iso-surface

turbulence intensity. Higher turbulence intensities correlate with higher fluctuations of loads and power and a decrease of power performance [1]. For the further analyses the vertical turbulence intensity profiles are depicted in “Fig. 3”. An increase of turbulence intensity at the top of the hill with a peak at $z = 25\text{m}$ showing values almost an order of magnitude higher than in the flat terrain case can be seen. This may result from separation effects at the hill top. At greater heights ($z > 100\text{ m}$) the turbulence intensity values approach the flat terrain curve again as the speed-up over the hill dominates over the created disturbances. These facts hint at higher load and power fluctuations of the turbine in the complex terrain situation. “Fig. 4” plots the mean power output obtained for the turbine normalized by manufacturer reference data. Because of the 120° symmetry of the power behavior, the whole time signal was splitted into parts of 120° . Afterwards, the standard deviation and average value for each azimuthal position were determined. These mean values and standard deviations are shown in the figure. The mean power curve of the complex terrain case fulfills the estimation made before and shows an increase of the mean power of about factor 1.8 compared to *CaseB*. Above this, the effect of the higher turbulence can be seen in the five times higher standard deviation compared to the flat terrain situation. Looking at the details of the fluctuations “Fig. 5” has to be considered showing a FFT (Fast Fourier Transformation) analysis of the power time signal. *CaseA* is plotted as a reference for the turbine under uniform inflow. Clearly visible is the third harmonic of the blade passing frequency as well as the higher harmonics of this frequency which are results of the tower passage of the blades. Adding turbulence to the setup leads to *CaseB*, for which a higher level of fluctuations over the whole spectrum is visible, but a reduced impact of the tower because of the atmospheric boundary layer profile can be seen as well which is approximately 20% at the third harmonic. In *CaseD* the fluctuation level increases significantly up to 0.5 Hz compared to *CaseB*. The tower impact gets stronger again as the wind speed is higher than in *CaseB* in the relevant area covered by the blades.

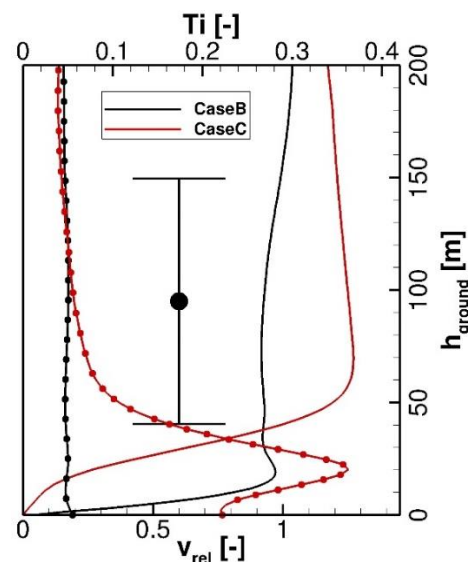


Figure 3: Vertical time averaged stream wise velocity (solid lines) and turbulence intensity (lines with dots)

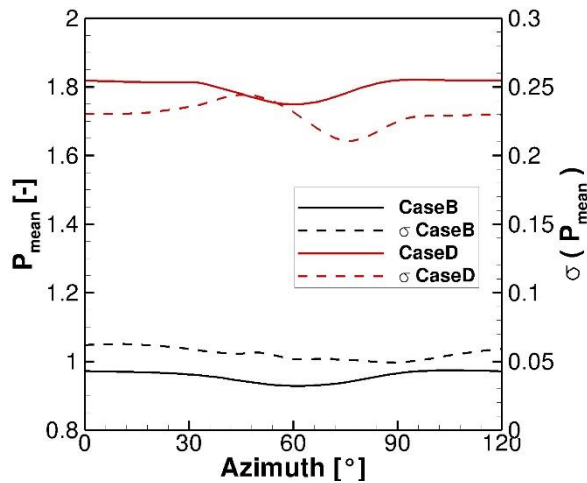


Figure 4: Time averaged normalized power output and its standard deviation for *CaseB* and *CaseD*

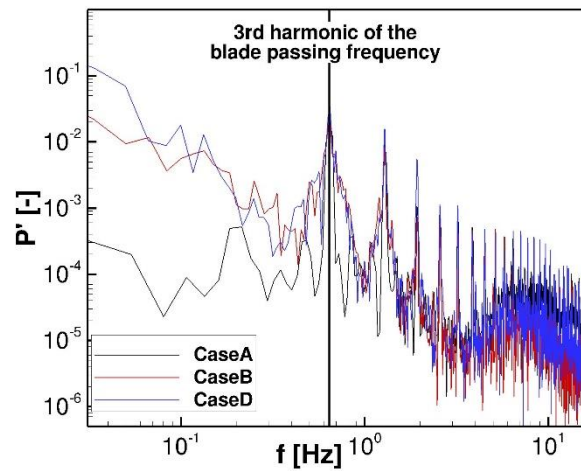


Figure 5: Spectrum of the normalized power output for *CaseA*, *CaseB* and *CaseD*

5 Conclusion

The results of a DES97 study on a wind turbine operating under atmospheric inflow conditions in complex terrain have been presented. The stepwise setup allowed to separate different effects emerging from the atmospheric inflow respectively the complex terrain. The siting of the turbine at the hill resulted in higher power output as the speed up at the hill top can be used. Nonetheless, the complex terrain also increases wind speed fluctuations and therefore impacts power variations. Not shown here but of major interest is the impact of the terrain on the blade loads and fatigue behavior of the turbine. Detailed information about this are given by [5] and [7]. In the future a further extension of the process chain will be done using field measurement data obtained from Lidar and unmanned aerial vehicle measurements as inflow conditions [2] in a terrain simulation of an area in South Germany. Furthermore, near and far wake measurements from these techniques will be available for a validation of the process chain and its results.

6 Acknowledgements

The authors gratefully acknowledge *the High Performance Computing Center Stuttgart* for providing the computational resources, *the German Federal Ministry for Economic Affairs and Energy* for funding the studies, *the State Agency for Spatial Information and Rural Development Baden-Württemberg* for supplying terrain data and *Kenersys* for supporting us with turbine data.

REFERENCES

- [1] E. Hau, “Wind Turbines: Fundamentals, Technologies, Applications, Economics” (2006)
- [2] M. Hofsäß, “IEA Topical Expert Meeting No.75” (2013)
- [3] K. Meister, Th. Lutz and E. Krämer, Proceedings: German Wind Energy Conference (2010)
- [4] C. Schulz, Th. Lutz “IEA Topical Expert Meeting No.75” (2013)
- [5] C. Schulz, L. Klein, P. Weihing, Th. Lutz, E. Krämer, CFD Studies on Wind Turbines in Complex Terrain under Atmospheric Inflow Conditions, “The Science of Making Torque from Wind“ (2014)
- [6] P. Weihing, K. Meister, C.Schulz, Th. Lutz, E. Krämer, Simulations on Interference Effects between Offshore Wind Turbines, “The Science of Making Torque from Wind“ (2014)
- [7] P. Weihing, C. Schulz, Th. Lutz, E. Krämer, CFD Performance Analyses of Wind Turbines Operating in Complex Environments, “High Performance Computing in Science and Engineering ‘14” (to be published) (2014)

3D stochastic gusts as an alternative to the Mexican hat wavelet

R. Bos¹, W. A. A. M. Bierbooms¹, G. J. W. van Bussel¹

¹Delft University of Technology, Wind Energy Research Group, Kluyverweg 1, 2629 HS Delft, the Netherlands, r.bos-1@tudelft.nl

ABSTRACT

During the design process of wind turbines, extreme loading is usually extrapolated from time series or otherwise assessed with deterministic waveforms. This raises some important issues. First, extrapolating maxima from time series results in uncertainty, which has to be countered by high safety factors. Second, a uniform perturbation velocity, as is assumed by most deterministic gust models, is likely to result in very high loads. In addition, control algorithms may be wrongfully tuned for such unrealistic events. In the work of Bierbooms [1], a methodology was developed that allows a designer to generate stochastic gusts embedded in time series. In the present work, an extension of this method, based on three-dimensional gusts, is compared with the current design practice. First results show that the extreme load distributions obtained from both methods agree well, indicating that using stochastic gusts may be a valid alternative to conventional ways of extreme load prediction.

INTRODUCTION

An important aspect of structural design is predicting the distribution of extreme loads over the design lifetime. For structures that suffer from continuous wind loading (e.g., aircraft, wind turbines, and suspension bridges), this means having to evaluate long periods of turbulence. In most cases, and certainly during a conceptual design phase, running an aeroelastic code for years of turbulent wind requires too much computation time. Therefore, two different approaches exist. First, extreme loads can be extrapolated from much shorter time series. Although the input is realistic, the disadvantage is that having to extrapolate can lead to high uncertainty. The alternative is to model the response to deterministic transients (e.g., step function, 1-cos function, and Mexican hat wavelet). These serve as an oversimplification of real-life wind gusts and have frequently found their way into design standards as a means to provide clear design objectives.

However, both approaches have the danger of being overly conservative. This is especially a problem for wind turbines, since the loads acting on the structure are inherently linked to the price of energy. In addition, with the current trend of increasing rotor sizes, the tower top mass also becomes more of an issue in terms of structural vibrations. This is while controllers have a hard time reacting to gusts because it is difficult to predict the shape and the spatial extent of real-life events.

The goal of this paper is to explain how a designer can generate individual stochastic gusts and to show how these can be used to make better extreme load predictions. First, we briefly outline the mathematics behind the method. Next, we show how this can be applied to make better load predictions. A quick comparison is made with load maxima extracted from ten-minute periods to show how the method relates to the conventional design practice.

GENERATION OF STOCHASTIC GUSTS

A common method to generate synthetic turbulence is by a 3D Fourier series:

$$\mathbf{u}(\mathbf{x}) \approx \sum_{\boldsymbol{\kappa}} e^{i\boldsymbol{\kappa} \cdot \mathbf{x}} \mathbf{C}(\boldsymbol{\kappa}) \mathbf{n}(\boldsymbol{\kappa}), \quad (1)$$

where $\mathbf{u} = [u, v, w]^T$ is a velocity vector, $\mathbf{x} = [x, y, z]^T$ a position vector, $\boldsymbol{\kappa} = [\kappa_x, \kappa_y, \kappa_z]^T$ the wave number vector, $\mathbf{C}(\boldsymbol{\kappa})$ a correlation tensor containing the spectral properties (e.g., see IEC 61400-1,

Annex B), and $\mathbf{n}(\boldsymbol{\kappa}) \sim N(0, \mathbf{I}_3)$ a vector of standard-normal distributed coefficients. This can be rewritten as a DFT matrix multiplication, $\mathbf{u}(\mathbf{x}) \approx \boldsymbol{\Psi}(\mathbf{x}, \boldsymbol{\kappa})\mathbf{n}(\boldsymbol{\kappa})$, according to

$$\mathbf{u}(\mathbf{x}) \approx \begin{bmatrix} \mathbf{C}_{1,1,1} e^{i\boldsymbol{\kappa}_{1,1,1} \cdot \mathbf{x}} & \mathbf{C}_{2,1,1} e^{i\boldsymbol{\kappa}_{2,1,1} \cdot \mathbf{x}} & \dots & \mathbf{C}_{N_x, N_y, N_z} e^{i\boldsymbol{\kappa}_{N_x, N_y, N_z} \cdot \mathbf{x}} \end{bmatrix} \begin{bmatrix} \mathbf{n}_{1,1,1} \\ \mathbf{n}_{2,1,1} \\ \vdots \\ \mathbf{n}_{N_x, N_y, N_z} \end{bmatrix}. \quad (2)$$

Since only the DFT matrix, $\boldsymbol{\Psi}$, is dependent on the position vector, \mathbf{x} , it holds that

$$\frac{\partial [\boldsymbol{\Psi}(\mathbf{x}, \boldsymbol{\kappa})\mathbf{n}(\boldsymbol{\kappa})]}{\partial x_i} = \frac{\partial \boldsymbol{\Psi}(\mathbf{x}, \boldsymbol{\kappa})}{\partial x_i} \mathbf{n}(\boldsymbol{\kappa}). \quad (3)$$

Therefore, it is possible to expand the DFT matrix to include the first derivatives, yielding a new linear system in the shape of $\mathbf{b}(\mathbf{x}) \approx \mathbf{A}(\mathbf{x}, \boldsymbol{\kappa})\mathbf{n}(\boldsymbol{\kappa})$:

$$\begin{bmatrix} u(\mathbf{x}) \\ v(\mathbf{x}) \\ w(\mathbf{x}) \\ \frac{\partial u(\mathbf{x})}{\partial x} \\ \frac{\partial u(\mathbf{x})}{\partial y} \\ \frac{\partial u(\mathbf{x})}{\partial z} \end{bmatrix} = \begin{bmatrix} \mathbf{C}_{1,1,1} e^{i\boldsymbol{\kappa}_{1,1,1} \cdot \mathbf{x}} & \mathbf{C}_{2,1,1} e^{i\boldsymbol{\kappa}_{2,1,1} \cdot \mathbf{x}} & \dots & \mathbf{C}_{N_x, N_y, N_z} e^{i\boldsymbol{\kappa}_{N_x, N_y, N_z} \cdot \mathbf{x}} \\ i\kappa_x \mathbf{C}_{1,1,1}^{(u)} e^{i\boldsymbol{\kappa}_{1,1,1} \cdot \mathbf{x}} & i\kappa_x \mathbf{C}_{2,1,1}^{(u)} e^{i\boldsymbol{\kappa}_{2,1,1} \cdot \mathbf{x}} & \dots & i\kappa_x \mathbf{C}_{N_x, N_y, N_z}^{(u)} e^{i\boldsymbol{\kappa}_{N_x, N_y, N_z} \cdot \mathbf{x}} \\ i\kappa_y \mathbf{C}_{1,1,1}^{(u)} e^{i\boldsymbol{\kappa}_{1,1,1} \cdot \mathbf{x}} & i\kappa_y \mathbf{C}_{2,1,1}^{(u)} e^{i\boldsymbol{\kappa}_{2,1,1} \cdot \mathbf{x}} & \dots & i\kappa_y \mathbf{C}_{N_x, N_y, N_z}^{(u)} e^{i\boldsymbol{\kappa}_{N_x, N_y, N_z} \cdot \mathbf{x}} \\ i\kappa_z \mathbf{C}_{1,1,1}^{(u)} e^{i\boldsymbol{\kappa}_{1,1,1} \cdot \mathbf{x}} & i\kappa_z \mathbf{C}_{2,1,1}^{(u)} e^{i\boldsymbol{\kappa}_{2,1,1} \cdot \mathbf{x}} & \dots & i\kappa_z \mathbf{C}_{N_x, N_y, N_z}^{(u)} e^{i\boldsymbol{\kappa}_{N_x, N_y, N_z} \cdot \mathbf{x}} \end{bmatrix} \begin{bmatrix} \mathbf{n}_{1,1,1} \\ \mathbf{n}_{2,1,1} \\ \vdots \\ \mathbf{n}_{N_x, N_y, N_z} \end{bmatrix},$$

where $\mathbf{C}_{i,j,k}^{(u)}$ denotes the u -component, or first row, of the correlation tensor, that is

$$\mathbf{C}^{(u)} = [C_{uu} \quad C_{uv} \quad C_{uw}].$$

A horizontal gust at a position \mathbf{x}_0 can be defined as $\mathbf{u}(\mathbf{x}_0) = [\hat{u}, 0, 0]^T$, where \hat{u} is the gust amplitude. Moreover, for this gust to be a local maximum, it is required that

$$\frac{\partial u}{\partial x} = \frac{\partial u}{\partial y} = \frac{\partial u}{\partial z} = 0.$$

These conditions can be stored in the constraint vector, \mathbf{b} , leading to a system that can be solved for

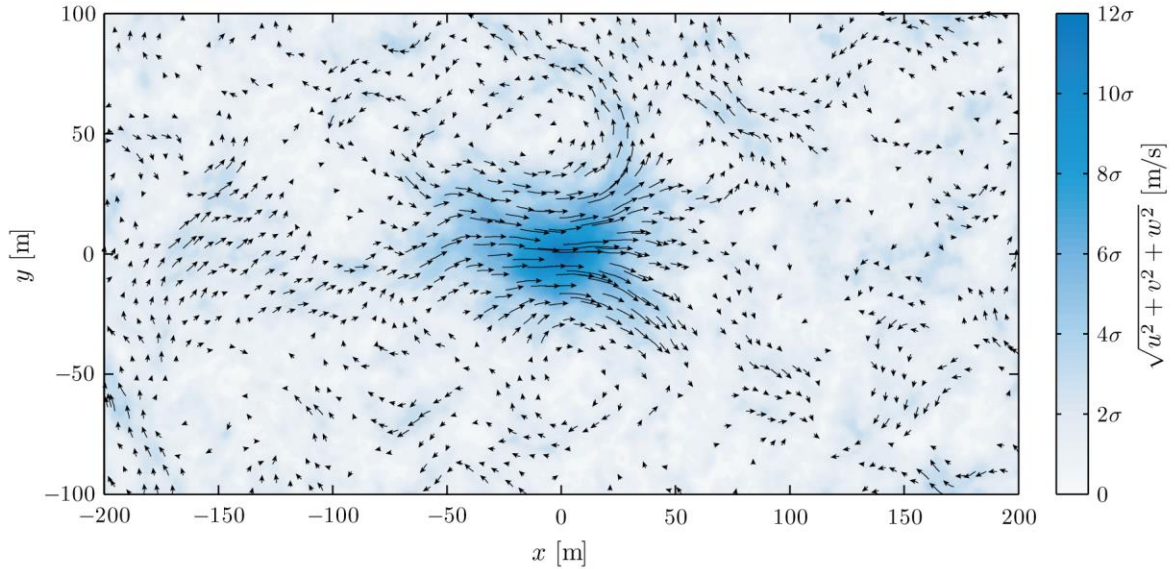


Figure 1: Example of a gust in the xy -plane.

the vector \mathbf{n} by applying the *maxtrix inversion lemma*. This yields a constrained white noise vector:

$$\mathbf{n}_c = \mathbf{n} + \mathbf{A}^*(\mathbf{A}\mathbf{A}^*)^{-1}(\mathbf{b} - \mathbf{A}\mathbf{n}). \quad (4)$$

When using this vector to evaluate the Fourier series in equation (1), the result is a constrained wind field that satisfies the conditions given by \mathbf{b} (e.g., see fig.1). Since the system covers 6 equations and a total of $N_x N_y N_z$ variables, there is still a high degree of randomization involved (although adding many constraints or demanding very high amplitudes may still result in a wind field that is too synthetic).

MONTE CARLO SIMULATION OF EXTREME GUST LOADS

The gusts described in the previous section can be used to simulate extremes in an aeroelastic model that would otherwise have resulted from very long time series. A 50-year return level can then be efficiently predicted by using a Monte Carlo method with importance sampling. For N samples yielding a set of loads x_1, \dots, x_N , an extreme load distribution can be approximated by

$$\hat{F}(L) \approx \frac{1}{N} \sum_{i=1}^N 1(x_i \leq L) \frac{f(\mathbf{k})}{w(\mathbf{k})}. \quad (5)$$

Here, \mathbf{k} is a set of environmental conditions (e.g., wind speed, turbulence intensity, gust properties, etc.), $1(x)$ is the indicator function, $f(\mathbf{k})$ is the probability density function of \mathbf{k} , and $w(\mathbf{k})$ is a sampling distribution.

The error in the approximation is minimized as $N \rightarrow \infty$ and when $w(\mathbf{k})$ mirrors the final distribution. Therefore, knowledge about which conditions are associated with extreme loads helps to reduce the uncertainty in predicting the 50-year return level. For example, fig. 2 shows that gusts are more likely to trigger extreme loads when the turbine is operating at the rated wind speed. Moreover, because the IEC prescribes a higher turbulence intensity at higher wind speeds, the spread in extreme loads increases somewhat near the cut-out point. Therefore, a designer would be able to allocate his computational resources more efficiently by adding this to a sampling distribution. Some more examples of this can be found in a previous paper [2].

The method can be validated by comparing it with a conventional extreme load prediction using ten-minute time series. As a first comparison, 361 ten-minute intervals and 2,000 individual wind gusts, each stored in a 100 s time series, are fed to a Bladed model of the DTU 10 MW reference

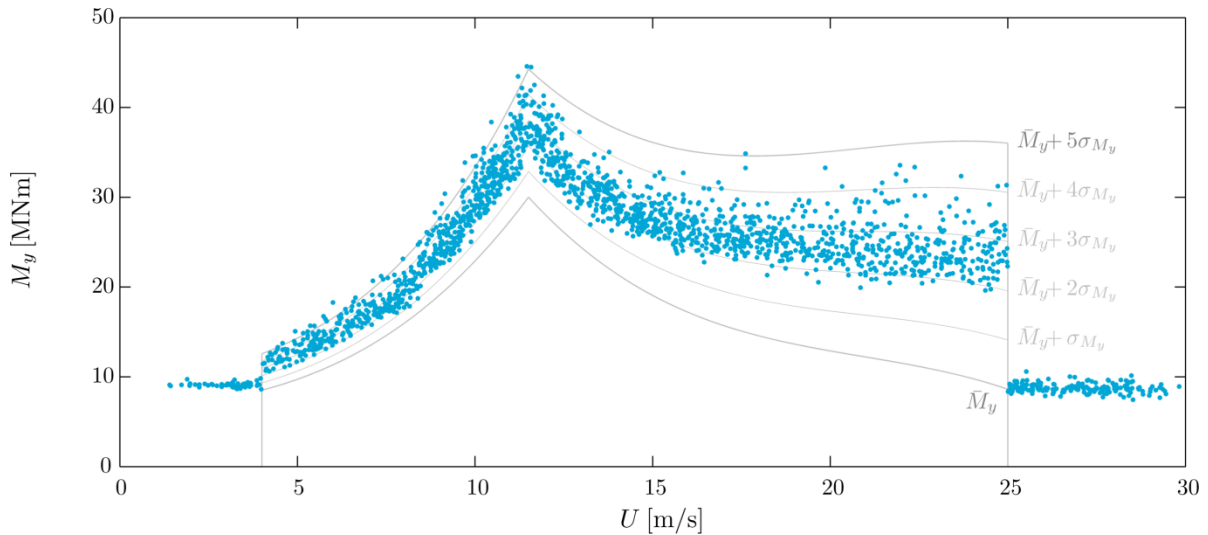


Figure 2: Variation of blade root flapwise bending moments, M_y , of the DTU 10 MW reference wind turbine with mean wind speed, U , in response to 2,000 gusts varying in amplitude up to $10\sigma_u$ (blue), where the turbulence intensity scales with wind speed according to what is specified by the IEC for an offshore site [3]. The lines refer to the *ten-minute mean* bending moment, \bar{M}_y , plus 1 to 5 standard deviation (grey).

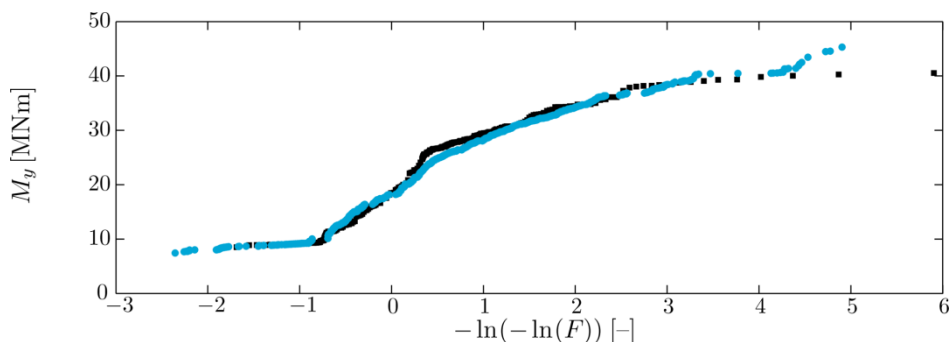


Figure 3: Distribution of maximum blade root flapwise bending moments of the DTU 10 MW reference wind turbine in response to 2,000 gusts (*blue*), compared to the maxima obtained from 361 ten-minute intervals (*black*). The external conditions are defined by the IEC DLC 1.1 using a predefined Rayleigh distribution of mean wind speeds.

turbine. The results in fig. 3 show that the bulk of the two data sets agrees well. However, there is some degree of uncertainty to be taken into account. Repeating the exercise will naturally yield different load sets where the difference is most pronounced at the tails (which, unfortunately, is also the region of interest). This makes it tricky to compare two individual sets and it would therefore be inappropriate to make any hard claims about how the method performs. Better would be to minimize the uncertainty in the conventional method to have a proper benchmark, for instance by using very long data sets (e.g., see [4]). This will be the topic of future research.

CONCLUSION AND OUTLOOK

It is possible to derive individual wind gusts from the properties of stochastic turbulence. Since these gusts represent the local extremes of long periods of turbulence, they can be used to predict the long-term loads of a wind turbine, for example using Monte Carlo methods. It may considerably improve the accuracy in the 50-year load prediction because of two reasons. First, calculating a gust response only requires a relatively short time interval, meaning more extreme loads can be generated in the same time to form the basis for extrapolation. In addition, importance sampling methods allow a designer to narrow down the search for extreme loads to critical areas, thereby wasting less computational resources on uninteresting events, such as gusts at low wind speeds.

A first comparison between this method and a conventional way of predicting extreme loads (i.e., on the basis of ten-minute intervals) has shown promising results. However, because of the uncertainty in the two sets of data, it is not possible to draw any hard conclusions. Future research will therefore focus on comparing the method against a proper benchmark, for instance by relying on the long-term data set generated by Barone et al. [4].

REFERENCES

- [1] W. A. A. M. Bierbooms (2009). “Constrained stochastic simulation of wind gusts for wind turbine design”, PhD thesis, Delft University of Technology, Delft, the Netherlands (2009).
- [2] R. Bos, W. A. A. M. Bierbooms, G. J. W. van Bussel (2014), “Towards spatially constrained gust models”, In: The Science of Making Torque From Wind, 18–20 June 2014, Kgs. Lyngby, Denmark.
- [3] International Electrotechnical Commission (2009). IEC 61400-3 Wind Turbines - Part 1: Design requirements for offshore wind turbines.
- [4] Barone, M., J. Paquette, B. Resor, and L. Manuel (2012). “Decades of Wind Turbine Load Simulation.” In: 50th AIAA Aerospace Sciences Meeting Including the New Horizons Forum and Aerospace Exposition, 9–12 January 2012, Nashville, TN, United States.

Modelling and Evaluation of Wind Speed Time Series for Reliability Analysis of Offshore Wind Farms

C.J. Smith, C.J. Crabtree, P.C. Matthews, B. Kazemtabrizi

Durham University, School of Engineering and Computing Sciences, c.j.smith2@dur.ac.uk

ABSTRACT

This paper outlines proposed testing criteria for wind speed time series (WSTS) models. The objective is to assess their suitability for reliability analysis that is dependent on an accurate representation of weather patterns. Two WSTS models were analysed for their suitability against these criteria. The Markov model was found to be suitable for resource assessment, but would require modification before it could represent weather patterns, whilst the random sampling model could represent weather patterns more accurately, but could not be used for resource assessment.

I. INTRODUCTION

In order to meet EU renewable energy penetration targets for 2020 and beyond, the Levelised Cost of Energy (LCoE) of offshore wind needs to be reduced from the current £140/MWh to be lower than £100/MWh [1]. To facilitate this, innovation in planning and operation is required, including the cost-benefit analysis of improving farm availability. As operation and maintenance accounts for around 30% of the LCoE [2], a number of researchers have carried out reliability studies on offshore wind.

One of the unique characteristics of wind generation is the stochastic nature of the fuel. As such, a number of these reliability studies aim to capture the stochastic nature of the wind resource, with a particular focus on a site's mean wind speed. As local wind speed data for a particular site is limited by the length of time a meteorological mast has been installed at the site, long term reliability studies require the wind speed to be simulated based on this limited data. This modelling has been carried out in a number of ways:

- Mathematical expectation calculations based on probability distribution functions [3].
- Wind speed time series (WSTS) produced by randomly sampling from probability distributions [4].
- WSTS produced from Markov processes [5].
- WSTS produced using an auto-regressive moving average (ARMA) model [6].

Mathematical expectation calculations can be used to quickly assess the performance of a wind farm configuration, but cannot be used to detail the effects of factors such as weather windows and maintenance delays. The production of WSTS is more appropriate for investigating these factors. For example, the use of a WSTS can more accurately represent the effect of a turbine failure by giving the range of impacts that may occur, along with their respective likelihood. This can give a confidence level in the energy production produced by the model. Therefore, the production of WSTS models is the focus of this research.

Whilst each method has qualitative benefits and disadvantages that may determine which method is used for reliability analysis, no work has been done to quantify whether the models produce similar values for key parameters such as the wind's available energy. This analysis is needed to justify the use of these WSTS models.

The paper is organized as follows. Section II details the tests to be carried out on WSTS models to assess their suitability. Section III gives information on two example WSTS models that has been tested. Section IV details the results of the tests carried out on the WSTS models. Section V summarises the conclusions from this work.

II. METHODOLOGY

To assess the quality of a WSTS model, an original data set is required. The original WSTS was taken from the meteorological mast at the Egmond aan Zee wind farm site [7]. Wind speeds from a height of 70 m, at 10 minute intervals from 01/07/2005 to 30/06/2006 were used, and the data has been cleaned to produce a complete data set.

To quantify the suitability of a WSTS generator for reliability analysis, the key measures needed to be considered:

- Produce an amount of energy in the wind close to that of the original WSTS.
- Produce an amount of energy from a typical wind turbine close to that of the original WSTS.
- The total time at all wind speeds should be similar to the original WSTS.
- Produce a similar number of transitions between wind speeds to the original WSTS.
- Capture the longer term seasonal trends and occurrence of sustained low and high wind speeds in the data.

By quantifying these measures, a metric was produced which could assess the adequacy of any WSTS model; the closer the measured metrics are to the original WSTS, the better the model. The following paragraphs detail how these metrics were quantified. Note, the wind speeds were discretized into 1 m/s bins, except for the frequency analysis.

To quantify energy availability, the expected power densities of original and produced WSTS were computed (1). Expected power density was used to remove any unrequired information such as turbine size and turbine life span.

$$E(p) = \sum_{u=0}^{u_{max}} 0.5\rho u^3 F(u) \quad (1)$$

Where $E(p)$ is the expected power density (W/m^2), ρ is air density (kg/m^3), u is wind speed (m/s), u_{max} is the maximum wind speed (m/s) and $F(u)$ is the probability distribution function of the wind speeds.

The expected power from a typical turbine was computed in the same way (2), but with limits to represent the cut-in, cut-out and rated wind speeds (3). The parameters of the wind and wind turbine can be found in Table 1.

$$E(p_t) = \sum_{u=0}^{u_{max}} 0.5C_p\rho u_t^3 F(u) \quad (2) \quad u_t = \begin{cases} 0, & u < u_{in} \\ u, & u_{in} \leq u < u_{rated} \\ u_{rated}, & u_{rated} \leq u < u_{out} \\ 0, & u \geq u_{out} \end{cases} \quad (3)$$

Where $E(p_t)$ is the expected power density from a typical turbine (W/m^2), C_p is the coefficient of performance, u_t is the equivalent wind speed for a wind turbine (m/s), u_{in} is the cut-in wind speed (m/s), u_{rated} is the rated wind speed (m/s), and u_{out} is the cut-out wind speed (m/s).

Parameter	Value	Parameter	Value
u_{in}	4 m/s	ρ	1.225 kg/m^3
u_{rated}	13 m/s	C_p	0.4
u_{out}	25 m/s		

Table 1: Parameter values for expected power calculations.

To compare the total time at all wind speeds, the total time at each wind speed for each WSTS were represented on a bar chart. The number of transitions between wind speeds was also counted and compared to the original WSTS.

To assess the quality of seasonal representation, two tests were carried out. Firstly, the frequency spectrum of the produced WSTS was compared to the original WSTS by taking their Fourier Transform (FT). In the spectrum, the frequencies for both WSTS should have similar amplitudes if the seasonal variation has been modelled successfully.

The second test quantified the occurrence of weather windows. A weather window is defined as a point in time where a maintenance team could be dispatched to repair a component offshore as the wind speed is below a threshold for a time period long enough to carry out the repair. This was quantified by calculated the percentage of time a maintenance team could be dispatched. The length of the weather window and the wind speed threshold is dependent on the type of maintenance being carried out and the travel distance. For this work, targets of a wind speed threshold of 10 m/s and a time of 48 hours was taken as a weather window, similar to those found for a jack-up vessel in [8].

To summarise, for the produced WSTS the $E(p)$, $E(p_t)$, wind speed residence times, the number of wind speed transitions, the frequency spectrum, and the percentage of time a weather window is available were compared to the original WSTS to assess the quality the WSTS models used.

III. WSTS MODEL EXAMPLES

Two WSTS models were analysed; a continuous-time Markov process model developed for this work, and a model that randomly samples from various probability distributions [4]. These two methods are outlined in this section.

The Markov process uses only the transitions between wind speeds within a real WSTS to dictate the transitions occurring in the produced WSTS. Like the random sampling from a probability function, the use of probabilities retains the stochastic nature of the wind but can capture how the WSTS moves between wind speeds more accurately. However, the calculation of transition rates introduces more complexity and requires a larger amount of data.

A Markov process approach assumes that the system is memory-less; future random behaviour is only dependent on the current state, and the process is stationary; the behaviour of the system is time independent. As such, the transition rates must be constant. The state residence times are assumed to follow an exponential distribution [6]. The transition rates are calculated using (4). The transitions times from the current state i to state j are calculated using (5).

$$\lambda_{ij} = \frac{N_{ij}}{T_i} \quad (4) \quad L_{ij} = \frac{h_{yr}}{\lambda_{ij}} \ln(R_j) \quad (5)$$

Where λ_{ij} is the transitions rate between states i and j (occurrences/year), N_{ij} is the number of transitions between states i and j , T_i is the total time at state i (years), L_{ij} is the transition time between state i and j (hours), h_{yr} are the number of hours in a year (8760), and R_j is a uniform random number between 0 and 1.

The Markov process model used is similar to that found in [5], with a number of key features:

- The initial state is determined by randomly sampling from a Weibull distribution based on the original WSTS.
- The input data is based on 10 minute average, rather than hourly average, wind speed data.
- Missing transition rates in the transition matrix due to having a small dataset were filled using linear interpolation.
- Transitions can occur to any other state from the current state, unlike the birth-and-death model used in [5]. The next state is determined by the smallest transition time calculated (5) and states are represented by 1 m/s bins.
- The original data was sampled at 10 minutes, so transitions that occur within 10 minutes of the current state in the model are rejected. As a continuous process is used, transition times can be a non-integer multiple of 10 minutes to produce a continuous-time WSTS.

For comparison, a WSTS model that randomly samples from Weibull and normal distributions with a smoothing algorithm was also tested against these criteria. The details of this WSTS model can be found in [4], but the model has been modified to produce 10-minute average wind speeds, rather than hourly average wind speeds.

Two WSTS models have been detailed here. A Markov process was used, with 1 m/s wind speed bins as states, and the process could move from the current state to any other state. The model used transition rates that were modified to minimise the effect of small data sets. Any transitions below 10 minutes were rejected. Another WSTS model based on randomly sampling from probability distributions was also used for comparison.

IV. RESULTS AND DISCUSSION

A WSTS lasting 8760 hours was produced 1000 times from both wind speed models so that a representative mean could be produced for each parameter, except for the frequency spectrum production. Figure 1 compares the residence times between original and produced WSTS, Figure 2 compared the results of the FT applied to the original and a sample produced WSTS, and Table 2 summarises the results of the time series testing.

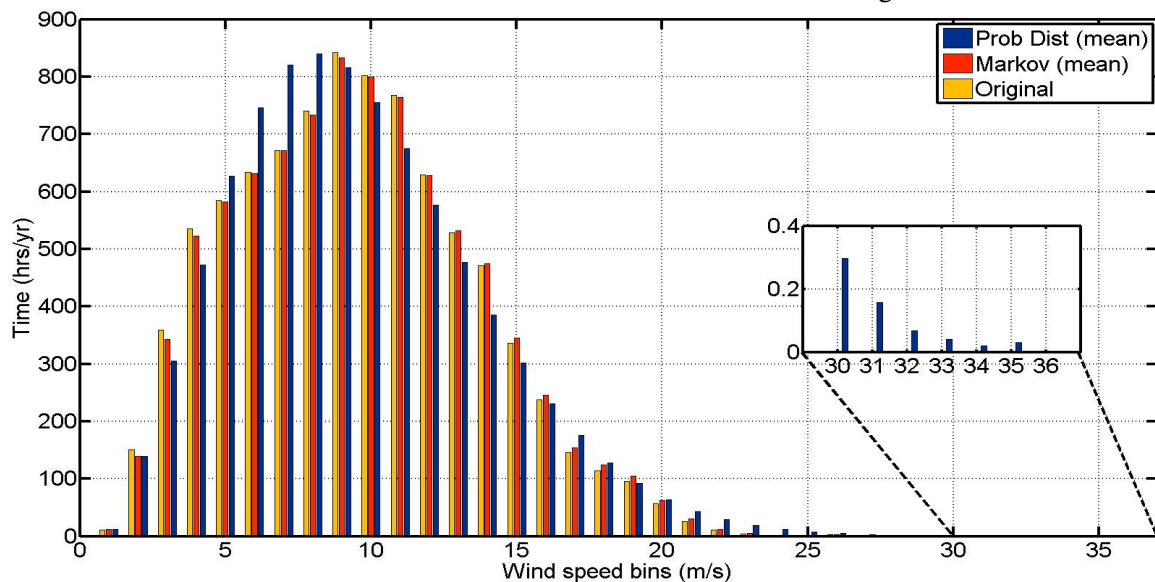


Figure 1: Comparison of wind speed bin residence times for original and mean of produced WSTS.

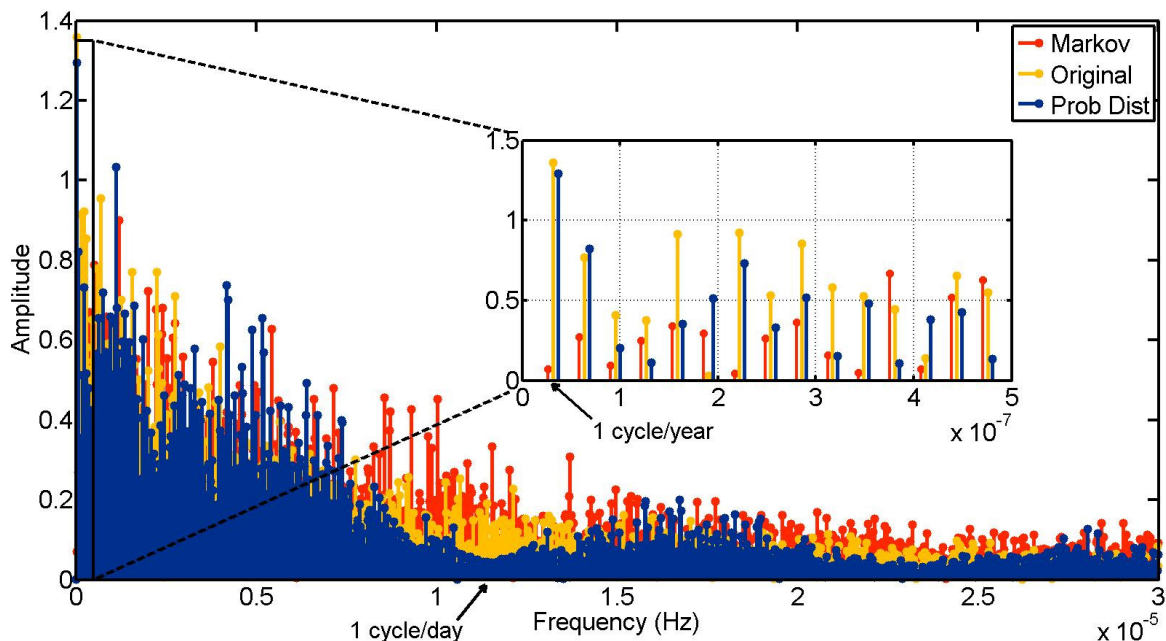


Figure 2: Frequency spectrum of original and produced WSTS.

Test criteria	Original time series	Markov Process (mean)	Probability Distribution (mean)
$E(p)$ (W/m ²)	657.3	678.8	692.7
$E(p_t)$ (W/m ²)	510.9	519.8	493.7
Number of wind speed transitions	19378	16244	41970
Weather window opportunities (%)	14.8	4.6	24.1

Table 2: Results of analysis of original WSTS and produced WSTS.

Firstly, $E(p)$ and $E(p_t)$ from the Markov process were 3.19% and 1.10% higher respectively than that of the original WSTS (Table 2). This is reflected in Figure 1, where the wind speeds are biased towards higher wind speeds. However, as this over-estimation is small, the Markov process is appropriate for capturing energy characteristics. In contrast, $E(p)$ for the random sampling method was 5.4% higher than the original WSTS, but $E(p_t)$ was 3.4% lower. The high $E(p)$ can be attributed to the higher wind speeds (Figure 1), whilst the lower $E(p_t)$ was due to the higher total time at lower wind speeds. Therefore the Markov process produces a more accurate energy availability estimate.

Secondly, Figure 1 reveals that the produced WSTS from the Markov process reproduced the total residence time at different wind speeds with some accuracy, though tended to favour higher wind speeds. The number of wind speed transitions was lower than in the original WSTS (Table 2) indicating that the Markov process had residence times that were longer than of those in the original WSTS. This suggests that an exponential distribution is not the best distribution to represent residence times. However, the random sampling method was a poor estimation of wind speed bin times (Figure 1) and produced more transitions (Table 1). Therefore, the Markov process represents the wind speed times and transitions numbers more accurately than the random sampling method.

Finally, Figure 2 reveals that the seasonality of the original WSTS (represented by peaks at the low frequencies) was not captured by the Markov Process. This reveals that seasonality should be added to any WSTS model using a Markov Process. The random sampling method used mean speeds for each month, and therefore replicated the high amplitude peaks at low frequencies of the original WSTS with some accuracy (Figure 2). Furthermore, the reduced number of weather windows (Table 2) indicates that the Markov process moved between low and high wind speed states more regularly than the original data. This is highlighted by the higher magnitudes around 10^5 Hz (~1 cycle/day) (Figure 2). The random sampling method was slightly more accurate at depicting weather windows, but did overestimate their occurrence (Table 2) due to the reduced number of high frequency transitions (Figure 2).

A basic continuous Markov process can be used for macro-scale resource assessment for a site as it represents the power densities and total residence times whilst maintaining the random nature of the wind, but this random sampling approach is inadequate. However, the Markov process is not a valid approach when analysing for effects of weather windows on maintenance, or reliability analysis that requires seasonality, without the need for detailed modifications to the process, whilst the random sampling approach captures seasonality more accurately.

V. CONCLUDING REMARKS

The features required of a produced WSTS for reliability analysis and the tests designed to assess the suitability of proposed WSTS models based on these features are detailed here. Example WSTS models in the form of a continuous Markov process and random sampling from probability distributions were analysed against these criteria. It was found that a basic Markov process would be suitable for resource assessment reliability analysis which required a stochastic wind resource. However, the basic model would require modification in order to capture more complex weather patterns before it would be suitable for more detailed reliability analysis. Conversely, this random sampling method is more accurate at producing seasonal variations, but cannot be used for resource assessment.

REFERENCES

1. E. Davey and A. Nimmo. *Offshore Wind Cost Reduction, Pathways Study*. 2012; Available from: <http://www.thecrownestate.co.uk/media/305094/offshore-wind-cost-reduction-pathways-study.pdf>.
2. W. Musial and B. Ram. *Large-Scale Offshore Wind Power in the United States: Assessment of Opportunities and Barriers*. 2010; Available from: <http://www.nrel.gov/docs/fy10osti/40745.pdf>.
3. M.A. Parker and O. Anaya-Lara, *Cost and losses associated with offshore wind farm collection networks which centralise the turbine power electronic converters*. IET Renewable Power Generation, 2013. 7(4): p. 390-400.
4. B. Kazemtabrizi, C. Crabtree, and S. Hogg, *Reliability Evaluation of New Offshore Wind Farm Electrical Grid Connection Topologies*, in *ASME Turbo Expo 2013: Turbine Technical Conference and Exposition*. 2013: Texas, USA. p. 1-10.
5. N.B. Negra, et al., *Aspects of Relevance in Offshore Wind Farm Reliability Assessment*. Energy Conversion, IEEE Transactions on, 2007. 22(1): p. 159-166.
6. R. Billinton and R.N. Allan, *Reliability evaluation of engineering systems*. 1983: Plenum press New York.
7. Noordzeewind. *Noordzeewind: Reports & Data*. 2014; Available from: <http://www.noordzeewind.nl/en/knowledge/reportsdata/>.
8. A.Z. J. Dowell, L. Walls, T. Bedford and D. Infield, *Analysis of Wind and Wave Data to Assess Maintenance Access to Offshore Wind Farms in European Safety and Reliability Association Conference*. 2013: Amsterdam.

Investigating the interaction between wind turbines and atmospheric flow with a coupling of the aeroelastic code FAST and the LES code PALM

M. Bromm, M. Kühn

ForWind, Carl von Ossietzky University of Oldenburg, Wind Energy Systems,
marc.bromm@forwind.de, +49(441) 798 5066

Extended Abstract

Introduction

During the design and the operation of a wind farm it is necessary to consider the mutual aerodynamic influence of the turbines. Wake flow conditions can lead to substantial losses in the energy yield as well as increases in structural loads due to larger inhomogeneity in the wind field and higher turbulence. For a more efficient and economic use of the limited number of sites that guarantee high power output, new concepts of wind farm control (e.g. wake deflection [1],[2], reducing the axial induction [3]) and management become more relevant. Recent studies investigating various control mechanisms by wind tunnel experiments or by simulations show promising results. Nevertheless a better understanding of the flow development in a wind farm and the wind turbine – flow interaction under the influence of various atmospheric conditions and turbine control concepts is of fundamental importance for a successful industrial application.

The PhD project aims at improving the understanding of wake development based on simulations and free field measurement data and at further advancing the investigation and development of wake models, which are suited for the application in wind farm control. In a first step a coupling of an aeroelastic and a large-eddy (LES) code based on the actuator line approach (ACL) was implemented. It will allow to investigate the impact of various key parameters (e.g. atmospheric conditions, farm layout, turbine setups) on the wake development in well-defined environments which are hard to capture in free field campaigns.

Methods

Aeroelastic modelling and atmospheric flow simulation

The calculation of the wind turbine response is based on the aeroelastic code FAST developed by NREL, Golden (US) [4] specifically for horizontal axis wind turbines. The code is open source and therefore can easily be adapted and combined with other codes for integrated simulation environments.

In FAST a wind turbine is modelled as a combination of rigid and flexible bodies. The AeroDyn component calculates the aerodynamic forces along the blades based on the blade element momentum theory (BEM) and tabulated airfoil data. Additionally the turbine model can be extended by controllers (e.g. pitch, torque, and yaw) for a more realistic overall turbine behaviour.

For simulating the atmospheric boundary layer the free software PALM developed by IMUK, Hannover (Germany) [5] is used which is a LES model for atmospheric and oceanic flows. It uses a modified Smagorinsky sub grid scale parameterization to diffuse the energy contained in scales smaller than the model grid length. PALM is specifically designed for performing on massively parallel computer architectures.

Coupling implementation

The modelling of the turbine(s) in the atmospheric boundary layer in PALM is based on the ACL approach [6]. The blades are divided into a series of segments where each is represented by a reference point. Local velocities at these elements are transferred to FAST to calculate the corresponding lift and drag forces from tabulated airfoil data. It furthermore determines the new positions of the blade elements based on the turbine response. This information is transferred to PALM where the forces are radially distributed onto the underlying grid. To avoid singular behaviour a 3D Gaussian regularization kernel η_ϵ which depends on the regularization parameter ϵ and the normal distance d of a grid point to the blade element reference point (see (1)) is being used to ensure the smoothness of the distribution.

$$\eta_\epsilon(d) = \frac{1}{\epsilon^3 \pi^{\frac{3}{2}}} \exp \left[- \left(\frac{d}{\epsilon} \right)^2 \right] \quad (1)$$

During co-simulations PALM runs as a server and exchanges data with possibly multiple turbine models (individual FAST instances) via TCP/IP sockets (Fig. 1). This offers a high flexibility concerning the involved systems and allows using the entire modelling capabilities of FAST.

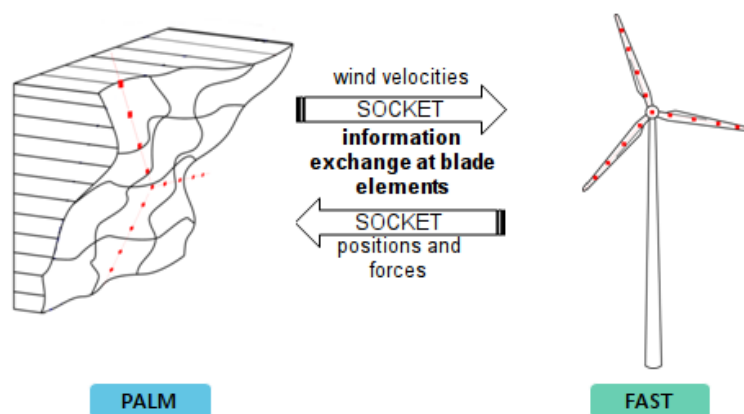


Figure 1: Scheme of the information exchange between the aeroelastic and the large-eddy code

Results

In this section a few results from the simulation with the publicly available turbine model of the NREL 5MW with a rotor diameter of 126 m and a hub height of 90 m in a stable onshore boundary layer are presented. Tower and nacelle are currently not included in the PALM simulation.

For running the simulations an initial wind field with the desired characteristics (e.g. velocity profile, atmospheric stability) needed to be generated in a precursor run. In the coupled runs the wind field with stationary boundary layer is imported for setting the initial conditions. The

concept of turbulence recovery downstream (1400 m) of the inflow boundary is applied. To limit the incremental movement of the blade elements the time step of the simulation in FAST and PALM is fixed to 0.02 s. The mesh resolution is uniformly 2.5 m in all coordinate directions. The presented results were simulated in a stable boundary layer (SBL) with a mean inflow velocity of 10 m/s at hub height and a turbulent intensity of 6.5 %. The simulation time was fixed to 900 seconds with the first 300 seconds being removed in the analysis to account for transient processes at the beginning of the simulation.

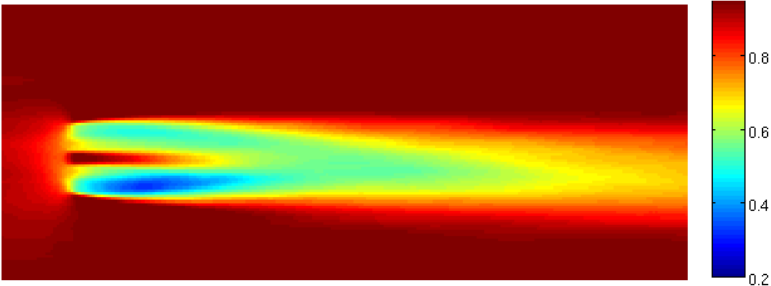


Figure 2: Normalized time-averaged (600 s) wake deficit (NREL 5MW, $U_{hub} = 10$ m/s, TI = 6.5 %)

The time-averaged velocity (Fig. 2) in this single turbine test case clearly shows the distinct deficit which only slowly recovers after several rotor diameters downstream. Furthermore the impact upstream on the approaching flow clearly can be seen.

Additionally scenarios of two turbine in wake configuration with different spacing were simulated. In the presented test case the second turbine is positioned directly behind the upstream turbine with respect to the main wind direction in a distance of 4D.

In this configuration the second turbine exhibits a severe power loss of approx. 60 %. The instantaneous power production of both turbines over time and the thrust force of the rotor can be seen in Figure 4.

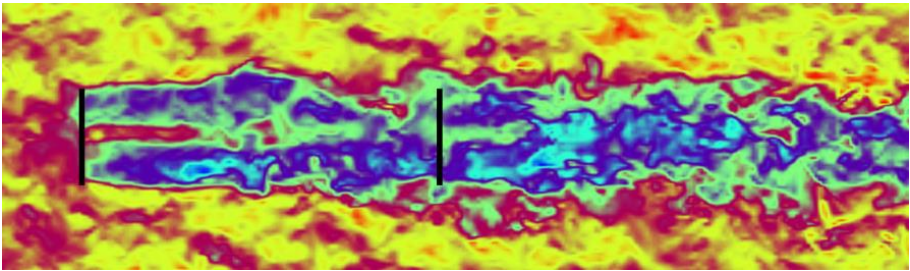
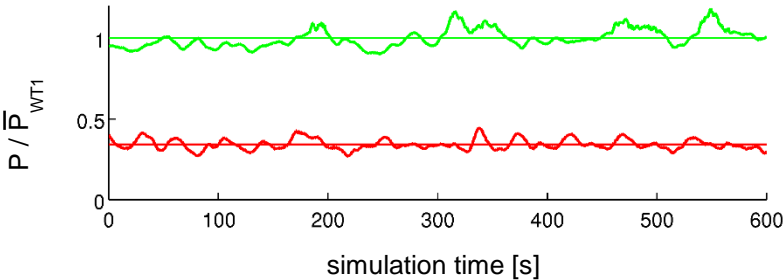


Figure 3: Instantaneous velocity deficit of two wind turbines (NREL 5MW, $U_{hub} = 10$ m/s, TI = 6.5 %, 4D turbine spacing)



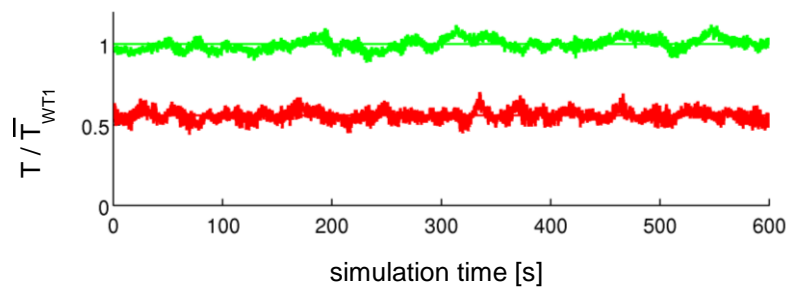


Figure 4: Power production and rotor thrust of wind turbine in free flow (green) and wake situation (red) (NREL 5MW, $u_{hub} = 10$ m/s, $TI = 6.5\%$, 4D turbine spacing)

Conclusions

A better understanding of the flow development in a wind farm and the interaction of wind turbine and flow, under various atmospheric conditions is of crucial importance for various applications in the field of wind energy.

Within the scope of the PhD research a simulation tool based on a coupling of an aeroelastic and a LES code was developed, offering high flexibility with respect to the inflow and turbine modelling. First simulation results were shown and will be further validated with measurements. Upcoming investigation will focus on the development of computationally less expensive models for capturing the wake development in wind farms which are suitable for the application in advanced control methods.

Acknowledgment

This work was partially funded by the German Federal Ministry for Economic Affairs and Energy (BMWi) in the scope of the CompactWind project (FKZ: 0325492B).

References

- [1] Dahlberg, J. Å., Medici, D., *Potential improvement of wind turbine array efficiency by active wake control (AWC)*, Proc. EWEC, 2003
- [2] Jiménez, Á., et al., *Application of a LES technique to characterize the wake deflection of a wind turbine in yaw*, Wind Energy, 2010, 13, 559-572
- [3] Corten, G.P. Schaak, P., *Heat and Flux: Increase of Wind Farm Production by Reduction of Axial Induction*, Proceedings of EWEC'03, Madrid, Spain, 2003
- [4] Jonkman, J.M., Buhl Jr, M.L., *FAST User's Guide*, Technical Report, 2005
- [5] Raasch, S., Schröter, M., *PALM - A large-eddy simulation model performing on massively parallel computers*, Meteorologische Zeitschrift, 2001, 10, 363-372
- [6] Sørensen, J.N., Shen, W.Z., *Numerical modeling of wind turbine wakes*, J. Fluids Eng.124, (2002), pp. 393–399.

UNSTEADY AND TURBULENT ROTOR LOADS

S. Ehrich¹, B. Stoevesandt², J. Peinke³

¹University of Oldenburg, Institute of Physics, ForWind, sebastian.ehrich@forwind.de

²Fraunhofer IWES, Oldenburg, bernhard.stoevesandt@iwes.fraunhofer.de

³University of Oldenburg, Institute of Physics, ForWind, peinke@uni-oldenburg.de

ABSTRACT

The content of this work is the implementation of a stochastic model for wind fields, which reproduces the important increment statistics correctly, in the Opensource Code OpenFOAM as an inflow model and LES subgrid model. The purpose of this project is the correct description and simulation of short scale fluctuations and extreme events which are interesting for load and fatigue calculations on wind turbines.

INTRODUCTION

Complex and unsteady interactions between highly turbulent atmospheric inflow and the flow over wind energy converting systems (WECS) are of crucial importance with respect to the loads on the rotor blades. The disturbed inflow leads to a strong variation of the effective inflow angle over the entire rotor blade radius. Unsteady aerodynamic effects are the reason for phase shifts between excitation and resulting loads, but those effects have not been well described by models yet.

At the present state, atmospheric wind inflow data for rotor-aerodynamic Computational Fluid Dynamic (CFD) simulations are generated with Large Eddy Simulations (LES) under a high computational cost, e.g. with the program PALM [1]. Another drawback of those wind fields are the missing intermittent statistics (fig.1) which have to be included in all simulations if one wants to consider extreme events of high wind speed fluctuations within a short time intervall which are highly important for load and fatigue calculations. In order to avoid those issues, a probabilistic model, the so called Continuous Time Random Walk (CTRW) model by Kleinhans/Friedrich [2,3], will be implemented in the Opensource Code OpenFOAM [4]. This model shall work for different meteorological conditions and wind behaviours as an inflow model. For industrial usage, an LES subgrid model will be modified in that way, such that the small scale intermittent properties will be transported through different mesh resolutions within the simulation area. LIDAR measurements are used for validation of the stochastic properties of the CTRW model, and load measurements on WECS will be compared to CFD simulated data.

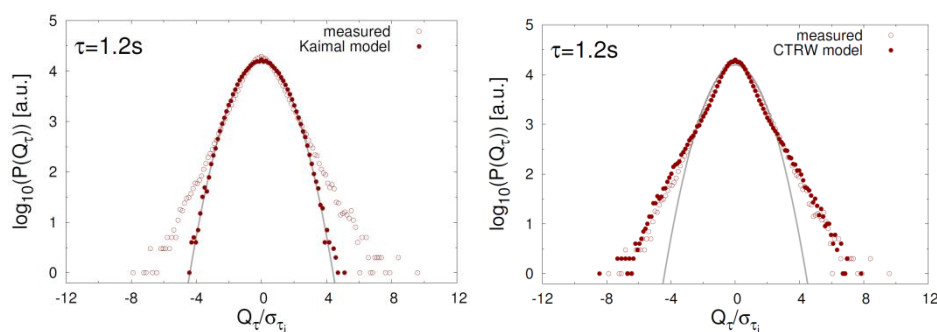


Figure 1: Torque increment statistics of the IEC Standard (Kaimal model, left) and the CTRW model (right) compared to measured data

THE MODEL

One of the basic properties of the CTRW model is the connection of a drift-diffusion process $\mathbf{u}(s)$ in the intrinsic time s to the physical time t via a time scale transformation, which guarantees spatial coherence and temporal intermittency at the same time. Because intermittency is strongly connected to anomalous diffusion and fractional processes, one can see the CTRW-model as a microscopic generator of fractional dynamics which describe the trajectories of Lagrange particles. The time transformation is done by the stochastic process

$$\frac{d}{ds}t(s) = \tau_\alpha(s)$$

where τ_α is the fully skewed α -stable Lévy distribution with stability index α . This distribution has to be fully skewed because of causality reasons, i.e. $t(s)$ has to be monotonically increasing. For generating wind fields in the physical time t , a transformation $\mathbf{u}(t) = \mathbf{u}(s = s(t))$ has to be done. About the properties and numerical procedure of this transformation the interested reader is referred to [3,4].

The model for the velocity field $\mathbf{u}(s)$ is more complex. In a two dimensional vertical plane like for a rotor plane, the velocity will be calculated at points (x_i, z_i) with $1 \leq i \leq N$ for N number of points.

For an adequate characterization of atmospheric winds the mean wind field is required, where the actual wind speeds can have a significantly deviation. Analysis of measurements from different sites substantiated the suspicion that changes are observed coherently at different measurement heights. In order to account for these changes in the wind speed, a reference wind speed u_r is introduced. u_r is modelled by means of an Ornstein–Uhlenbeck process shifted by the desired mean wind speed u_0 , defined by the stochastic differential equation

$$\frac{d}{ds}u_r(s) = -\gamma_r(u_r(s) - u_0) + \sqrt{D_r}\Gamma_r(s)$$

Γ_r is a normally distributed and delta-correlated stochastic force with zero mean, i.e. $\langle \Gamma_r(s) \rangle = 0$ and $\langle \Gamma_r(s)\Gamma_r(s') \rangle = 2\delta(s - s')$. The reference wind speed u_r is normally distributed around the mean wind speed u_0 with variance D_r/γ_r . The autocorrelation function of u_r decays while the parameter γ_r increases.

The reference wind speed u_r is now used to generate the velocity fields on the entire plane. The three wind field components u , v and w are calculated independently. As a placeholder for the individual components, the super-scripted variable k will be used. The subscripts i refer to the locations (x_i, z_i) of the grid points in the rotor plane.

Wind speeds observed in the atmospheric boundary layer depend on the measurement height z . We now assume that the mean wind speed at simulation point i at time s linearly depends on the respective reference wind speed and is given by the term

$$\langle u_i^k \rangle (s) = \xi_i^k \cdot u_r(s)$$

where ξ_i^k is determined under assumption of a logarithmic wind profile as

$$\xi_i^k = \frac{\log\left(\frac{z_i}{z_0}\right)}{\log\left(\frac{z_r}{z_0}\right)}$$

and $\xi_r^u = 1$ at hub height.

The velocities on all grid points depend on the reference wind speed, the wind speed in the past and on the neighbouring grid points. Those requirements can be fulfilled by the equation

$$\frac{d}{ds} u_i^k = -\gamma^k \left(u_i^k(s) - \xi_i^k u_r(s) \right) + \sum_j H_{ij}^k \Gamma_j^k(s) \quad \forall i$$

Γ_j^k is again a normal distributed, uncorrelated random variable with zero mean. The matrices H^k represent the correlations between the velocity fluctuations at different grid points. Here is assumed that the correlations decays exponentially with the distance between two grid points in the plane. For further details the reader is referred to [5].

GOALS AND ISSUES

The goal of this project is the implementation of the CTRW model in OpenFOAM as an inflow model in a 3 dimensional domain and the correct transport behaviour within this domain. Because the velocity components are calculated separately and independent of each other, the velocity field will not be divergence free and the Navier-Stokes equations are not fulfilled at the beginning. One of the main points will therefor be the correction of this model. An ansatz can be the transformation of the generated velocity field to Fourier space, where the spectrum is corrected in that way that the inverse Fourier transform leads to a divergence free field.

Another issue is the transport of turbulence, which normally decays after a short time in the domain. For an LES simulation the attempt will be started to induce the same amount of kinetic energy in each cell to the resolved scale which is transported to the unresolved scale.

Different meteorological conditions and wind behaviours will be tested and a validation is done by means of LIDAR measurements.

In addition to that, load measurements on WECS will be compared to CFD simulated data.

ACKNOWLEDGEMENTS

The authors would like to thank the Bundesministerium für Bildung und Forschung and the federal state government of Lower Saxony, Germany.

The simulations were performed at the HPC Cluster FLOW (Facility for Large-Scale Computations in Wind Energy Research), located at the University of Oldenburg (Germany) and funded by the Federal Ministry for the Environment, Nature Conservation and Nuclear Safety (Bundesministerium für Umwelt, Naturschutz und Reaktorsicherheit, BMU) under grant number 0325220.

REFERENCES

- [1] <http://palm.muk.uni-hannover.de>
- [2] Kleinhans D, Friedrich R. Simulation of intermittent wind fields: A new approach. DEWEK 2006 Proceedings, Bremen, Germany, 2006.
- [3] Kleinhans D. Stochastische Modellierung komplexer Systeme - Von den theoretischen Grundlagen zur Simulation atmosphärischer Windfelder. PhD Thesis, Westfälische Wilhelms-Universität Münster, 2008.
- [4] <http://www.openfoam.com>
- [5] Mücke T., Kleinhans D., Peinke J. Atmospheric turbulence and its influence on the alternating loads on wind turbines

INFLUENCE OF THE ATMOSPHERIC BOUNDARY LAYER ON WIND FARM CONTROL

L. Vollmer¹, G. Steinfeld¹, D. Heinemann¹, M. Kühn¹

¹University of Oldenburg, Institute of Physics, Energy Meteorology,
lukas.vollmer@uni-oldenburg.de

INTRODUCTION

In densely populated areas like central Europe the expansion of onshore wind energy is limited by environmental restrictions. To efficiently utilize the available space, wind turbines are usually grouped in so-called wind farms. A disadvantage of this strategy is the mutual influence of the turbines by the wakes formed as a result of the extraction of energy from the wind. Turbines exposed to the wakes experience a lower wind speed and increased turbulence and thus extract less energy and its components tend to fatigue earlier.

With the challenge to increase overall power output of wind farms on limited space, wind farm control strategies that aim on influencing wakes become more relevant. Current turbine control intends to optimize the performance of a single turbine without considering the influence the individual control has on the other turbines of the wind farm. In contrast, wind farm control strategies explicitly consider the influence on the adjacent turbines. Currently discussed wind farm control either focuses on decreasing the wake deficit behind the rotor by a reduction of the induced thrust force or on a cross-stream deflection of the wake by yawing the rotor.

Model studies and wind tunnel experiments indicate, that these strategies could increase the combined power output of wind farms by several percentages [4,5,8]. The mean characteristics and the dynamics of wind turbine wakes are however not only subject to the turbine-induced forces but show also a strong dependency on the state of the atmospheric boundary layer [2,3]. A precise knowledge of the atmospheric conditions and the wake response is thus essential to predict wind farm power production as well as structural loads on the individual turbines.

The PhD-project aims for the construction and free field implementation of a control model to increase combined power output of a wind farm by using turbine control to modify the wake behavior.

The results shown in this paper represent a part of the work, that focuses on the influence of atmospheric stability on mean parameters of the atmospheric boundary layer and on mean wake characteristics. The effect of different stabilities on the wind farm control concept of a yawed turbine is studied with a focus on the mean wake deflection.

For the study a Large-Eddy-Simulation (LES) model of the atmospheric boundary layer was used with a newly implemented turbine parametrization.

METHODS

Characteristics of the atmospheric boundary layer

A parameter to describe the stability in the atmospheric boundary layer is the Monin-Obukhov length

$$L = \frac{\Theta}{\kappa g} \frac{u_*^3}{w'\Theta'}$$

using the average potential temperature θ , the friction velocity u_* and the vertical turbulent potential heat flux $w'\Theta'$. The constants κ and g are the Kolmogorov constant and the gravitational acceleration, respectively. The Monin-Obukhov length is positive when the heat flux is positive towards the bottom, i.e. when the atmosphere is cooled by the ground. In a stable boundary layer (SBL) a positive L of the order of less than 100 m up to several hundred meter can be measured. In a convective boundary layer L is negative [9]. High Monin-Obukhov lengths of over ± 1000 m indicate a well mixed neutral boundary layer (NBL) with little stratification.

Meteorological variables considered by the IEC are among others the vertical shear α , the turbulence intensity TI and the directional shear β of the horizontal wind between different heights z_i , which all

depend on L . These variables can be obtained from horizontal wind measurements with either one (TI) or two anemometers (α, β). For a better comparison with measured data we use these three variables to characterize the boundary layer. They are defined as

$$TI = \sqrt{\frac{\sigma_u^2}{\mathbf{u}^2}}$$

$$\alpha_{z_1, z_2} = \ln\left(\frac{|\mathbf{u}_2|}{|\mathbf{u}_1|}\right) / \ln\left(\frac{z_2}{z_1}\right)$$

$$\beta_{z_1, z_2} = \beta_2 - \beta_1$$

with \mathbf{u} and σ_u^2 representing the 10 min average of the wind speed and its variance and β_i the angle between the velocity components at height z_i .

Boundary layer modeling

To model the atmospheric boundary layer the LES model PALM [10] is used. The simulations consist of a pre-run for the spin-up of a stationary boundary layer and of main runs, during which turbine models are used to simulate the extraction of energy by the rotating rotor. The simulations that will be analyzed in the following are a SBL following the set-up conditions described in [1] and a NBL capped by a strong inversion layer. A roughness length of $r_0 = 0.1 \text{ m}$ is chosen to represent onshore bottom land use. Both simulations exhibit the same hub height wind speed at 90 m height (hub height) of 8.3 m/s but differ in the other introduced variables of the wind field. The characteristics of the two boundary layers after the spin-up time are shown in tbl.1. Vertical profiles of horizontal velocities, TI and of the potential temperature θ are shown in fig.1.

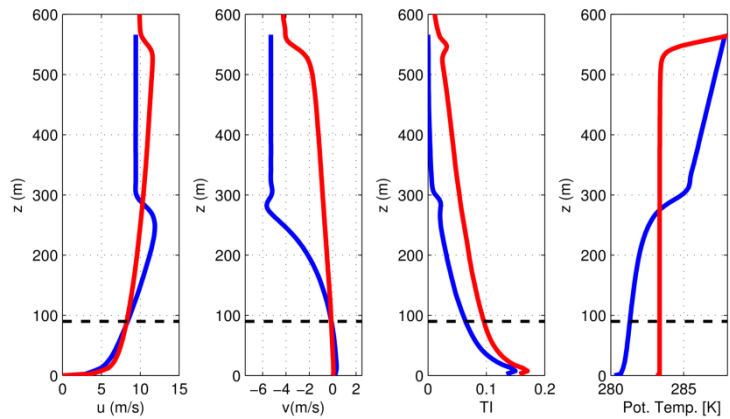


Figure 1: Average vertical profiles of the simulated atmospheric boundary layers. SBL (blue). NBL (red)

Run	T (h)	H (m)	u_{90} (m/s)	TI_{90} (%)	$\alpha_{30,150}$	$\beta_{30,150}$ (°)	L (m)
SBL	12	300	8.3	6.3	0.30	-7.5	170
NBL	18	600	8.3	9.5	0.17	-2.0	Inf

Table 1: Characteristics of the two simulated boundary layers

Wind turbine modeling

The turbine model used for the investigations is based on blade element momentum theory. Local velocities at the blade element positions are used in combination with the lift and drag coefficients of the airfoils of the turbine blade at these positions to calculate lift and drag forces.

The model calculates forces for around 40 virtual blades evenly distributed over the rotor area.

The forces are afterwards averaged over circle segments of the rotor, resulting in a representation of the rotor as a permeable disc with unevenly distributed thrust and an additional force component parallel to the sense of rotation[11]. As part of the PhD project, the model was extended by the possibility to yaw and tilt the rotor. The turbine used in the simulations is the NREL 5MW turbine [7], with a rotor diameter (D) of 126 m, a hub height of 90 m and a rated wind speed of 11.4 m/s.

RESULTS

The wind field behind a single turbine was recorded for 25 minutes for each of the boundary layers simulations and yaw angles of the turbine from -30° to 30° with steps of 10° . In addition to the yaw, the turbine is tilted by 5° as described in the default configuration of the turbine. The rotational speed of the turbine is fixed for each simulation, following the relation of hub height wind speed to rotational speed from the description of the turbine. For yawed turbines the hub height wind speed

seen by the turbine is adjusted by using the cosine function of the yaw angle. The first 5 minutes of each simulation were discarded as the wake is still developing. The mean vertical profile of the boundary layer wind speed was subtracted from the 20 min averaged velocities to receive the wake deficits. A 2D-Gaussian fit is applied on cross sections of the wake deficit downstream of the rotor.

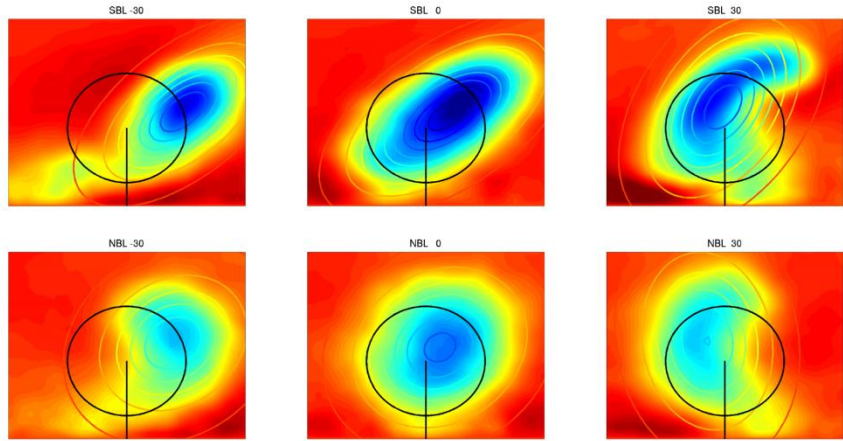


Figure 2: Wake deficit 5D downstream for different stabilities (SBL, NBL) and yaw angles (-30°,0°,30°) and fitted 2D-Gauss-functions. Black contours denote original turbine position.

The amplitude of the resulting Gaussian is considered as the mean deficit, the center position of the function is taken as the center position of the mean wake. Fig.2 shows the wake deficit at a certain distance downstream of the turbine for chosen simulations. The wake in the simulations of the stable boundary layer exhibits a strong skewness, for the NBL simulations a skewed wake can also be found when the turbine is in yaw. The downstream development of the mean deficit and of the center of the wake is shown in fig.3. The lower deficit and the faster recovery for the wake in a more turbulent environment (neutral stability) are in line with previous observations. The deficit is largest in the NBL simulations at around 1.5D while it reaches its largest values at around 2D in the SBL simulations. The deficit difference due to the different atmospheric stability is still present at the furthest considered distance of 8D. A deviation of the downstream wake center position from the mean wind direction was calculated. As the mean wind direction coincides with the x-axis of the model domain, the deviation is equal to a displacement on the y-axis. Results of the simulations are compared with an analytical description [6] for the deviation angle of the deflected wake,

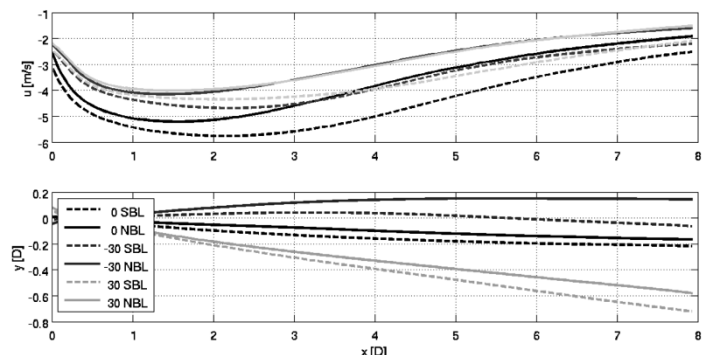


Figure 3: Wake deficit and horizontal wake center deviation from the mean wind direction for the simulations shown in fig.2.

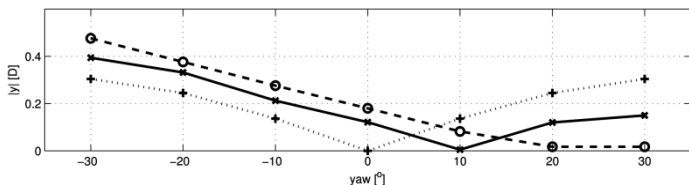


Figure 4: Horizontal deviation of the wake center from the mean wind direction at hub height at x = 5D

$$\alpha(C_T, \gamma, x) = \frac{0.5C_T \cos^2(\gamma) \sin(\gamma)}{(1 + \beta_x x)^2}$$

where C_T is the thrust coefficient of the turbine for the reference state and $\beta_x = 0.3$ a model-dependent parameter. The thrust coefficient of the reference state, which is considered for the analytic description, is $C_T = 0.8$. From the angle α the displacement on the y-axis is calculated by integrating along x. Results for the displacement from the analytic solution as well as from the simulations are shown in fig.4. The comparison shows, that the deflection of the wake differs between the two boundary layers and that it has a bias compared to the analytic approach. Furthermore the deflection is

not purely symmetric to the reference state, hinting to a dependency of the wake deflection on the sense of rotation of the rotor. An interesting result is that even in the non-yawed case the wake is reflected. This effect is strongest for the SBL with a deflection that corresponds to a yawing of 10° - 20° .

DISCUSSION & CONCLUSION

With the goal to construct a wind farm control model to increase combined power output by using individual turbine control, the presented paper shows first results from a numeric study.

To study the influence of atmospheric stability on wind field parameters and on the control strategy of wake deflection, LES simulations of wind turbines in different atmospheric boundary layers were set up. The two simulated boundary layers of stable and neutral stability have the same wind speed at hub height but differ in TI, α and β . The wake characteristics that are extracted by a fitting procedure are the maximum deficit and the center position of the wake. Both characteristics show clear dependencies on a change of atmospheric stability. In addition to widely researched results like the earlier deficit recovery in a more turbulent environment, we find some results that need more investigation.

The shear parameters for vertical shear α and for horizontal shear β seem to have a large influence on the shape of the wake and on its position. While the skewness of the wake in the SBL can possibly be largely explained by the higher directional shear β , the difference in wake deflection for the same turbine yaw angle in the two simulations must be further verified.

The observation, that the wake is already deflected for 0° yaw by a distance as large as a yaw angle of 10° (neutral) to 20° (stable) would create, underlines the claim of this work, that the atmospheric parameters have to be considered for an operation wind farm control. To further study the influence of atmospheric parameters additional LES with modified hub height wind speed and different stabilities will be conducted. In addition a validation of the LES results with measured data is planned. For this purpose nacelle-based LiDAR measurements as well as wind tunnel experiments are scheduled. A modified version of the analytic description of the wake deflection by yaw will be developed and included into one of the current simplified wind farm models.

REFERENCES

- [1] RJ Beare and MK Macvean, "Resolution sensitivity and scaling of large-eddy simulations of the stable boundary layer", *Boundary-layer meteorology*, 112 (2):257–281, 2004.
- [2] LP Chamorro and F Porté-Agel, "Effects of thermal stability and incoming boundary-layer flow characteristics on wind-turbine wakes: a wind-tunnel study", *Boundary-layer meteorology*, 136(3):515–533, 2010.
- [3] MJ Churchfield, S Lee, J Michalakes, and PJ Moriarty, "A numerical study of the effects of atmospheric and wake turbulence on wind turbine aerodynamics", *J. Turbulence*, 13:1–32, 2012.
- [4] GP Corten and P Schaak, "Heat and Flux – Increase of Wind Farm Production by Reduction of the Axial Induction", In *EWEC 2003*, 16-19 June, Madrid, Spain, 2003.
- [5] P Fleming, P Gebraad, S Lee, J van Wingerden, K Johnson, M Churchfield, J Michalakes, P Spalart, and P Moriarty, "High-fidelity simulation comparison of wake mitigation control strategies for a two-turbine case", In *Proceedings of ICOWES*, 2013.
- [6] A Jimenez, A Crespo, and E Migoya, "Application of a LES technique to characterize the wake deflection of a wind turbine in yaw", *Wind Energy*, 13:559–572, 2010.
- [7] JM Jonkman, S Butterfield, W Musial and G Scott, "Definition of a 5-MW reference wind turbine for offshore system development", *Technical Report*, February 2009.
- [8] D Medici, "Wind Turbine Wakes - Control and Vortex Shedding", *Phd thesis*, 2004.
- [9] AS Monin and AM Obukhov, "Basic laws of turbulent mixing in the surface layer of the atmosphere", *Tr. Akad. Nauk. SSSR Geophys. Inst.*, 24(151):163–187, 1954.
- [10] S Raasch and M Schröter, "PALM - A large-eddy simulation model performing on massively parallel computers", *Meteorol. Z.*, 10(5):363–372, 2001.
- [11] Y Wu and F Porté-Agel, "Large-Eddy Simulation of Wind-Turbine Wakes: Evaluation of Turbine Parametrisations", *Boundary-Layer Meteorol.*, 138:345–366, 2011.

Analysis of inflow parameters using LiDARs

A. Giyanani ¹, W.A.A.M. Bierbooms ², G.J.W. van Bussel³

¹Delft University of Technology, Wind Energy Research Group, Faculty of Aerospace Engineering, , Kluyverweg 1, 2629HS Delft, The Netherlands, a.giyanani@tudelft.nl

²Delft University of Technology, w.a.a.m.bierbooms@tudelft.nl

ABSTRACT

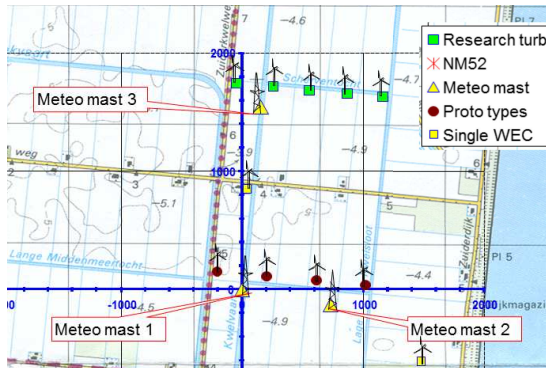
Remote sensing of the atmospheric variables with the use of LiDAR is a relatively new technique for wind resource assessment and oncoming wind prediction in wind energy. The validation of LiDAR measurements and comparisons with other sensing elements thus, is of high importance for further applications of the data. A measurement campaign with two vertical scanning pulsed LiDARs and met mast measurements was used here for comparison of inflow wind variables from LiDAR, sonic and cup anemometers. A comparison of the wind directions, wind speed and wind shear was performed to determine the validity of LiDAR measurements in wind energy applications. The LiDAR measurements correlated well with met mast measurements and a major cause for wind direction bias was found.

INTRODUCTION

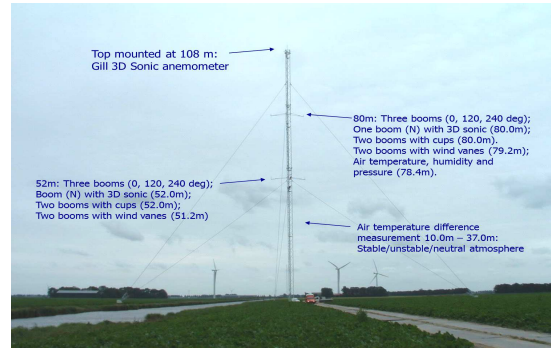
LiDAR is an acronym for light detection and ranging. LiDARs are laser based systems working on principles similar to that of Radars or SODARs. In case of LiDAR, a light pulse is emitted in the atmosphere. The light beam is scattered in all directions from molecules and particles in the atmosphere. Some portion of this light is scattered back in the direction of the LiDAR system, which is then collected by a telescope and focussed upon a photodetector that measures the amount of backscattered light as a function of distance from the LiDAR.

The LiDAR technology is continuously upgrading to provide accurate measurements and information about the atmospheric processes much higher than the present masts. By correctly analysing the wind data coming towards the wind turbine, the wind evolution towards the blade could be realised using a prediction model. Such a model when incorporated in the control system of the wind turbine can be used to adapt the wind turbine to the incoming wind conditions in real time and hence achieve load reductions and higher energy output [1]. In order to successfully develop a wind model, a study aimed at validation of the LiDAR measurements with other measurement sensors was performed. The met mast measurements from sonic and cup anemometer are compared for wind directions, wind speed correlations and shear ratio comparisons.

Within the LAWINE (Lidar Applications for Wind farm Efficiency) project initiated by ECN, The Netherlands in cooperation with XEMC Darwind, AventLidar Technology and TU Delft under the framework of Top consortium for Knowledge and Innovation Offshore Wind (TKI-WoZ), two measurement campaigns are carried out to evaluate the applications of LiDAR in wind energy. The project lays emphasis on testing and developing the LiDAR technology, wind resource and power performance assessment, optimisation of wind turbine control, load reduction and optimisation of wind farm operation [2].



(a) EWTW test site with MM3



(b) Boom heights and sensors

Figure 1: Site details of the EWTW test site

The meteorological mast 3 (MM3) at the test site (EWTW) in the Wieringemeer was considered for the study, see fig. 1(a). The test site is characterised by flat terrain, consisting of mainly agricultural farms with individual spread out farmhouses and rows of trees. The lake IJsselmeer is located at the distance of 2 km East of MM3. Around the MM3, several wind turbines are operating, a row of 5 Nordex N80 turbines in the North, the prototype turbines and a NEG Micon NM52 turbine in the South [3].

The MM3 is a lattice tower with guy wires fixed at a radius of 60m from the tower base at 60° , 180° and 300° with respect to the North. The booms are constructed in three directions namely 0° , 120° and 240° following the IEC and Measnet guidelines as shown in fig. 1(b). The sonic anemometer is installed at 0° boom at three heights 52m, 80m and 108m, the cup anemometers are installed on the 120° and 240° respectively at heights 52m and 80m, while two WindCube LiDAR systems are located at the foot of one of the guy wires i.e. 180° . The wind vanes are installed on the booms at 120° and 240° at 51.2m and 79.2m. We consider them to be the same height as the cup and sonic for this study.

COMPARISON OF LIDAR WITH OTHER SENSORS

The LiDARs at the EWTW test site are used for comparison against the metmast sensors at three heights basically namely 52m, 80m and 108m heights. The data consists of 10 min averages for 30 weeks, from 1st July 2013 to 26th January 2014 and 30240 data points in total. The cup anemometers at 120° and 240° are averaged to reduce the tower shadowing effects. Data filtering for stuck sensors, low CNR < -17 dB, availability lower than 75%, wake and tower shadows and other common filters have been applied to the respective data.

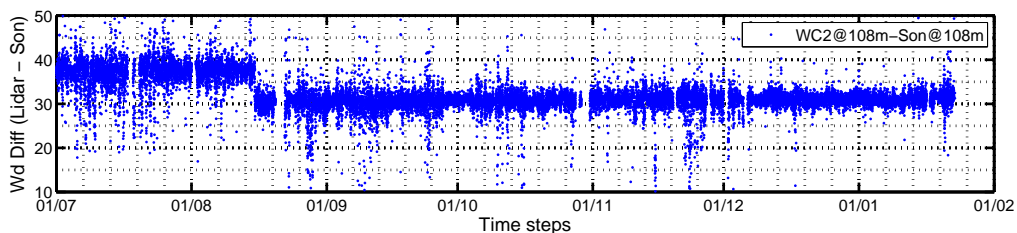
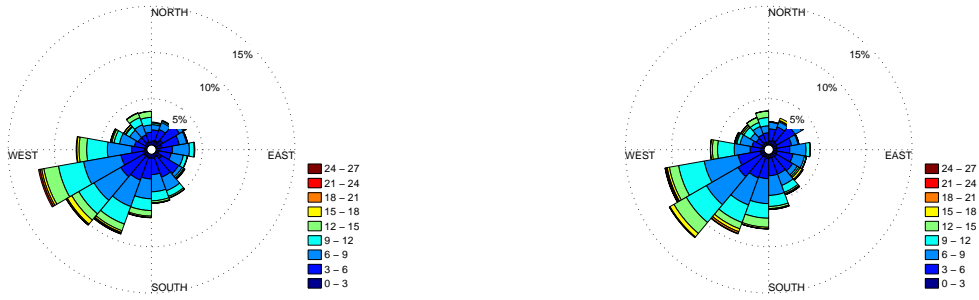


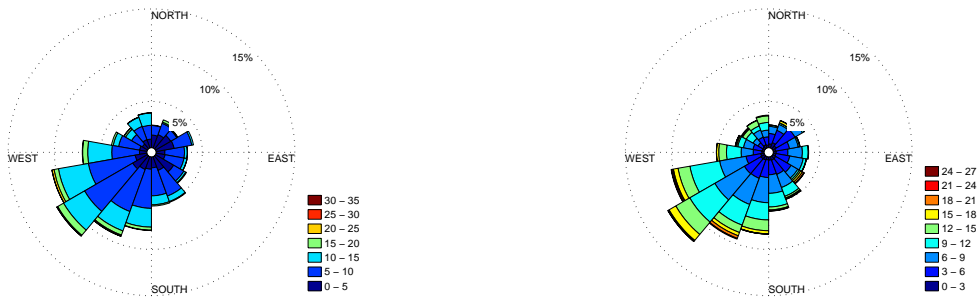
Figure 2: Effect of metal guy wires on LiDAR wind direction measurements

The comparison of wind direction between two sensors are intended to find general errors in data and to detect the wake and tower shadow sectors which can be then eliminated for the power calculations. The results for comparison of windroses between LiDAR and cup anemometer after filtering and removing error records is shown in fig. 3. A bias was observed in one of the LiDAR wind direction values which changed further once during the measurement as seen in fig. 2. The reason for such drastic change



(a) Windrose vane at 80m height after filtering (b) Windrose LiDAR at 80m height after bias correction

Figure 3: Comparison of Windroses at 80m height



(a) Windrose sonic at 108m height after filtering (b) Windrose LiDAR at 108m height after bias correction

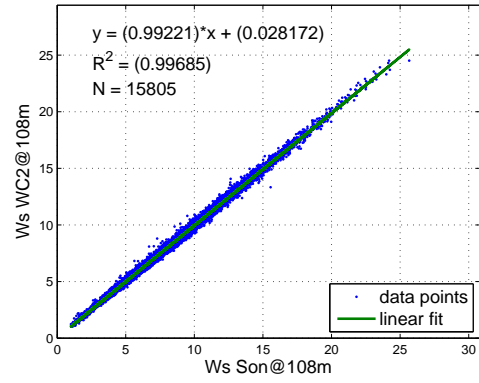
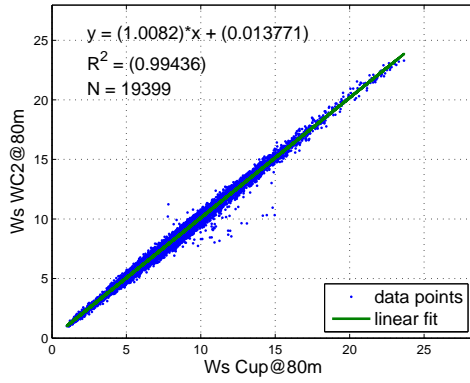
Figure 4: Comparison of Windroses at 108m height

was associated with the presence of guy wires in the vicinity and error in recalibration of the LiDAR compass. The LiDAR wind directions after bias correction correlate well with the cup anemometer wind directions. A similar correlation can be seen in the comparison with sonic anemometer at 108m height in fig. 4.

The linear regression analysis of wind speeds from LiDAR, cup and sonic anemometers are compared to check the performance of the LiDARs. The filtering due to tower and wake effects reduce the data substantially. However, as can be seen from fig. 5, the LiDAR wind speed data correlates well with wind speeds from cup and sonic anemometers.

The wind shear was compared using the wind shear ratio i.e. ratio of wind speed at higher height against the wind speed at a lower height from the same sensor. The wind shear ratio was then expressed as S_r , while h_1 and h_2 are the maximum and minimum measurement heights respectively, see eq. (1). The correlation between the shear ratio from LiDAR data and cup and sonic anemometer correlated moderately well. LiDAR data correlates better with the cup anemometers (0.8) than the sonic anemometers (0.7). Considering that the LiDAR performs volumetric averaging, it was assumed that this averaging reduced the correlation.

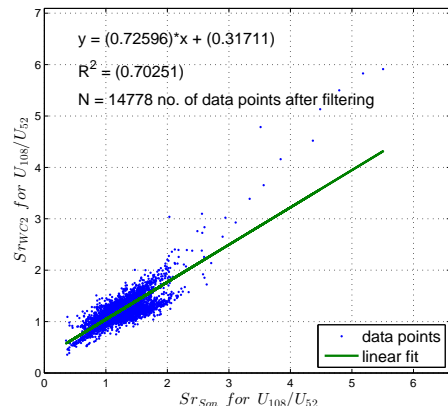
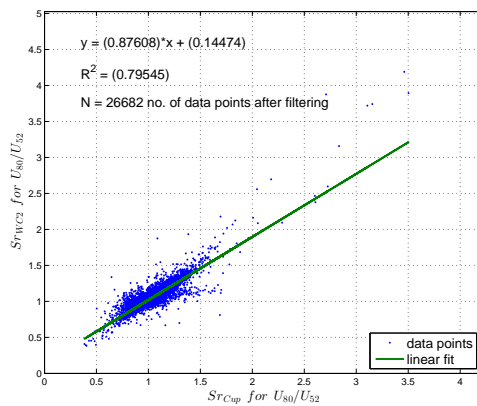
$$S_r = \frac{U_{h1}}{U_{h2}} \tag{1}$$



(a) Linear regression with LiDAR and cup anemometer

(b) Linear regression with LiDAR and sonic anemometer

Figure 5: Linear Regression of Lidars with other sensors



(a) LiDAR versus cup anemometer

(b) LiDAR versus sonic anemometer

Figure 6: Linear Regression for Shear ratios of LiDAR with other sensors

CONCLUSIONS

The LiDAR's wind direction and the wind speed measured at different heights correlated well with the other measurement sensors like the cup and sonic anemometer. The shear ratios measured at site correlated moderately well. Hence, the pulsed LiDARs prove to be a reliable measurement system and are optimal for developing wind evolution models by predicting the wind speed in flat terrain. At the EWTW test site, the wind direction self calibration was affected by presence of huge metal installations near the LiDAR. Hence, it is necessary to avoid the auto-correction of the wind directions by offsets in such cases.

REFERENCES

- [1] F. Dunne and E. Simley, "LIDAR Wind Speed Measurement Analysis and Feed-Forward Blade Pitch Control for Load Mitigation in Wind Turbines," no. October, 2011.
- [2] J. W. Wagenaar, G. Bergman, and K. Boorsma, "Measurement plan LAWINE project tasks A and C." 2013.
- [3] P. Eecen and J. P. Verhoef, "EWTW Meteorological database." 2007.

“

Wind Energy Sector Integration

”

POWER SYSTEM DYNAMIC RESPONSES – COMPARISON BETWEEN SIMPLE SIMULINK MODEL AND MORE COMPLEX TIME-STEP BASED DYNAMIC RESPONSE MODELLING

M. Argent¹, W. E. Leithead¹

¹University of Strathclyde, Doctoral Training Centre in Wind Energy Systems, Dept of Electronic and Electrical Engineering, Rm 3.36, Royal College Building, 204 George Street, Glasgow, G1 1XW, United Kingdom, michael.argent@strath.ac.uk

ABSTRACT

With an increasing proportion of energy being produced from wind turbines, potential difficulties can arise for the power system, especially maintaining the grid frequency. Conventional fossil-fuel power plants have assisted in power system stability through the mechanisms of system inertia, droop control, primary response and secondary response. Modern wind turbines tend to be asynchronous variable speed machines which are decoupled from the grid through power electronics, and therefore tend not to supply inertia to the grid. Control techniques need to be developed to allow wind turbines to provide these ancillary systems to the grid, in order for wind penetration of the power network to increase.

Simulations of power systems are modelled in various commercial software packages such as PowerFactory and PSS®E. These systems can be processor intensive and slow to compute. In addition, they are proprietary software which require licences and are not easy to link to other software. This can make modelling the effects of wind turbine control strategies, that consider the wind farm as a whole, cumbersome and difficult. A simpler power system stability model has been developed at Strathclyde in Simulink, which runs much quicker and can easily be linked with other models designed within the Matlab environment, therefore allowing for research into the effect of various wind turbine control strategies on the grid.

This project looked to validate the Simulink model against a similar model built in PSS®E; specifically by comparing the frequency response of the system after a sudden loss in generation. The Simulink model provided reasonable agreement with the PSS®E model in the simplified scenario tested, but will require testing under a wider range of scenarios before it can be fully validated.

BACKGROUND

Continued drive to reduce carbon emissions by the EU, is resulting in increasing wind generation across Europe with EWEA estimating 442 TWh of electricity generation from wind in 2020 (15% of total electricity consumption)[1]. With the increase in this alternative generation, the transmission network comes under increased stress to handle the different characteristics of these power sources.

Traditional power plants (e.g. coal, gas, nuclear), with large synchronous generators, have naturally contributed to transmission network stability through the following mechanisms. System inertia slows the rate of change of frequency when there is an imbalance between demand and generation, which allows the system operator more time to respond to a frequency event. Droop control relates to the ratio of frequency change to the change in steady-state power output [2] (e.g. a 5% droop means that a 5% frequency deviation causes a 100% change in power output [3]), while primary response involves stabilising the system to a steady-state frequency after a power event. Finally, secondary response (activating around 30 seconds after the frequency event occurs) acts to return the frequency back to its defined operational range (in the UK this is defined by National Grid as 50.0 ± 0.5 Hz [2]). One method to provide secondary response is Automatic Generation Control (AGC), which among other

tasks adjusts the reference set-point of the turbine-governor to alter the power production to help return the frequency back to operational range [3].

In order to evaluate the effect of alternative generation on the transmission network, dynamic simulation needs to be carried out as part of detailed analysis before approving increasing generation from these sources. There are commercial packages designed to investigate power system stability and this project aims to compare one of these programs to a simplified model developed in Simulink.

METHODOLOGY

This was a two-month project in which the aim was to compare the Simulink model (created by Adam Stock, University of Strathclyde) with a similar model created in a commercial power systems engineering program like PSS®E.

The Simulink model is a simplified model of a power system concentrating purely on the active power flow and the frequency response of the system. It is composed of several power station models simulating common power stations (coal, nuclear, gas, wind and hydro-electric) as shown in Figure 1.

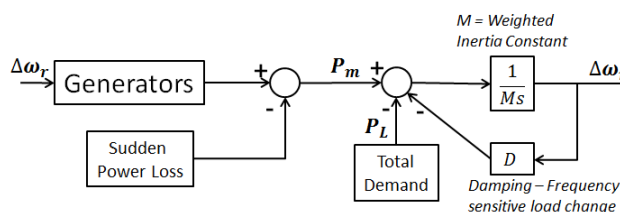


Figure 1: Top-level representation of Simulink model

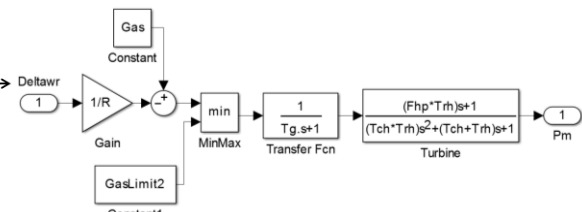


Figure 2: Simulink block diagram of gas powered steam turbine.

The synchronous generators are modelled based on a steam reheater model as described by Kundar[3] (Figure 2). The model also includes the effects of generator inertia, and the load damping of the system. The load is comprised of two components, the demand and the frequency-dependent load. The demand can be set as a time-varying function to simulate a demand increase, while the other component reacts to a change in frequency from the set-point. This is normally expressed in terms of a damping constant D which is typically around 1 to 2 percent. A value $D = 1$ (as used in this model) means that a 1% change in frequency would cause a 1% change in load [3].

In order to provide a fair comparison for the Simulink model, a similar model had to be constructed in a commercial power engineering package, PSS®E from Siemens. PSS®E deals with both active and reactive power flows, as well as analyzing the dynamic effect of transmission lines being tripped or generators failing. A simple model was created with several generators each connected by a single line connecting to a central bus with a single load. A number of built in modules (from the PSS®E Model Library [4]) were used to represent the dynamics of various components in the model. The turbine-governors were modelled using the GAST gas-turbine model, the round-rotor generators using GENROU, and the load motor was modelled using the complex load CLODBL. The models do not match up exactly to the Simulink block diagram equivalents, so a best estimate had to be made; in addition some parameters did need to be estimated due to there being no comparable value in the Simulink model.

MODEL COMPARISON

The comparative test involved a total generation of 1000MW, all from generators based on traditional steam turbines (e.g. coal, gas, nuclear), with a sudden drop in generation of 100MW after 10 seconds of operation. The effects on system frequency and power flow were then recorded and compared for both the Simulink and PSS®E models.

The frequency response of the system can be seen in Fig. 3. This shows a drop of frequency in both models of around 8% (from 50 Hz to 46Hz) at their steady state, however the Simulink model drop faster and stabilizes around 25 seconds after the generator event, compared to around 70 seconds for the PSS®E model.

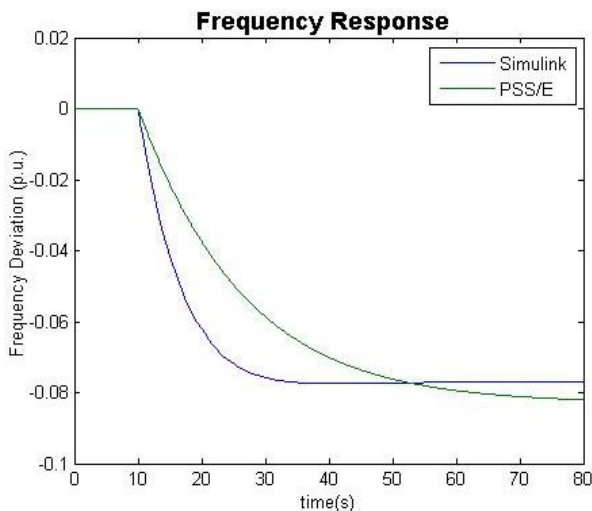


Fig. 3. Frequency Response Comparison

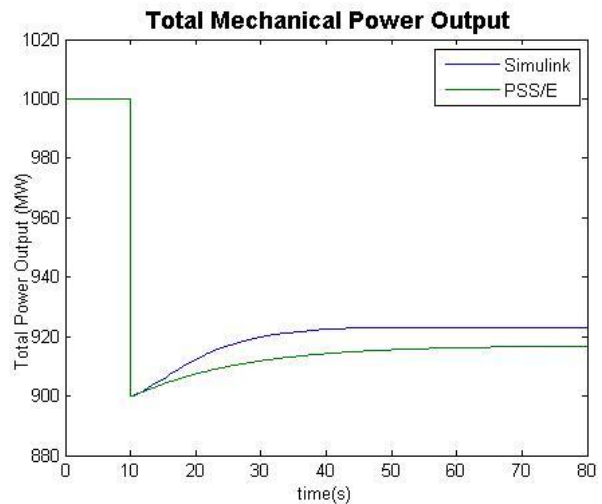


Fig. 4. Power Output comparison

The power response can be seen in Fig. 4. After the loss of 100MW it can be seen that the Simulink model recovers at a faster rate than the PSS®E model and settles to a steady state sooner as well, however neither gets close to its initial 1000MW. The faster rate of recover from the Simulink model is surprising given the more rapid decrease in frequency (Fig. 3). Both models reach a steady state mechanical output of 920MW or 92% of the initial generation; since the load damping $D=1$, that meant that the 8% drop in frequency would cause an 8% drop in load, therefore generation and load match each other and both models show a similar end result even if they reach it at different rates.

FURTHER INVESTIGATIONS

Additional tests were carried out on the Simulink model, in order to discover more about the model, but due to time constraints were not carried out on the PSS®E model.

Automatic Generation Control (AGC) was tested in Simulink demonstrating secondary response to return to the nominal frequency, but it appears that AGC would involve writing user-scripted modules in Python to be used in PSS®E[5], therefore was dropped due to lack of time and experience in Python.

The effect of increasing the proportion of wind on the system was also tested, varying the base scenario with two additional tests. For the first test, wind would make up a steady 30% of generation (assuming wind provides zero inertia). Compared with the base scenario (Fig. 3), there is a slightly steeper rate of frequency drop in this case (Fig. 5) due to the wind generation and the subsequent reduced total inertia across the network. At steady state the results were identical to the base scenario in Simulink, stabilising at 46Hz and 920MW output (8% drop in both).

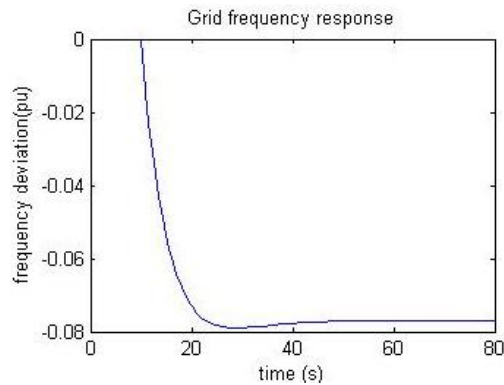


Fig. 5. Frequency Response with 30% wind (Simulink)

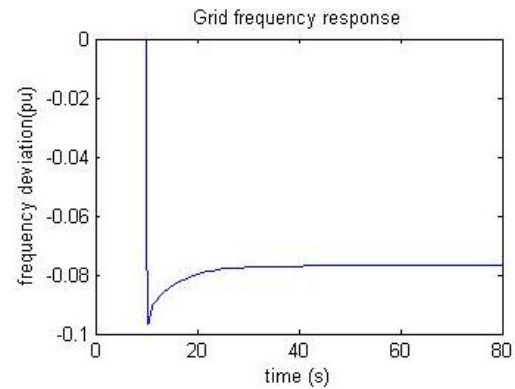


Fig. 6. Frequency response with 1% inertia (Simulink)

For the second test, the inertia was reduced to 1% of their default values. The result (see Fig. 6) is a very steep drop in frequency of 10% (to 45Hz) compared with the control test case (Fig. 3) recovering 2% (up to 46Hz) after 25 seconds. If this principle was taken to the extreme case of 100% wind generation (providing zero inertia) then a loss of 10% of generation would result in an drop of frequency of 10% (to 45Hz). Attempts to include wind turbines in the PSS®E model resulted in oscillations in the frequency and power traces and thus were removed from analysis.

CONCLUSIONS

In the short time of the project, it was not possible to completely validate the Simulink model, but the scenario tested provided a reasonably close match to the frequency response of the PSS®E simulation. In order to provide complete validation of the Simulink model, more test scenarios including AGC and renewable generators like hydroelectric and wind turbines would have to be compared. PSS®E has a graphical model builder which may be able to create block models to more closely represent the Simulink model being compared.

The deviations experienced in these tests are larger than that of a full-scale transmission network as the test network was much smaller in scale and therefore had a lot less inertia. On a large scale network it would take several power stations to go out at once to produce a 10% drop in generation.

The significantly shorter processor time of the Simulink model does potentially make it a useful tool in providing a first approximation to test potential network configurations before using packages like PSS®E to provide more detailed analysis once the number of permutations has been reduced.

ACKNOWLEDGEMENTS

The author would like to thank A. Stock for providing his Simulink power system model for analysis and for his assistance in understanding the model. In addition the author would like to thank S. Gill and R. Tumilty for their assistance with regard to setting up and understanding how to use PSS®E.

REFERENCES

- [1] European Wind Energy Association, "Wind energy scenarios for 2020," July 2014 [Online 23/07/14]: <http://www.ewea.org/fileadmin/files/library/publications/scenarios/EWEA-Wind-energy-scenarios-2020.pdf>.
- [2] National Grid Electricity Transmission plc, "The Grid Code," 1 July 2014. [Online 24/07/14]: <http://www2.nationalgrid.com/UK/Industry-information/Electricity-codes/Grid-code/The-Grid-code/>
- [3] P. Kundar, Power System Stability and Control, 1994.
- [4] Siemens PTI, "PSS®E 33.5 Model Library," 2013.
- [5] L. Wang and D. Chen, "Automatic Generation Control (AGC) Dynamic Simulation in PSS®E," *Siemens Power Technology*, no. 107, 2011.

“

Electricity conversion

”

Investigating the Effects of Pitch Control Strategy on the Power Electronics Lifetime of a Vertical Axis Wind Turbine

Rafael Dawid¹, Dr Max Parker², Peter Jamieson³, Alex Giles³.

^{1,2,3}School of Electrical and Electronic Engineering, University of Strathclyde, Glasgow, UK.

Abstract – The power converters in Vertical Axis Wind Turbines (VAWTs) have a much shorter lifetime compared to Horizontal Axis Wind Turbines, which is due to much higher cyclic torque VAWTs experience. The blades of a VAWT can be pitched at different points in the cycle to reduce the magnitude of the cyclic loading. This paper investigates how the application of various pitch regimes affects the lifetime of Insulated Gate Bipolar Transistors (IGBTs) and diodes within the power converter. Testing was done using StrathDMS (Double Multiple Streamtube model) and an IGBT module thermal model. The results show that the both C_p and converter lifetime can be maximised by using a pitch regime that maintains high torque, while the torque ripple is kept low. It was also found that the torque ripple can be reduced by operating at a slightly higher Tip Speed Ratio (TSR).

Keywords – renewables, power converter lifetime, pitch regime, Vertical Axis Wind Turbine.

I. INTRODUCTION

THE UK Wind Energy sector is growing rapidly, particularly offshore, with 1GW of capacity installed between July 2012 and June 2013 [1]. The wind turbines being installed are almost entirely Horizontal Axis Wind Turbines (HAWTs). Large scale Vertical Axis Wind Turbines (VAWTs) are not yet commercially viable; however, significant amount of research is being done on them. There is a number of reasons why VAWTs are not widely used in the industry: they have a lower Power Coefficient (C_p), longer blades for equivalent swept area and high variations in torque. However, VAWTs do have some advantages over HAWTs: they do not require a yaw system, the transmission and generator are usually placed at ground level facilitating maintenance and resulting in low centre of gravity.

VAWTs will experience much higher torque variations than HAWTs. As VAWT blade goes round its cycle, the angle of attack and the direction of the lift force change. These large torque variations in VAWTs reduce the lifetime of the power converter significantly. Power converters have the highest failure rates of all systems in a wind turbine [2], which is why increasing their operational lifetime is so important.

There are number of concepts which are aimed at minimising the torque variations in VAWTs. These include the

Gorlov's Turbine, which was shown by Gorlov himself to produce more power and less torque fluctuation than standard Darrieus rotor in a series of tests in water [3]. As the blades are helical, each part of the blade will be at a different azimuthal position of the cycle, resulting in torque averaging effect. The torque variation at the generator side can also be reduced through the application of hydraulic drive-train systems, such as the Artemis Digital Displacement Technology (DDT) [4]. In this system, liquid is pressurised by the rotor, and this high pressure liquid is then used to drive the generator, resulting in a much smoother torque profile. DDT eliminates the need for the power converter, as synchronous generator can be used. In pitch regulated VAWTs, using variable pitch regimes will affect the Angles of Attack (AOA) at each point in the cycle, hence affecting the torque profile. This paper will focus on the use of various pitch regimes in order to reduce the variation in rotor loads of VAWT, to extend the lifetime of the power electronics.

Predicting the lifetime of IGBT modules can be done using statistical, physical or empirical models. Statistical lifetime models are no longer considered accurate enough, as they do not deal well with external factors such as temperature cycling or variations in the environment; their use is often restricted to devices with the same failure mechanism [5]. Physical models utilise stress calculations, often on the smallest of components such as the bond wire, to predict the lifetime of the power electronics module. However, these models often do not depend on the cyclic loading, they also require the mode of failure to be specified before simulation [6]. The power converter model used in this research is an empirical model - it calculates the number of cycles to failure using parameters of the temperature cycle, which will in turn depend on the VAWT rotor torque.

To date, very little research was conducted on the effect of variable torque on wind turbine power electronics and their lifetime. To investigate the effect of pitch regimes on the lifetime of power electronics, StrathDMS model [7] is joined with a thermal model of IGBT modules. Simulations are then run for a variety of pitch regimes and results are analysed, with conclusions drawn on the inevitable trade-offs between performance and the lifetime of power electronics.

II. STRATHDMS MODEL

StrathDMS (Double-Multiple Streamtube model), devised by Soraghan et al. [7], is a MATLAB-based simulation, which

can be used to model VAWTs with variable pitch regimes. For the purposes of this research, Soraghan's model was updated to include correct wind shear and blade position calculation. The model considers the effect of wind shear and dynamic stall, the tip loss calculation is also included within the model. StrathDMS allows its users to specify the rotor geometry, vary wind speed and TSR, choose the airfoil geometry and pitch regime.

Once the inputs are defined, the model discretises the rotor swept area into multiple streamtubes with pre-defined angles (these streamtubes are two dimensional, in plane with the ground). In VAWTs, air crosses the actuator surface twice, with energy being extracted from the flow in the upwind part of the cycle first, then downwind. As energy is being extracted from the flow, it expands, meaning the actuator surfaces downstream will have larger areas. StrathDMS is able to estimate both intermediate and downstream induction factors by calculating blade force coefficients using flow state method and momentum theory. The induction factor is found at the point of crossover of these 2 coefficients.

This allows the downstream actuator areas to be calculated, which in turn enables blade force calculations to be carried out. The calculation described above only takes into account a single horizontal plane (parallel to the ground), it has to be repeated for the remaining planes. Forces exerted on a blade at each plane are then summed up, resulting in a total force for one each blade, allowing torques and power to be computed. The simulation can handle a variety of TSR to create C_p -TSR curve.

The results from StrathDMS model were validated against experimental data from 4 VAWTs [7] and seem to be in good agreement. The torque data generated in this model is then fed into the IGBT module thermal model, described in the following section, to calculate the effect of various pitch regimes on the lifetime of the power electronics.

III. IGBT MODULE THERMAL MODEL

Power converters utilise Pulse Width Modulation (PWM) to convert power from AC to DC and vice versa. This is often done with the use of IGBT modules, which will experience thermal cycling due to a pulsating loss caused by the alternating current at the converter terminals. Each thermal cycle will cause some damage to the IGBTs and diodes within the power converter, reducing its lifetime. Hence, a thermal model of the IGBT module is required to predict the impact of the thermal cyclic loading on the lifetime of the power converter, given the torque profile the module has to deal with.

The IGBT module thermal model [8] contains a number of subsystems - generator, IGBT module and a rainflow counting algorithm to calculate the cumulative damage of the IGBTs and diodes. The model is based in MATLAB/Simulink environment, meaning StrathDMS outputs can be easily used as inputs in this model. As the power, torque and rotor speed values from StrathDMS are fed into the model of a generator, voltage, current, power factor and frequency of the power output from the generator are calculated. These are then used to calculate the appropriate duty cycle, which is input into the

IGBT model. Given the coolant temperature and DC voltage, the device temperatures and losses are computed. This data is then fed to the rainflow counting algorithm, which calculates the cumulative damage caused by thermal cycling, in turn allowing to calculate the lifetime of the IGBTs and diodes within the power converter.

IV. TESTING PROCEDURE

Once the 2 models have been integrated, so that the output of StrathDMS was compatible with the input of the IGBT module thermal model, the pitch regime tests were conducted. Overall, 26 pitch regimes were devised, ranging from constant and sinusoidal pitch, to variable regimes. It is important to point out that the actuators will have a limited maximum speed of pitching, which was assumed to be 10° per second [9].

The wind speed chosen for the tests was 10m/s. Although the power electronics suffer the most in above rated conditions, in a variable pitch VAWT, power limiting would take place, most likely by pitching the blades so that AOA tends to 0° at all points in the cycle. This would interfere with the pitch regime testing, so below rated wind speed was used. The tests were conducted for an H-rotor, 3 bladed VAWT with a radius of 18.75m and blade length of 50m in StrathDMS.

V. RESULTS

The TSRs chosen for the tests were 3, 3.5 and 4 respectively, as most pitch regimes will have maximum C_p around these values. At low TSR, AOA tends to vary more along the azimuthal position, which can often lead to both static and dynamic stall in some parts of the cycle. Figure 1 shows the Rotor Torque values along the azimuthal position, with no pitch regime applied (0° pitch all around). The azimuthal position is measured from the centreline downstream (0°), counter-clockwise.

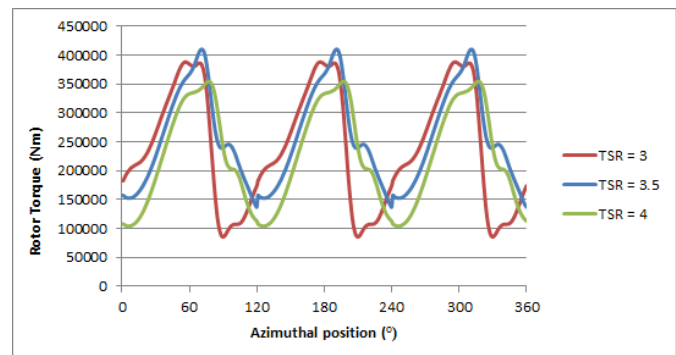


Fig. 1: Rotor torque along the azimuthal position for different TSRs.

The sudden drops in torque occurring at TSR equal to 3 are due to the aforementioned rapid changes in AOA and are highly undesirable when considering power electronics lifetime. Rapid changes in torque at TSR equal to 3 can be seen in almost all pitch regimes, hence the power electronics lifetimes were only calculated for TSRs of 3.5 and 4.

Figure 2 shows the C_p values and Diode Lifetimes for various pitch regimes, with all the tests being conducted at

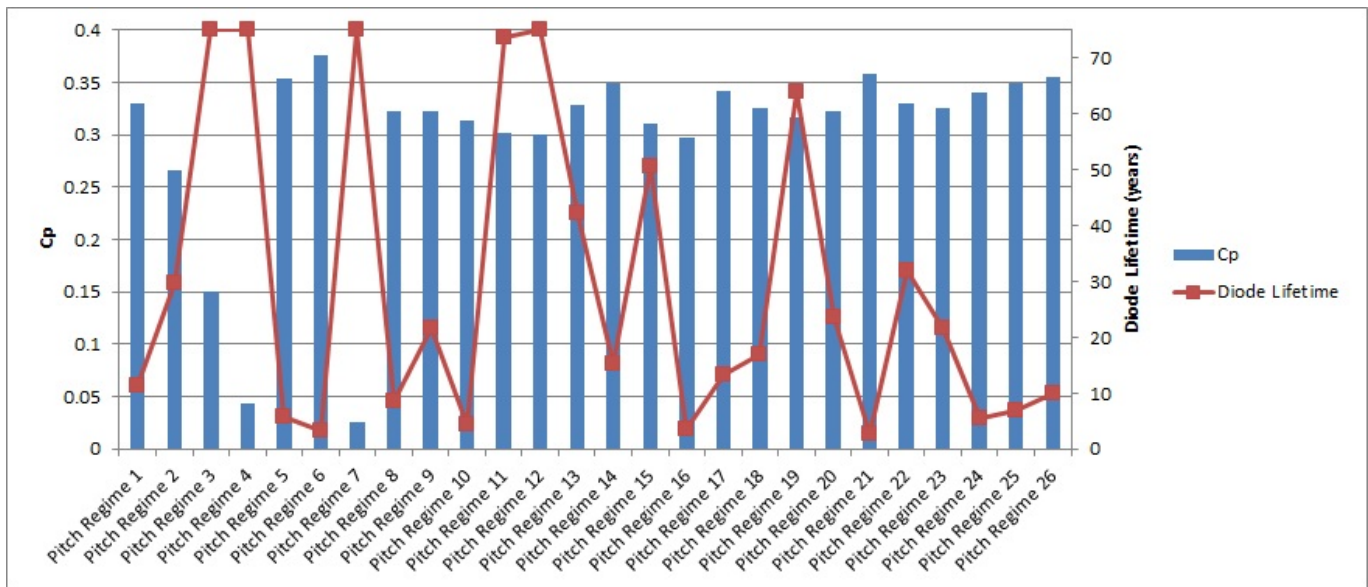


Fig. 2: Cp and Diode Lifetime for TSR=4

TSR equal to 4 (Note: some of the Diode Lifetimes were higher than 70 but were limited for easier viewing of the graph). In general, it was noted that the Cp values remained similar at TSRs equal to 3.5 and 4, while the diode lifetime was higher for the latter value of TSR. Power, and TSR can be simply expressed as:

$$P = T\omega; \quad TSR = \frac{\omega R}{U} \quad (1)$$

where P is power, T is torque, ω is the rotational speed of the turbine, R is the radius of the turbine and U is the undisturbed incoming wind speed. As throughout the tests, TSR was varied by changing the rotational speed of the turbine, higher TSR will require a lesser torque to generate the same power, and lower torques increase the operational lifetime of the power electronics.

As shown in Figure 2, there are a few cases where the Cp is very low but the diode lifetime is high (i.e. Pitch Regimes 3, 4 and 7). This is due to the fact that rotor torques are well below rated, putting little strain on the IGBT module. The opposite is also true for some pitch regimes, i.e. 6 and 21, whereby the range of rotor torques is very high, resulting in a very short power electronics lifetime.

It is important to understand what makes some pitch regime perform better than others, both in terms of Cp and diode lifetime. As shown in Figure 2, Pitch regimes 14 and 25 have a very similar Cp (0.35 and 0.349 respectively), but different diode lifetime (15.1 years and 6.8 years respectively). To understand what causes the difference, a closer look at the rotor torques produced by each pitch regime is required, which is shown in Figure 3. It can be seen that the range of torques for pitch regime 25 is higher than pitch regime 14; it is this high torque range that reduces the diode lifetime. However, the Cp values of both pitch regimes are very close, as although pitch regime 25 has a higher maximum torque, the blue line of pitch regime 14 is above the orange line in the regions near 0,

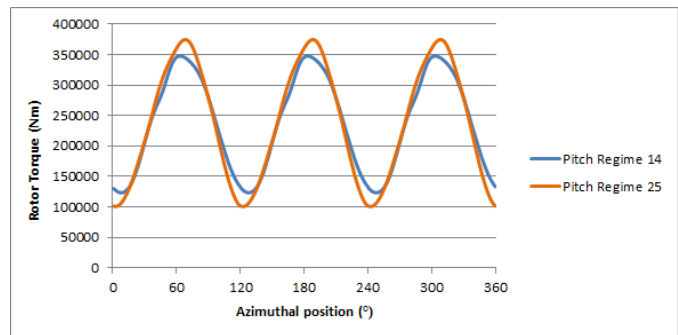


Fig. 3: Rotor torque along the azimuthal position for pitch regimes with similar Cp.

120 and 240°, compensating for the lower maximum torque. Hence, it can be concluded that to increase both the Cp and diode lifetime, the desired shape of the rotor torque would be a sinusoidal wave with a small amplitude but high mean value.

Pitch regimes change the effective AOA of the blades at each point in the cycle. For the best performance, the magnitude of AOA should always be around 10° - high enough to produce a very good Lift to Drag ratio, but still well below the stall angle (the airfoil used in this research was NACA0012, with a stall angle, depending on Reynold's Number, of between 12-16°). However, maintaining AOA magnitude of 10° is not possible, as there are physical limits on the actuators and the AOA changes sign twice along the azimuth.

TABLE I: Pitch regime characteristics

	Characteristic	Cp	Diode life (years)
Pitch Regime 1	No pitch (baseline)	0.33	11.4
Pitch Regime 6	High Cp short life	0.38	3.3
Pitch Regime 12	Low Cp long life	0.3	124
Pitch Regime 16	Low Cp short life	0.3	3.4
Pitch Regime 26	High Cp long life	0.36	10

Table 1 shows 5 pitch regimes with different characteristics, which will be used to illustrate the effect of AOA on the given pitch regime's performance, as shown in Figure 4.

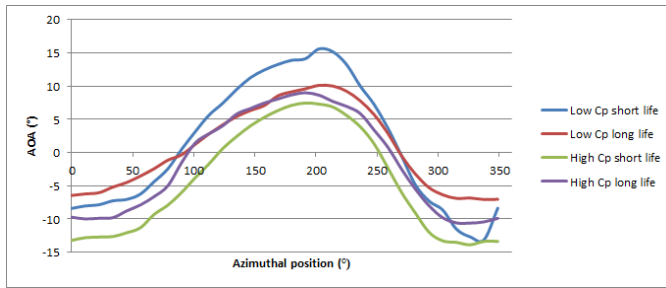


Fig. 4: Angle of Attack along the azimuthal position for different pitch regimes.

Pitch Regime 12 is characterised by low AOA (approx. -6°), in the downstream part of the cycle ($0-90^\circ$ and $270-360^\circ$), resulting in low torque variations, hence low Cp but long lifetime.

Pitch Regime 16 had low Cp and short diode lifetime. The reason for this is shown in Figure 4: the AOA reaches very high values ($>15^\circ$), most likely resulting in stall, which reduces the Cp and shortens the lifetime of power electronics.

Pitch Regime 26 manages to achieve high Cp by maintaining a relatively steady AOA of approx 10° downstream, without exceeding AOA of 10° in the upstream part, which limits the maximum torque, allowing to achieve a relatively long lifetime, compared to other pitch regimes at similar Cp.

Pitch Regime 6 reaches a high Cp value, which could be due to a large downstream AOA (approx. 13°), just bordering on stall. The diode lifetime for this regime is short, as the torques produced downstream contribute significantly to the maximum torque on a blade, resulting in a rotor torque with large variations.

Based on the results presented so far, pitch regime 26 seems to display the best balance between performance and power electronics component lifetime.

A. IGBT Thermal Model Results

As mentioned previously, the diode lifetime was the key factor determining the overall lifetime of the power converter, as IGBT lifetime was significantly higher than diode for all pitch regimes.

Figure 6 shows the diode temperature vs time graph. The high frequency variation is simply due to the current going through the diode, which fluctuates at the switching frequency (50Hz). The ripple is much more pronounced at higher temperatures, as the mean current transferred through the diode is higher. The lower frequency sinusoidal variation is due to the rotor torque fluctuation. Both high and low frequency fluctuations will contribute to the damage of the diode.

Depending on the voltage rating, the operational temperatures of current IGBT modules are limited to $125-150^\circ\text{C}$ [10]. The diode and IGBT temperatures have been recorded for all the tests and all remained well within these limits.

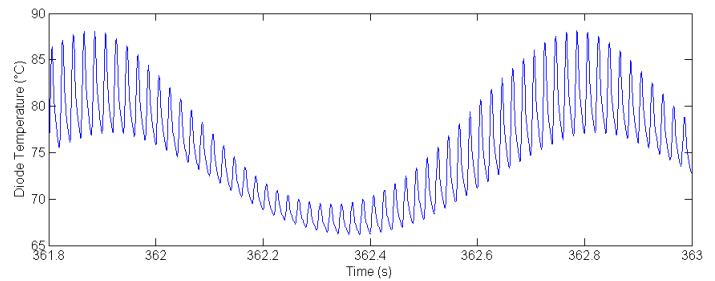


Fig. 5: Diode temperature over time.

VI. CONCLUSION

The tests of 26 different pitch regimes shed some light on the reasons why some regimes perform better than others. For example, a pitch regime that ensures AOA is below 10° at all points in the cycle will avoid stall and large lift and drag forces, hence will have a very long power electronics lifetime, but low Cp. On the other hand, a pitch regime which results in AOA of $12-13^\circ$ (bordering on stall) in some parts of the cycle can result in a higher Cp but short power electronics lifetime due to high torque ripple. The key to designing the right pitch regime for a given turbine is maintaining approximately 10° in the downstream part of the cycle, while having slightly lower AOA upstream, as the upstream plays an important part in determining the peak magnitude of torque, which is an important parameter when determining the power electronics lifetime. Reducing the magnitude of torque ripple is also important from the structural point of view: as cyclic loading decreases, the lifetime of the structure increases. It was also found that it is beneficial for the lifetime of power electronics to run VAWTs at higher TSR (preferably $\text{TSR}=4$), as in many cases it allows to achieve comparable Cp's with a torque ripple of smaller magnitude.

REFERENCES

- [1] Department of Energy and Climate Change, *UK Renewable Energy Roadmap Update 2013*. 2013.
- [2] Wilkinson, Harman, Hendriks, *Measuring Wind Turbine Reliability - Results of the Reliawind Project*. GL Garrad Hassan 2011.
- [3] A. Gorlov, *Development of the helical reaction hydraulic turbine*. The US Department of Energy, 1998.
- [4] Sasaki, Yuge, Hayashi, Nishino, Uschida, Noguchi, *Large Capacity Hydrostatic Transmission with Variable Displacement*. Elsevier, 2014.
- [5] Bluder, Waukmann, *Bayesian Lifetime Modeling for Power Semiconductor Devices*. WCEC, 2009.
- [6] Busca, *Modeling Lifetime of High Power IGBTs in Wind Power Applications An overview*. IEEE, 2011.
- [7] Soraghan, *Aerodynamic Modelling and Control of Vertical Axis Wind Turbines*. CDT in Wind Energy Systems, University of Strathclyde, 2014.
- [8] Givaki, Parker, Jamieson, *Estimation of the power electronic converter lifetime in fully rated converter wind turbine for onshore and offshore wind farms*. IEEE, 2014.
- [9] Troester, *Constant Speed Wind Turbines on a Grid with Variable Frequency - A Comparison in Terms of Energy Capture*. 7th International Workshop on Large-Scale Integration of Wind Power into Power Systems, 2008.
- [10] Schlapbach, Rahimov, von Arx, Mukhitdinov, Linder, *1200V IGBTs operating at 200°C ? An investigation on the potentials and the design constraints*. IEEE, 2007.

Vertical Axis Wind Turbine Hydraulic Drivetrain Options

Euan MacMahon¹, Dr Alasdair McDonald¹.

¹School of Electronic and Electrical Engineering, University of Strathclyde, Glasgow, UK.

Abstract – The aim of the project is to consider design options for vertical axis turbines with hydraulic drivetrains. Many companies are looking at the possibility of using vertical axis wind turbines offshore with several drivetrain options being considered [1]. One of which is using hydraulic pumps connected with pipes to a hydraulic motor which is then connected to a generator. Vertax is one such company that has designed an offshore vertical axis turbine [2]. It is used as a case study to analyse the effect of using hydraulics. Specifically an evaluation of the mass and efficiency of the hydraulic system is compared to that of a permanent magnet generator. Consideration is also given to the height at which the motor and generator is placed in the tower. The effect on the centre of mass, availability and efficiency is analysed.

Keywords – hydraulic drivetrain, vertical axis.

I. INTRODUCTION

AS wind turbines move offshore an increased emphasis is being placed on reliability of the turbines. It is for this reason that alternative drivetrains are being considered. With a conventional gearbox, generator and power conversion set up there are many areas where a fault may occur [16]. With offshore turbines moving to deeper waters and many floating turbine designs being considered, lowering the centre of mass will be beneficial. Not only will the turbine be more balanced due to the reduction in overturning moment but cost will also be reduced for the floating foundation.

Hydraulic drivetrains are being considered as a solution to these problems. A basic hydraulic transmission system proposed for a HAWT consists of a hydraulic pump which converts rotational energy of the rotor into pressure in the fluid. The fluid is transferred through pipes to the hydraulic motor which works as a pump in reverse. The rotational speed of the output shaft connected to the generator is able to be controlled over a range of wind speeds. In effect it replaces the gearbox and ensures constant rotational speed at the generator. This means that a synchronous generator may be used and so there is no need for power conversion. With no gearbox and no power conversion the reliability is increased resulting in greater availability [3]. By placing the motor and generator at the bottom of the turbine the distribution of mass will be moved further down the turbine. However hydraulics have traditionally been dismissed due to their low efficiency at partial loads.

Vertax are one company considering the benefits of using a hydraulic drivetrain as opposed to their direct drive permanent magnet design. A design for the hydraulic transmission for this vertical axis machine will be proposed with the mass distribution and efficiency analysed and compared with that of the original direct drive system.

II. VERTAX DESIGN

Vertax Wind Ltd provide the case study used for assessing the use of hydraulic drive trains in vertical axis machines. Their proposal is for an “h-type” offshore vertical axis turbine initially conceived to have three blades, as seen in figure 1, but is now considering two blades. There are proposals for both a 4MW and 10MW turbine however this paper will focus on the 10MW version.

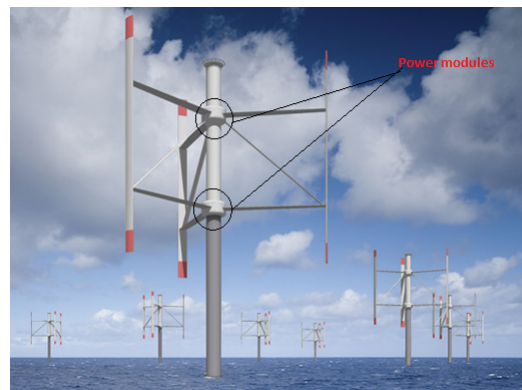


Fig. 1: Vertax Turbine Proposal [5]

The current design of the turbine is to have two direct drive 5MW permanent magnet generators located at the connection between the rotor arms and the tower. The generators themselves are inverted with the stator connected to the tower and the rotor directly driven by the support structure of the blades.

III. BASIC EQUATIONS AND PART LOAD EFFICIENCIES

Figure 2 is a basic diagram for a positive displacement pump attached to a rotating shaft. From this, basic equations can be set down and an explanation for the low part load efficiency can be given.

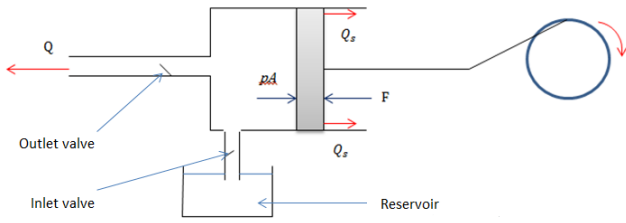


Fig. 2: Illustration of single piston

The power is given in equation 1.

$$P = pQ = T\omega \quad (1)$$

p is the pressure, T is torque and ω is the rotational speed with units of rad/s . Q is the rate of flow of the liquid given by equation 2.

$$Q = Av \quad (2)$$

A is the area and v is the velocity of the fluid. If we have the displacement of the piston D in units of m^3/rev and the rotational speed n in units of rev/s we then have an alternative expression for the rate of flow given in equation 3.

$$Q = Dn \quad (3)$$

This represents an ideal situation. For practical applications not all of the flow will be transferred to the output as some of the liquid will leak through the sides of the piston [6]. This is known as slip and along with frictional forces in the piston and compression of the liquid cause losses and therefore a decrease in efficiency.

At part loads the efficiency decreases for a traditional variable displacement system. If the power was halved for example and the pressure is held constant the displacement must be halved also. It is shown that efficiency decreases for non-maximum displacement [7]. Leakage is primarily dependent on pressure and can be simplified to be directly proportional to pressure for most cases [8]. If the displacement has decreased the ideal flow must also decrease. However as the leakage is constant and so the efficiency will decrease. A similar argument can be made for a change in speed of the system.

In order to overcome the problem of part load efficiencies mechanical valves have been replaced by computer operated solenoid valves. Artemis Intelligent Power operates this system naming it Digital Displacement. The process by which the part load efficiencies are improved is by idling. This means that the low pressure valve is kept open. The low pressure fluid is drawn in and pushed out of the pistons doing no useful work. Relatively little energy is lost in this state and so at low power only a certain proportion of the pistons are operating. This ensures that if the pistons are operating, they are close to or at full capacity and so are operating efficiently.

IV. HYDRAULIC DESIGN AND ANALYSIS

The 7MW Mitsubishi Sea Angel which uses the Artemis technology [11] is currently in testing. However with the

technology not being widely available a traditional set up is proposed. Aachen University has set up a 1MW test bench intended to replicate a horizontal axis turbine [12]. It was found that two pumps provided the highest efficiency across the range of loads. The pumps are arranged so that if the turbine were operating at rated power, 80% of the power would come from one pump and 20% from the secondary pump. Two generators are used at the electrical side of the transmission. At low wind speeds only one generator is operational. The generators will be synchronous as both the pumps and motors are variable displacement machines.

In order to apply hydraulic transmission to the Vertax machine four pumps are needed. Two at each rotor arm connection. An accumulator as well as multiple motors are placed in the lower part of the turbine. Four generator are used initially to enable simplified modelling of the efficiency. To find the mass of these components a scaling process is done from existing technology covered in the next section. A schematic diagram can be seen in figure 3.

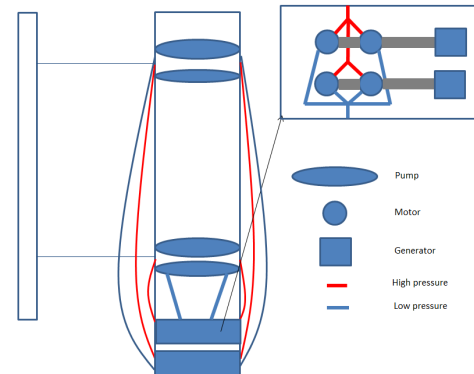


Fig. 3: Schematic of proposed hydraulic transmission

A. Torque Ripple and Mass of Pumps

In order to predict the masses of the components of the turbine an accurate representation of the mechanical torque is needed. A small scale estimation of the torque curve is provided by Vertax for a three bladed turbine. The torque ripple is modified to two peaks 180 degrees apart to represent a two bladed machine with the blades at opposite sides. The summation of these torque curves gave the torque for the whole rotor.

In order to scale to a 10MW machine at rated speed the average value of the torque is found. Assuming that the turbine has an average rotational speed of 6rpm then, using equation 1, average torque needed to achieve 10MW is found. This value is then divided by the small scale average torque to find a multiplying factor. Every value on the torque ripple curve is then multiplied by this factor. Degrees are also changed to time using the rotational speed. The results are shown in figure 4.

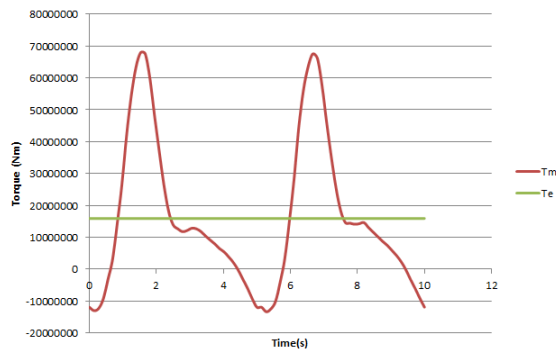


Fig. 4: Full Scale Torque Ripple Curve

Using these torque values the size of pump needed can be calculated. Using equation 1, 3 and 4, equation 5 for the displacement of the pump is found.

$$\omega = 2\pi n \quad (4)$$

$$D_p = \frac{2\pi T_p}{p} \quad (5)$$

D_p and T_p represents the displacement of the pump and the torque experienced by the pump respectively. To estimate the displacement the maximum pressure of the pump is taken to occur at the point where the torque is at a maximum. The maximum pressure is taken from Hägglunds radial piston motors [13]. The masses of both pumps and motors are modelled to be the same, as a motor can be considered to be a pump in reverse. The maximum pressure for every motor is 35Mpa and so is independent of size. This value is taken along with the peak mechanical torque. A displacement of $12.19m^3$ is needed resulting in two large pumps with displacement of $4.88m^3$ and two small pumps of displacement of $1.22m^3$.

The CBP 840 has a displacement of $0.058m^3$ and a mass of 2170kg. The radius is 0.4m and the length is 1.154m giving a volume of $0.58m^3$ assuming the pump to be cylindrical. The volume of the pumps is found by assuming that the ratio of the displacement to the volume of the pump is constant across all sizes. The displacement volume ratio is multiplied by the displacements calculated previously to obtain a volume of $53.58m^3$ and $13.39m^3$ for the large and the small pump respectively. The density of the CBP 840 is then found and assumed to be constant across all sizes. This gives a mass of 200424.7kg and 50106.2kg. It is worth noting that the scaling process is taken from a standard pump, the scaled up version of the pump would be inverted similar to the permanent magnet case. The volume of the pump would be wrapped around the tower.

This mass is actually double that of the original permanent magnet generators and so no reduction in mass occurs. An alternative method would be to have many small CBP 840 pumps in order to achieve the displacement of $12.19m^3$. However this results in four times the mass of the generators. It may be that a reduction in top head mass is possible with specific design of a large scale motor. This assumption will be taken when calculating the centre of mass in section V.

B. Mass of Motors

To find the mass of the motors the displacement first needs to be calculated. Noting that the flow at the pump must be the same as the flow at the motors equation 3 is used to find equation 6.

$$D_m = \frac{D_p n_p}{n_m} \quad (6)$$

n_m is found using equation 7 assuming that the generator has six poles and grid frequency is taken to be 50Hz. n_p is taken to be 6rpm.

$$n_m = \frac{2f}{p_f} \quad (7)$$

A total displacement of $0.073m^3$ is needed which will be separated eight motors, as seen in figure 3, with four connected to the upper pumps and four connected to the lower pumps. The four pumps will be connected to two generators which will result in a total of four generators of 2.5MW each. The percentage of displacement of the four motors will be 14.0%, 19.5%, 27.6% and 38.9% [12]. Using the same method for finding the mass as that used for the pumps results in motors of mass 210.6kg, 292.45kg, 415.3kg and 584.9kg. This gives a total mass of 3006.4kg for all eight motors. All the motors will be located at the bottom of the tower connected to the pumps through pipes.

C. Mass of Generators

The mass of the 2.5MW generators are calculated from scaling down from a 3MW generator by keeping the stress and radius to length ratio constant. All of the mass of the generator is considered to be in a cylinder. The values for the 3MW turbine are found from [14]. The mass 2.5MW turbine is found to be 5.24 tonnes.

D. Mass of Accumulator

An accumulator is added to this system to cope with the great changes in torque. It stores and releases energy and keeps the pressure constant. A piston accumulator is modelled for the system. The mass of the accumulator is calculated by finding the change in speed of the rotor due to the fluctuations in mechanical torque. Equation 8 is used to find the rotor speed through a cycle.

$$T_m - T_e = J \frac{d\omega}{dt} \quad (8)$$

The mechanical torque, T_m , is taken from figure 4. The electrical torque is assumed to be constant reflecting that the power demand is constant. It is the theoretical reaction torque experienced by the pump rather than any electrical torque of the generators. The value for the inertia is given by Vertax is $98343000kgm^2$.

By combining equation 3 and equation 9 and subtracting the average rate of flow the extra volume needed in a cycle is calculated.

$$Q = \frac{dV}{dT} \quad (9)$$

The extra volume needed in a cycle is $0.75m^3$ and so the mass of the accumulator is estimated. The accumulator is essentially a cylinder with the volume assumed to be double the volume just calculated. This would mean the piston reaches halfway up the cylinder at full displacement but has the potential to rise further if for example a large gust of wind occurred. This gives a total volume of $1.5m^3$. With a thickness of 0.1m and using stainless steel of density $8000kgm^{-3}$ the mass of the accumulator is 4353.5kg. Assuming that the density of hydraulic oil is $920kg/m^3$ the mass of fluid in the accumulator is 690kg.

V. CENTRE OF MASS

The calculated masses of the pumps, motors, generators and accumulators are placed in the tower at specific heights. A large and small pump replace the permanent magnet generators at the rotor arm connections and the motors, generators and accumulator are placed in the lowest section of the tower. The mass of the pipes is added afterwards with four pipes of radius of 0.1m used. Two pipes are connected to the first set of pumps and two pipes connect to the second set of pumps at the top of the tower. The same hydraulic oil is used as before. The bottom of the tower is taken to be sea level.

Centre of mass can be calculated given the position and the mass of each component is known for the original permanent magnet set up and the new hydraulic set up. As the methods used to calculate the mass of the pumps actually returned a greater value the effect of moving mass down from the top of the turbine is investigated. This would represent a hydraulic system which has been a specifically designed for vertical axis turbine. 10% to 50% of the mass of the generator is taken away and placed at the bottom of the turbine. The change to the centre of mass of the turbine can be seen in figure 5.

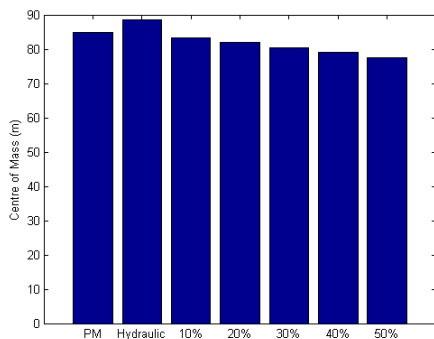


Fig. 5: Centre of Mass for different mass distributions

VI. EFFICIENCY, AVAILABILITY AND ENERGY

The efficiency at each wind speed for the two pump, four motor and two generator set up is taken from the test bench analysis[12]. As the pressure is kept low by choosing the right displacement the efficiency curve is applied to the scaled up Vertax system.

A comparison is now done to compare the annual energy capture of the different transmission assemblies. A power

curve is supplied by Vertax for the 10 MW turbine. The turbulence intensity is taken to be 0.16 [20], a Weibull distribution is used with the shape and scale parameters of 2 and 11.06 and the average wind speed is taken to be 9.8 m/s.

A value of 32615425kWh/year is found for the hydraulic set up. The permanent magnet direct drive set up has a different efficiency curve. Efficiency is measured against the percent of rated power for a 1.5MW machine [21]. The corresponding wind speed for each power percentage is found from the power curve. The values are interpolated so that an efficiency curve against wind speed is achieved. This is then multiplied by an efficiency curve for the power converter [22]. The annual energy is found using the same process as before with availability set to 93.22% [3] and is found to be 33193554kWh.

If the Artemis style hydraulic set up is able to maintain constant efficiency at partial loads the annual energy yield is increased. Using a constant value of 90% across all wind speeds a value of 34454607kWh is achieved.

VII. DISCUSSION

Significant advantages could be reached if a specifically designed pump for a vertical axis turbine of 10MW scale were designed altering the mass distribution of the turbine. Specifically a design which operates at increased pressures would reduce the mass of the components. Looking at equation 5, doubling the pressure would result in half the displacement and potentially half the volume. This would significantly reduce the mass although the thickness of the pump walls would have to be increased. However with increased pressure the slip will also increase causing a decrease in efficiency. With a design capable of moving mass further down the turbine, considerable benefits could be reached in terms of both dynamics and cost. Figure 5 shows that the centre of mass can be lowered substantially making the turbine more stable. Costs will be reduced for not only on the floating foundation but with many of the components easily accessible when lower down maintenance costs may be reduced for the turbine. It is worth noting though that as the hydraulic system acts as a gearbox the displacement of the pump must be greater than that of the motor. This means the volume of the pump will be greater than the volume of the motor resulting in larger masses at the top of the turbine. Advantages are also seen in that accumulators are able to mechanically deal with large variations in torque and the larger availability due to many of the components being modular and no gearbox or converter failures is also beneficial.

Hydraulic drivetrains remain a viable option for vertical axis turbines if an acceptable level of efficiency is reached. For a traditional set up, even if the an arrangement of pumps, motors and generators is such that efficiency is maximised, the energy capture is too low at partial loads. This seen in section VI where the annual energy capture of the hydraulic transmission is about 578MWh less than the permanent magnet system. Potentially if an easily adaptable or custom built Artemis style system is designed for a VAWT, hydraulic transmission would become a realistic option.

REFERENCES

- [1] C. Warnock, A. McDonald, *Vertical Axis Wind Turbine Drivetrain Options*, Wind Energy Systems DTC, University of Strathclyde, 2013.
- [2] Vertax Wind Ltd. (2009) Vertax Wind Ltd. [Online] <http://vertaxwind.com/technology.php#electrical>
- [3] J. Carroll, A. McDonald, D. McMillan, J. Feuchtwang, *Offshore Availability for wind turbines with hydraulic drive train*, 2014.
- [4] N.F.B. Diepeveen, *On Fluid Power Transmission for Offshore Wind Turbines* 2013.
- [5] Vertax Wind Ltd. (2009) Vertax Wind Ltd. [Online]. <http://vertaxwind.com/images.php>
- [6] W.E. Wilson, *Positive Displacement Pumps and Fluid Motors*, 1950.
- [7] K.E. Rydberg, *Efficiencies for variable hydraulic pumps and motors - Mathematical models and operation conditions*, 2009.
- [8] A.J. Laguna, N.F.B. Diepeveen, J.W. Van Wingerden, *Analysis of dynamics of fluid power drive-trains for variable speed wind turbines: parameter study*, 2013.
- [9] M. Sasaki, A. Yuge, T. Hayashi, H. Nishino, M. Uchida, T. Noguchi, *Large Capacity Hydrostatic Transmission with Variable Displacement* 2014.
- [10] WHCP. "Hydraulic Accumulators". Accessed at: <http://www.whcp-oilgas.com/hydraulic-accumulator/>
- [11] Artemis Digital Displacement Wind Transmission <http://www.artemisip.com/sites/default/files/docs/2011-11>
- [12] J. Schmitz, N. Vatheuer, H. Murrenhoff, *Hydrostatic drive train in Wind Energy Plants*, RWTH Aachen University.
- [13] Compact CBP Product manual, <http://www.boschrexroth.com/ics/Vornavigation/VorNavi.cfm?Language=EN&PageID=p537321>
- [14] H. Polinder, F.F.A. van der Pijl, G. de Vilder, P.J. Tavner, *Comparison of Direct-Drive and Geared Generator Concepts for Wind Turbines*, 2006
- [15] C. E. Soraghan, W. E. Leithead, H. Yue, J. Feuchtwang *Double Multiple Streamtube Model for Variable Pitch Vertical Axis Wind Turbines*
- [16] J.Carroll, A. McDonald, J. Feuchtwang, D. McMillan, *Drivetrain Availability in Offshore Wind Turbines* EWEA 2014
- [17] <http://www.artemisip.com/our-technology>
- [18] J. Schmitz, N.Diepeveen, N. Vatheuer, H. Murrenhoff, *Dynamic Transmission Response of a Hydrostatic Transmission measured on a Test Bench*, 2012. <http://www.boschrexroth.com/ics/Vornavigation/VorNavi.cfm?Language=EN&PageID=p537321>
- [19] The Engineering Toolbox http://www.engineeringtoolbox.com/metal-alloys-densities-d_50.html
- [20] D.C. Quarton, *An international design standard for offshore wind turbines: IEC 61400-3* GL Garrad Hassan, 2005.
- [21] G. Bywaters, V. John, J. Lynch, P. Mattila, G. Norton, J. Stowell, M. Salata, O. Labath, A. Chertok, D. Hablanian, *Northern Power Systems WindPACT Drive Train Alternative Design Study Report* Period of Performance: April 12, 2001 to January 31, 2005.
- [22] C. Walford, K. Lybarger, T. Lettenmaier, D. Roberts, *Medium-Speed Drivetrain Test Report* September 1, 2002 December 30, 2007

“

Reliability and uncertainty modelling

”

MARE-WINT: New Materials & Reliability in Offshore Wind Turbines Technology

Improving the Reliability and Optimising O&M Strategies for Offshore Wind Turbines

S.G.Horcas, E. di Lorenzo, J. Martinez, R. Mehdi¹, D. Mehta, G. Pereira, R. Soman

¹World Maritime University, Maritime Risk & System Safety (MaRiSa) Group, rm@wmu.se

ABSTRACT

The aim of the European Commission funded MARE-WINT project is to ‘reduce cost of energy, by improving reliability of [offshore] wind turbines (OWTs) and their components, and optimizing operation and maintenance (O&M) strategies’ [1]. The project is divided into seven work packages (WPs), and between 15 Early Stage Researchers (ESRs), spread across 17 institutes [2]. This paper describes some of the current work being undertaken by a selection of ESR’s in MARE-WINT.

1. Introduction

Improving the reliability of offshore wind turbines is currently an area of great research interest. Organizations such as the European Commission are funding various projects and researchers in the domain; MARE-WINT is one such project. The aim of MARE-WINT as mentioned above is essentially, to improve the reliability, and optimize the operation and maintenance of offshore wind turbines. In order to fulfill this aim, the research is carried out in the context of a reference wind turbine. The reference wind turbine under research in MARE-WINT is the DTU (Technical University of Denmark) 10 MW Reference Wind Turbine (RWT).

Description	Value
Rating	10 MW
Rotor orientation, configuration	Upwind, 3 blades
Control	Variable Speed, Collective Pitch
Drivetrain	Medium Speed, Multiple Stage Gearbox
Rotor, Hub Diameter	178.3m, 5.6m
Hub Height	119m
Cut-in, Rated, Cut-out Wind Speed	4m/s, 11.4m/s, 25m/s
Cut-in, Rated Rotor Speed	6RPM, 9.6RPM
Rated Tip Speed	90m/s
Overhang, Shaft Tilt, Pre-Cone	7.07m, 5°, 2.5°
Pre-bend	3m
Rotor Mass	229 tons (Each Blade ~ 41 tons)
Nacelle Mass	446 tons
Tower Mass	605 tons

Table 1 – Specifications of the DTU 10 MW Reference Wind Turbine. Source [3]

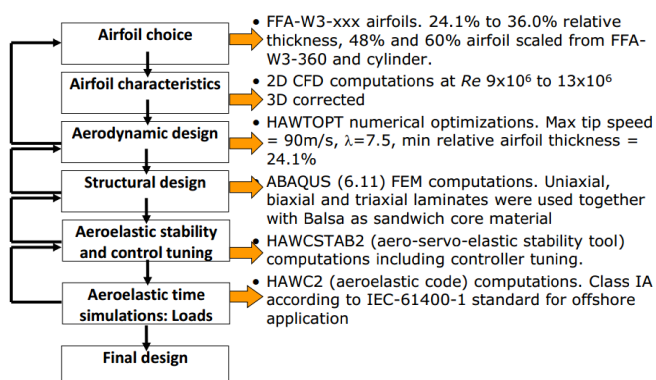


Fig.1: Method followed by DTU for designing the Reference Wind Turbine. Source: [4]

In MARE-WINT, the tasks of further optimizing various components of the wind turbine system are distributed between various researchers, with each researcher working in a specific Work Package (WP). The project’s six work packages are structured as shown in the following figure. Since all the researchers are working on optimizing the same reference wind turbine, collaboration and cooperation between is an important core aspect of MARE-WINT.

As this conference paper has been prepared for an entire project, rather than an individual researcher, the structure of the paper is unorthodox. Instead of typical sections such as Introduction, Discussion, and Conclusion, the paper is divided into sections that detail the work under progress in each of the various project Work Packages 1 to 5.

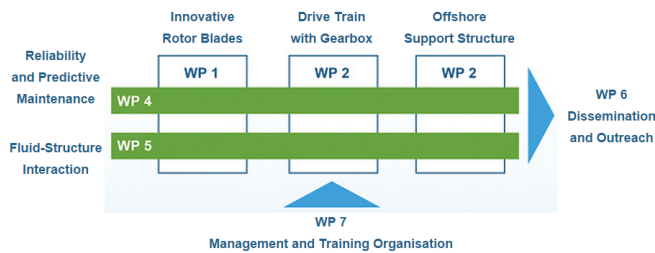


Fig.2 – The ‘Structure’ of the Work Packages in MARE-WINT. Source: [5]

2. WP 1 – Innovative Rotor Blades (ESR 1 & 2)

ESR 1’s task includes *modelling of manufacturing defects in OWT blades*; the aim of ESR 1 is to develop the damage tolerance approach in wind turbine blade sub-structures, focusing on the crack growth mechanisms and detection methods. The trailing edge of the blade can develop damage in the composite material and adhesive interface. The delamination is accompanied by the formation of a crack bridging zone, where intact fibers connect the crack faces behind the tip thus increasing the energy required for crack propagation (Damage tolerance mechanism) [6]. A finite element model of the crack growth mechanisms in a double cantilever beam (DCB), representative of the trailing edge, was developed where different fracture modes were addressed. Experimental tests were conducted in order to fully characterize this structure and support the model. Then a crack monitoring technique was implemented using Fiber Bragg Grating (FBG) sensors in order to track the crack tip and its’ propagation. This sensor approach was incorporated with the finite element model in order to predict the sensor output and extrapolate to a real trailing edge case. Experiments were conducted on DCB specimen crack growth with FBG monitoring under several fracture modes.

The focus of ESR 2 is on *CFD investigations of near-blade 3D flow for a complete OWT configuration*. The current work of ESR 2 is not covered further in this conference paper.

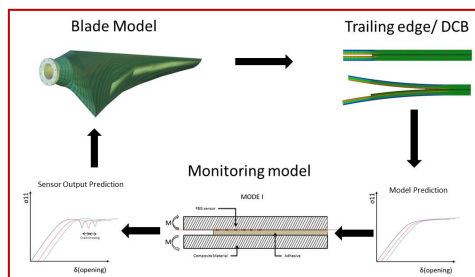


Fig. 3: Investigating the presence of damage in blades, understanding damage propagation mechanism & providing solutions for more reliable structure design using new materials, processes, and sensorisation. ESR 1

3. WP 2 – Drive Train & Gearbox (ESR 3 & 4)

The gearbox is one of the key subsystems in a geared wind turbine providing the task to transfer power from the low speed shaft connected to the rotor to the high speed shaft connected to the generator. As turbines become larger, more power is demanded and gearboxes with higher load capacity need to be designed. A deep knowledge into gearbox dynamics becomes of fundamental importance and noise and vibration measurements are demanded.

ESR 3’s task involves *simulation & experimental validation of drive train loads for offshore specific conditions*. Like ESR 2, further details of this task are not covered in this paper.

The task of ESR 4 primarily involves the *derivation of a strategy for model updating based on experimental data from drive train test facility*. Since several components properties depend on the applied torque and on the rotational shaft speed, a validation in operational conditions needs to be performed. Building on existing techniques such as “Order Tracking” and “Operational Modal Analysis”, a dedicated methodology is going to be developed, by ESR 4, for the analysis of operational gearbox dynamic behavior. Particular attention will be reserved to the separation between structural resonances and excitation orders.

Operational Modal Analysis (OMA) is used by ESR 4 to derive an experimental dynamics model from vibration measurements in operational conditions. It cannot be applied in a straightforward way due to the self-induced vibrations at several rpm-dependent frequencies (gear meshing orders). These frequencies can be wrongly considered resonance frequencies of the system. In order to face these problems, an extensive measurement campaign has been performed at ZF Wind Power on a 13.2MW test rig facility [1] (Fig.1). Accelerations have been measured at more than 250 locations on the test rig and for different load levels and operating conditions. For stationary conditions (at constant rpm) the gear meshing orders will give component discrete constant frequencies that need to be filtered out from the signal in order to determine the resonances. Run-up tests can be considered as a multi-sine sweep excitation and the resonances can be identified combining advanced order tracking methods with operational modal analysis by using a dedicated methodology, named Order-Based Modal Analysis (OBMA). The developed algorithms will be evaluated by means of flexible multi-body simulation models and real experimental data.

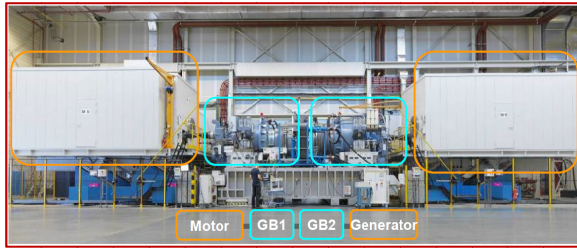


Fig. 4: Building further on existing Order Tracking & Operational Modal Analysis techniques, to develop a new method, and validate it by means of numerical models (flexible MBS model) & experimental data (test rig measurement). ESR 4

4. WP 3 – Offshore Support Structure Analysis (ESR 5 & 6)

The task of **ESR 5** is to develop dynamic modelling and analysis of a floating wind turbine concept, and to compare the results with laboratory test data or field measurements. **ESR 6** by contrast, will focus on bottom fixed substructure analysis, model testing and design for harsh environment. A detailed description of the work carried out by ESR 5 & 6 is omitted from this paper.

5. WP 4 – Reliability & Predictive Maintenance (ESR 7, 8, 9, 10, 11a & 11b)

ESR 7 aims to address OWT condition monitoring based on acoustic emission and long range ultrasonic. **ESR 8's** research focuses on damage detection in metallic & composite structures through the use of Kalman Filter based Neutral Axis tracking. ESR 8's task tries to setup a damage detection strategy at the system level and hence encompasses the selection of the damage detection feature, optimisation of sensor placement to get optimal information using minima resources, signal processing and the damage detection.

Due to the different nature of the materials used in the structures two different damage detection strategies are proposed for the damage detection. The damage detection in towers is carried out using the change in neutral axis (NA) position as the damage sensitive feature while in blades the use of elastic waves is being investigated. The NA of a beam like structure is the property of the cross section of the structure and its condition, and hence is independent of the loading conditions thus through the use of strain sensors we can track the location of the NA accurately and any change in the location of the NA will be an indication of damage. In order to account for the change in the mass orientation of the wind turbine due to the yawing of the nacelle a data fusion strategy using extended Kalman filter (EKF) was proposed in [7]. The EKF yields robustness to the NA tracking even in the presence of measurement noise and temperature changes [8].

ESR 8's methodology was applied on a FE model of the 10MW DTU reference wind turbine and yields reasonably accurate damage detection. The use of EKF uses the strain measurements and yaw angle measurements as the input and yields the NAE location as an estimate. The use of EKF improves the prediction of the NA and as such gives robustness performance of the damage detection strategy in noisy environments and allows us to fuse data. The future plan is to incorporate the rotation of the wind turbine in the data fusion strategy to allow online damage detection in actual working conditions. The damage detection strategies for blades are slightly complicated due to the composite materials and the complex geometry. Furthermore embedding the sensors inside the blade is a problem, thus the use of IR thermography and using remote sensing is being investigated. The entire study undertaken in the task will focus on structural health monitoring for online damage detection. The proposed methodology will be validated on experimentally available data and FE models of the structure available.

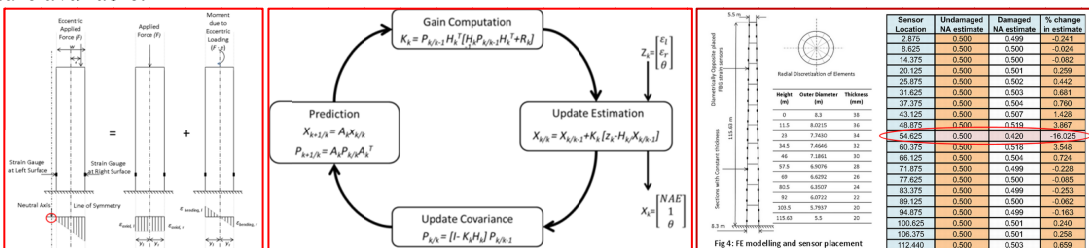


Fig. 5 (L to R): Flexural Strain Distribution over the beam cross-section subject to eccentric loading; Flow Chart for the implementation of KF; Numerical Model of the Tower. Initial investigations have shown promise in the technique to detect damage, & the metric is sensitive to even small extents of damage and shows robustness to presence of measurement noise. ESR 8.

Sensor Location	Undamaged NA estimate	Damaged NA estimate	% change in estimate
2.875	0.500	0.499	-0.241
3.825	0.500	0.500	0.000
4.375	0.500	0.500	-0.082
20.125	0.500	0.501	0.259
28.875	0.500	0.500	0.442
31.825	0.500	0.503	0.681
37.375	0.500	0.504	0.780
43.325	0.500	0.507	1.428
48.875	0.500	0.518	3.887
54.825	0.500	0.420	-16.025
60.375	0.500	0.515	3.048
66.125	0.500	0.504	0.724
71.875	0.500	0.499	-0.228
77.825	0.500	0.500	0.085
83.375	0.500	0.499	-0.253
88.125	0.500	0.500	0.062
94.875	0.500	0.499	-0.163
100.825	0.500	0.501	0.200
106.375	0.500	0.501	0.258
112.440	0.500	0.503	0.659

ESR 9, through his research, aims to reduce wake effect fatigue loads using Large Eddy Simulations (LES). **ESR 10's** research has a focus on navigational risk assessment of vessels operating near OWTs, Lastly, **ESR 11a and 11b** are carrying out research on overall OWT reliability modelling analysis. The work of these researchers is not covered in any further detail in this paper.

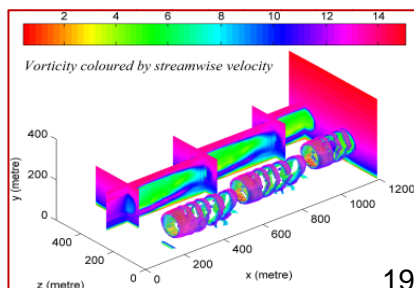


Fig 6: Using Large Eddy Simulation with Energy-Conserving Schemes to study wind farm wake aerodynamics towards predicting loading & fatigue on offshore wind farms. ESR 9

6. WP 5 – Fluid Structure Interaction (ESR 12, 13 & 14)

ESR 12's task involves RANS simulation for hydro-elastic floating substructure prediction. Horcas, et al. [9], summarize ESR 12's work as 'a new development aiming to deform multi-block structured viscous meshes during fluid solid interaction simulations. The focus will be put on the deformation of external aerodynamic configurations accounting for large structural displacements and 3D multimillion cells meshes. In order to preserve the quality of the resulting mesh, it was understood as a fictitious continuum during the deformation process. Linear elasticity equations were solved with a multi-grid and parallelized solver, assuming a heterogeneous distribution of fictitious material Young modulus. In order to improve the efficiency of the system resolution an approximate initial solution was obtained prior to the elastic deformation, based on Radial Basis Functions and Transfinite interpolators. To validate the performances of the whole algorithm, the DTU 10MW reference offshore wind turbine described by [10] is analyzed'.

ESR 13's research focuses on analysis of a twist-coupled aero-elastic design for passive loads reduction on a full scale blade. Further details are not provided in the current paper.

ESR 14 is carrying out investigations into active flow control to improve aerodynamic performance using blade modelling & high quality grid generation. ESR 14 looks forward to achieve an aerodynamic performance improvement of wind turbine blades by decreasing the flow separation and associated noise in real time. This goal will be reached through the implementation into the 10 MW MARE-WINT wind turbine reference of a new rod vortex generator technology that in its MEMS configuration allows an active control. Due to the lack of experimental data for the reference turbine, the 2 bladed 10 m rotor diameter NREL UAE Phase VI wind turbine was selected for validation purposes. A considerable effort was put into the geometry modelling and grid generation for obtaining the high quality structured mesh adequate for the flow study. The upwind and downwind boundaries were located three blade radius away from the rotational plane. The farfield was situated at the same distance from the rotational axis.

In Fig. 7 below, the definition of the domain boundaries for the simulation can be found. At the inlet the static temperature and velocity were specified, meanwhile the static pressure was imposed at the outlet. The blade was defined as Navier-Stokes adiabatic wall.

The RANS simulations were done employing both, Spalart-Allmaras and SST k- ω models. Good agreement was found between experimental and numerical data. In the figure 2 the C_p distribution along the chord for a couple of sections for a 7 m/s inflow speed are shown as example. Once validated through the numerical methods, the vortex generators will be implemented in the NREL blade and their aerodynamic and aeroacoustic effects studied.

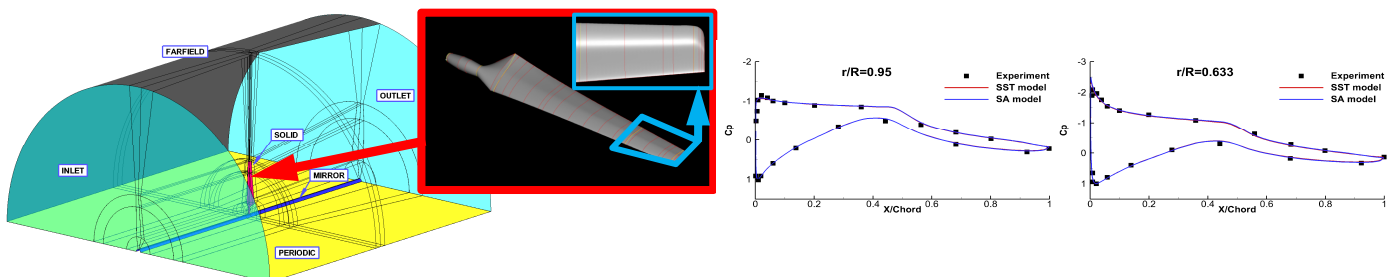


Fig. 7 (L to R): Grid domain; blade geometry with tip detail; C_p distributions along the cross sections 95% & 63% for 7 m/s. ESR 14

7. Conclusions

The work and research in MARE-WINT is on-going, with project deliverables due in September 2015. This paper has presented the results of only a selection of the researchers and research activities. Even the limited results shown in the paper, however, indicate a promising level and quality of knowledge and information. There is utmost confidence that the current and future results from MARE-WINT will be used to improve the reliability of offshore wind turbines, and optimize the operations of the system as a whole.

REFERENCES

- [1][2][5] <http://marewint.eu/> - last accessed on 30th May 2014, 17.00 CET
- [3][4][10] C.Bak, F.Zahle, R.Bitsche, T.Kim, A.Yde, L.C.Henriksen, M.H.Hansen, J.P.A.A.Blasques, M.Gaunaa, A.Natarajan, *The DTU 10-MW Reference Wind Turbine*. Danish Wind Power Research 2013, Fredericia, Denmark (2013). Related data publicly available at <http://dtu-10mw-rwt.vindenergi.dtu.dk/>
- [6] Bent F. Sørensen, "Cohesive laws for assessment of materials failure: theory, experimental methods and application. Doctor of techniques thesis, Risø-R-1736(EN)
- [7] Soman, R, Malinowski, P and Ostachowicz, W. Neutral Axis Tracking for damage detection in wind turbine towers, In: Proceedings of the EWEA 2014, Barcelona, Spain. 10-14 March 2014.
- [8] Soman, R, Malinowski, P and Ostachowicz, W. Kalman-filter based data fusion for neutral axis tracking for damage detection in wind-turbine towers, In: Proceedings of the EWSHM 2014, Nantes, France. 7-12 July 2014.
- [9] Horcas S G., Debrabandere F., Tartinville B., Hirsch Ch., Coussement G., 'Mesh Deformation Tool for Offshore Wind Turbines Fluid Structure Interaction', In: Proceedings of WCCM XI, ECCM V, ECFD VI, 20 – 25 July 2014.

Wind Prediction Enhancement by Supplementing Measurements with Numerical Weather Prediction Now-Casts

A. Malvaldi, J. Dowell, S. Weiss, D. Infield, D. Hill.

Electrical and Electronic Engineering, University of Strathclyde, Glasgow, UK.

Abstract – This paper explores how the accuracy of short-term prediction of wind speed and direction can be enhanced by considering additional spatial measurements. To achieve this, two different data sets have been used: (i) wind speed and direction measurements taken over 23 Met Office weather stations distributed across the UK, and (ii) outputs from the Consortium for Small-scale Modelling (COSMO) numerical weather model on a grid of points covering the UK and the surrounding sea. A multivariate complex valued adaptive prediction filter is applied to these data. The study provides an assessment of how well the proposed model can predict the data one hour ahead and what improvements can be accomplished by using additional data from the COSMO model.

I. INTRODUCTION

THE growth of wind power requires improvements in short-term wind forecast at wind energy sites. As the wind penetration becomes more and more important in the national grids, the accuracy of the wind farms' power output is of fundamental importance for power system operators and for trading on the energy market. The reliability and stability of power systems are decreased, and the operational costs increased, by the high uncertainty in wind. Therefore, it is essential to improve wind prediction at wind farms sites [4], [5] particularly for short forecast periods.

In literature, several different methods have been used to reduce the uncertainty in the forecast of wind speed and direction. Numerical Weather Prediction (NWP) models are mathematical models of the atmosphere and oceans that use current weather observations as inputs. Although these models have a good performance in forecasting the wind speed, their computational time is highly demanding and therefore they are run typically only every six hours. Hence, as NWP models do not provide hourly wind forecasts, many study in recent years have focused their attention to the problem. In order to achieve hourly wind prediction, statistical methods have been employed that do not require long running time and expert knowledge to be used. Moreover, the spatial resolution of NWP is such that a statistical method based on measurements at the site of interest would still out perform the NWP if it could be run quickly.

In previous works, it has been considered the spatio-temporal prediction of wind speed and direction by means of linear complex valued prediction filters [2], [3]. In this paper, it is investigated how the accuracy of temporal prediction can be enhanced by considering additional spatial measurements.

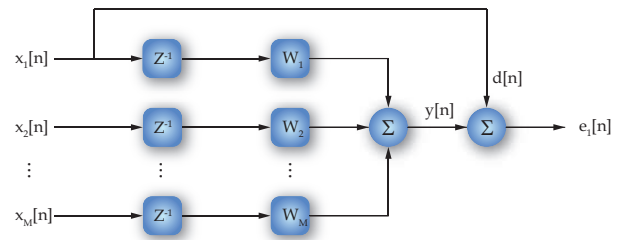


Fig. 1: Multi-channel filter.

II. SPATIO-TEMPORAL PREDICTION

A. Complex Multichannel Data

This study uses hourly mean time series of wind speed and direction measured in M geographically separate sites. These time series are converted in complex-valued vector time series $x_m[n] \in \mathbb{C}$, $m = 1 \dots M$, where the wind speed is the magnitude of the complex variable, the wind direction is the phase, and n is a discrete time index. Moreover, the mean of the time series is calculated and removed to create zero-mean signals.

Using the expectation operator $\mathcal{E}\{\cdot\}$, the cross-covariance of the data is given by $r_{x_i x_j}[\tau] = \mathcal{E}\{x_i[n]x_j^*[n - \tau]\}$, $i, j = 1 \dots M$, which for $i = j$ provides the special case of the covariance for site i . From the values of $r_{x_i x_j}[\tau]$, a covariance matrix \mathbf{R} and \mathbf{p}_m will be defined later. For simplicity, it will be assumed a stationarity model so that the covariance matrix will depend only on the lag time τ .

B. Minimum Mean Square Error Prediction

To predict the time series $x_m[n]$ at the m site at time index n , we utilised past measurements from this site and other sites, whereby $m = 1 \dots M$, with M the total number of sites available. The structure of the predictor, exemplary for $m = 1$, is shown in Figure 1, representing an M channel linear predictor with prediction coefficients $\mathbf{w}_{1,m} \in \mathbb{C}^N$, where N is the temporal window over which prediction is performed. A tap delay line vector

$$\mathbf{x}_m[n] = \begin{bmatrix} x_m[n] \\ x_m[n-1] \\ \vdots \\ x_m[n-L+1] \end{bmatrix} \quad (1)$$

holds this data window at the m th site during iteration n .

The adjustment of the coefficients $\mathbf{w}_{i,m} \in \mathbb{C}^N$, $i, m = 1 \dots M$ is performed such that the prediction error

$$e_m[n] = d_m[n] - \sum_{i=1}^M \mathbf{w}_{i,m} \mathbf{x}_i[n] = d_m[n] - \mathbf{w}_m^H \mathbf{x}[n] \quad (2)$$

with $d_m[n] = x_m[n+1]$ is minimised in the mean square error (MSE) sense, with the vectors \mathbf{w}_m and $\mathbf{x}[n]$ formed from concatenations of $\mathbf{w}_{i,m}$ and $\mathbf{x}_i[n]$, $i = 1 \dots M$, such that

$$\mathbf{x}[n] = \begin{bmatrix} \mathbf{x}_1[n] \\ \mathbf{x}_2[n] \\ \vdots \\ \mathbf{x}_M[n] \end{bmatrix}, \quad \mathbf{w}_m[n] = \begin{bmatrix} \mathbf{w}_{1,m}[n] \\ \mathbf{w}_{2,m}[n] \\ \vdots \\ \mathbf{w}_{M,m}[n] \end{bmatrix} \quad (3)$$

contain all measurement time series and filter coefficients, respectively.

The MSE of the prediction error $e_m[n]$ is given by

$$\xi_m = \mathcal{E}\{e_m[n]e_m^*[n]\} \quad (4)$$

$$= \sigma_{x_m}^2 - \mathbf{w}_m^H \mathbf{p}_m - \mathbf{p}_m^H \mathbf{w}_m - \mathbf{w}_m^H \mathbf{R} \mathbf{w}_m \quad (5)$$

By minimising the mean-squared error the result

$$\mathbf{w}_{m,\text{opt}} = \mathbf{R}^{-1} \mathbf{p}_m, \quad (6)$$

is known as the Wiener-Hopf solution [2], [7], where $\mathbf{R} = \mathcal{E}\{\mathbf{x}[n]\mathbf{x}^H[n]\}$ is the covariance matrix of the data, and $\mathbf{p}_m = \mathcal{E}\{d_m[n]\mathbf{x}^*[n]\}$ the cross-covariance vector between the desired signal $d_m[n]$ for site m and the data vector. Its minimum value for the MSE in (5) can be calculated by inserting (6),

$$\xi_{m,\text{min}} = \sigma_{x_m}^2 - \mathbf{p}_m^H \mathbf{R}^{-1} \mathbf{p}_m \quad (7)$$

Therefore, the prediction is made by using N previous values of the M time series that are weighted by the optimal coefficients, $\mathbf{w}_{m,\text{opt}}$, with the objective to minimise the MSE of the forecast at site m , $m = 1 \dots M$.

C. Thinning of the Predictor

In order to investigate which of the remaining $M - 1$ sites have the greater contribution on the wind forecast for a target site m , the aim is to create a sparse prediction filter combining only dominant contributions. The effect of not taking particular spatial/temporal information into account can be investigated based on reduced or thinned versions of the covariance matrix and cross-correlation vector in (6)

Thinning of \mathbf{R} and \mathbf{p}_m has been computed by removing a tap at position k , $k \in [1; K]$ and discarding the appropriate entries from \mathbf{R} and \mathbf{p}_m using a matrix

$$\mathbf{V}_{K,k} = \begin{bmatrix} \mathbf{I}_{k-1} & \mathbf{0} & \mathbf{0} \\ \mathbf{0} & \mathbf{0} & \mathbf{I}_{K-k} \end{bmatrix} \in \mathbb{Z}^{(K-1) \times K} \quad (8)$$

Thinning is applied recursively to eliminate an increasing number of coefficient. Generally, at the i th iteration the coefficient is removed that minimises the minimum mean-squared error (MMSE). At each iteration the MMSE is calculated, and the removed coefficient is noted. Therefore, after L iterations, only $MN - L$ dominant coefficient remain.

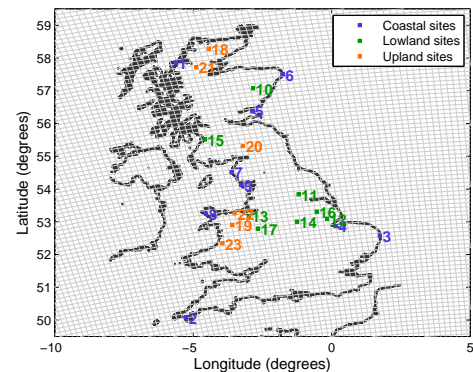


Fig. 2: Map of the Met Office sites overlapping the COSMO model grid.

III. WIND DATA

For this study, two different type of data set have been used to test the prediction filter, which are described below.

A. Met Office Data

The British Atmospheric Data Centre [6] provided the Met Office Integrated Data Archive System (MIDAS) set of onshore weather data from 37 weather stations across the UK, from which a selection of 23 sites with at least 98% of good data has been made shown in Figure 2. The observations are taken at 10m from ground and provide wind speed [knots] and direction [deg] sampled every hour. The time window chosen for this study is of two years, starting from 00:00h on 1/01/2006 to 23:00h on 31/12/2007.

B. COSMO Model Data

The Consortium for Small-scale Modelling (COSMO) [1] has developed a non-hydrostatic limited-area atmospheric prediction model. The data provided are the zonal and meridional wind speeds [m/s], u and v respectively, at 10m above ground and Figure 2 shows the area covered by the model grid points. The resolution of the data is of 0.1deg; the original resolution of the model has been reduced. For the purpose of this study, data for the two years of interest, 2006 and 2007, have been selected and converted in to complex-valued time series.

IV. RESULTS

The algorithm has been tested on the MIDAS and COSMO data set. The filter coefficients have been calculated using the data from 2006 as training data, and then the prediction algorithm has been tested on the data from 2007.

A. Prediction Based on MIDAS Data Set

To analyse the spatial and temporal correlation between the different sites, the elements of the covariance matrix have been investigated. In figure 3, it is shown a colour plot of the covariance matrix for the 23 Met Office weather stations: on the main diagonal there are the covariance of each site and on the off-diagonal the cross-covariance between different

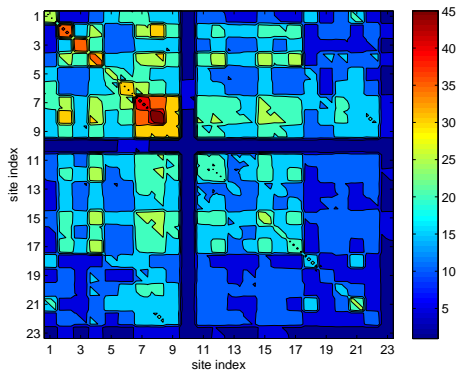


Fig. 3: Colour plot of the covariance matrix for the 23 Met Office weather stations.

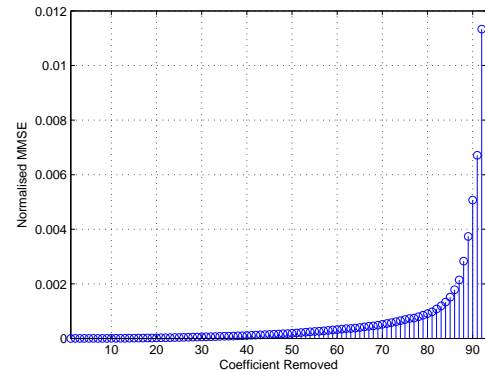


Fig. 4: Plot of the normalised MMSE for site 7 as a function of the removed coefficients from the covariance matrix.

Site 8 analysis:	Site 7 analysis:
Normalised MMSE: 0.0539	Normalised MMSE: 0.0664
site 8, lag 0: 99.4[%]	site 7, lag 0: 98.9[%]
including site 8, lag 2: 99.5[%]	including site 8, lag 0: 99.3[%]
including site 2, lag 0: 99.6[%]	including site 8, lag 3: 99.5[%]
including site 7, lag 0: 99.7[%]	including site 9, lag 0: 99.6[%]
including site 1, lag 0: 99.7[%]	including site 1, lag 0: 99.7[%]

TABLE I: Dominant coefficients that contribute to the MMSE for the prediction of sites 8 and 7.

sites. As evident from figure 3, some sites have a high cross-correlation; e.g. sites 7, 8 and 9 which are situated in the Gwynedd and Cumbria areas respectively. Whereas other wind measurements are poorly correlated together. In particular, sites 10 (in Aberdeenshire) and 23 (in Dyfed) have negligible variance with all the stations.

To investigate the contribution of each site to the prediction of one target site, the respective coefficients inside the covariance matrix have been removed one by one and the mean-squared error calculated at each step. Results from two interesting sites are shown in table I, where the MMSE obtained for the prediction of each site is reported together with the contribution to the MMSE from the first 5 more important sites. It is interesting to note that, for site 8, one important contribution appears to be from site 2 (situated on the coast of Cornwall, see figure 2) that is upstream to site 8. In fact, site 2 together with the target site 8 contribute more than 99% to the MMSE. Results for site 7 shows the correlation between sites 7, 8 and 9, as mentioned earlier. Considering the relative position of each weather station, it can be deduced that sites located upstream have the major impact on the prediction of the target site. This is confirmed by results in table I where sites 8 and 9 contribute up to 99.6% of the MMSE for the prediction at site 7.

Another interesting aspect to notice is that only few sites contribute to the MMSE, as evident from figure 4. The plot shows the contribution to the MMSE for the prediction at site 7; it is apparent that only the last coefficients have a significant impact on the error. Similar results are obtained for all the 23 MIDAS sites.

B. Prediction with Additional COSMO Data

The attention was focused on the analysis of only site 8. The procedure previously described has been carried out using other two data sets: one set considers only the measurements from the MIDAS site 8 (the target site) and the surrounding data from the COSMO model, and the other data set contains all the 23 MIDAS sites plus the COSMO data around site 8. The COSMO data have been selected considering the closest grid point to the target site and then selecting the data every 5 grid points from a 20x20 grid around it.

Table II shows the normalised minimum mean-squared error of the prediction for site 8. The MMSE previously obtained with all the MIDAS site was 0.0539 (see table ??). It is evident that the addition of the COSMO data provides an improvement in the prediction, especially when added to all the MIDAS sites; where the MMSE is reduced by more than 8%. In table II are also reported the first five more important contributions to the error from each site or COSMO grid point. It is evident that the most important contribution comes from the previous measurements of the target site. It is interesting to note that, when the COSMO data are added to the Met Office weather data, the next contributions come from neighbouring COSMO grid points instead of site 7 that is situated downstream to site 8. As expected, the COSMO grid points 44 and 46 are situated respectively south-west and south to site 8. This result suggests that depending on the position of the target site and the prevailing direction of weather systems, the contribution to the prediction can be improved by including only the appropriate data. When considering only the measurements from the site 8 and the COSMO data, the prediction error is the same as for the case with all 23 sites. From table II, it can be seen that the most important COSMO grid points are the closest one (grid point 13) and the one south to the target site.

C. Wind Forecast

Finally, the algorithm prediction has been tested for all the sites. It has to be noticed that, to avoid transient behaviours and problems in the prediction, it is necessary that the time series considered do not have missing data. For this purpose, a

MMSE contributions [%]

Prediction made with site 8 and COSMO data:

Normalised MMSE: 0.0530

site 8, lag 0: 99.3

including site 8, lag 1: 99.4

including COSMO grid point 13, lag 0: 99.4

including COSMO grid point 24, lag 0: 99.5

including COSMO grid point 9, lag 2: 99.6

Prediction made with all MIDAS Site and COSMO data:

Normalised MMSE: 0.0492

site 8, lag 0: 98.9

including site 8, lag 1: 99

including COSMO grid point 2, lag 0: 99.1

including COSMO grid point 44, lag 0: 99.1

including COSMO grid point 46, lag 0: 99.2

TABLE II: Dominant coefficients that contribute to the MMSE for the prediction of site 8 using 3 different data set.

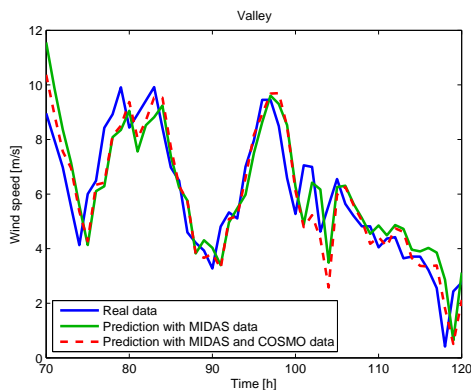


Fig. 5: Time series from site 8 (in blue), prediction with only MIDAS sites (in green) and COSMO data (in red). Zoom on the time window between hours 70 and 120

time window of 170 hours has been selected, from 8/02/2007 to 15/02/2007.

As an example, the forecast for site 8 is shown in figure 5, where a zoom in has been made for a better legibility. The prediction has been made in two different ways; the first method uses all the 23 Met Office sites, and the second technique considers additional COSMO model data to the wind measurements from MIDAS sites. To compare the two forecasts the root-mean-square error has been calculated. As confirmation of the previous results, the prediction made using additional COSMO data has a smaller error than the other; 1.89 and 1.94 respectively.

In general the COSMO data do help in the prediction of MIDAS site time series. However, it has to be mentioned that for few exceptions the additional data from the model are not beneficial for the forecast. It is important to note that the results depend on the method and criteria used to select the COSMO data to add to the MIDAS time series. Moreover, in this study the selection of the COSMO data has been carried out using the same method for all sites. It is believed that, by adapting the selection technique for the model data to the target site, the COSMO data can improve the prediction for all sites. This aspect certainly requires further investigations.

V. CONCLUSION

This paper has analysed the relative importance of each time series within the prediction algorithm in order to achieve the lowest forecast error with the minimum number of data. The results showed that some sites have a strong correlation and therefore only few sites contribute to minimise the prediction mean-squared error. This suggests that the computational time for the forecast can be reduced and optimised without compromising its accuracy.

Moreover, it has been analysed whether the addition of data from the COSMO model has an impact in the forecast performance. The effect of the COSMO data depends on the position of the target site respect to other MIDAS weather stations and the criteria chosen for the selection of the additional data from the model. In general, with few exceptions, COSMO data do aid in the prediction of MIDAS site time series. A particular case has been analysed more in detail; the selected measurements were from Valley (site 8) on the north-western coast of Wales. In that case the prediction error has been reduced by adding some data from neighbouring points around the target site.

As several methods can be used to include additional data from the COSMO model, this requires further investigation on the best technique to select the data. It has to be noticed that the results seem to be site specific, therefore a deeper analysis of this aspect is needed.

Further improvement can certainly be achieved by considering the non stationarity of wind. Annual cycles as well as seasonal variation in wind regimes have motivated the development of a cyclo-stationary Wiener filter [3]. Future work is planned to test the cyclo-stationary filter with the additional COSMO model data. In addition to this, diurnal variations, as sea breeze regimes, remain to be analysed and need to be explored.

ACKNOWLEDGEMENTS

The authors gratefully acknowledge the UK Meteorological Office and the British Atmospheric Data Centre for their supply of meteorological data.

REFERENCES

- [1] COSMO (Consortium for Small-scale Modelling): available at: www.cosmo-model.org
- [2] J. Dowell, S. Weiss, D. Hill, and D. Infield, *A Complex-Valued Multichannel Filter Approach to Short Term Directional Wind Forecasting*. Wind Energy, 2013.
- [3] J. Dowell, S. Weiss, D. Hill, and D. Infield, *A Cyclo-Stationary Complex Multichannel Wiener Filter for the Prediction of Wind Speed and Direction*. In 21st European Signal Processing Conference, Marrakech, Morocco, September 2013.
- [4] T. Gneiting, K. Larson, K. Westrick, M. Genton and E. Aldrich, *Calibrated Probabilistic Forecasting at the Satellite Wind Energy Center: The Regime-Switching Space-Time Method*. Journal of the American Statistical Association, **vol.101** (2006), No. 475, pp. 968-979.
- [5] A. Hering, and G. Genton, *Powering Up with Space-Time With Forecasting*. Journal of American Statistical Association, **vol.105** (2010), No. 489, pp. 92-104.
- [6] UK Meteorological Office. Met Office Integrated Data Archive System (MIDAS) Land and Marine Surface Stations Data (1853-current), [Internet].NCAS British Atmospheric Data Centre, 2012. Available from http://badc.nerc.ac.uk/view/badc.nerc.ac.uk__ATOM__dataent_ukmo-midas.
- [7] B. Widrow, and S. D. Stearns, *Adaptive Signal Processing*. Prentice Hall, Englewood Cliffs, New York, 1985.

“

offshore environmental aspects

”

“

Offshore

”

Authors Index

Abdulrahim, Anas.....	127
Ahmad, Tanvir.....	123, 131
Ahmet, Gökhan.....	71
Anik, Ezgi.....	127
Argent, Michael.....	179
Bartolini, Nicola.....	105
Bierbooms, Wim.....	155, 175
Bortolotti, Pietro.....	96
Bos, René.....	155
Bottasso, Carlo L.....	96
Brand, Carl Robert.....	109
Bromm, Marc.....	163
Castellani, Francesco.....	105
Chatelain, Philippe.....	15, 55
Chivae, Hamid.....	55
Crabtree, Christopher.....	131, 159
Danzerl, Daniel.....	147
Dawid, Rafael.....	183
Di Lorenzo, Emilio.....	192
Dowell, Jethro.....	196
Duponcheel, Matthieu.....	15
Ederer, Nikolaus.....	19
Ehrich, Sebastian.....	167
Elmontaser, Ashraf.....	39
Feuchtwang, Julian.....	139
Fischer, Annette.....	51, 119
Frère, Ariane.....	55
Garinei, Alberto.....	105
Gilmour, Conor.....	100
Giyamani, Ashim.....	175
Gonzalez Horcas, Sergio.....	192
Hegberg, Terry.....	76
Heinemann, Detlev.....	171
Hill, David.....	196
Hillewaert, Koen.....	55
Holst, David.....	67
Infield, David.....	84, 196
Jamieson, Peter.....	84, 143

Jost, Eva.....	51, 119
Kazemtabrizi, Behzad.....	123, 131, 159
Kim, Taeseong.....	92
Klein, Levin.....	47
Krämer, Ewald.....	47, 51, 119, 151
Kühn, Martin.....	31, 35, 135, 163, 171
Lahuerta, Francisco.....	10
Leblebici, Engin.....	71
Leithead, William.....	139, 143, 147
Lutz, Thorsten.....	47, 51, 119, 151
Macmahon, Euan.....	187
Malvaldi, Alice.....	196
Martinez, Javier.....	192
Matthews, Peter.....	123, 131, 159
Mcdonald, Alasdair.....	187
Mcgugan, Malcolm.....	1
Mehdi, Raza.....	192
Mehta, Dhruv.....	192
Mikkelsen, Lars.....	1
Mikkelsen, Robert.....	55
Mills, Peter.....	84
Moens, Maud.....	15
Muskulus, Michael.....	6, 80
Nayeri, Christian.....	67
Nijssen, Rogier.....	10
Ostovan, Yashar.....	127
Ozgen, Serkan.....	88
Paschereit, Christian.....	67
Pavese, Christian.....	92
Pechlivanoglou, George.....	67
Peinke, Joachim.....	43, 63, 167
Pereira, Gilmar.....	1, 192
Pignattini, Roberto.....	105
Reguera, Luis.....	139
Robb, David.....	143
Rott, Andreas.....	35
Sandal, Kasper.....	6
Schafhirt, Sebastian.....	80

Schramm, Matthias.....	43
Schulz, Christoph.....	151
Schwarz, Michael.....	63
Seume, J.r.....	109, 114
Siddons, Craig.....	143
Sluys, Lambertus.....	10
Smith, Christopher.....	131, 159
Soman, Rohan.....	192
Steinfeld, Gerald.....	171
Stock, Adam.....	143
Stoevesandt, Bernhard.....	43, 63, 167
Tuncer, Ismail.....	71, 88
Ungurán, Róbert.....	135
Uzol, Oguz.....	127
Vali, Mehdi.....	31
Van Bussel, Gerard.....	155, 175
Van Der Meer, Frans.....	10
Vollmer, Lukas.....	171
Vorspel, Lena.....	43
Wang, Zi.....	59
Weiss, Stephan.....	196
Winckelmans, Grégoire.....	15
Wolff, Torben.....	114
Yirtici, Ozcan.....	88
Yue, Hong.....	147
Zwick, Daniel.....	6

